Damping in Monopile-Supported Offshore Wind Turbines

by

Chao Chen

A thesis submitted for the degree of
Doctor of Philosophy

Department of Civil, Environmental and Geomatic Engineering
University College London

March 2020

Declaration

I, Chao Chen, confirm that the work presented in this thesis is my own. Where information has been derived from other sources, I confirm that this has been indicated in the thesis.

Signature:

Date: 02.03.2020

Abstract

Vibration damping in offshore wind turbines (OWTs) is a key parameter to predict reliably the dynamic response and fatigue life of these systems. However, a comprehensive review of damping in OWTs identified the difficulties in quantifying the individual contributions from different damping sources that lead to considerable variation in the recommended values.

First-principle models were developed to quantify the damping contributions from aerodynamics, hydrodynamics, and soil-structure interaction. Results from these models were systemically compared to published values and where appropriate with simulation results from the software package FAST. The range of values obtained for aerodynamic damping confirmed those available in the literature. The modelling of hydrodynamic damping showed that this damping is much smaller than usually recommended for large-size OWTs. Soil damping strongly depends on the soil specific nonlinear behaviour.

Then the study focused on the aerodynamic damping in operating wind turbines. It is evident that even for the simplest free vibration test, conventional damping ratios assigned separately in the fore-aft (FA) and side-side (SS) directions cannot correctly characterise the vibration of wind turbines. A new aerodynamic damping model was developed to account for this coupling. This model is based on blade element momentum (BEM) theory and a linearisation of the aerodynamic forces, resulting in an aerodynamic damping matrix providing a new description of aerodynamic damping. The derivation of the aerodynamic damping matrix initially assumes that the inflow wind field is constant and uniformly distributed in the rotor plane. Then a turbulent and non-uniform wind field was considered. The aerodynamic damping model was successfully verified against FAST.

In practice, the identification of damping from measured data is required. A novel approach based on the measurement of frequency response functions was developed to identify the aforementioned aerodynamic damping matrix. Numerical simulations confirmed the potential of this identification approach.

Impact Statement

Europe has witnessed the fast development of offshore wind over the past two decades and offshore wind is believed to meet more than 5.2% of the electricity demand in the near future [1]. However, OWTs suffer from severe fatigue damage caused by ambient excitations. It is very important to assign damping values in the preliminary design stage of OWTs as the fatigue life prediction and any other vibration-based analysis depend on the damping level. The comprehensive review on the vibration damping provided in this study can be used as a guide for engineers to determine the range of damping values for monopile-supported OWTs. The developed physics-based models can be used to estimate the contribution from aerodynamic, hydrodynamic, and soil damping quickly and separately.

Aerodynamic damping has the largest damping contribution for operating wind turbines and this study investigated it in detail. A new aerodynamic damping model was developed, which considers the coupling between the FA and SS motions neglected in conventional models based on damping ratios. In cases when the definition of aerodynamic damping is required, the aerodynamic damping matrix proposed in this work can be used to capture the tower-rotor interaction and allows faster computation compared to a fully-coupled model, *e.g.* for mechanical finite element (FE) models of wind turbine substructures including soil-structure interaction aiming at detailed fatigue analysis.

Furthermore, the developed aerodynamic damping model gives new insights into the mechanism of aerodynamic damping in operating wind turbines. The aerodynamic damping matrix can be used as the target of aerodynamic damping identification. The identification procedure based on frequency response functions developed in this study provides a feasible way to obtain the aerodynamic damping matrix from measured data in practice. The damping identification based on aerodynamic damping matrix has the potential of replacing the current mainstream damping identification procedures based on damping ratios.

To disseminate the novel contributions from this work to the research community, several papers have been published or are in the process of publication:

Published papers:

Chen C, Duffour P. Modelling damping sources in monopile-supported offshore wind turbines. *Wind Energy* 2018; 21: 1121-1140.

Chen C, and Duffour P, Fromme P. Novel aerodynamic damping identification method for operating wind turbines. *J. Phys.: Conf. Ser* 2019; 1222: 012008.

Paper under review:

Chen C, Duffour P, Fromme P. Modelling wind turbine tower-rotor interaction through an aerodynamic damping matrix. *J. Sound Vib* 2019; research article under review.

Paper to be submitted:

Chen C, Duffour P, Fromme P. Identification of aerodynamic damping matrix for operating wind turbines.

Acknowledgements

First and foremost, I am very grateful to my primary supervisor, Philippe Duffour, for the valuable guidance and continuous support he provided throughout this research project. His patience and encouragement helped me overcome difficulties and grow as an independent researcher. I would like to show my gratitude to my second supervisor, Paul Fromme, for his precious and effective advices provided in our enjoyable meetings.

I thank my parents and sister for their everlasting support and love. Without them, I would never have had the chance to pursue a PhD degree abroad.

Finally, I thank my friends in the UK for their company and help.

Table of Contents

List of Figures

List of Tables

Chapter 1 - Introduction

1.1 Overview

The increasing global energy consumption and the risks associated with the use of traditional energy resources like oil, coal, and natural gas generate a strong incentive to utilise renewable energy. Therefore, the development of renewable energy has received widespread attention. Wind energy technology has developed significantly over the last few decades due to its cost-effectiveness and relative ease of deployment. In the European Union (EU), the cumulative capacity of wind energy has been continuously increasing in recent years with the fastest growth rate compared to other energy sources, as shown in Figure 1-1. Wind energy currently provides 18.8% of the total installed power generation capacity [2], and the best case scenario expects that this energy source can account for 31% of the total power generation capacity by 2030 in the EU [1].

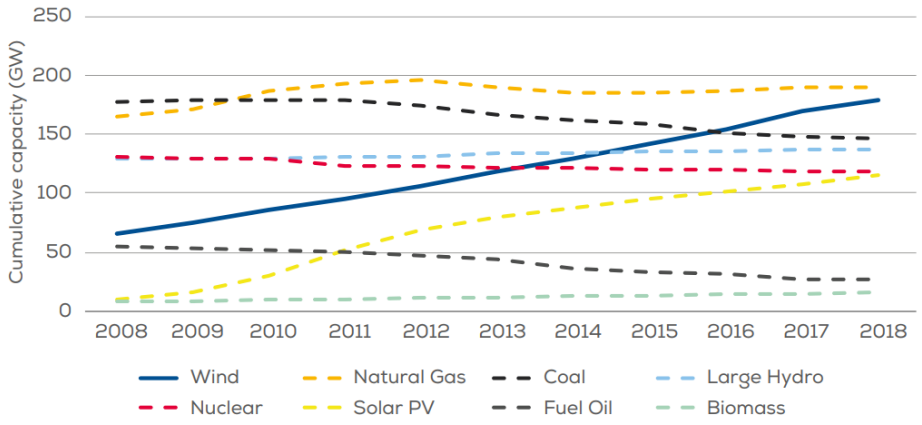

Figure 1-1. Total energy generation capacity in the EU from 2008 to 2018 [2].

Considering that onshore turbines are restricted by geographical and political constraints, offshore wind farms (OWFs) have recently attracted much more emphasis in many countries. In Europe, around 10% of the power generation capacity by wind energy is offshore [2]. In the UK and Belgium, offshore wind accounted for more than 50% of the new wind energy installations in 2018. As wind is stronger and steadier offshore, it is anticipated that this is where future developments in wind energy generation will mostly occur. In the best case scenario [1], offshore wind will provide 25% of the total power generation capacity of wind energy in the EU. Except for some

prototypes such as the floating wind farm, Hywind Scotland Pilot Park Offshore Wind Farm [3]**,** OWFs mostly consist of wind turbines supported by substructures fixed to the seabed. Several different substructure types exist for OWTs including gravity foundations, monopiles, jackets, and tripods. Nevertheless, OWTs supported by monopiles account for more than 80% of the total installed OWTs in Europe [4].

However, the design and maintenance of site-specific OWF with monopile-supported OWTs is still a challenge in spite of valuable past experience and research. The complexities and difficulties in developing more advanced OWTs can be attributed to the following reasons. The offshore environment is extremely harsh and uncertain due to wind, wave, current, and soil conditions. The wind turbine system itself is fairly complex because it integrates blades which interact with the wind, an articulated nacelle which converts mechanical energy into electricity, a control system which adjusts the various components to guarantee a rated output and safety, and a support structure including tower and foundation which protects the whole turbine system against catastrophic failure. The design method for OWTs must consider the relationship between all these components. Therefore, offshore wind farm assets are riskier and more difficult to manage than onshore wind assets.

Most OWTs are currently designed with a slender substructure because using a wider (and therefore stiffer) scheme would require much larger foundations at sea, which would probably be uneconomical. Slender structures are flexible, and this flexibility makes OWTs sensitive to vibration caused by environmental excitations, which greatly increases the possibility of resonance. For instance, previous research has shown that an OWT with low natural frequency can easily be made to resonate due to waves [5]. Resonance amplifies the wind turbine dynamic response, which causes larger fatigue damage and thus can reduce the life span of the turbine [6]. Moreover, during the turbine's lifetime, the impact of variations from the environment, such as scour and change in soil conditions, is not well researched. This reduces the reliability of turbines and makes their management and maintenance more difficult. As the technology matures, OWTs also tend to become larger and installed further away from the coast, as shown in Figure 1-2. Larger wind turbines are more flexible and susceptible to more severe vibration, so more effort is required to investigate their dynamic behaviour.

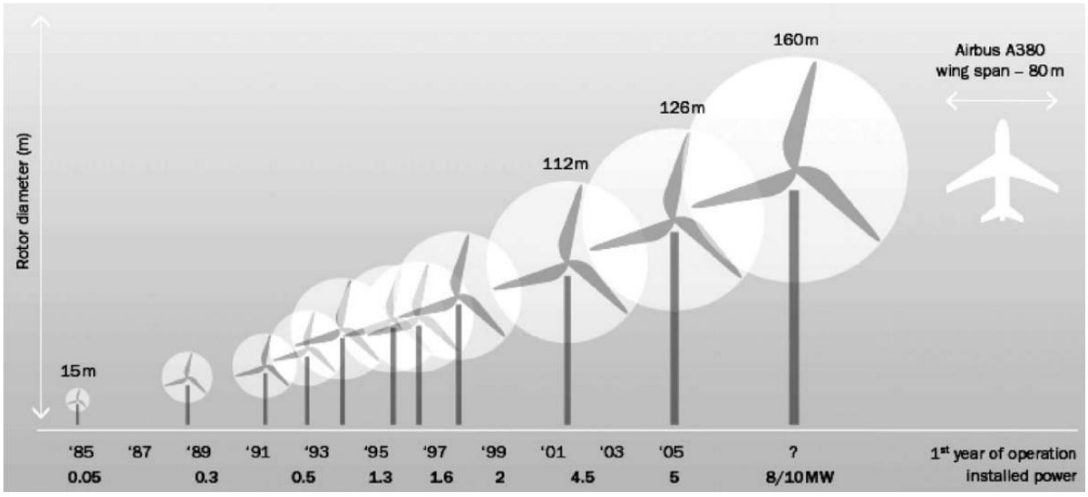

Figure 1-2. Wind turbine size evolution over time [7].

The dynamic behaviour of OWTs is considered critical for their design as they are flexible and thus prone to resonate with environmental excitations. However, the characterisation of dynamic properties of OWT is currently quite limited. For example, the natural frequencies change over the lifetime of OWTs due to environmental variations such as scour at the seabed and tide levels, but the current models hardly consider these long-term effects and therefore doubts remain on the accuracy of their dynamic behaviour predictions [8]. Damping is particularly important for OWTs as it is the only mechanism reducing their vibration amplitude. However, the quantification of damping is difficult because damping in OWTs is strongly dependent on the environmental and operational conditions (*e.g.* wind and wave conditions, parked/operating wind turbines) [9]. Also, it is necessary to consider all the probable load combinations of wind, wave, accidental loads, and even seismic loads to cover the loading experienced in a turbine lifetime. The above considerations render the accurate modelling of turbine systems extremely difficult. Thus, accurate wind turbine models and data from real site conditions are required to consider appropriately the dynamic behaviour over the turbine lifetime and estimate reliably the remaining useful life of existing wind turbine [10]. The importance and complexity of damping in OWTs motivates this study. This study provides insights into the mechanism of damping in OWTs and a new type of simplified wind turbine model was developed to study the aerodynamic damping of wind turbines. This is particularly beneficial for fatigue and reliability analyses which require a large number of simulations.

1.2 Research objectives

The objective of this research was to investigate and characterise more accurately vibration damping in monopile-supported horizontal axis offshore wind turbines. This research started with developing first-principle damping models able to estimate aerodynamic, hydrodynamic and soil damping efficiently. The focus then moved onto developing a new aerodynamic damping model considering the coupling of the FA and SS tower motions. Finally, an identification procedure was proposed based on the new aerodynamic damping model.

1.3 Thesis structure

Chapter 2 starts with a general review of the literature on the dynamics of OWTs, covering basics of aerodynamics, hydrodynamics and soil-structure interaction. This is followed by a comprehensive review of theory, numerical simulations, and experimental measurements of damping in offshore wind turbines. In Chapter 3, first-principle physics-based damping models for aerodynamic, hydrodynamic and soil damping are developed, and the damping estimations using these models compared with results from numerical simulations and results reported in literature. Chapter 4 introduces the theoretical derivations leading to an aerodynamic damping matrix which is the core of a new aerodynamic damping model considering the coupling between the FA and SS tower motions. Further verifications and discussions for this new aerodynamic damping model follow. Chapter 5 is an extension of Chapter 4, in which the aerodynamic damping model is modified so that a non-uniform turbulent inflow wind field can be considered. Chapter 6 proposes a novel aerodynamic damping identification procedure which can be used to predict the parameters in the new aerodynamic damping model. Numerical simulations are used to test the feasibility of the proposed damping identification procedure. Chapter 7 concludes this thesis and recommends possible future works.

Chapter 2 - Literature Review

2.1 Introduction

This chapter gives a comprehensive review in terms of tower damping for monopile-supported OWTs. Section 2.2 reviews the fundamentals of the dynamics of OWTs, followed by a brief introduction to the offshore wind turbine simulation tool FAST (Fatigue, Aerodynamics, Structures, and Turbulence) in Section 2.3. In Section 2.4, previous theoretical and numerical studies of different damping sources in OWTs are reviewed in detail. Section 2.5 focuses on the experimental studies aimed at identifying the damping in both parked and operating wind turbines. Section 2.6 summarises the chapter and concludes on the research questions to be answered in this thesis.

2.2 Dynamics of offshore wind turbine

2.2.1 Basics

A typical monopile supported OWT is comprised of a rotor-nacelle assembly (RNA), a variable-section steel tower, a grouted transition piece transferring the loads from the tower to the foundation, and a monopile substructure partly embedded in the seabed, as shown in Figure 2-1. Currently three-bladed rotors are most popular due to their efficiency in converting wind energy and stability compared to two-bladed rotors. The three blades are connected to a hub and a shaft connected to the hub drives the power generator inside the nacelle. Zaaijer [11] gave the definition of the support structure, namely the whole structure below the yaw system, including the tower, the transition piece, and the foundation. This is also the definition adopted in this thesis, but some researchers exclude the monopile from the support structure.

From the perspective of dynamics, the overall behaviour of the OWT is well described by considering it as a flexible slender cantilever structure coupled with a rotational machine on top subjected to different loads mainly from wind and waves. The slenderness of the tower and of the blades and the large unsteady loads cause the OWT to vibrate continuously and sometimes severely. The support structure itself is a simple structure similar to a cantilever beam with the dynamic response mainly occurring in the FA and SS directions. The FA direction is the main wind direction perpendicular to

the rotor plane for operating wind turbines, while the SS direction is the other lateral direction perpendicular to the FA direction.

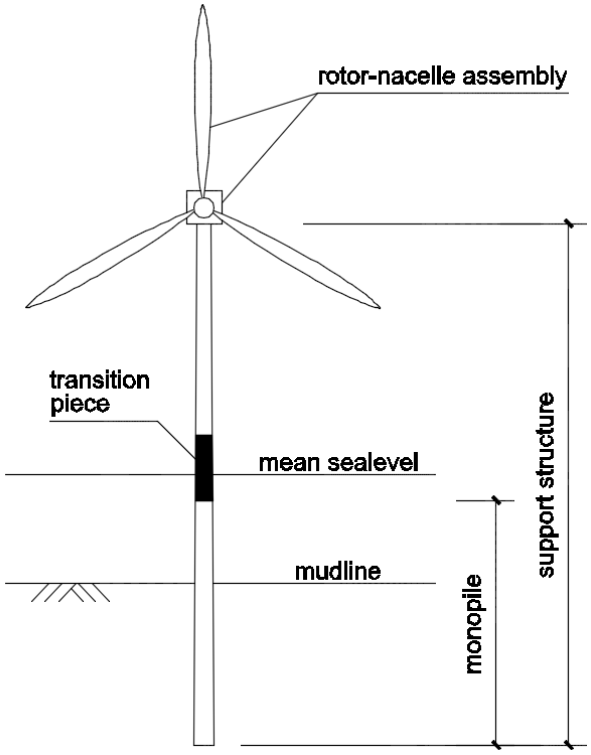

Figure 2-1. Schematic of a monopile-based OWT.

The complexities of its dynamics arise mainly from the stochastic nature of the loads and the rotation of blades [12]. First, the uncertainties from loads complicate the dynamic analysis, and the computational simulations of the loads rely on statistical simplifications which only partially capture the uncertainties. Second, the rotational machinery results in coupled effects with the support structure such as aerodynamic damping and causes harmonic forces transferred from rotor to tower. Third, the components are controlled by electric systems in modern turbines to optimise the wind energy harvested and reduce loads applied to blades and tower in extreme weather. For instance, the yaw angle and pitch angle can be regulated according to operational and weather states, which is very important in a dynamic analysis. Fourth, the geotechnical state of soil under the mudline, the sea state and wind characteristics vary significantly over time and from location to location. The types of soil surrounding the foundations of OWTs, tides, potential earthquakes, ice, currents, and marine growth also have impacts on the dynamic behaviour of OWTs.

As fundamental dynamic properties, natural frequencies are extremely important for slender structures like OWTs. The fundamental natural frequency of OWT towers is relatively low due to their flexibility, with the frequency of the first bending mode usually around 0.3 Hz for currently designed monopile-based OWTs [13]. These low frequencies are close to environmental excitations, increasing the occurrences of resonance. The bulk of the spectral power of the waves is usually between 0.04 Hz and 0.1 Hz, but significant spectral density is also present at higher frequencies ([5][14][15]). The frequency of gusty wind is typically 0.02 Hz according to [14]. Therefore, when the first natural frequency of OWTs decreases due to mechanisms like scour around the monopile at the mudline or the degradation of the soil due to long-term cyclic loading originated from pile-soil interaction, the danger of resonance with environmental excitations increases further, especially for wave loads.

Another key issue is the rotational excitation of the tower from the rotor. The rotation of the blades leads to two important frequencies to be considered, namely the fundamental rotational frequency 1P, and the blade passing frequency 3P if the rotor has three blades. The variable-speed turbines have the rotor operating at different speeds to maximise power output, which consequently widens the 1P and 3P frequency ranges. The design strategy is to keep the first natural frequency away from the 1P and 3P range to avoid resonance. Therefore, the design strategies can be divided into three categories: soft-soft, soft-stiff and stiff-stiff, as illustrated in Figure 2-2.

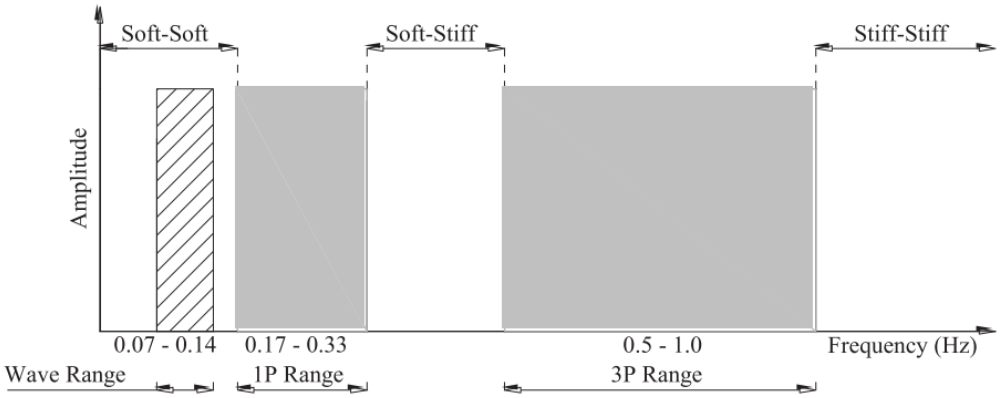

Figure 2-2. Variable design schemes [5].

OWTs are more cost-sensitive than traditional energy offshore structures like oil platforms. A stiff-stiff design would require larger member sizes or more members to

increase the stiffness of the support structure, which would be deemed an uneconomical design for OWTs. By contrast, if OWTs are designed according to a soft-soft design, their stability and strength are more difficult to guarantee because they are more susceptible to resonance with waves and are less able to resist large loads from extreme weather. As a result, the current preferred design is the soft-stiff option between the 1P range and the 3P range [15].

Figure 2-3 shows the potential resonance region and safety region for a soft-stiff OWT. From it, it appears that during the start-up period, resonance may occur as the 3P frequency passes through the value of the first natural frequency. During the operational regime marked by grey area there is no significant resonance happening [15]. However, the determination of the natural frequencies is difficult due to the complexity of the turbine system and the natural frequencies of system change over the lifetime due to various effects. Firstly, the tower-rotor interaction has been proven to have an impact on the natural frequencies of the whole system. Secondly, the sea water dynamically interacting with the substructure forms a so-called hydrodynamic mass, which also has an impact on the natural frequencies. Thirdly, the soil around the foundation adds flexibility to the turbine, and variations in soil conditions caused by mechanisms such as degradation or stiffening under dynamic loads and scour have a significant impact on the natural frequencies [16]. The sensitivity of these factors has been studied ([16][17]).

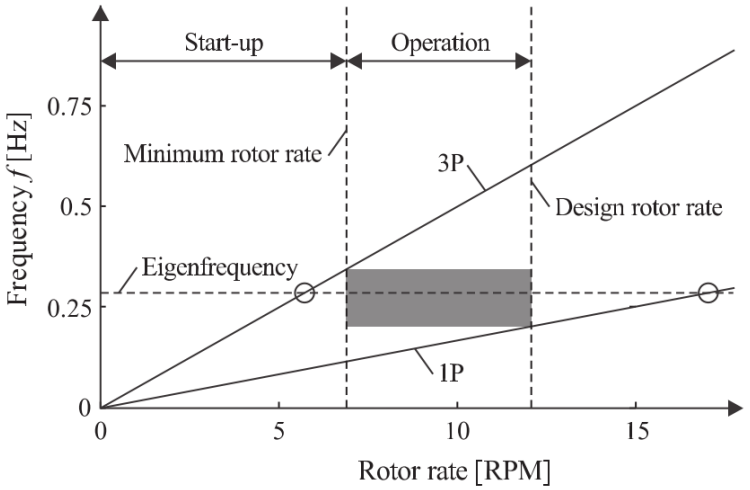

Figure 2-3. Sparse Campbell diagram for a soft–stiff design [15].

The simplest way to model an OWT is to consider the monopile and tower as a cantilever beam and lump the mass of rotor and nacelle assembly at the top, as shown diagrammatically in Figure 2-4. This assumes that the connection between the monopile and the ground is rigid. For this simple model, Tempel and Molenaar [18] proposed the following formula to calculate approximately the first natural frequency:

$$f_1 = \sqrt{\frac{3.04EI}{4\pi^2(M + 0.0227\mu L)L^3}}. \tag{2-1}$$

where M is the lumped RNA mass, EI is the tower bending stiffness, L is the effective length of the tower-pile combination above soil, μ is mass per metre of tower. A significant deficiency of this approach is to ignore tapering of the tower and the finite stiffness of soil which is particularly unrealistic for monopile foundations and will lead to a significant overestimation of the natural frequencies. To capture more detailed dynamic features of the wind turbine system, the interactions between the wind turbine structure and the ambient loading must be considered. These interactions are mainly the rotor-wind interactions described by the rotor aerodynamics, the wave/current-structure interaction described by the hydrodynamics, and the soil-structure interaction. These three interactions are briefly reviewed in the following three subsections.

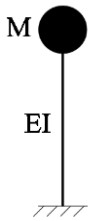

Figure 2-4. Simplified model with a fixed end.

2.2.2 Aerodynamics

Wind profile

The first step to analyse the interaction between wind and rotor is to know the wind speed distribution over the rotor plane. In a real offshore environment, wind speed and direction fluctuate in time and space [19]. It is usual to treat separately low-frequency winds and high-frequency wind components using different statistics and theories. The well-known Weibull function describes the low-frequency or long-term wind (*e.g.* the

mean wind speed with an averaging period of 10 minutes to 1 hour) based on measurements as shown in Figure 2-5. A two-parameter Weibull distribution can be generated by the following equation [20]:

$$F(x) = 1 - e^{-\left(\frac{x}{s}\right)^k}, \tag{2-2}$$

where s is a scale parameter and k is a shape parameter. Using the Weibull function, the distribution of the average wind speed in the long term can be probabilistically determined.

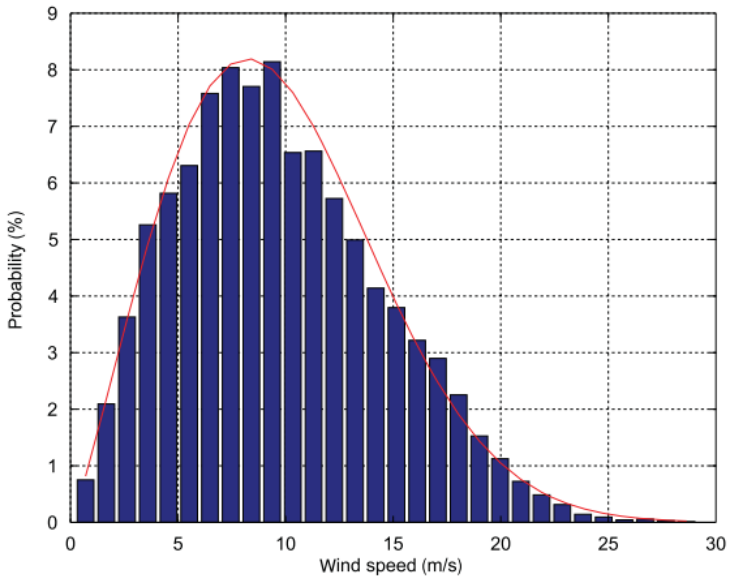

Figure 2-5. Weibull chart [19].

On the other hand, the variation of wind speed in the short term (usually 10 minutes to 1 hour) is found related to the intensity of turbulence and the height. Theoretically, the variation of wind speed with regard to height is influenced by the shear stress within the atmospheric boundary layer. Prandtl's logarithmic law is widely used to describe this variation, in which the average wind speed at height of z is given by:

$$\bar{U}(z) = \bar{U}\left(z_{Ref}\right)\frac{\ln(z/z_0)}{\ln(z_{Ref}/z_0)}, \tag{2-3}$$

where $\bar{U}\left(z_{Ref}\right)$ is the wind speed at the reference height z_{Ref} and z_0 is the roughness length determined by the surface condition.

In most design codes for offshore wind turbines, an empirical method, the power law of wind speed profile is also widely used for simplicity. This law is written as

$$\overline{U}(z) = \overline{U}(z_{Ref})\left(\frac{z}{z_{Ref}}\right)^{\alpha} \tag{2-4}$$

where α is an exponent obtained by measurements (a value of 0.11 is recommended in the Germanischer Lloyd (GL) guideline [21]). The fluctuation of the wind speed in the short term can be generally described with the mean speed and turbulence. The turbulence intensity is defined as $I_t = \sigma/\overline{U}$, in which σ is the standard deviation of the wind velocity time series. The turbulence intensity varies for different sites, and a recommended value of 12% is given in the GL guideline for offshore environment. In wind turbulence modelling, spectral methods are often used. For example, the Kaimal spectrum recommended by Det Norske Veritas (DNV) [22] is widely adopted. The Kaimal spectrum [18] is defined by

$$S(f) = \frac{\frac{4\sigma_v^2 L_v}{U_w}}{\left(1 + \frac{6fL_v}{U_w}\right)^{5/3}}, \tag{2-5}$$

where σ_v is the standard deviation of the wind velocity, L_v is the integral length scale (model dependent), U_w is the mean wind speed and f is the frequency. An inverse fast Fourier's transform (FFT) process can be used to generate the time series of the wind speed from this spectrum. Another widely used spectrum for turbulent wind was developed by von Karman [23].

Blade element momentum theory

Given the inflow field, the aerodynamic loading on the blades must be calculated before applying this loading to the rotor structural model. Several different methods are available to calculate the aerodynamic loading on a wind turbine rotor. The most common method is BEM theory. BEM introduced by Glauert [24] is an efficient approach and has been successfully used for years in industry for helicopters and wind turbines due to its satisfactory results and fast computation. BEM is a combination of one-dimensional momentum theory and blade element theory. The momentum theory assumes a drop in wind pressure when the wind passes the rotor plane, and the drop in pressure is caused by the thrust subjected to the rotor. The blade is divided into several elements and the relationship between the induced velocities, the inflow wind velocity

and the rotational speed is established for every blade element. The basics of BEM theory is to find the attack angle of each blade element provided that the induced velocities are known and then applying the drag and lift coefficients from experimental measurements to calculate the forces on the blade element.

Generally, an iteration process is employed to find the attack angle and induction factors before obtaining the aerodynamic forces. The following steps outline a standard BEM iteration to calculate the aerodynamic forces applied to a blade element. However, further in depth explanations are not provided as the theoretical background can be found in many textbooks on wind turbine aerodynamics [25]. Figure 2-6 shows the relationship between the inflow wind velocity V_0, the rotation speed $V_r = \omega r$ and the relative wind speed V_{rel} seen by the blade element located at the radius r, where ω is the rotation speed of the rotor. A first guess of the axial and tangential induction factors a and a' leads to the relationship between the axial induced velocity $(1-a)V_0$ and the tangential induced velocity $(1+a')\omega r$:

$$\tan\phi = \frac{(1-a)V_0}{(1+a')\omega r}. \tag{2-6}$$

where ϕ is the angle between the plane of rotation and the relative velocity and is the sum of the local attack angle α and the local pitch angle θ. θ can be obtained by summing the pitch angle and the initial twist angle of this blade element. Once ϕ is obtained, the attack angle α can be determined as $\alpha = \phi - \theta$.

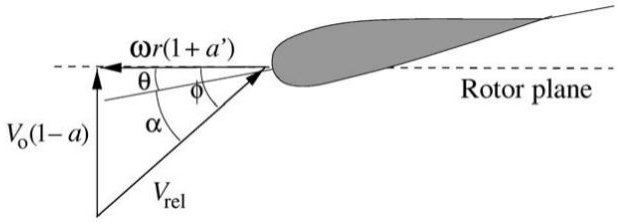

Figure 2-6. Relationship of velocities at the rotor plane [26].

Then the lift coefficient C_l and the drag coefficient C_d can be found given α as the relationship between these two coefficients and the attack angle is one of the basic properties of an airfoil. Equalising the expressions for the elemental thrust and moment leads to the relationship between the two induction factors and ϕ:

$$a = \frac{1}{\frac{4sin^2\phi}{\sigma C_n} + 1}, \tag{2-7}$$

and

$$a' = \frac{1}{\frac{4sin\phi cos\phi}{\sigma C_t} - 1}. \tag{2-8}$$

where $C_n = C_l \cos\phi + C_d \sin\phi$, $C_t = C_l sin\phi - C_d cos\phi$ and $\sigma = (cN_B)/(2\pi r)$, called solidity. c is the chord length and N_B is the number of blades. The difference between the initial guess of the induction factors and the induction factors calculated by Equations (2-7) and (2-8) can be minimised by a number of iterations. If this difference is smaller than a predefined tolerance, then the corresponding induction factors can be used to calculate the elemental thrust and moment by:

$$dT = \frac{1}{2}\rho \frac{V_0^2(1-a)^2}{sin^2\phi} cC_n dr, \tag{2-9}$$

and

$$dM = \frac{1}{2}\rho \frac{V_0(1-a)\omega r(1+a')}{sin\phi cos\phi} cC_t r dr, \tag{2-10}$$

where ρ is the air density. Besides the basic BEM theory, corrections have been developed by Glauert and Prandtl [25] to improve the calculation accuracy. These corrections account for geometric features (*e.g.* hub-loss correction). The skew wake correction, which accounts for the change in wake angle caused by non-perpendicular inflow wind velocity, is important to obtain accurate aerodynamic forces acting on the rotor. The widely used approach for the skew wake correction has been developed by several researchers such as Glauert [27] and Pitts and Peters [28]. The review by Micallef and Sant [29] gives further details on this topic. The classic BEM theory assumes a quasi-steady inflow and wake. Further improvements can be realised by including the dynamic wake/flow model which considers the time delay in the equilibrium between the wake and the aerodynamic loads and the dynamic stall model.

BEM theory has some limitations. First, it is highly dependent on the airfoil data, especially for the values of the lift and drag coefficients. As stated by Hansen *et al*. [26], the BEM model including all engineering corrections is often successful in predicting the aerodynamic loading, but it still requires reliable airfoil data. The airfoil data is derived from experimental measurements and sometimes it is difficult to obtain reliable

airfoil data due to experimental limitations. Second, even with the dynamic inflow/wake correction included, BEM is not suitable for highly loaded rotors because it assumes that the mean induced velocity is relatively smaller than the mean inflow velocity [30]. Third, the blade element theory assumes the aerodynamic forces at one element are two-dimensional, so the spanwise flow is neglected.

More complex models of rotor aerodynamics have been developed to describe a more detailed 3D flow field that develops around a wind turbine, such as the vortex wake model which is a combination of blade aerodynamics and wake analysis. The vortex wake model assumes the flow is inviscid and incompressible, in which the flow around the rotor, and the trailed and shed vorticity released to the wake are described by a lifting line theory, lifting surface theory, or panel method [26]. Compared to BEM, the vortex wake models provide more physics of rotor aerodynamics using boundary layer corrections. Computational fluid dynamics (CFD) models based on Navier-Stokes (NS) equations are able to provide more consistent and physically realistic flow fields around a wind turbine than the BEM and vortex models [31]. Currently, CFD models mainly include generalized actuator disc models which combine the classic actuator disc model and NS equations, and the direct method which directly models the rotor by constructing a body-fitted grid. However, the computational cost of CFD models is extremely high and thus they are not practical methods in the design process yet.

Tower-rotor coupling

It is common to use a coupled model containing the rotor model and tower model to evaluate the air-structure interaction. For the rotor model, the widely used approach to simulate the vibration of the blades is to use the BEM model to calculate the aerodynamic forces experienced by the blades and then use classic beam theory to determine the internal forces in the blades. This is the basis of the rotor design. On the other hand, the rotor model is coupled with the tower model to simulate the overall vibration of OWTs. In addition, the motion of the nacelle and other mechanical components such as shaft and generator are usually modelled as rigid bodies whose motions are coupled with the rotor and tower.

The complexities of the aerodynamic forces experienced by the rotor comes from different sources. For example, as a result of the large size of the rotor and the wind turbulence, the wind speeds seen by different blades of the rotor can differ and cause a

resultant unbalanced aerodynamic force in the side-side direction, which contributes to the 1P loading. In addition, the tilt or yaw of the rotor, and the inertia and weight of the blades can result in unbalanced forces. The introduction of the unbalanced forces acting on a rotor can be found in [32]. Due to the coupling effect between the tower motion and the aerodynamic forces on the rotor, the aerodynamic forces differ significantly from the forces experienced by a static rotor. This coupling effect could cause nonlinear aerodynamic damping and more complicated unbalanced aerodynamic forces. Furthermore, the operational state of the turbine and the tower itself can have an impact on the aerodynamic forces. For example, a parked turbine suffers from higher vibration amplitude compared to an operational turbine, since the wave excitation cannot be mitigated by the aerodynamic damping and in this case the aerodynamic damping can be lower due to the change of pitch angle. The effect of wake for an OWT cluster is another important aspect, which affects the power output and actual loads applied to turbines which are spaced in distance. A brief introduction of the tower-rotor interaction can be found in [19].

Simplified models have been developed to model the tower-rotor interaction. In some studies (*e.g.* [33][34][35]) the RNA is lumped at the top of the flexible tower and the aerodynamic interaction is modelled by applying the rotor thrust at the tower top as a point load and using a dashpot or an equivalent Rayleigh damping to represent the aerodynamic damping. Such decoupled models make it easier to include more detailed soil-structure interaction features (*e.g.* [33][35]) than many integrated simulation tools such as FAST currently allow. Muskulus [36] and Schafhirt and Muskulus [37] used a decoupling strategy based on a simplified rotor load model. A simple expression for the thrust was derived based on actuator disc theory in terms of pitch angle and rotor speed by fitting a thrust coefficient to fully coupled simulation results. However, the damping force in these models relied on damping coefficients obtained by fitting the response to that of an integrated simulation.

2.2.3 Hydrodynamics

Wave theories and spectra

Wave and current loads are important excitations for OWTs. Usually, the waves exciting OWTs mostly are wind waves. However, the waves can be caused by other mechanisms such as earthquakes and tides. Here only wind waves are discussed. When

modelling waves, regular or irregular waves can be used depending on the compromise between accuracy and computational effort. Wave theories have been developed and are well described by many textbooks such as the one by Sarpkaya [38].

A regular wave can be simply defined by the wave height, wave length and water depth. It is suitable when the wave height is much smaller than the wave length and the water depth. An irregular wave can be generated by established wave spectra using inverse FFT similar to the wind spectra. The most widely used spectra are Pierson-Moskowitz Spectrum and JONSWAP Spectrum [39].

Wave-structure interaction

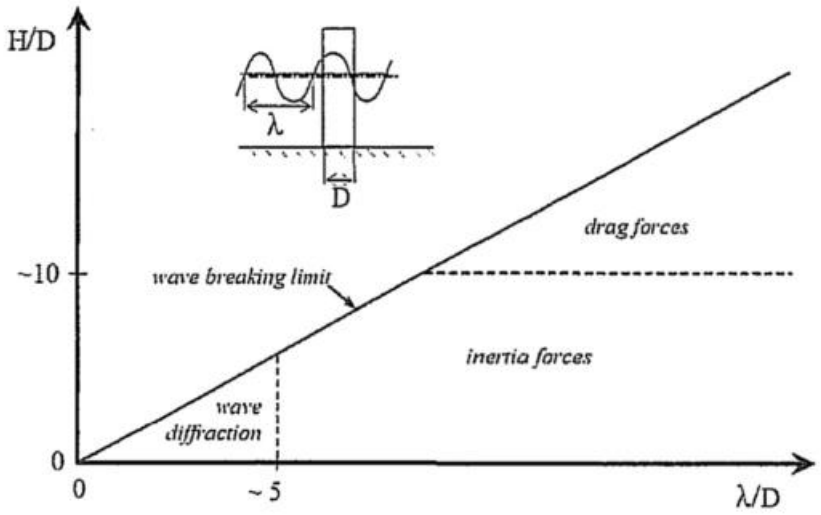

Figure 2-7. Hydrodynamic regime schematic [40].

Unlike onshore turbines, OWTs are exposed to waves and currents which have stochastic characteristics and cause fatigue damage, especially for parked turbines when low aerodynamic damping is present. The theories of wave-structure interaction have been researched for a long time to support the design of ships and offshore structures like oil platforms. The physics of the wave-structure interaction depends significantly on the dimension of the waves and of the structure. The influential parameters include the well-known Keulegan–Carpenter (KC) number, Stokes parameter, Reynolds number, diffraction factor, water depth and the dimension of the submerged structure such as monopile diameter. The available calculation methods for the force experienced by the structure include Morison's equation, diffraction analysis, and the Froude-Krilov

model. The introduction of these methods for OWTs can be found in the work by Henderson *et al*. [41] and hydrodynamics-related textbooks [42].

Figure 2-7 shows the regimes related to OWTs with regard to the water depth-diameter ratio H/D and the wave length-diameter ratio λ/D (diffraction factor). Viscous drag forces represented by Morison's equation are dominant when the cross sections of the structure are small, whereas the wave diffraction which represents non-viscous forces becomes more important for structures with larger cross sections, as structures with large cross sections can modify the wave pattern. Negro *et al.* [40] pointed out that any wave force calculation needs to identify the correct regimes first. Most papers usually adopt Morison's equation to calculate the wave forces, which may cause inaccuracy and lead to errors in fatigue damage calculation, as Morison's equation is better suited to slender structures, while for monopile based large-size OWTs considering other methods like Froude–Krilov model and diffraction analysis to calculate hydrodynamic forces could be more accurate.

2.2.4 Soil-structure interaction

The characterisation of soil-structure interaction is crucial to correctly predict the dynamic behaviour of the turbine system. An appropriate modelling of the foundation is essential since the stiffness and natural frequencies of the entire system largely depend on the foundation and subsoil. The soil also provides damping to the system [43]. Currently monopile supports provide the optimal solution for shallow water depths up to 30 m. Gravity base foundations are also used in some situations, although their instability caused by heave force and overturning moment hinders their more widespread use [44]. For larger turbines located in deeper water, there are several options, such as jacket foundation, suction caisson and special foundations like suction anchors for floating wind turbine systems. However, this thesis focuses on monopiles. There are several methods to analyse and model embedded monopile foundations, such as fixity length method, lumped parameter models (LPMs), distributed springs method based on p-y curves, and FE based methods [45].

Methods based on lumped-parameter springs

In lumped parameter models, the properties of the foundation and the soil are captured through discrete elements such as lateral and rotational springs and dampers as shown in Figure 2-8. These models are particularly useful to determine efficiently the natural

frequencies of the OWT including the influence of axial loads and foundation flexibility [14].

In the studies by Adhikari and Bhattacharya ([14][46]), the flexibility of the foundation in a lumped parameter model was represented by a lateral spring with stiffness k_L and a rotational spring with stiffness k_R, as shown in Figure 2-8(a). The analytical solution of the natural frequencies can be obtained by substituting the spring stiffnesses to a simplified fourth-order differential equation in which the properties of the turbine model are mainly represented by several non-dimensional parameters. The determination of these stiffnesses was through static tests on the 1:100 scale model of a Vestas V90 3 MW wind turbine. Furthermore, a spring accounting for the coupling effect between these two springs can also be added to improve the above method ([47][48]). This is shown diagrammatically in Figure 2-8(b). However, it should be noted that an accurate stiffness for the springs is difficult to obtain since either site measurements or numerical models which require large computational power are needed. In addition, most practical monopiles will likely be surrounded by different layers of soil which complicates further the determination of the discrete spring stiffnesses.

(a) (b)

Figure 2-8. Lumped-parameter model with two springs (a) and three springs (b).

Zania [49] and Damgaard *et al*. [50] both used the concept of dynamic impedance to capture the frequency response of the soil at the location of the pile in the relevant directions. Zania [49] modelled the OWT above the mudline as a single degree of freedom while Damgaard *et al*. [50] used a more realistic HAWC2 aerodynamic model for the structure above the mudline. The dynamic impedances were truncated to the

frequency range of interest and an equivalent lumped parameter model of the soil could be fitted to produce a close frequency response within that range. The coupling of the soil and structure was achieved through the rotation and horizontal displacement of the pile head. This method modifies the frequencies and the initial damping ratio calculated for a fixed bottom model, thus allowing the investigation of the coupling effect of damping on eigenfrequencies by a two-step iterative process. Damgaard *et al.* [15] showed that the inclusion of soil-structure interaction has a strong influence on the calculated fatigue damage compared with the fixed-base model and that the turbine structure is sensitive to soil type. Damgaard *et al*. [50] also studied the impact of soil variability using a probabilistic approach and their previously developed LPM. The results confirmed that the soil type significantly influences the dynamic behaviour of the turbine system. Carswell [13] developed an iterative method using a LPM and three other models used to compute the dynamic behaviour of the superstructure and to determine the parameters in the LPM. The LPM approximates the soil-pile interaction with a rigid bar supported by springs which are represented by a 2×2 stiffness matrix. This stiffness matrix was calculated from an in-house FE program INFIDEL. Harte *et al*. [51] attempted to use sub-structure methodology to construct a multiple degree of freedom system which accounts for the coupling effect between the rotor and the soil flexibility. However, this method is for the analysis of onshore wind turbines. It appears that LPMs can be very useful to investigate the influence of the soil finite stiffness and dissipative properties. They allow rapid predictions of the response of the overall system and are particularly suited to parametric studies, but require careful calibration.

Methods based on p-y curves

The conventional method to model and design monopile foundation for wind turbines is to use Euler-Bernoulli beam elements to represent the pile, and to use Winkler's springs model (p-y curve model) to simulate the subsoil. Such a model is shown in Figure 2-9, in which the lateral resistance is provided by the lateral springs whose stiffness are obtained using p-y curves. Other curves can be used to obtain the stiffness of soil springs in other directions and positions, such as Q-z curves (representing the plug resistance) and t-z curves (representing the vertical resistance by shaft friction). These curves are obtained from measurements of actual piles under static or cyclic loads. This method has been adopted in many design codes for OWT such as DNV [22], International Electrotechnical Commission (IEC) [52], and American Petroleum

Institute (API) [53]. According to API, the formula to determine the p-y curve in the horizontal direction for laterally loaded pile in sand is

$$P = AP_u \tanh\left(\frac{kH}{AP_u}y\right), \tag{2-11}$$

where P is the resisting force, y is the lateral displacement, P_u is the ultimate bearing capacity of soil at depth H, k is initial modulus of subgrade reaction and A is a factor to account for cyclic or static loading condition. More details (different soil types like clay, inclusion of water, layered soil *etc.*) about p-y curve models can be found in [54].

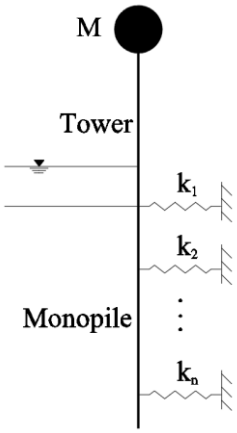

Figure 2-9. Model with discrete springs using p-y curves.

As stated by Naggar and Bentley [55], the classic p-y curve is developed using a pseudo-static method involving the nonlinearities with depth and strain magnitude, but does not consider the stress history and loading frequency. This type of p-y curves cannot assess the impact of hardening, softening, and pore-pressure accumulations which could happen in the soil during the lifetime of OWTs. To improve the current p-y curve model, a dynamic p-y curve was recommended in the paper of Buren and Muskulus [56], which is able to predict the dissipated energy of the turbine system through the foundation.

Methods based on FE method

Considering the deficiencies of traditional p-y curves, Achmus *et al.* ([57][58][59]) used a 3D FE model in ABAQUS in which an elastoplastic material law of sandy soil was adopted. Results were compared to those obtained with p-y curves. It was found that the pile deformation is underestimated by the p-y curves provided in API and p-y

curves cannot correctly capture the change of soil stiffness with increasing loads for large-diameter piles. Moreover, the impact of cyclic loads on stiffness degradation was included in the finite element models [60]. Results of FE method agreed well with existing laboratory results. Their research shows that the displacement accumulation strongly relies on the amplitude of external loads and that the embedded length of the monopile has a large impact on the ultimate loads.

Byrne *et al*. [61] and Zdravković *et al*. [62] also suggested that the previous design method for large-scale monopiles with diameters larger than 5 m may not be appropriate, and the joint industry project, PIle Soil Analysis (PISA), aims to develop new design methods for large-size monopiles. This new method is an extension of the p-y curve method, including four separate components, namely a distributed load curve which corresponds to the conventional p-y curves, distributed moment curve, base shear curve, and base moment curve. In PISA, a 3D finite element model shown in Figure 2-10 was used to provide soil-structure interaction curves, and these curves were used for a 1D model to assess this method. Results showed a good fit for these two models.

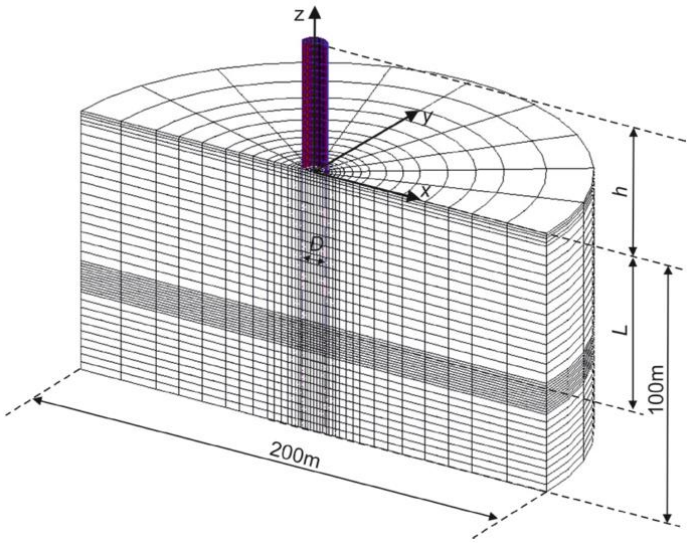

Figure 2-10. 3D model for soil-structure interaction [62].

2.3 Brief introduction to FAST

Current mainstream wind turbine modelling software packages such as FAST [63] by the US National Renewable Energy Laboratory (NREL) and HAWC2 [64] by the Technical University of Denmark, capture the interaction between the tower, rotor,

nacelle, and foundation of the wind turbine system by coupling aerodynamic capabilities with electromechanical and structural models. In this thesis, the wind turbine simulation package FAST was used to validate the proposed models. FAST v8 contains several modules which together simulate a fully coupled nonlinear aero-hydro-servo-elastic system in time domain [65]. As shown in Figure 2-11, the core modules in FAST are AeroDyn, HydroDyn, ElastoDyn and ServoDyn. AeroDyn calculates the aerodynamic loading on the blades and tower given the inflow wind field defined by the module InflowWind. The generation of a turbulent inflow wind field requires TurbSim which is a stochastic, full-field, turbulent-wind simulator [66]. HydroDyn calculates the hydrodynamic loading caused by waves and currents. ElastoDyn solves the structural dynamics of the multi-body system and ServoDyn controls the operational states by changing the pitch angles of blades, generator torque *etc*.

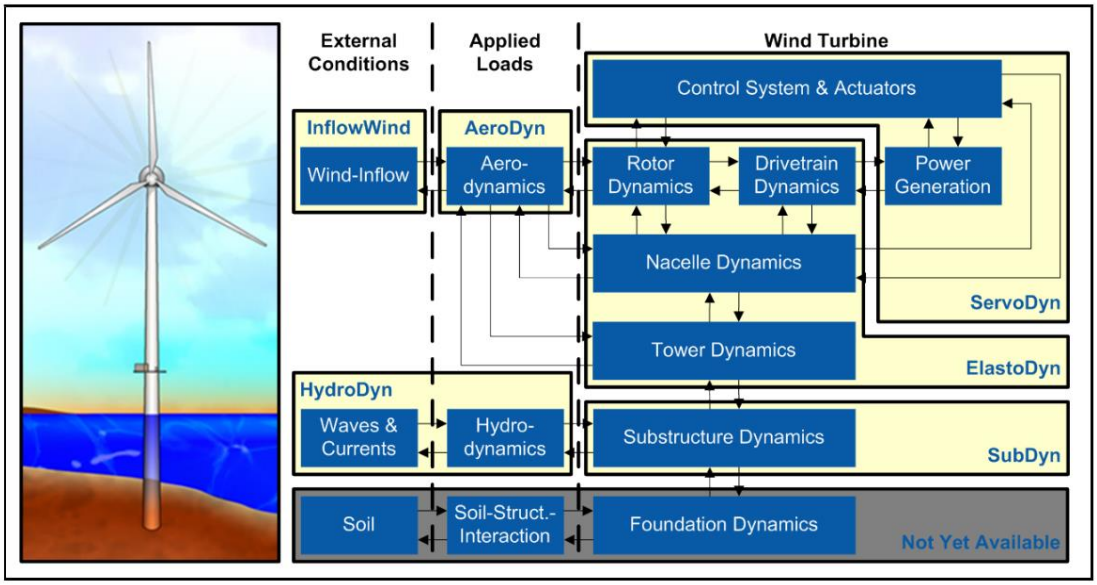

Figure 2-11. FAST control volumes for bottom-fixed offshore wind turbines [67].

In FAST, nacelle and hub are modelled as rigid bodies, whereas the tower, blades and drive shaft are modelled as flexible bodies. Their motions are coupled during time integration. At each time step, the unsteady BEM theory [25] is applied to calculate the aerodynamic loads on the rotor, while Morison's equation and potential flow theory are used to calculate the hydrodynamic loading. Such fully coupled models are usually computationally intensive. In FAST only structural damping can be explicitly defined for the substructure and the blades, but aerodynamic damping and hydrodynamic

damping are implicitly introduced in the calculated aerodynamic and hydrodynamic loading considering the coupled motions of the entire wind turbine system in the time integration. As a result, the quantification of aerodynamic damping and hydrodynamic damping in FAST can only be achieved by further identification with underlying damping models and simulated dynamic responses.

2.4 Theoretical and numerical study of damping in wind turbines

There are five main sources of damping in OWTs, namely aerodynamic damping, hydrodynamic damping, structural damping, soil/foundation damping and damping from dissipative devices [68]. OWTs are lightly damped structures so it is usual to assume the total damping of the turbine system is the sum of the damping from different sources. Damping ratios which represent the level of damping in a system relative to critical damping are widely used to quantify damping. In this way, the total damping ratio ζ_{Total} in an OWT can be expressed by:

$$\zeta_{Total} = \zeta_{Aero} + \zeta_{Struc} + \zeta_{Hydro} + \zeta_{Soil} + \zeta_{Damper}. \quad (2\text{-}12)$$

where ζ_{Aero} , ζ_{Struc} , ζ_{Hydro} and ζ_{Soil} represent the aerodynamic, structural, hydrodynamic and soil damping ratio respectively, ζ_{Damper} stands for the damping ratio from dissipative devices. The significance of damping sources for OWT varies depending on whether the OWT is in operation or parked. In operation, the aerodynamic damping, which is due to the interaction between the blades and wind accounts for a large proportion of the total damping effect (*e.g.* [13]). Hence the other damping sources are sometimes lumped together under the name of "additional damping" [21]. As lower damping is found in non-operational stormy conditions, more research has been devoted to the determination of damping when the OWT is parked. In literature, damping has usually been expressed either by damping ratios or logarithmic decrements. For consistency and ease of comparison, damping ratios are used throughout this thesis (as opposed to logarithmic decrement) and all published damping values cited have been converted accordingly. The conversion of logarithmic decrement values into damping ratios (a division by 2π) as well the varying precision with which results are available in the literature has caused some difficulty in reporting damping values with a consistent level of significant figures. It should also be noted that the repeatability of damping measurements is usually quite poor (typically with 10-20% of variability)

rendering the precision of many damping values reported in the literature somewhat spurious. However, this was deemed necessary for the sake of comparison.

2.4.1 Aerodynamic damping

Aerodynamic damping is mainly generated by the interaction between the rotating blades and wind. The flapwise vibration of blades is reduced due to the drag force from wind, which has the strongest contribution to the damping of the FA vibration of the support structure. The side-side vibration can also be reduced by blades with large pitch angles due to larger attack angles to the blade surface. For instance, in the experimental study reported by Devriendt *et al.* [69], the damping ratio in the SS mode is larger than that of the FA mode, and this is caused by the effect of a pitch angle of 88.2 ° which provides greater impedance for the side-side mode. It is evident that the wind speed and rotation speed of blades have a great impact on the aerodynamic damping from blades ([70][71]). The complexity of aerodynamic damping is due to its dependence on the inflow wind speed, the rotational speed of blades and the control system inside the wind turbine which changes the pitch angles of blades to optimise the power output. As a result, it is difficult to predict aerodynamic damping if all these factors are considered. The vibrating tower can also experience air drag, which causes small aerodynamic damping. This small amount of damping ratio contribution is assumed to be in the range of 0.08% to 0.24% when wind speed is between 5 m/s and 15 m/s, according to [72].

The study of the impact of aerodynamic damping on the support structure of OWTs is relatively limited. Salzmann and Tempel [73] summarised several analytical solutions for aerodynamic damping from constant-speed turbines, including the method by Garrad [74] and the method by Kühn [75]. These closed-form solutions account for the relationship between wind speed and the motion of turbine, deriving the analytical expression for aerodynamic damping. These theoretical solutions are all based on BEM theory. An analytical solution for variable-speed turbines was also proposed by them. The theoretical solution of the damping ratio for the entire rotor of a variable-speed turbine proposed by Salzmann and Tempel [73] is:

$$\zeta_{Aero}(V_0) = \Omega(V_0) \cdot \frac{N_b \rho C_{L_\alpha} m_{1b}}{4 M_0 \omega_n}, \tag{2-13}$$

where V_0 is the wind speed, Ω is the rotor rotation speed, N_b is the number of blades, ρ is air density, C_{L_α} is the slope of the lift coefficient C_L when the attack angle is α,

m_{1b} is the first order moment (static moment) of the area of the chord along a blade, ω_n is the natural frequency of the whole turbine, M_0 is an equivalent mass of a single mass-spring model to which the turbine is converted.

The result from the proposed analytical solution expressed by Equation (2-13) was compared with simulations and results from measured data from a real turbine using frequency-domain fitting. It was found that there is some difference between the simulation and the prediction, and that both simulation and theory would largely underestimate the aerodynamic damping for a real turbine when the wind speed is much higher than the rated wind speed, as shown in Figure 2-12.

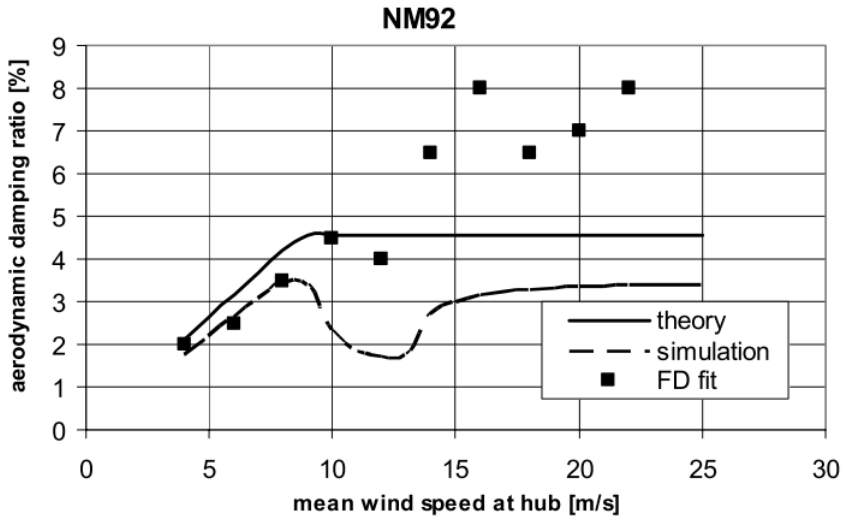

Figure 2-12. Aerodynamic damping ratio vs mean wind speed [73].

Valamanesh and Myers [70] proposed a closed-form analytical solution also based on BEM for aerodynamic damping both for FA and SS vibration, in which the impact of rotational speed of blades and wind speed could be accounted for by two components A and B respectively. The equations used to determine the FA damping ratios for an equivalent single degree of freedom (DOF) system to the wind turbine are as follows:

$$A = \rho \int V_w(1-a)(C_l cos\phi + C_d sin\phi)c(r)dr, \tag{2-14}$$

$$B = \frac{1}{2}\rho \int \Omega r(1+a')[(\frac{\partial C_l}{\partial \alpha} + C_d)cos\phi + (\frac{\partial C_d}{\partial \alpha} - C_l)sin\phi)]c(r)dr, \tag{2-15}$$

$$\zeta_{Aero} = \frac{N_b(A+B)}{2\sqrt{km}}, \tag{2-16}$$

where V_w is the uniform upstream wind speed, Ω is the rotation speed, k and m are the modal stiffness and mass for an equivalent single degree of freedom wind turbine model, other terms have same definitions in the BEM theory introduced in Subsection 2.2.2. This is an improved version of the approach proposed by Salzmann and Tempel [73]. Their estimations from the closed-form analytical solutions were compared with the results from FAST. Their study concluded that when the wind speed is low, the rotation speed of the blades contributes a larger portion of the whole aerodynamic damping, and that when the wind speed is higher the damping contribution from the rotation component becomes smaller. However, no experimental verification has been carried out for this analytical solution.

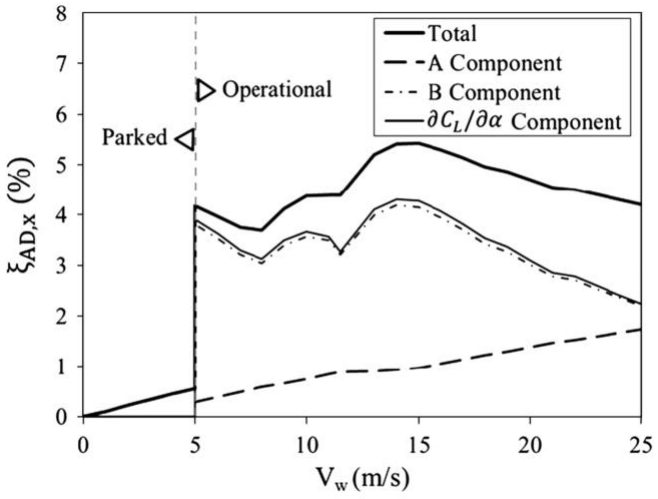

Figure 2-13. Aerodynamic damping ratio from contribution of wind speed and rotation speed [70], *A*-component-wind speed, *B*-component-rotational speed of rotor.

Liu *et al.* [76] developed a FA aerodynamic damping representation including the tower-top motion of a constant-speed wind turbine and modified this model for a variable-speed wind turbine using a correction factor. They compared their method with the aforementioned method proposed by Salzmann and Tempel [73] and the method by Kühn [75]. They found that the aerodynamic damping prediction by their method is lower than the other two methods for a wind speed range from 5 m/s to 25 m/s. In addition, the aerodynamic damping for the entire rotor was found to be time-varying for a turbulent wind field.

2.4.2 Hydrodynamic damping

Hydrodynamic damping comes from two sources: (1) wave radiation damping and (2) viscous damping due to hydrodynamic drag [42]. The wave radiation is proportional to wave velocities whereas viscous damping is proportional to the relative velocities squared [9]. The hydrodynamic damping for a cylinder interacting with waves and currents has long been a subject of research since it is a fundamental part of the classical fluid-wave interaction problems. The methods used to estimate analytically viscous and radiation damping can be found in [77], in which viscous damping is calculated based on Morison's equation and radiation damping is calculated based on potential flow theory. Some examples of experimental studies are reported in ([78][79]). However, only a few studies have been conducted on hydrodynamic damping in OWTs. GL [80] suggests values of 0.15% for viscous damping and 0.11% is proposed for the radiation damping in [77]. A radiation damping ratio of 0.24% was suggested by Tarp-Johansen *et al*. [72] after simulating the radiation/diffraction component using the wave modelling program WAMIT. Using HAWC2 time-domain simulations (implementing Morison's equation), Shirzadeh *et al*. [9] estimated the viscous hydrodynamic damping ratio at around 0.004%. The reported values for this source of damping vary widely but for an OWT on a monopile located in relatively shallow water, these damping values are consistently very low compared to other sources.

2.4.3 Soil/foundation damping

Soil damping plays an important role when the rotation of blades is stopped or when the side-side behaviour is considered. There are two types of source for soil damping, namely radiation damping which is in the form of wave propagation, and hysteretic material damping which involves the rearranging of the soil particle layout and the changes in soil particle contact interaction ([13][56]). Radiation damping varies depending on the frequency of external excitation. Radiation damping can be neglected when frequencies of OWT and external loads are lower than 1 Hz [13], and the frequencies of wind and wave loads are normally lower than 1 Hz.

However, soil damping is uncertain compared to other sources and can possibly have a large contribution. As stated by Carswell *et al*. [13], the contribution of soil damping has not been studied in depth, although it is possible to predict it by back-calculation when the total damping and other damping sources except soil damping are known.

Many published papers used this back-calculation approach to quantify the damping contribution from soil [81]. Nevertheless, to obtain the accurate damping contribution from soil is still difficult and deserves further research.

The study by Zania [49] developed a rigorous analytical solution for modified soil-structure interaction eigenfrequency and damping. Damgaard *et al*. [81] modelled the influence of soil damping directly by introducing hysteretic springs in a cantilever model of the turbine to account for the soil-structure interaction. From this they found the contribution of soil damping to range between 0.8% and 1.3%, which is in good agreement with an experimental estimate of soil damping (1%) they obtained by back calculation. They also found that scour and backfilling can change the frequency and soil damping contribution according to the numerical investigation. Carswell *et al*. [13] developed a method for converting hysteretic energy loss into a viscous, rotational mudline dashpot that represents OWT foundation damping in a lumped parameter model. The damping contribution of foundation is stated to be in the range of 0.17%-0.28%, from the numerical simulation of the NREL 5 MW reference turbine. However, a higher damping value of 0.72% was obtained from time history analyses in response to extreme wind and wave conditions. By comparing the load acting on the foundation at mudline, foundation damping decreases the maximum moment by 7-9%, but has little effect on the shear force (approximately 2% reduction). Moreover, Carswell *et al*. stated the increasing significance of foundation damping when the natural frequency of structure approaches the wave frequency. Modelling the soil as a viscoelastic soil block in ABAQUS, Tarp-Johansen *et al*. [72] found a soil damping ratio of 0.56%. They suggested that 0.80% should be used to account for the nonlinear behaviour of the soil. Their values are currently recommended by GL guidelines [80]. It should be noted that back calculating soil damping tends to increase the final uncertainty by propagating the uncertainties from other damping sources. Although very few studies have attempted to model directly soil damping in OWTs, the damping in a standard single pile in horizontal vibration has been the subject of many past papers (*e.g*. [55][82][83]). These could form the basis for modelling soil dissipation in monopiles. Geotechnical earthquake engineers also have a long history of studying soil damping (*e.g*. [84][85]).

2.4.4 Structural damping

Structural damping in offshore wind turbines has received very little specific attention. It is usually assumed to follow the behaviour of standard steel structures for which damping values are available. For instance, Eurocode 1 [86] recommends a value of 0.19% for unlined welded steel stacks without external thermal insulation. More specific values can be found in the Offshore Oil and Gas literature [87]. Offshore wind farms tend to have much larger turbines than those investigated in the studies reported in this subsection so it is not clear how reliably these values can be generalised to current larger OWTs.

2.4.5 Contribution from damper

The installation of dampers in flexible structures like OWTs is a possible way of mitigating their vibration. The blades and support structure both suffer from severe vibration, so dampers can be installed both for the blades and the support structure. However, this subsection mainly considers dampers for the support structure. To date, many offshore wind farms have been equipped with dampers to reduce dynamic amplitude. The strategies for damping a structure mainly fall into three different categories: passive, semi-active and active. The passive approach is the easiest and most widely used for practical structures [88]. The most classic type of passive damper is the tuned mass damper (TMD), which has been widely researched for OWTs [89]. The basic concept of the TMD uses a mass-spring-damper system to dissipate the dynamic energy. It was shown that the displacements at tower/nacelle for a wind turbine can be reduced by up to 50% [89]. However, an effective TMD requires that the mass should be installed in the position where the motion of the targeted vibration mode is large, which causes an increase in mass at the top the tower. The increased mass at the top of the tower can have adverse effect for slender OWT because the top motion could be amplified due to larger inertia forces [90]. This restricts the usage of TMD for large-scale OWTs.

Another type of passive control system for OWT, tuned liquid column damper (TLCD) has been investigated by Colwell and Basu [91]. TLCD is a U-shaped liquid damper, which absorbs the vibration energy of the structure by the passive oscillation of the liquid when the frequency of the damper is tuned to that of the structure. Although the TLCD might also be located in the nacelle due to the horizontal space requirement, the

TLCD has several advantages compared to the traditional TMD. First, the TLCD can act on very low excitation amplitudes and is feasible for a range of excitation levels; Second, the TLCD needs minimal auxiliary equipment and easy set-up because it utilises the nature of gravity-restored liquid. Third, the TLCD is somewhat lighter than a TMD. In Colwell and Basu's research, a model with TLCD was established and the environmental loads were considered. Their comparable research outcome shows that TLCD can result in up to 55% lower peak response for OWT.

To avoid the difficulties related to installing dampers at the top of wind turbine, some researchers have attempted to install dampers at other positions in OWTs. For instance, Brodersen and Høgsberg studied the toggle-brace damper system installed inside the tower [90] according to the concept that is used in shear frames. This brace system aims to reduce the local curvature of the corresponding tower bending deformation [92].

Semi-active or active dampers have been studied to optimise the dynamic performance of OWTs. For instance, active TMD is more effective than passive TMD ([93][94]). Adding an actuator in a damper system, however, requires more devices such as sensors which can detect the structural response to control the needed forces, and for a pure active damper system, there is the possibility of instability. The active damper itself requires power to operate, which makes it less cost-effective. More recently, a type of hybrid damper system was studied by Broderson and Høgsberg [92], which is proposed to be placed at the bottom of the turbine tower. In this system a series of viscous dampers and sensors are installed inside the tower, in which stroke amplification is realised by active control. Their numerical simulation proved that this approach is able to increase damping ratios by 1.25% and reduces fatigue damage

In previous research into vibration control of OWTs, numerical models have been used extensively to find the impact of placing such dampers, but little actual experimental research has been done. One experimental study was carried out by Li *et al.* [95] in which a type of ball vibration absorber at the top of tower was used to significantly reduce the dynamic response by around 40% for parked conditions. For operational condition, the reduction is much lower, around 25%. For TLCD, Chen *et al*. [96] conducted a scaled-down test using simulated loads from wind, wave, and earthquake and compared the results to a numerical model. The effect of TLCD can lead to up to 50% reduction in stress amplitude at the bottom of the tower. However, their research

did not consider the impact of aerodynamics of blades and hydrodynamics of water-structure interaction. For more details of the development of dampers in wind turbine, see the review paper by Rahman *et al.* [89].

2.4.6 Other damping sources

It is expected that the transition piece which usually includes a grouted connection would have some effect on the damping of the whole OWT substructure which is usually made of steel. Nevertheless, few papers account for this. A paper by Schaumann *et al*. [97] studied the impact of dynamic behaviour due to the nonlinear properties of the grouted transition. This simulation work concluded that the nonlinearity hardly affects the damping ratio of the system. However, it was observed that a significant decrease in the first natural frequency would occur if some parameters of the grout connection change, such as the overlap length and contact friction.

2.5 Damping identification in wind turbines

2.5.1 Damping identification on parked wind turbines

Two main methods have been used to measure damping experimentally in OWTs, depending on the type of excitation. Modal properties (including damping) have been obtained by operational modal analysis (OMA) when the system is excited by ambient sources (wind and waves) or standard time or frequency domain damping identification techniques when the dynamic response of the system is due to a controlled measurable excitation. Applying a controlled excitation to an actual OWT presents a number of practical difficulties due to access and size. Loads from the environment could also influence the results. The so-called "rotor stop" test is the most commonly used technique (*e.g.* [98][99][100][81][72]). It consists in suddenly turning the blades into feathered position so that the tower experiences a downward step in rotor thrust. "Overspeed test" is a similar technique that has also been used extensively (*e.g.* [9][101][69][102][103]). Other types of excitations have also been used – for instance, Koukoura *et al*. used boat impact at sea level [104]. These techniques intrinsically reduce the influence of aerodynamic damping by keeping the rotor speed low or at zero, so that they are better suited at estimating the additional damping. As a result, the difference in damping between the FA and SS directions obtained from parked turbines tends to be small.

Using these various techniques, a range of values have been reported. Tarp-Johansen *et al*. [72] measured the additional damping ratio in a 3.5 MW OWT using rotor stop tests and estimated it at 1.91%. Versteijlen *et al*. [98] measured the additional damping in 3.6 MW Siemens OWTs using spectra of the bending moment at the base of the tower. They obtained a damping ratio of 3% for the first FA bending mode of the turbine. Damgaard *et al.* ([99][100][81]) used "rotor stop" tests and OMA on turbines subjected to ambient excitation in four wind farms. The rotor stop tests gave a first FA mode damping ratio in the range 2.39-2.55%. Results from ambient excitation tests gave fairly close results with damping ratios in the range 2.55-2.86%. A series of comprehensive damping studies on 3 MW Vestas V90 OWTs in the Belwind Wind farm were completed by Shirzadeh *et al*. ([9][101][69][102][103]). Using overspeed tests and OMA under ambient excitation they measured the damping ratios of the first FA and SS modes at 1.05% and 1.27% respectively (with an installed tuned-mass damper kept inactive). Koukoura *et al.* [104] studied the damping in both parked and operating turbines excited by a boat impact and ambient excitation. They measured FA and SS damping ratios of 1.8% and 1.9% respectively for a parked 3.6 MW turbine. Dampers were installed and active in their study, but their contribution was not specified. Bajrić *et al*. [105] investigated the damping identification for an 8 MW offshore wind turbine in non-operating conditions using three different algorithms: eigensystem realization algorithm (ERA), covariance driven stochastic subspace identification (COV-SSI) and the enhanced frequency domain decomposition (EFDD). Results from COV-SSI showed that the estimated FA damping ratio is around 0.7%, which is considerably lower than the SS damping ratio around 1.2%.

Structural damping in onshore wind turbines was measured by Schaumann and Seidel [106] and it was found to be between 0.2% to 0.5% (excluding soil damping). Ozbek and Rixen [107] measured the structural damping of an 2.5 MW onshore wind turbine at 0.3% in the FA direction and between 0.3% and 0.9% in the SS direction. However structural damping in OWTs could be larger (from 0.5% to 1.5% according to [9]) as the damping from other structural parts like the grouted connection may have a significant contribution.

In conclusion the damping ratios for parked turbines have been found to vary between 1% and 3% with reasonable agreement between published results.

2.5.2 Damping identification in operating wind turbines

Measuring damping in operating wind turbines has been more difficult than for parked turbines [71]. Most research shows that the aerodynamic damping contribution is around 5% and can vary depending on the wind speed and rotation speed of the rotor.

Hansen *et al*. [108] used two experimental methods to estimate the aerodynamic damping in an 2.75 MW operating OWT, however no measurement of the additional damping was provided in their study so their results are effectively overall damping values. One method estimated the damping from the decay in the OWT free response obtained after an artificial periodic pitching of the blades was stopped. One deficiency of this method is that the estimated damping is not exactly modal damping because the vibration of the excited turbine is not purely modal. The measured overall damping ratios obtained this way were extremely scattered, averaging around ζ^{FA}~8% in the FA direction and ζ^{SS}~2.4% in the SS direction. The other method used was OMA with wind excitation. Stochastic subspace identification (SSI) was used to extract the damping ratios, resulting in an overall damping ratio of 13.2% for the FA mode and 7.96% in the SS mode. The damping ratio for the side-side mode can decrease to around 3.18% when the wind speed is higher, which is much smaller than the result for the rated wind speed. These damping ratios were simply calculated from the logarithmic decrements. Assuming a 2% additional damping component, overall damping results from their study give an estimated ζ_{Aero}^{FA}~6% and ζ_{Aero}^{SS}~ 0.4% for the aerodynamic contributions using the controlled excitation. Subtracting 2% from their OMA overall damping ratios gives ζ_{Aero}^{FA}~11.2% and ζ_{Aero}^{SS}~6%. The comparison between these two methods indicates that OMA requires no advance knowledge of the turbine to be measured, but needs long time series, while the exciter method should be carried out away from the natural frequency to avoid inaccuracies in damping extraction but can be done more quickly. The difference between the results obtained from the two methods is large and OMA gave much higher values than those usually found in the literature. Furthermore, the reported damping ratios were scattered in this research and the contribution solely due to aerodynamic damping remains unclear.

Ozbek and Rixen [107] studied experimentally the aeroelastic damping of a 2.5 MW onshore turbine also using OMA. They used photogrammetry and laser vibrometry to measure the vibration response. The least square complex exponential (LSCE) method

was used to obtain the damping ratios. As onshore foundations are stiffer, onshore wind turbines are expected to experience much less soil damping and no hydrodynamic damping at all. Also, they have no transition piece as such, so their structural damping is bound to be low. Therefore, the additional damping is likely to be very small so that a good estimate of the aerodynamic damping can be obtained by measuring the overall damping in operation. They found 5% in the FA direction and around 0.5% in SS mode. These values were in good agreement with results from matching HAWCS simulations they carried out, but not consistent with the findings of the work by Hansen *et al*. [108]. The comparison for FA and SS vibrations is shown in Figure 2-14.

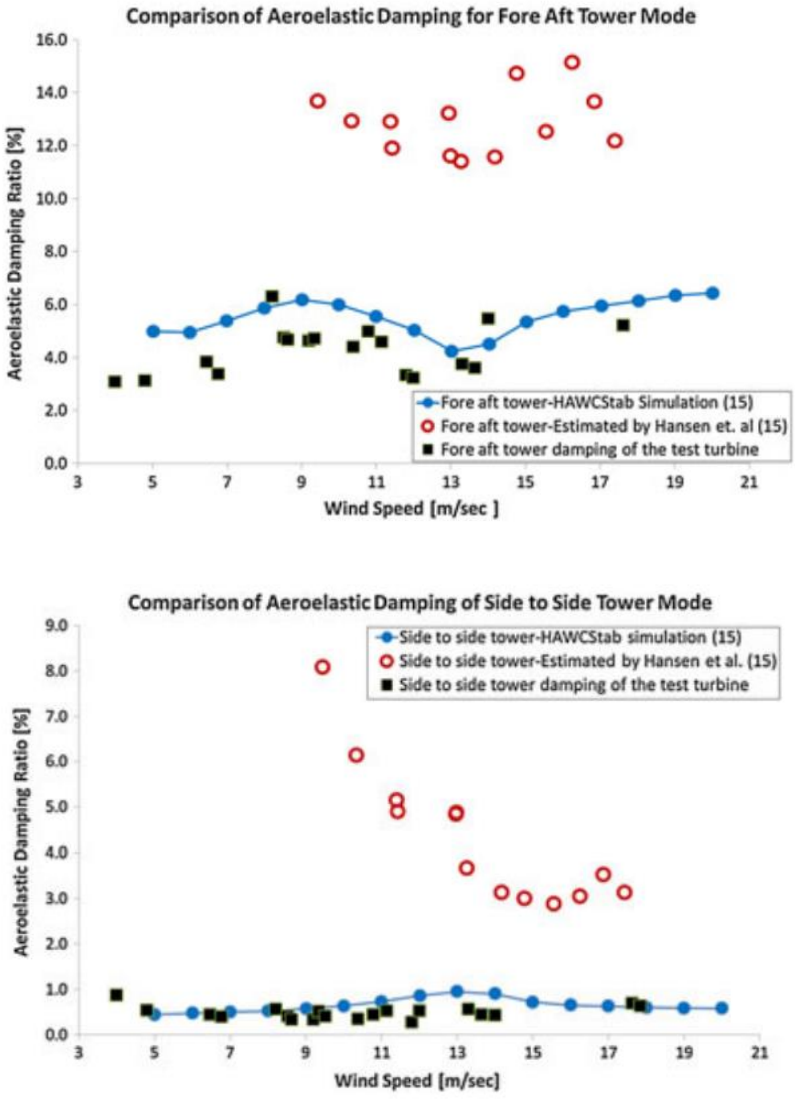

Figure 2-14. Damping ratio comparison for fore-aft and side-side modes from [107].

The measurements on wind turbines withrated power from 1.8 MW to 3.6 MW using opto-mechanical system by Zendehbad *et al*. [109] showed that the aerodynamic damping ratio for an operating turbine is around three times that of an parked turbine. However, the damping ratio obtained by them for an operating turbine, around 0.8% is much lower than the results reported by other researchers. Devriendt *et al.* [110] used a poly least-squares complex frequency-domain (p-LSCF) estimator to identify the overall damping for a 3 MW wind turbine in operation. They emphasised that harmonics in the excitation would hinder the usage of classical OMA methods which require that measured responses are only caused by structural resonance. The measurements show that the damping ratio in the FA direction increased from 1.8% to 6.5-7% for different wind speed bins from 1.5 m/s to 22.7 m/s, while the SS damping ratio varied from 1.8% to 3%.

Koukoura *et al*. [104] found that the overall FA damping ratio for an 3.6 MW operating OWT in a relatively high wind speed of 19 m/s is 10.35% and 4.77% in the SS direction. The EFDD method was used for the damping estimation. They found that a beating phenomenon observed on the autocorrelation function of the response made the identification less reliable, especially for side-side vibrations. However, this again seems to include some unspecified supplemental damping. Dong *et al.* ([111][112]) applied the harmonic modification SSI (HM-SSI) method to identify the frequency and damping of an 2.5 MW operating turbine, and obtained a wide range of damping values from 0.87% to 5.32% in different operating conditions with mean wind speeds up to 15.7 m/s. Hu *et al*. [113] also implemented the p-LSCF method to identify the total damping in a 5 MW operating turbine with different rotation speeds. The resonance due to 3P loading was observed to have a significant effect of the identified total damping. The averaged total damping ratios for operating wind turbines with rotor rotation speeds between 4 rpm to 15 rpm were found in the range of 0.5% to 4%. Chen *et al.* [114] presented a wavelet-based approach to continuously identify the different components of aerodynamic damping for an operating wind turbine. Using a lumped-mass model of the wind turbine and BEM theory, simulated time series for turbulent wind were analysed in the time-frequency domain and the long-time variation of the aerodynamic damping matrix was estimated.

In conclusion, there is a lot of uncertainty in the measured overall damping in operating wind turbines and it transpires that further work is needed to establish a reliable methodology to measure it.

2.5.3 Difficulties in aerodynamic damping identification on operating wind turbines

In practice only the total damping can be measured directly. The aerodynamic damping can be inferred by subtracting other damping contributions from this total damping if they can be isolated reliably. For wind turbines in operation the FA aerodynamic damping contributes the most, so the measured total damping could also be seen as a close substitute for the aerodynamic damping even without subtraction. In many published studies the distinction between the total damping and the aerodynamic damping for operating wind turbines is not always clear.

Although much research has been conducted to identify the aerodynamic damping in operating wind turbines using traditional OMA methods or modified versions, limitations in these methods still exist. The need to extract dynamic parameters for wind turbines resulted in the development of OMA methods suitable for large structures under ambient excitations. The OMA method "the natural excitation technique" (NExT) by James *et al*. [115] was initially used for the modal parameter extraction of operating vertical-axis wind turbines. However, for operating wind turbines the validity of some basic assumptions underpinning the implementation of most OMA methods remain doubtful. This causes difficulties in applying current OMA techniques to wind turbines. These difficulties have been described by Tcherniak *et al*. [116] and Ozbek *et al.* [71]. First, the excitations to the structure need to be uncorrelated, but the forces exciting wind turbine are not uncorrelated as they are coupled due to the influence of the rotor rotation. Second, traditional OMA methods assume that the resultant responses due to ambient excitation only include harmonics caused by the natural modes of the structure but not harmonics due to ambient excitations themselves. This assumption is also violated by the rotation of the rotor which causes 1P, 2P, 3P *etc*. loadings to the tower. Third, traditional OMA techniques require that the structure system itself is a time-invariant system, which is not the case for wind turbines as aerodynamic damping is influenced by the inflow wind speed, the rotation speed and the pitch angles. None of these parameters are constant for wind turbines in normal operation due to the stochastic

nature of wind turbulence and the variability of controlled conditions [117]. Fourth, and maybe less important, the excitations caused by turbulent wind field are not white noise. Fifth, all previous studies tried to find the damping ratios in the FA or SS directions separately, which implicitly assumed that the vibration of wind turbines in these two directions are separate. However, it is possible that the vibration of wind turbines is unconventional because of the coupling between the FA and SS motions. This coupling will be further studied in Chapters 4 and 5.

2.6 Summary

2.6.1 Uncertainties in reported damping values from past studies

In Table 2-1, the damping ratios from some recent papers are listed. From this table, it can be concluded that the reported damping ratios for parked turbines vary from 1% to 3% - a relatively small range compared to the damping ratios reported for wind turbines in operational condition.

Table 2-1. Measured overall damping ratios for first bending mode of the tower.

Author	Year	Parked		Operational	
		FA	SS	FA	SS
Hansen *et al.* [108]	2006	-	-	4.77%-12.7%	1.11-3.98%
Tarp-Johansen *et al.* [72]	2009	1.91%	-	-	-
Versteijlen *et al.* [98]	2011	3%	-	-	-
Damgaard *et al.* [99][100][81]	2012 &2013	2.39-2.86%	-	-	-
Shirzadeh *et al.* [9][101][69]	2013		1.27%	-	-
Ozbek *et al.* [107]	2013	0.3%	0.3-0.9%	5.0%	0.5%
Shirzadeh *et al.* [102][103]	2014	1.69%	2.18%	-	-
Koukoura *et al.* [104]	2015	1.8%	1.9%	10.35%	4.77%

The environmental condition and the state of turbines can influence the aerodynamic damping contribution, resulting in the large difference in the contribution of aerodynamic damping to the overall damping. The variation of aerodynamic damping in both FA and SS directions for an operational turbine is the result of a combination of several factors, for example, the pitch angle, the wind speed and the rotation speed of blades. Furthermore, despite the large amount of research effort on damping of OWT, it is still difficult to determine the overall damping and its components due to the difference between papers and the large range of damping values.

Assuming that the various damping contributions are independent of each other, the usual way to interpret the measured overall damping is to divide it into several categories. The damping estimations from past papers are summarised and listed in Table 2-2 for convenience and comparison to reflect the range and uncertainties of damping from different sources for different modes and operational states. In Table 2-2, yellow cells indicate large uncertainties while green cells indicate small uncertainties.

Table 2-2. Range of damping ratios based on past papers.

Operation Condition	Mode	Overall damping	Structural damping	Aerodynamic damping	Soil damping	Hydrodynamic damping
Parked	FA	1.05%-2.55%	0.2-1.5%	0.08%-0.24%	0.17-1.3%	0.07-0.24%
Operational	FA	5.0%-10.35%	0.2-1.5%	3.7%-8%	0.17-1.3%	0.07-0.24%
Parked	SS	1.05%-2.18%	0.2-1.5%	0.08%-0.24%	0.17-1.3%	0.07-0.24%
Operational	SS	1.05%-4.50%	0.2-1.5%	0.08%-3.5%	0.17-1.3%	0.07-0.24%

Structural damping from steel material is commonly assumed at around 0.2%, whereas the whole structural damping could vary significantly from 0.2% to 1.5% as the damping from other sources like the grouted connection is added. The damping from soil/foundation is in the range of 0.17% to 1.3%, which makes a relatively large contribution to the total damping. It should be noted that it is possible to propagate inaccuracies when using back calculation to estimate the damping ratio from foundations, indicated by the differences between the results from [13] and those from previous papers. The aerodynamic damping is stable for parked turbines and has more uncertainties for operational turbines, which is simply because the rotor has minimal impact on the vibration for parked turbines. For an operating turbine, the aerodynamic

damping could vary in a large range according to the wind speed and rotor speed, both for the FA and SS directions. The study by Koukoura *et al*. [104] reported on actual damping measurements in operating conditions leading to an estimate of the aerodynamic damping of 8% in the FA direction if the additional damping is assumed to be around 2%, which reveals the possibility of high damping ratios from aerodynamics. However, the hydrodynamic damping is relatively low compared to other sources. It should be noted that the total damping ratio significantly differs for an OWT in operating condition and parked condition.

2.6.2 Research questions arising from the literature review

Three main research questions arose from the literature review:

1. There is significant uncertainty in damping ratio values reported by previous researchers, especially for aerodynamic damping in operating wind turbines, soil damping and structural damping. Can first-principle physics-based models estimate these damping values and be used to check how reliable these reported damping values are?
2. Decoupled wind turbine models require the definition of aerodynamic damping for the tower vibration. However, relevant studies are still limited as most research only concentrates on the damping for FA tower vibrations. What is the damping level in SS tower vibrations and what is the nature of the coupling between the FA and SS directions?
3. The damping identification for wind turbines has many limitations, as discussed in Subsection 2.5.3. One issue is that current studies all tried to identify the damping ratios separately in the FA and SS directions. To what extent can a new aerodynamic model be used to develop a new damping identification methodology?

Efforts have been made in this study to provide some answers to these questions.

Chapter 3 - First-principle Damping Models

3.1 Introduction

As shown in the literature reviewed in Sections 2.4 and 2.5, damping in offshore and onshore wind turbines has been researched fairly extensively, however the variations in published values for most damping sources remain large. This directly translates into uncertainty in the prediction of the dynamic response and fatigue life of the system. As a result, designs may be unsafe or overly conservative. Although fully coupled wind turbine packages such as FAST, where the aerodynamic and hydrodynamic damping is implicitly included, are widely used, directly defining damping in wind turbine models is still needed in many situations. For example, specialised decoupled foundation models require the definition of the aerodynamic damping to include the wind loads transferred from the rotor to the foundation [118]. On the other hand, compared with the fully coupled models whose computation speed is relatively slow, simplified models with explicitly defined damping are faster for fatigue and reliability analyses, which usually demand thousands of calculations. For these reasons, there is a need to better characterise each source of damping in OWT systems. This chapter introduces direct methods to estimate the various damping contributions including aerodynamic, hydrodynamic, and soil damping through simple but physics-based models. More specifically, the damping studied in this chapter refers to the tower damping of OWTs.

Section 3.2 introduces the FE model used to model the wind turbine. Sections 3.3 to 3.5 describe the aerodynamic, hydrodynamic, and soil damping models respectively, in which the predicted damping values are compared with results from FAST and values reported in the literature. Section 3.6 concludes this chapter.

3.2 Description of 2D finite element model

3.2.1 Formation of the FE model

The behaviour of a monopile-supported OWT was modelled using a bespoke decoupled finite element model. “Decoupled” here means that the tower FE model predicts the dynamic response of the system but does not include the wind/rotor aerodynamic interaction simultaneously. The model is based on the widely used 5 MW reference offshore wind turbine for which NREL has published detailed technical data [119]. The

schematic is shown in Figure 3-1, and the basic properties of this turbine are listed in Table 3-1.

Table 3-1. Basic properties of the NREL 5 MW reference OWT.

Rotor Diameter, R	126 m
Hub Height from MSL	87.6 m
Water Depth, h	20 m
Tower Diameter, D	3.87-6 m
Tower Thickness, t	0.019-0.06 m
Monopile Diameter, D_{Pile}	6 m
Monopile Thickness, t_{Pile}	0.09 m
Lumped RNA Mass at Top	3.5×10^5 kg
Natural Frequency for Model fixed at Mudline	0.293 Hz
Natural Frequency for Model considering Soil-structure Interaction	0.25-0.28 Hz

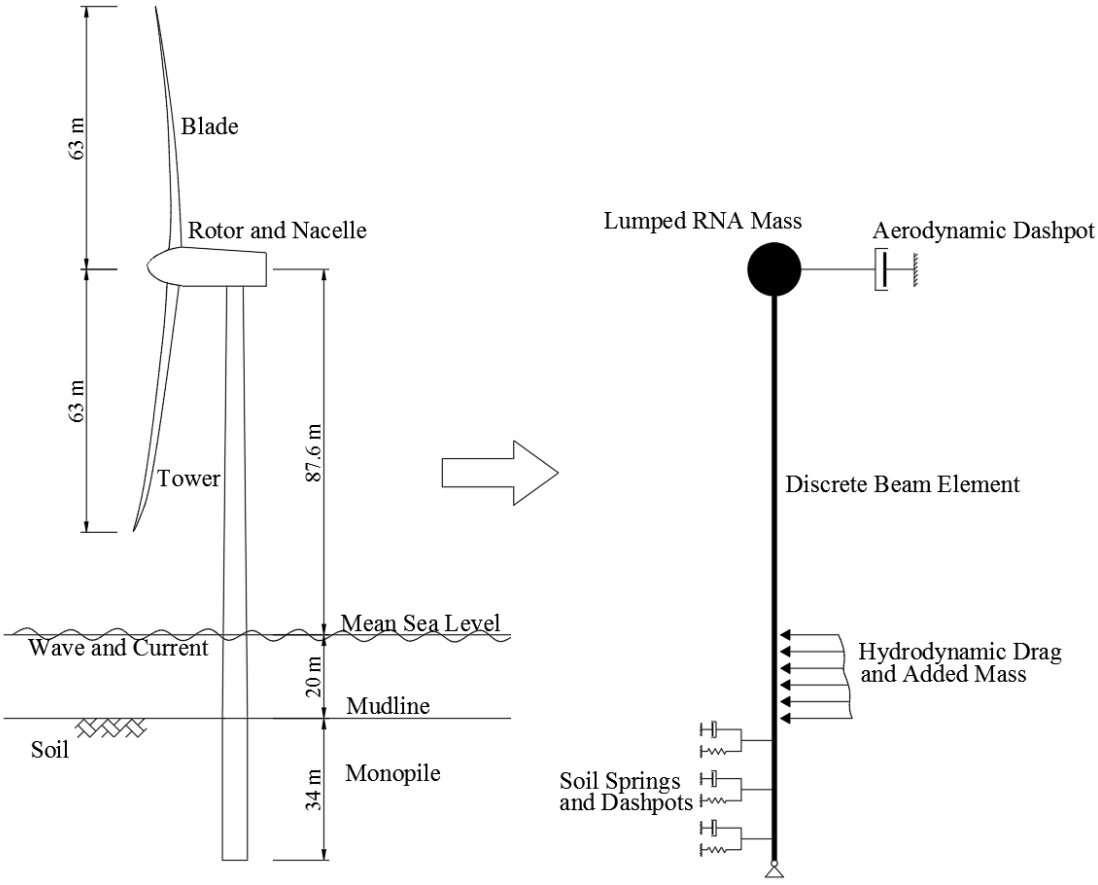

Figure 3-1. Definition of the established model from a 5 MW reference OWT.

At this stage, this is a plane model so only two translations and one rotation are considered. The vertical degree of freedom is ignored as the magnitude of the tower vertical motion is much smaller than that of the tower horizontal motion, as confirmed by FAST simulations. This model is marked as "2D" implying that only planar motions are considered.

A monopile is usually a long steel tube with the bottom embedded into soil strata. The behaviour of a monopile supported OWT is close to a cantilever with the bottom restrained by soil, so it is sensible to model its substructure as a beam. A lumped mass at the top of the tower represents the RNA. The tower/monopile is modelled with an assembly of 39 elements. Following the segmentation in the data provided for the turbine, the tower is discretised into 13 beam elements. The monopile is divided into 20 elements. A convergence study confirmed that this element size was adequate. The general expression of motion equation for the beam is

$$\mathbf{M}\ddot{\mathbf{u}}(t) + \mathbf{C}\dot{\mathbf{u}}(t) + \mathbf{K}\mathbf{u}(t) = \mathbf{F}(t), \tag{3-1}$$

where $\mathbf{M}$, $\mathbf{K}$ and $\mathbf{C}$, stand for the global mass matrix, stiffness matrix and damping matrix respectively, $\mathbf{u}(t)$ is the displacement vector, $\mathbf{F}(t)$ is the external force vector.

Using for example Euler-Bernoulli beam elements, it is easy to form the global mass matrix and stiffness matrix given the properties of the sections of tower with height. For a two dimensional beam element, the elemental mass and stiffness matrices, $\mathbf{M}^e$ and $\mathbf{K}^e$, can be obtained by the following expressions according to [120]:

$$\mathbf{M}^e = \frac{m}{420}\begin{bmatrix} 156 & -22l & 54 & 13l \\ -22l & 4l^2 & -13l & -3l^2 \\ 54 & -13l & 156 & 22l \\ 13l & -3l^2 & 22l & 2l^2 \end{bmatrix}, \tag{3-2}$$

$$\mathbf{K}^e = \frac{EI}{l^3}\begin{bmatrix} 12 & -6l & -12 & -6l \\ -6l & 4l^2 & 6l & 2l^2 \\ -12 & 6l & 12 & 6l \\ -6l & 2l^2 & 6l & 4l^2 \end{bmatrix}, \tag{3-3}$$

where l is the length of element, m is the mass of this beam element, E is the Young's modulus, I is the second moment of area, ρ is the material density.

The damping calculations from each source will be described in detail in turn in the following sections, but there are broadly two approaches. For aerodynamic and

hydrodynamic damping, the dissipation models produce directly a modal damping factor which was calculated with a separate MATLAB program. In this case, the FE model was only used to compute the modal properties of the system (see Subsection 3.2.2), and the model was fixed at the mudline to avoid having to choose a particular soil profile. In the second approach, relevant for soil damping, nonlinear springs and dashpots in parallel were included below the mudline to model the SSI which contributed to the damping and stiffness matrices in Equation (3-1). The overall modal damping in the system was then extracted through time history analysis. This is described in more detail in Subsection 3.2.3.

3.2.2 Modal analysis

Modal damping factors were related to the system properties by writing the equation of motion in modal coordinates. Although standard, this is briefly described here to introduce the notation used later. Pre-multiplying Equation (3-1) with the transpose of the ith mode shape vector $\mathbf{\Phi}_i^T$, the equation of motion becomes:

$$\bar{m}_i\ddot{\alpha}_i(t) + \bar{c}_i\dot{\alpha}_i(t) + \bar{k}_i\alpha_i(t) = \bar{f}_i(t), \tag{3-4}$$

where $\bar{m}_i$, $\bar{k}_i$, $\bar{c}_i$ are modal mass, modal stiffness and modal damping coefficient respectively with regard to ith mode, and $\alpha_i(t)$ is the ith modal coordinate. $\bar{f}_i(t)$ is a generalised external force which can be written as

$$\bar{f}_i(t) = \mathbf{\Phi}_i^T\mathbf{F}(t). \tag{3-5}$$

Rearranging Equation (3-4) and introducing the modal frequency ω_i, the equation of motion for ith mode becomes

$$\ddot{\alpha}_i(t) + 2\zeta_i\omega_i\dot{\alpha}_i(t) + \omega_i^2\alpha_i(t) = \frac{\mathbf{\Phi}_i^T\mathbf{F}(t)}{\bar{m}}. \tag{3-6}$$

In most cases, the contribution from higher modes is negligible, so the quantities of interest are the fundamental frequency ω_1, the corresponding damping ratio ζ_1 and the first modal mass $\bar{m}_1$. Numerical tests using FAST or the MATLAB 2D FE model confirmed that the dynamic responses of the 5 MW OWT are dominated by its first bending mode. Higher modes are not substantially excited as their natural frequencies lie in a range where wind and wave loads have no significant spectral density, and they therefore do not contribute to the response. However, in terms of the damping in higher modes, the damping estimation methods proposed in this chapter would still be feasible, if modal parameters related to those modes (for aerodynamic and hydrodynamic

damping) are used or the responses clearly include components due to higher modes. The mode shape used in this chapter was normalised at the tower top with corresponding modal stiffnesses and masses. If a 3D model of the turbine is available then the FA and SS modal properties might be slightly different as the two corresponding rotor moments of inertia associated are quite different. In this case, the relevant values for $\bar{m}_1$ and ω_1 should be used in the subsequent calculations.

3.2.3 Time history analyses and damping identification

Whenever the damping models did not produce damping ratios directly (*i.e.*, the damping ratios were not calculated from equations based on modal analysis such as Equation (3-6)), time domain analyses were conducted by implementing the numerical integration scheme Hilber-Hughes-Taylor-α (HHT-α) [121], which is a generalized version of the Newmark-β method. The nonlinear stiffness and damping coefficients of the soil springs were directly added to the stiffness and damping matrices at the beginning of each time step. The accuracy of this method was checked by comparing the model with a convergence algorithm (Newton-Raphson method), and a good agreement was found.

To extract damping factors from the simulated response time histories, a decaying oscillation was triggered in the system by assigning an initial displacement or acceleration to the tower top causing a transient response superimposed on the steady-state behaviour. A sonogram FFT technique was then used on the transient decay so that the damping of the first mode could be isolated [122]. In principle, this damping identification technique assumes that the underlying dissipation mechanism is linear. This is not quite the case for the soil model used here as the soil damping is changing over time due to the nonlinearity in soil stiffness and damping. However, given that the damping ratios were identified over the whole time series length, the shape of the decays obtained were close enough to those of a linear system to justify the use of the method.

3.3 Aerodynamic damping

3.3.1 Theoretical derivation of the aerodynamic force

Aerodynamic damping is caused by the drag forces experienced by the oscillating rotor in the surrounding air flow. In the FE model, the rotor is represented by a lumped mass

at the top of the beam representing the tower. The motion of the entire rotor is assumed to be consistent with that of the beam tip in terms of translation but not rotation. In BEM theory, the resultant aerodynamic force applied to the hub can be obtained by introducing a relative wind speed experienced by each blade element and summing up the element thrust component. These resultant forces and relative speeds are different in the FA and SS direction so these two cases must be dealt with separately.

Fore-aft aerodynamic damping

It is assumed that the rotor is rotating in its own plane with the angular speed ω and exposed to a uniform steady incoming wind field of average speed V_{Wx}, as shown in Figure 3-2. When the rotor does not oscillate, the three blade elements at radius r from the hub, with thickness dr experience an elemental thrust $dT|_{V_x}$:

$$dT|_{V_x} = \frac{1}{2}\rho_a N_b \frac{V_x^2}{sin^2\phi} c C_n dr, \tag{3-7}$$

where V_x is the axial component of the relative wind speed felt by the blade element; N_b is the number of blades, ρ_a is the air density, c is the chord length, $C_n = C_l cos\phi + C_d sin\phi$, with $C_{l/d}$ the lift/drag coefficients and ϕ is the sum of the attack, pitch and twist angles. If the tower top moves in the fore-aft direction with a velocity $\dot{x}$, the element now feels a relative velocity V_{xRel}:

$$V_{xRel} = V_x - \dot{x}. \tag{3-8}$$

Assuming that $\dot{x}$ is a small compared to V_x and that it is the same throughout the rotor (the rotor remains parallel to itself), $dT|_{V_{xRel}}$, the thrust felt by the three blade elements under a relative speed of V_{xRel}, can be obtained from $dT|_{V_x}$ through a first-order Taylor expansion:

$$dT|_{V_{xRel}} = dT|_{V_x} + dT'|_{V_x}(V_{xRel} - V_x) = dT|_{V_x} - \frac{d(dT)}{dV_x}\dot{x}. \tag{3-9}$$

From this derivation, it is clear that the aerodynamic damping will come into the equation of motion of the tower through the viscous term $\frac{d(dT)}{dV_x}\dot{x}$. The objective is to calculate this term and obtain the resultant thrust.

Assuming that dT is a function of V_x and ϕ, and that ϕ is a function of V_x, $\frac{d(dT)}{dV_x}$ can be calculated as

$$\frac{d(dT)}{dV_x} = \frac{\partial(dT)}{\partial V_x} + \frac{\partial(dT)}{\partial \phi}\frac{d\phi}{dV_x}. \tag{3-10}$$

In Equation (3-10), $\frac{\partial(dT)}{\partial V_x}$ and $\frac{\partial(dT)}{\partial \phi}$ can be obtained by differentiating Equation (3-7):

$$\frac{\partial(dT)}{\partial V_x} = \rho_a N_a \frac{V_x}{sin^2\phi} c C_n dr, \tag{3-11}$$

$$\frac{\partial(dT)}{\partial \phi} = \frac{1}{2}\rho_a N_a V_x^2 \frac{\frac{dC_n}{d\phi} sin^2\phi - 2sin\phi cos\phi C_n}{sin^4\phi} c dr, \tag{3-12}$$

where

$$\frac{dC_n}{d\phi} = \frac{\partial C_l}{\partial \phi} cos\phi + \frac{\partial C_d}{\partial \phi} sin\phi + C_d cos\phi - C_l sin\phi, \tag{3-13}$$

$$\frac{dC_t}{d\phi} = \frac{\partial C_l}{\partial \phi} sin\phi - \frac{\partial C_d}{\partial \phi} cos\phi + C_l cos\phi + C_d sin\phi. \tag{3-14}$$

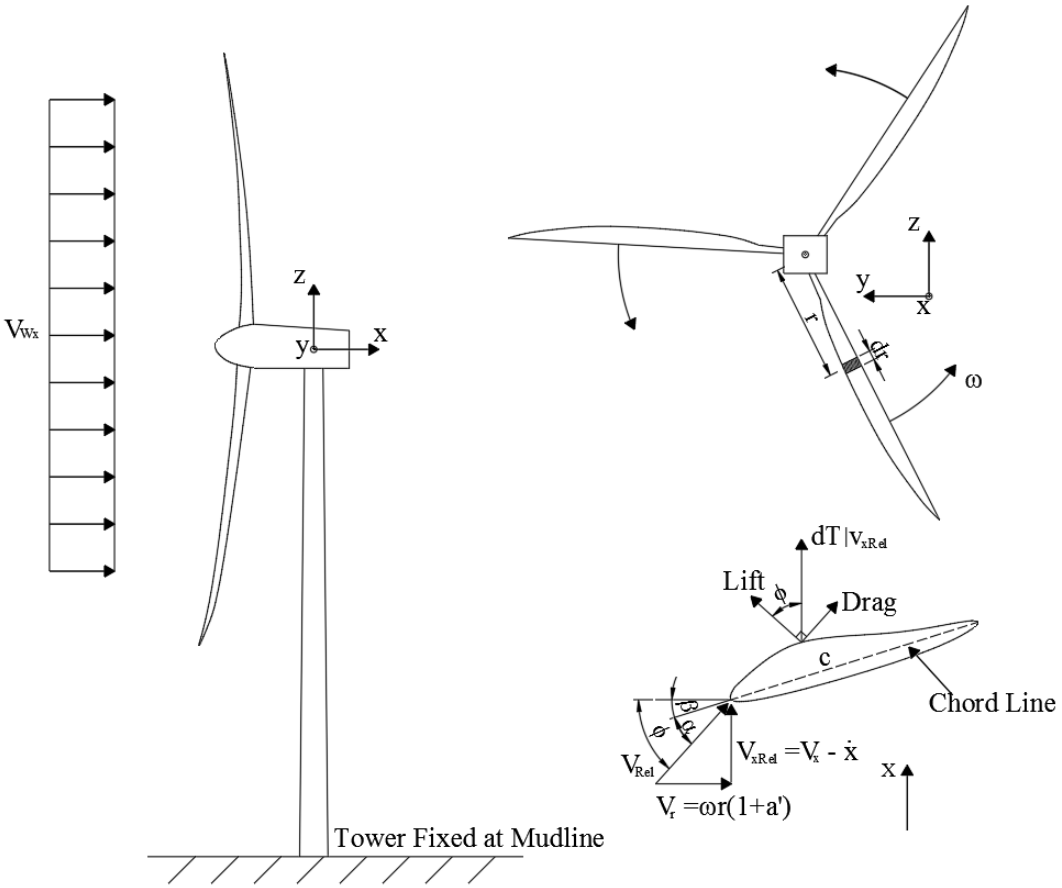

Figure 3-2. Blade element forces for fore-aft vibration.

To obtain an expression for $\frac{d\phi}{dV_x}$, the following two equations can be used:

$$tan\phi = \frac{V_x}{\omega r(1+a')}, \tag{3-15}$$

$$a' = \frac{1}{\frac{4sin\phi cos\phi}{\sigma C_t} - 1}. \tag{3-16}$$

Differentiating Equation (3-15) with regard to V_x and Equation (3-16) with regard to ϕ gives

$$\frac{d\phi}{dV_x} = \frac{1}{\omega r\left(\frac{1+a'}{cos^2\phi} + \frac{da'}{d\phi}tan\phi\right)}, \tag{3-17}$$

and

$$\frac{da'}{d\phi} = \frac{-4\left(2cos2\phi C_t - \frac{dC_t}{d\phi}2\phi\right)}{\sigma C_t^2\left(\frac{4sin\phi cos\phi}{\sigma C_t} - 1\right)^2}. \tag{3-18}$$

Equations (3-11), (3-12) and (3-17) can be substituted into Equation (3-10), and the resultant $\frac{d(dT)}{dV_x}$ can be used to obtain $dT|_{V_{xRel}}$ in Equation (3-9), which is the aerodynamic force acting on the rotor element. For simplicity, denote

$$A \cdot dr = \frac{\partial(dT)}{\partial V_x}, \tag{3-19}$$

$$B \cdot dr = \frac{\partial(dT)}{\partial\phi}\frac{d\phi}{dV_x}. \tag{3-20}$$

So, the thrust felt by the three blade elements is:

$$dT|_{V_{xRel}} = dT|_{V_x} - (A+B)dr \cdot \dot{x}. \tag{3-21}$$

The total thrust felt by the rotor is:

$$F_x = \int_0^R dT|_{V_{xRel}} = \int_0^R dT|_{V_x} - \int_0^R (A+B)dr \cdot \dot{x}, \tag{3-22}$$

where R is the radius of the rotor. Equation (3-22) shows that the total thrust can be divided in two parts: the first part $\int_0^R dT|_{V_x}$ represents the static force caused by the steady wind on a rigid structure; the second part $-\int_0^R (A+B)dr \cdot \dot{x}$ is the aerodynamic damping force proportional to the oscillating velocity of the entire rotor. Applying the total thrust on the top of the tower, the turbine model can account for the aerodynamic

damping at a given rotor speed, wind speed and pitch angles without coupling the tower and the rotor models. The damping part $\int_0^R (A+B)dr$ can be used to calculate the damping ratio with the following equation:

$$\zeta_{Aero\_FA} = \frac{\int_0^R (A+B)dr}{2\overline{m}_1\omega_1}. \tag{3-23}$$

Side-side aerodynamic damping

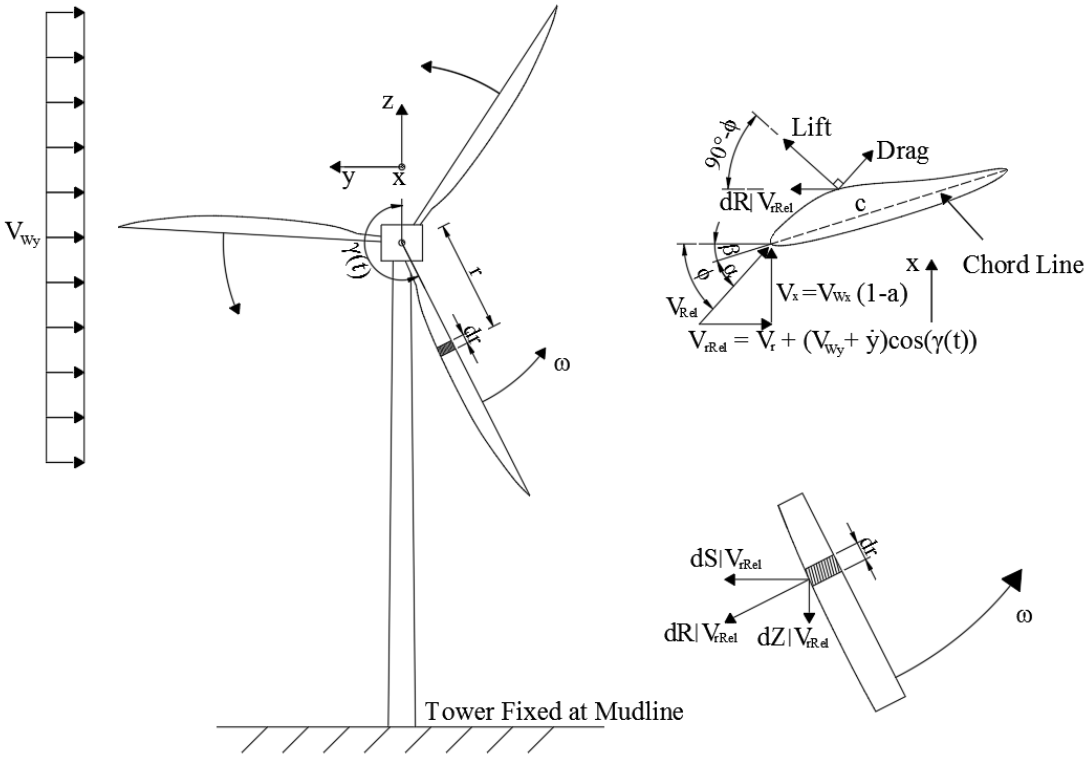

Figure 3-3. Blade element forces for side-side vibration.

For the side-side direction a similar approach can be followed. Calling V_r the speed component in the tangential direction, BEM theory gives $V_r = \omega r(1+a') + V_{Wy}\cos(\gamma_i(t))$ [25] where V_{Wy} is the inflow wind speed in the side-side direction and $\gamma_i(t)$ is the azimuth angle of the blade which is a function of time t when the turbine is in operation. The force in the y direction felt by an element at distance r along the ith blade is

$$dS|_{V_r} = \frac{1}{2}\rho_a \frac{V_r^2}{cos^2\phi} c C_t \cos(\gamma_i(t))\, dr, \tag{3-24}$$

where $C_t = C_l sin\phi - C_d cos\phi$ and $\gamma_i(t)$ is the azimuth angle of the blade, which is a function of time t when the turbine is in operation. It is noted that here the elemental force in y direction is assumed to be a function of V_r and ϕ. If there is a small change in V_r due to the overall tower top motion, the relative speed of the element in tangential direction V_{rRel} becomes:

$$V_{rRel} = V_r + \left(V_{Wy} + \dot{y}\right)\cos\left(\gamma_i(t)\right). \tag{3-25}$$

In the following derivation we can always assume that $V_{Wy} = 0$ since the turbine can be controlled and oriented so as to face the wind. Again a first order Taylor's expansion of the side-side force gives the expression of $dS|_{V_{rRel}}$ which is the tangential force felt by the blade element at a relative speed of V_{rRel}:

$$\begin{aligned} dS|_{V_{rRel}} &= dS|_{V_r} + dS'|_{V_r} \cdot (V_{rRel} - V_r) \\ &= dS|_{V_r} + \frac{d(dS)}{dV_r}\dot{y}cos\left(\gamma_i(t)\right). \end{aligned} \tag{3-26}$$

Assuming that dS is a function of V_r and ϕ, and ϕ is a function of V_r, $\frac{d(dS)}{dV_r}$ can be calculated as:

$$\frac{d(dS)}{dV_r} = \frac{\partial(dS)}{\partial V_r} + \frac{\partial(dS)}{\partial \phi}\frac{d\phi}{dV_r}. \tag{3-27}$$

$\frac{\partial(dS)}{\partial V_r}$ and $\frac{\partial(dS)}{\partial \phi}$ can be obtained by differentiating Equation (3-24):

$$\frac{\partial(dS)}{\partial V_r} = \rho_a \frac{V_r}{\cos^2\phi} c C_t \cos\left(\gamma_i(t)\right) dr, \tag{3-28}$$

$$\frac{\partial(dS)}{\partial \phi} = \frac{1}{2}\rho_a V_r^2 \frac{\frac{dC_t}{d\phi}cos^2\phi + 2cos\phi sin\phi C_t}{cos^4\phi} ccos\left(\gamma_i(t)\right)dr. \tag{3-29}$$

To obtain an expression for $\frac{d\phi}{V_r}$, the following two equations can be used:

$$cot\phi = \frac{V_r}{V_{Wx}(1-a)}, \tag{3-30}$$

$$a = \frac{1}{\frac{4sin^2\phi}{\sigma C_n} + 1}. \tag{3-31}$$

Differentiating Equation (3-30) with respect to V_r and Equation (3-31) with respect to ϕ results in

$$\frac{d\phi}{dV_r} = \frac{1}{V_{Wx}\left(\frac{1-a}{sin^2\phi} - \frac{da}{d\phi}cot\phi\right)}, \tag{3-32}$$

and

$$\frac{da}{d\phi} = \frac{-4\left(sin2\phi C_n - \frac{dC_n}{d\phi}sin^2\phi\right)}{\sigma C_n^2\left(\frac{4sin^2\phi}{\sigma C_n} + 1\right)^2}. \tag{3-33}$$

Equations (3-28), (3-29) and (3-32) can be substituted into Equation (3-27), and the resultant $\frac{d(dS)}{dV_r}$ can be used to obtain $dS|_{V_{rRel}}$ in Equation (3-26) which is the side-side aerodynamic force acting on the rotor element. For simplicity, denote

$$A'\cos\big(\gamma_i(t)\big)\cdot dr = \frac{\partial(dS)}{\partial V_r}, \tag{3-34}$$

$$B'\cos\big(\gamma_i(t)\big)\cdot dr = \frac{\partial\,(dS)}{\partial\phi}\frac{d\phi}{dV_r}. \tag{3-35}$$

So, the side-side aerodynamic force for one element is

$$dS|_{V_{rRel}} = dS|_{V_r} + (A' + B')dr\cdot\dot{y}cos^2\big(\gamma_i(t)\big). \tag{3-36}$$

The side-side aerodynamic force felt by the ith blade is

$$\begin{aligned} F|_{y_i} &= \int_0^R dS|_{V_{rRel}} \\ &= \int_0^R dS|_{V_r} + \int_0^R (A' + B')dr\cdot\dot{y}cos^2\big(\gamma_i(t)\big). \end{aligned} \tag{3-37}$$

Following a similar procedure to that outlined in the fore-aft case, the total side-side aerodynamic force felt by the rotor can be expressed as:

$$F_y = \sum_{i=1}^{N_b}\int_0^R dS|_{V_r} + \sum_{i=1}^{N_b}\int_0^R (A' + B')dr\cdot\dot{y}cos^2\big(\gamma_i(t)\big). \tag{3-38}$$

For a symmetric three-blade rotor on steady condition without vibration and inflow wind in side-side direction, the total force on side-side direction, $\sum_{i=1}^{N_b}\int_0^R dS|_{V_{rRel}}$ is zero, so dF_y can be simplified to

$$F_y = \frac{N_b}{2}\int_0^R (A' + B')dr\cdot\dot{y}, \tag{3-39}$$

since $\sum_{i=1}^{N_b}\int_0^R dS|_{V_r} = 0$ and $\sum_{i=1}^{N_b} cos^2\big(\gamma_i(t)\big) = \frac{N_b}{2}$. It should be noted that the term $A' + B'$ is negative. Using modal analysis, the side-side damping ratio can be expressed as:

$$\zeta_{Aero\_SS} = \frac{-\frac{N_b}{2}\int_0^R (A' + B')dr}{2\bar{m}_1\omega_1}. \tag{3-40}$$

3.3.2 Aerodynamic damping comparison

Equations (3-23) and (3-40) were implemented in MATLAB and coupled with the modal properties obtained from the FE model to calculate the aerodynamic damping ratios in the FA and SS directions. These results are compared to FAST simulations obtained with identical settings for verification purposes. For a range of steady wind speeds, FAST simulations were run, allowing the control module in FAST to alter the pitch angles and the rotational speed of the rotor to achieve the desired power output. Figure 3-4 shows the relationship obtained this way between rotor speed, pitch and wind speed for the same NREL 5 MW turbine.

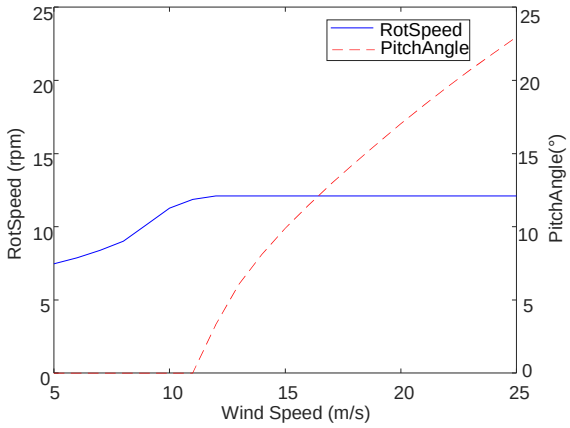

Figure 3-4. Steady state pitch angles and rotor speeds with different inflow wind speed in the FA direction.

For each average wind speed, an initial displacement of 1 meter was applied to the tower top and FAST was used to calculate time series of the tower top response. From these time series damping ratios were estimated as described in Subsection 3.2.3. Figure 3-5 shows the comparison of damping ratios in the FA and SS directions (respectively)

using FAST and the proposed modelling approach for varying wind speeds. The FA and SS degrees of freedom were decoupled in the FAST simulations to mirror the BEM modelling assumptions. For example, when looking at the FA damping, the FA DOF was switched on but the SS DOF was switched off and vice-versa. In the FA direction, a good agreement is found between FAST and BEM results. Figure 3-5 confirms that for the turbine modelled here, FA aerodynamic damping increases from 5% at low wind speed to 7% at the rated speed after which it remains broadly constant. This range is in full agreement with the results reported in the literature. In the SS direction, the damping ratios obtained from BEM and FAST follow similar trends and the damping ratios are much lower than in the FA direction and they increase steadily from 0.2% to 1.2-1.6% at the top wind speed in the operating range. BEM results appear systematically higher than those from FAST by a fraction of a percent. In summary, the proposed aerodynamic model based on BEM theory is adequate to model the aerodynamic damping in the FA direction and gives a reasonable estimate in the SS direction. However, as the model is planar it cannot capture more detailed effects related to coupling in the FA and SS motions which appear to affect the dependency of the damping ratio on the wind speed above the rated speed of the turbine. A more advanced aerodynamic damping model considering this coupling will be introduced in Chapters 4 and 5.

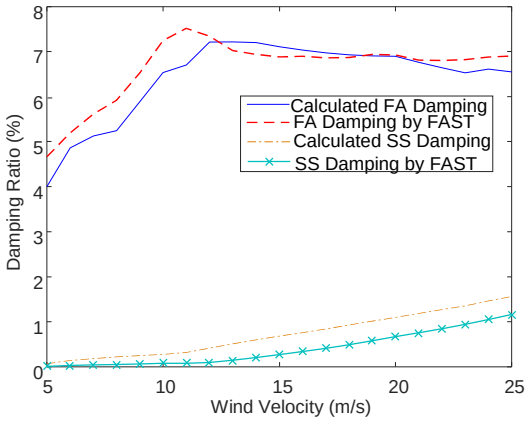

Figure 3-5. Comparison of FA and SS damping between proposed method and FAST.

3.4 Hydrodynamic damping

In this section hydrodynamic damping is quantified directly on the basis of classical theories and numerical simulations. As a simple but representative model, a flexible cantilevered cylinder immersed in water up to MSL is considered and subjected to wave excitation as shown in Figure 3-6. There are mainly two approaches to calculate the hydrodynamic forces resulting from the interaction between the cylinder and the seawater: (1) through Morison's equation or (2) potential flow theory. Morison's equation deals with the viscous effects when flow separation is significant, while potential flow theory accounts for the diffraction and radiation phenomena.

The physics of the water-cylinder interaction can be very different depending on the value of key non-dimensional parameters. The most relevant ones here are the KC number, the Stokes parameter β_{Stokes} and the diffraction factor D/λ where λ is the wavelength and D the diameter of the pile. By definition, $KC = 2\pi\hat{x}/D$ where $\hat{x}$ is the amplitude of the sideway motion, and $\beta_{Stokes} = D^2/\nu_w T$ where ν_w is the kinematic viscosity of water and T is the oscillation period. In the case of a large monopile submerged in water, the KC number is in the range of low values, around 10^{-2}, while the Stokes parameter and the diffraction factor are relatively large. These parameter values indicate that the flow separation tends to be small but not insignificant while diffraction and radiation are the dominant phenomena [38]. This is supported by Johanning *et al.* [78], who found that the damping of an oscillating cylinder can be influenced by both the viscous damping and radiation damping caused by hydrodynamic forces. In this section, hydrodynamic damping is estimated by modelling the viscous (Morison's equation) and wave (potential theory) contributions separately.

In addition to the two dissipative effects mentioned above, the added mass of the volume of water moving together with the cylinder can influence the mass distribution of the monopile below mean sea level (MSL). The added mass tends to reduce the damping ratio, but this effect has been found to be negligible [17]. The low relative acceleration of the submerged tower (since this part is near the clamped end) results in a very small effect on the frequency and dynamic response of the whole system. Therefore, in the subsequent calculations, the modal mass does not account for the hydrodynamic added mass.

Both for viscous and radiation damping, the wave height and wave period were set to 6 m and 10 s for all calculations and the wave velocities were calculated using linear wave theory [123]. This single combination of wave period and wave height was selected for simplicity, but is representative of the most common sea states [6].

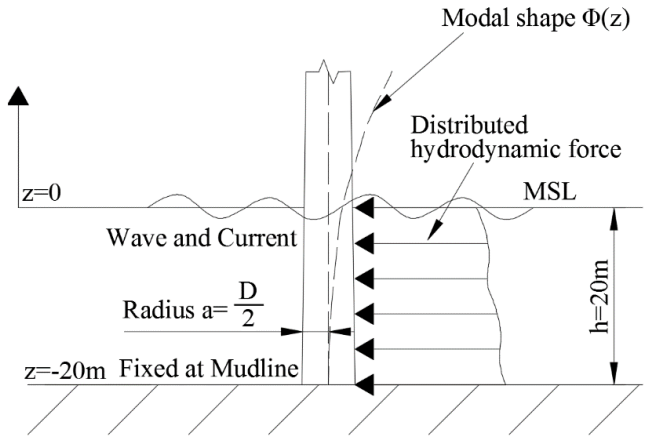

Figure 3-6. Schematic of hydrodynamic forces on OWT substructure.

3.4.1 Viscous damping

For an oscillating cylinder excited by waves, Morison's equation gives the forces on a strip of cylinder at depth z:

$$F_{Morison} = \frac{1}{2}\rho_w D C_d |\dot{u}_w - \dot{v}_{tower}|(\dot{u}_w - \dot{v}_{tower}) + \frac{\pi}{4}\rho_w D^2 C_a(\ddot{u}_w - \ddot{v}_{tower}) + \frac{\pi}{4}\rho_w D^2 \ddot{u}_w. \quad (3\text{-}41)$$

where u_w is the velocity of water particles, u_{tower} is the velocity of tower vibrating below the MSL, C_d is the drag coefficient and C_a is the added mass coefficient and ρ_w is the density of water. The damping term is quadratic to the relative velocity and influenced by the drag coefficient C_d. The value of C_d is mainly dependent on the KC number and Stokes parameter ([124][125]). According to Johanning *et al.* [78], for low values of the KC number (up to 5) and high values of Stokes number (of the magnitude of 10^5), C_d can be obtained by the following equation:

$$C_d = \frac{2 \times 26.24}{KC\sqrt{\beta_{Stokes}}} + 0.08KC, \quad (3\text{-}42)$$

where the second term in this equation can be neglected for even smaller KC numbers. As KC number depends on the vibration amplitude, C_d could be made to vary along the depth of the cylinder according to Equation (3-42). This was tested and the damping did not show much sensitivity to C_d so $C_d = 1$ was used throughout, based on the velocity amplitude of the pile at MSL obtained from simulations of the 5 MW reference turbine and recommendations from past studies (*e.g.* [9]).

The viscous drag term in Morison's equation varies along the immersed cylinder as a result of the non-uniform distribution of vibration accelerations and velocities. Following [126] and after rearranging, the damping ratio for a single pile subjected to viscous drag can be written as:

$$\zeta_{Hydro,Vis} = \frac{\int_{-h}^{0} \frac{1}{2}\rho_w D C_d \sqrt{\frac{8}{\pi}}\sigma_r(z)\boldsymbol{\Phi}_1^2(z)dz}{2\bar{m}_1\omega_1}, \tag{3-43}$$

where $\sigma_r(z)$ is the root mean square of the relative speed between the water wave particle and the pile (and other notation as defined in Subsection 3.2.2). For large OWTs, the velocity of the pile can be estimated by $2\pi\hat{x}/T$~0.1 m/s. This is much smaller than the wave particle velocity (usually above 10 m/s), so $\sigma_r(z)$ can be replaced by the root mean square of the particle velocity. Usually, the wave profile can be generated using specific spectra, so $\sigma_r(z)$ could be calculated from these spectra.

3.4.2 Radiation damping

According to linear potential flow theory, when only wave radiation is considered (*i.e.* ignoring the fluid viscosity), wave-structure interaction produces two kinds of forces: those produced by the incoming wave field on a rigid cylinder and those due to the motion of the structure in a disturbance-free fluid. Only the latter gives rise to dissipation and can be expressed in Equation (3-4) by

$$\bar{f}_1(t) = -\int_{-h}^{0} C_{Rad}dz \cdot \dot{\alpha}_1(t). \tag{3-44}$$

Here only the damping force for the first tower mode is considered. The derivation for C_{Rad} is based on a well-established diffraction theory and can be expressed by:

$$C_{Rad} = \rho_w \pi a \sigma h G_0(kh) P_1(ka) cosh\big(k(z+h)\big)\boldsymbol{\Phi}_1(z). \tag{3-45}$$

where σ is the frequency of radiated waves, k is the wave number. $G_0(kh)$ and $P_1(ka)$ are functions of wave numbers, and more details can be found in [127]. Substituting

Equation (3-45) into Equation (3-4) and after rearranging, the motion equation for the first tower mode is written as

$$\bar{m}_1\ddot{\alpha}_1(t) + \left(\bar{c}_1 + \int_{-h}^{0} C_{Rad}dz\right)\dot{\alpha}_1(t) + \bar{k}_1\alpha_1(t) = 0. \tag{3-46}$$

The radiation damping ratio can be obtained by

$$\zeta_{Hydro,Rad} = \frac{\int_{-h}^{0} C_{Rad}dz}{2\omega_1\bar{m}_1}. \tag{3-47}$$

3.4.3 Hydrodynamic damping comparison

For the model of the 5 MW reference OWT considered here, the viscous damping ratio calculated by Equation (3-43) is 0.0006%, while the radiation damping ratio according to Equation (3-47) is 0.007%, giving a total hydrodynamic damping ratio of 0.0076%. This result is much smaller than what has been reported in the literature such as [9] which suggested the viscous damping ratio around 0.004% and the radiation damping ratio 0.12%. This difference is explained by the size of the structure which is much larger in our case than those considered in the literature. In [127] from which the 0.12% value for radiation damping value seems to originate, the diameter of the pile considered was 1.2 m (4 ft) and the structure was much shorter above MSL (so the dynamics of the structures were very different). When these dimensions are used in the equations presented in this section, 0.11% is obtained confirming the soundness of the calculation and the effect of the size. To explore this further, plausible dimensions for tower height, water depth and pile thickness (based on the turbine scaling equations proposed in [128]) were estimated so that damping values could be calculated for various turbine sizes. The results are shown in (3-7), confirming that both viscous and radiation damping are always very small for large diameter rotors.

The conclusion from these models is that hydrodynamic damping in OWTs is much smaller than usually assumed (such as the values recommended by GL [80]) and for all practical purposes could be safely ignored.

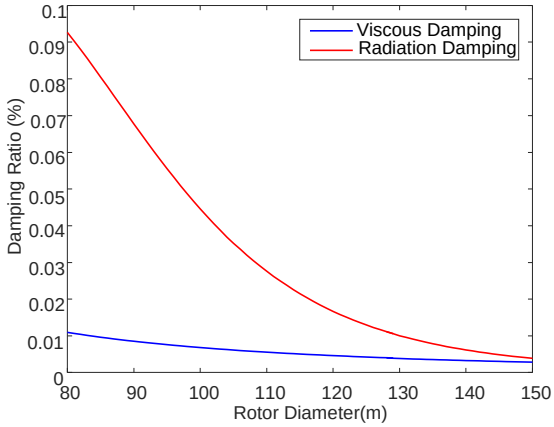

Figure 3-7. Variation of viscous and radiation damping ratios for different turbine sizes.

3.5 Soil damping

The soil surrounding the monopile foundation can dissipate vibrational energy in two ways: (1) the motion of the pile can cause waves to radiate away from the pile into the ground (radiation damping), and (2) hysteretic material damping can occur as the soil is being cyclically stressed ([13][56]). Radiation damping depends on the frequency ω of the external excitation. The non-dimensional parameter $a_0 = \omega D/V_s$ can be used to assess the significance of the wave phenomenon. It compares the order of magnitude of the pile lateral velocity and the shear wave velocity of the soil stratum V_s. The shear wave velocity ranges from 150 m/s to 300 m/s depending on the soil type (see Table 3-3 below). For a monopile-supported OWT, the forces experienced by the soil will usually have a low frequency around the first natural frequency of the wind turbine system (less than 1 Hz and 0.25-0.28 Hz for the OWT used in this chapter) as the response of the system is dominated by the first vibration mode. In these conditions, a_0 can be expected to be of the order of 10^{-2}, indicating that the behaviour of the soil is largely quasi-static so that radiation damping for a monopile-supported OWT can be ignored [83].

3.5.1 Soil model

Stiffness and damping coefficients for soil springs and dashpots

Soil-pile interaction can be modelled using different approaches such as linear or non-linear Winkler's springs or finite element solid modelling. For design purposes, p-y curves, which capture the nonlinear displacement-force relationship in the soil, are frequently used. In the present study, a combination of classic p-y curves and the study by Gazetas and Dobry [83] is adopted. The soil is represented by a series of horizontal springs and dashpots in parallel from the mudline to bottom of the pile. The stiffness of the springs was obtained from p-y curves while the dashpot coefficients representing the soil material damping were calculated following Gazetas and Dobry [83]:

$$c_m = 2k\frac{\beta_m}{\omega}, \tag{3-48}$$

where β_m represents the material damping ratio, k is the secant modulus defined as the ratio between the static local soil reaction for a unit length of pile and the corresponding local pile deflection, ω is the circular frequency of the excitation at the pile head. The magnitude of material damping ratio for a soil stratum is related to the shear strain in the soil and can be influenced by the properties of soil such as plastic index and mean effective confining stress. Darendeli [85] proposed an analytical model to calculate material damping curves for various values of the over consolidation ratio (OCR) and plasticity index (PI). This study adopts this method and uses the coefficients for sand and clay from Southern California provided by Darendeli as the parameters he uses are somewhat idiosyncratic and not available from standard data tables. However Darendeli's data as well as other experimental studies in soil damping [84] show that the curves produced using his formulae are representative of many soil types.

Figure 3-8 shows the relationship between the material damping ratio and soil shear strain for clay in which the damping depends on the PI to some extent, so various curves were plotted for different PI values. The PI values used for the clay soils is shown in Table 3-2. Sandy soils (not shown) have a very similar relationship between material damping ratio and shear strain but their PI should be 0. Soil material damping also depends slightly on the OCR but in the context of offshore wind turbines, OCR should be 1 and this value was used for all soil types considered in this study.

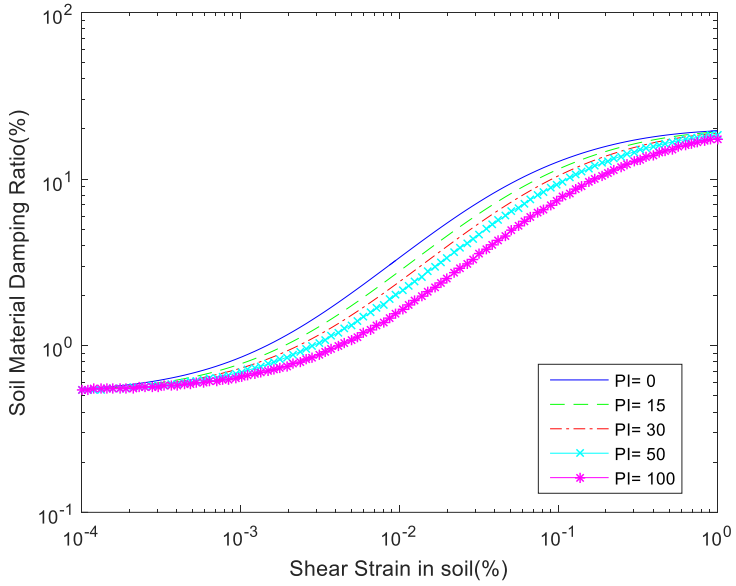

Figure 3-8. Relationship between material damping ratio and shear strain in clay for different PI values.

Following [83], the shear strain γ_e can be determined by

$$\gamma_e = \frac{1+\nu}{2.5D} y_{Amp}(z,t), \tag{3-49}$$

where $y_{Amp}(z)$ is the oscillating amplitude of the pile in the horizontal direction, ν is Poisson's ratio for the soil stratum, and D is the diameter of the pile. k is determined from the non-linear p-y curves:

$$k = \frac{p(z,t)}{y(z,t)}. \tag{3-50}$$

The soil around a wind turbine experiences cyclic strain on top of a constant strain caused by the mean wind thrust. Whether the total amplitude or simply the dynamic component should be used for $y_{Amp}(z)$ is not obvious. In this study, the amplitude y_{Amp} used to calculate the strain (and subsequently the damping ratio) was half the range of oscillation. An alternative method commonly used in earthquake engineering [84] is to evaluate the damping constant using 65% of the maximum strain reached in the soil strata during a response time history. Earthquake ground motion does not usually have a static component so it is still not clear how to implement this rule in the

context of offshore wind, but this was also tested and found to give very similar results to those obtained using Equation (3-49).

Soil properties and p-y curves

Here six soil profiles are selected to investigate the soil damping contribution. Profiles 1-4 are single material soils made of medium clay, stiff clay, medium sand and dense sand, respectively. The low stiffness of soft clay and loose sand would significantly reduce the stiffness of the entire system and lead to unrealistic designs, so they were excluded as monolayered soils. Profiles 5 and 6 are layered soil profiles combining a mix of clay and sandy soils respectively. The layered clay profile is a combination of stiff clay, medium clay and soft clay from bottom to pile head with the height of 14m, 14m and 6m respectively. The layered sandy profile is a combination of loose sand, medium sand and dense sand from bottom to pile head with the height of 14m, 14m and 6m respectively, which is a typical layered profile based on the data provided in Appendix B in [129]. The different soil profiles used are summarised in Table 3-2 while the properties of the different soil types are listed in Table 3-3.

Table 3-2. Soil profiles definition.

Profile 1	Profile 2	Profile 3	Profile 4	Profile 5	Profile 6
medium clay	stiff clay	medium sand	dense sand	28m-34m Soft clay 14m-28m Medium clay 0m-14m Stiff clay	28m-34m Loose sand 14m-28m Medium sand 0m-14m Dense sand
PI=20	PI=20	PI=0	PI=0	PI=20	PI=0
OCR=1	OCR=1	OCR=1	OCR=1	OCR=1	OCR=1

The soil-structure interaction effect was modelled using static or cyclic p-y curves recommended in DNV 2014 [22] and API standards [53], and the steps to establish the p-y curves are detailed in Reese and Van Impe [54]. Although it would seem more sensible to use the cyclic curves to represent the soil-structure interaction of an OWT under long-term excitations, both static and cyclic p-y curves were used to allow for comparison with published results. Figure 3-9 shows the static and cyclic p-y curves for each soil types at the depth $z = -8.5\ m$ from the mudline. These figures illustrate that, whether static or cyclic p-y curves are used, the reaction forces from the soil plateau vary quickly in sandy soils as the pile moves sideway. By contrast, the

behaviour of clay soils is more complex and variable as the lateral displacement of the pile increases. The cyclic p-y curves are recognisably similar to the static ones except that much larger forces can be reached in the cyclic case.

Table 3-3. Mechanical properties of the soil profiles used in the model.

	Soil type	Density γ (1×10^3 kg/m^3)	Undrained shear strength c_u (kPa)	Poisson's ratio ν	Friction angle φ	Shear modulus G_s (MPa)	Shear wave velocity V_s (m/s)	Elastic Modulus E_s (MPa)
Clay	Soft Clay	1.75	30	0.45	-	43	158	15
	Medium Clay	1.90	80	0.45	-	87	214	30
	Stiff Clay	2.00	125	0.45	-	145	269	50
Sand	Loose Sand	1.75	-	0.30	33 º	47	164	18
	Medium Sand	1.90	-	0.30	36 º	109	240	42
	Dense Sand	2.07	-	0.30	38 º	182	297	70

In this section, the finite element model of the OWT included soil springs and dashpots, with properties obtained using Equations (3-48) and (3-50) respectively. As the response of the soil is strongly strain-dependent, the model was subjected to forces of increasing intensity. This was implemented using thrust time series obtained from FAST with mean speed increasing from 5 m/s to 25 m/s by 1 m/s increments. To avoid the stochastic component of the wind adding noise to the response of the system and interfering with the damping calculation, these time series were averaged, and the average was used as a static force applied at the tower top in the finite element model. Then the soil damping was calculated from the vibration decay following the application of 1m initial displacement, consistent with the response of the system to the given force. For these simulations, the control system was kept on in FAST. This enables blade pitching and causes a decrease in aerodynamic force in the FA direction for wind speeds above the rated speed (12 m/s in this case).

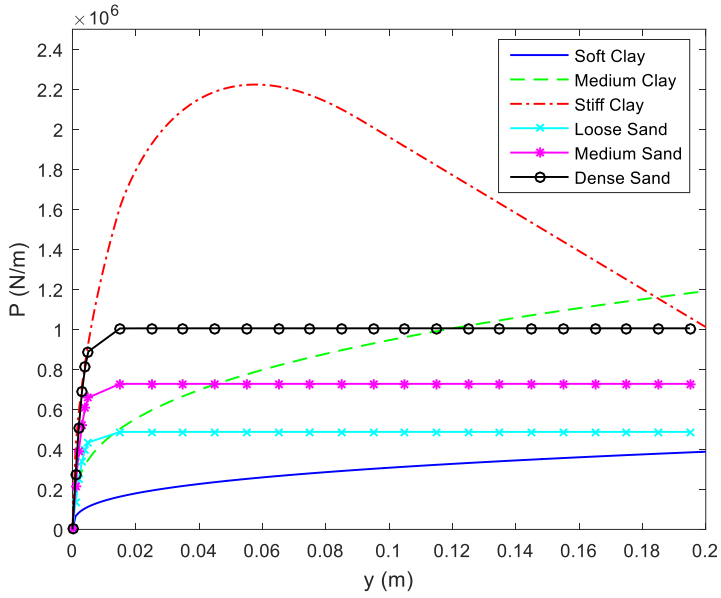

(a)

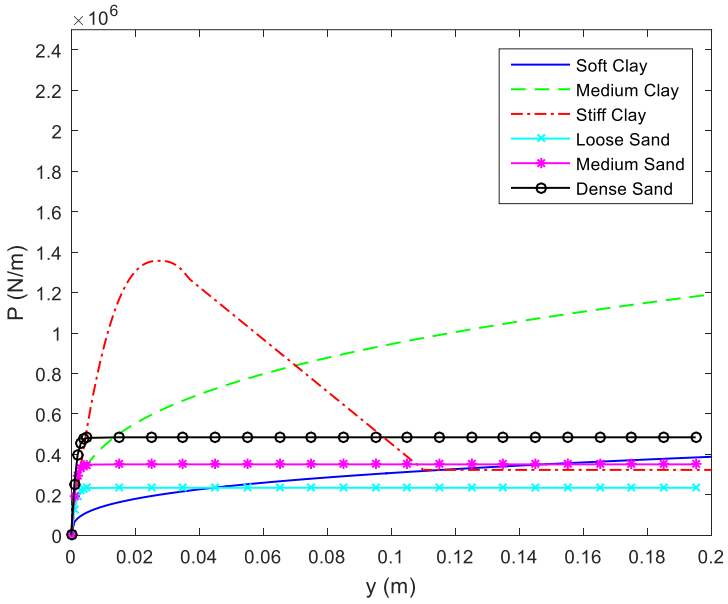

(b)

Figure 3-9. Static (a) and cyclic (b) p-y curves for different soil types.

3.5.2 Soil damping results and discussion

Figure 3-10 shows the variation of the damping ratios in the various soils for mean wind speeds ranging from 5 m/s to 25 m/s. The plots in Figure 3-10 all show a similar behaviour. Soil damping ratios increase from 0.2%-0.3% at low wind speeds up to

around 1.3% at the rated wind speed 12 m/s. Thereafter it decreases back to 0.3%-0.6%. This range is in agreement with the published results reported in Subsection 2.4.3 and our results confirm that soil damping is quite variable and can become quite significant for some tower amplitudes.

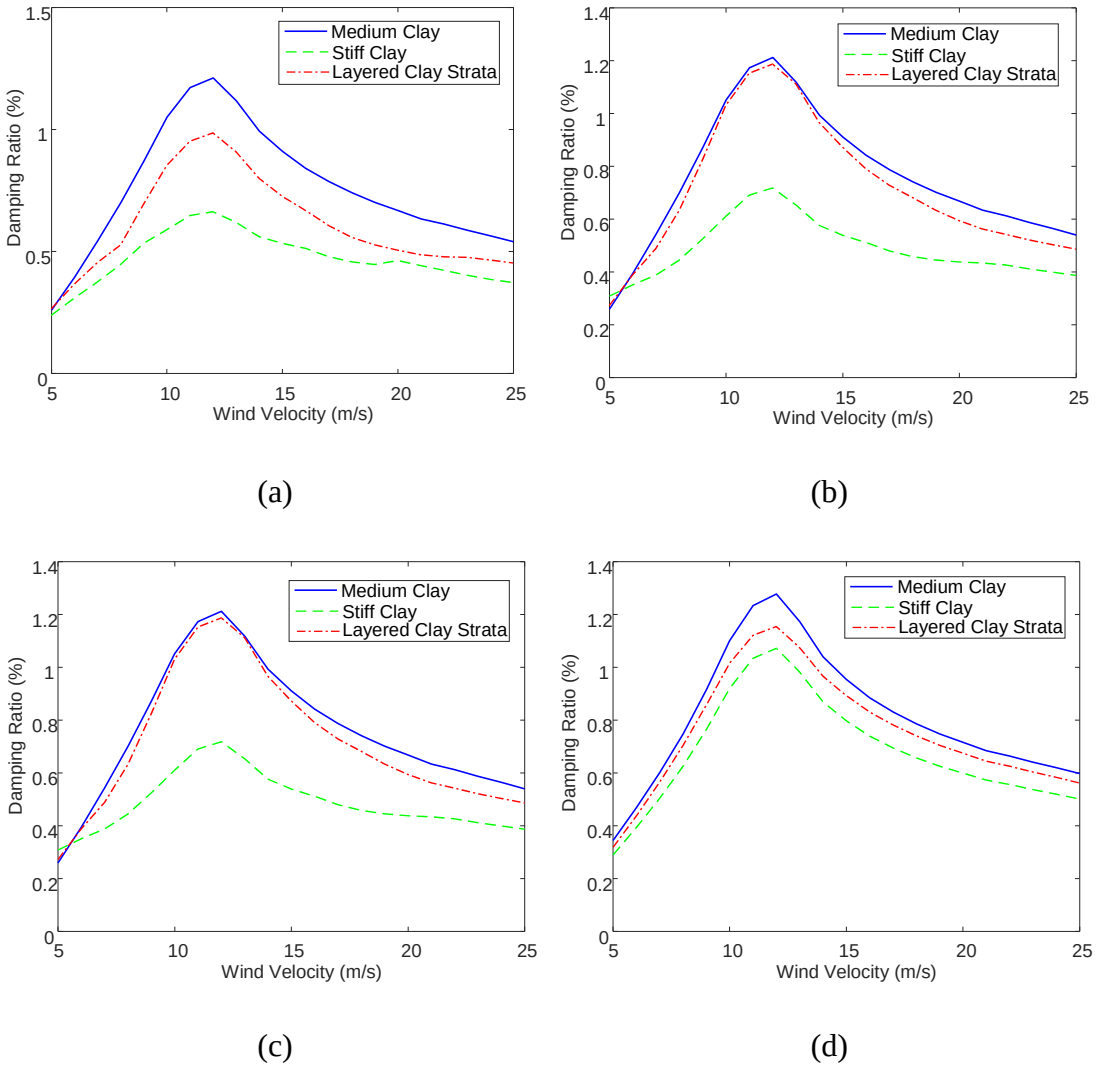

Figure 3-10. Soil damping in terms of wind speed for various soil profiles and p-y curves. (a) shows the clay profiles using static p-y curves; (b) shows the clay profiles using cyclic p-y curves; (c) shows the sand profiles using static p-y curves; (d) shows the sand profiles using cyclic p-y curves.

To understand these results better, Figure 3-11(a) shows the average thrust for varying wind speed and Figure 3-11(b) shows the modal stiffnesses for the clay soils obtained with static p-y curves. The behaviour for sands is very similar, so the corresponding

graph is not shown. Figure 3-11(a) shows that up to the rated wind speed, the thrust increases. Then the control system starts feathering the blades so that the overall thrust decreases despite increasing wind speeds. It can be seen that the shape of the damping curves in Figure 3-10 follow closely that of the thrust. This phenomenon is a consequence of two concomitant mechanisms: (1) the non-linear softening of the soil as described by p-y curves (Figure 3-9); (2) the increase in soil material damping with increasing strain described by Figure 3-8.

When the deflection caused by the wind speed increases beyond critical values (the abrupt change in slope in the p-y curves), the soil stiffness decreases sharply, which reduces the stiffness of the whole system. This stiffness reduction leads to an increase in the soil damping contribution. The drop in stiffness in Figure 3-11(b) occurs when the wind speed is around the rated wind speed. This is when the largest rotor thrust and thus the largest displacement amplitude is experienced. According to Equation (3-48), the increased displacement magnitude also results in increased soil material damping ratio. As the constant of each soil dashpot increases the overall soil damping is further increased.

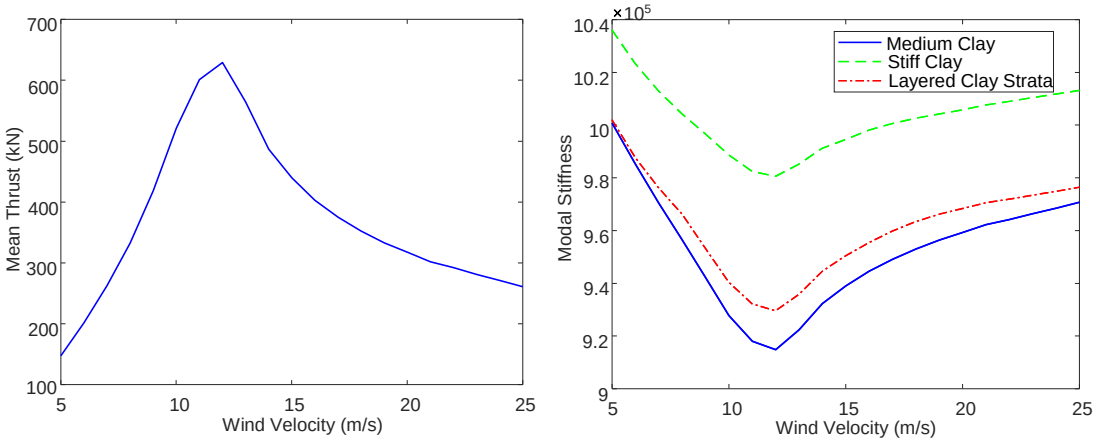

(a) (b)

Figure 3-11. (a) Wind speed-thrust at tower top relationship (b) Modal stiffness (no physical unit) in terms of wind speed using static p-y curve soil model.

It should be noted that the above observations are based on the assumption that the soil behaviour is well described by p-y curves. Some soils actually stiffen due to cyclic

loading (ratchetting behaviour) and in these cases the dependence of soil damping on the wind speed may be very different. This should be the subject of further study.

3.6 Conclusion

This chapter proposed a series of first-principle physics-based models that allowed the quantification of aerodynamic, hydrodynamic, and soil damping separately for monopile supported OWTs. The dissipation models were based on a bespoke finite element model of the system based on the 5 MW NREL offshore wind turbine. The damping results in this study are for the first FA or SS mode, which dominate the OWT dynamic response. These damping values can be easily implemented in a FE model at the design stage either specifying the damping ratio for the first mode or by inputting Rayleigh damping coefficients so that the first mode damping reaches the desired level.

Results showed that aerodynamic damping is in the range of 5-7% in the FA direction and 0.2-1.6% in the SS direction depending on the wind speed.

The viscous and radiation components of hydrodynamics damping were modelled from first principle. Results showed that for the current size of offshore wind turbines, hydrodynamic damping is much lower than what is usually quoted in the literature and for all practical purposes could be ignored.

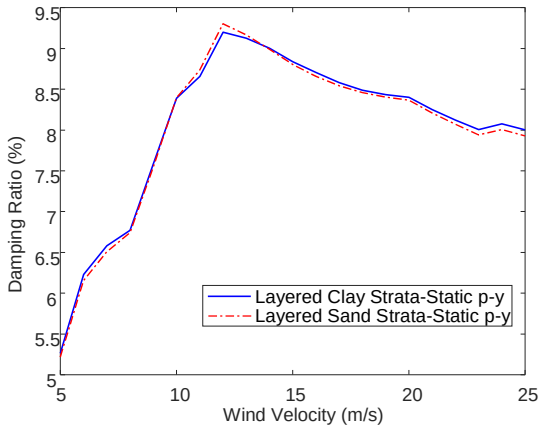

Figure 3-12. Overall FA damping ratio in a 5 MW offshore wind turbine in terms of wind speed for two representative soil profiles.

Soil damping was modelled in the form of dissipative springs distributed along the embedded length of the pile. The properties of these springs are based on relevant p-y

curves, which are nonlinear and as such their overall dissipative effect depends on the amplitude of vibration. Soil damping was calculated for different types of soils and wind speeds. Results showed that ζ_{soil} ranges from 0.2% to 1.3% with a strong dependence on the stiffness of the system. As the thrust increases, the springs weaken so the amplitude increases relatively. This increases the material damping and decreases the overall stiffness of the system, thereby increasing the damping ratio. This effect has not previously been studied systematically.

Figure 3-12 combines the results from the various models by adding up the contribution from various damping sources in the FA direction. $\zeta_{struct} = 1\%$ was used. The similarity between the FA damping curves in Figure 3-12 and Figure 3-5 shows that the overall damping is dominated by the aerodynamic component. It increases sharply from 6% to 9% up to the rated wind speed and then decreases slowly down to 8%.

Outside the operational range of the turbine, the aerodynamic damping drops dramatically so that the overall damping is dominated by the structural and soil components. Therefore, a reasonable range for the total damping in a non-operating turbine could be between 1% and 1.5%.

For the purpose of calculating the dynamic response of the system to design a currently non-existing turbine, it is important to obtain damping values in the correct range, bearing in mind that lower damping values will lead to safe but potentially over-conservative designs. By testing published values against simple but robust models, the study in this chapter can hopefully contribute to more optimal OWT designs.

Chapter 4 - Aerodynamic Damping Model Considering Aerodynamic Coupling

4.1 Introduction

As reviewed in Subsection 2.2.2, the available studies on decoupled models for tower/rotor interaction and aerodynamic damping mainly concentrate on aerodynamic damping in the FA direction and do not take into account the interaction between FA and SS motions. In Section 3.3, the derivation of aerodynamic damping ratios in the FA and SS direction was still based on the assumption that the aerodynamic forces at the tower top in one direction is only related to the perturbation of velocities seen by blade elements in that direction. However, an operating wind turbine vibrates in both directions simultaneously and its FA and SS motions are coupled. This coupling can be observed from FAST simulations, which will be shown in Section 4.2. In this chapter, we investigate in detail the nature of this coupling using a BEM-based derivation of the aerodynamic damping, and show that it can be represented through a non-standard aerodynamic damping matrix. This allows the wind-rotor interaction to be reduced to static forces applied at the tower top, with additional terms in the aerodynamic damping matrix proportional to the tower top velocities. The term "aerodynamic damping matrix" has been used to describe the aerodynamic damping for blade vibrations in the report by Petersen *et al.* [130], which implemented a similar force linearisation method. However, this chapter discusses the overall aerodynamic damping in tower vibration caused by the interaction between the air and the rotor. In the field of aircraft aeroelasticity, "aerodynamic influence coefficients" [131] relates the lift on the aerofoil element to its angle of incidence and the dynamic pressure and this phrase has similar meaning to "aerodynamic damping matrix" introduced in this chapter. Aerodynamic damping matrix can be regarded as a special case of the aerodynamics influence coefficient.

This aerodynamic model was implemented as part of the finite element model of the tower already described and was successfully verified against the fully-coupled modelling package FAST. The damping matrix components explain key features of the coupling between FA and SS vibrations of the wind turbine. This coupling causes energy transfers between the two directions, complicating aerodynamic damping

identification. The aerodynamic damping matrix offers a new method to describe the aerodynamic damping of wind turbines and is potentially better than the conventional description of the aerodynamic damping by one or two modal damping ratios (FA and SS).

4.2 Problem statement

The coupling between FA and SS motions is illustrated in this section using simulation results from a fully coupled wind turbine model of the NREL reference three-blade onshore wind turbine available in FAST [119]. An onshore wind turbine is used here instead of offshore wind turbines since this chapter only describes wind turbine aerodynamics. The modifications and settings used in these simulations will be described in Section 4.5, but they do not affect the general dynamic behaviour of the wind turbine highlighted here. The main properties of this wind turbine model are listed in Table 4-1.

Table 4-1. Basic properties of the modified NREL 5 MW reference onshore wind turbine.

Rotor Diameter, R	126 m
Hub Height from MSL	87.6 m
Tower Diameter, D	3.87-6.00 m
Tower Thickness, t	19-27 mm
Lumped Mass at Top	3.5×10^5 kg
Rated Wind Speed	12.1 m/s
Natural Frequency	0.34 Hz

Figure 4-1 shows the tower top FA (a) and SS (b) displacements time histories from the FAST software. These responses were triggered by a 1 m initial displacement in the FA direction of the tower top while the turbine is operational at a steady-state wind speed of 20 m/s. No initial displacement was given in the SS direction. Two types of dynamic responses were considered. For one case, the system was free to move both in the FA and SS directions (solid lines). For the second case (dashed lines), the system was only permitted to move in the FA direction, considering the SS DOF as rigid. The dynamics

of the tower in FAST is modelled as the superposition of the first two SS and FA bending modes, so it is possible to disable a particular DOF to prevent the corresponding motion. The wind speed, rotor rotation speed (12.1 rpm) and pitch angles (17.6 °) of the blades were kept constant at the nominal values during the simulation.

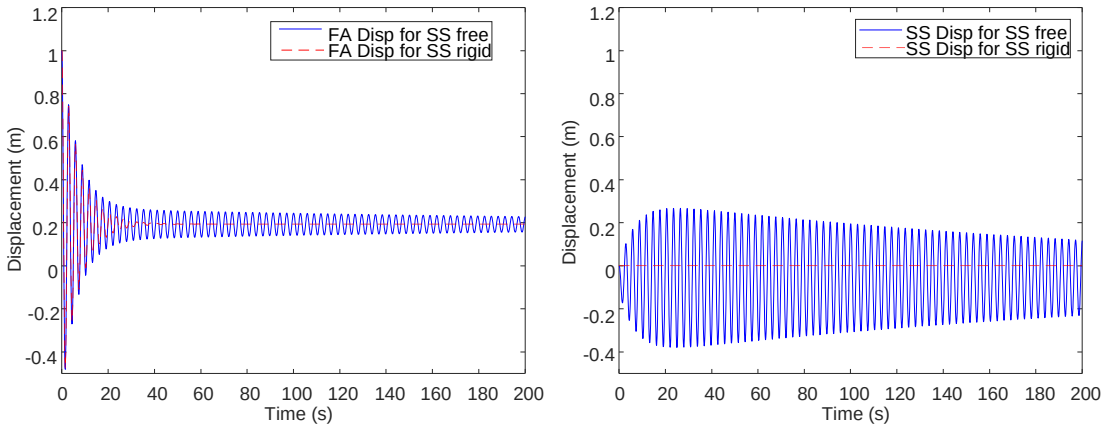

(a) (b)

Figure 4-1. Tower top displacements in the FA (a) and SS (b) directions simulated using FAST with SS direction free (solid) or kept rigid (dashed).

Figure 4-1(a) shows that the SS motion influences the FA motion damping, as can be seen from the slower FA response decay in the solid curve (SS free) compared to the dashed curve (SS rigid). Such an apparent change in damping in the FA direction would have a significant effect for fatigue analyses. Figure 4-1(b) shows that even without any initial displacement in the SS direction, a sideways response at the tower top is excited, growing initially as energy is transferred from the FA direction, before gradually decreasing. The SS motion is caused by the aerodynamic torque corresponding to the rotor rotation in addition to the forces related to the FA motion. This coupling effect is due to the aerodynamic forces on the rotor in the two directions. When the tower bends, the rotor plane moves and is no longer perpendicular to the incoming wind. This phenomenon causes unbalanced resultant forces in the SS and vertical directions as well as unbalanced moments, which cause a static deflection and oscillations. Conversely, the SS motion affects the FA motion and causes the damping to undergo an apparent change over time: the FA amplitude reduces at a fast rate initially but then decays at a much slower rate after 25 s (in the case shown in Figure 4-1, SS free), leading to very

different apparent damping values depending on which part of the curve is analysed. The details of this coupling depend on the inflow wind speed, pitch angle, and rotor speed, and for different combinations of these parameters, the vibration response may look slightly different than demonstrated in Figure 4-1. The study in this chapter was motivated by these observations. The intention was to propose an efficient methodology allowing the dynamics of the coupled system to be modelled without the requirement of unsteady aerodynamic simulations and to better characterize and understand how the aerodynamic damping affects the behaviour of wind turbines.

4.3 Description of 3D finite element model

Similar to the 2D FE model described in Section 3.2, a 3D FE model was coded in MATALB based on the 5 MW reference onshore turbine whose basic properties are described in Table 4-1. The tower was again modelled using 11 Euler-Bernoulli beam elements of equal length. However, unlike the model in Section 3.2 which only allows nodes to move in one horizontal direction, each node in this model can translate and rotate in two perpendicular directions, x (FA) and y (SS), as shown in Figure 4-2(a). θ_x and θ_y denote the rotations about the x and y axes respectively. The DOFs related to vertical displacement and the rotation about the z axis are ignored due to their negligible magnitudes.

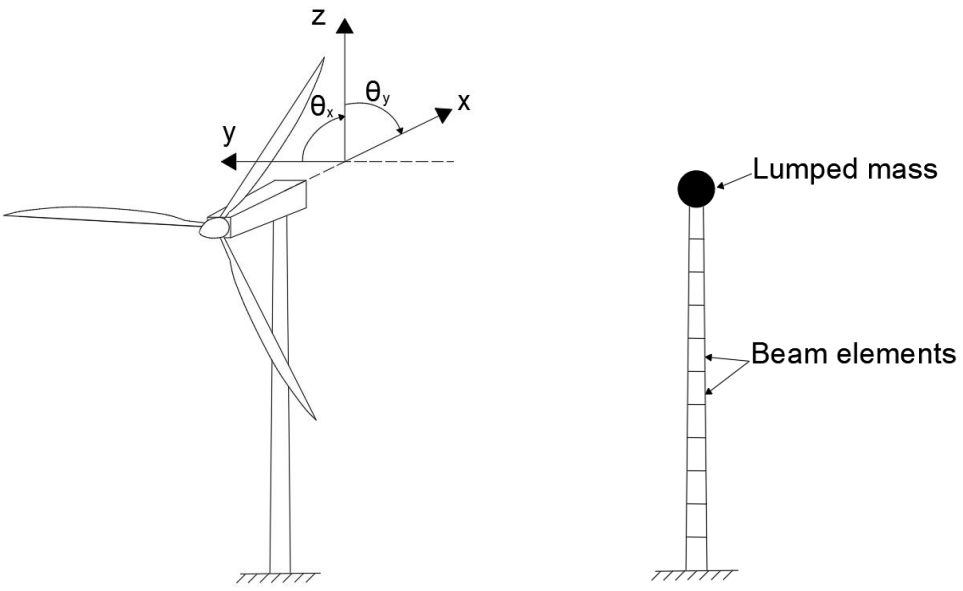

(a) (b)

Figure 4-2. Schematics of the wind turbine (a) and the numerical model (b)

The equations of motion for the 3D model can also be expressed in matrix format according Equation (3-1). The elemental mass and stiffness matrices denoted by $\mathbf{M}^e$ and $\mathbf{K}^e$ are expressed by

$$\mathbf{M}^e = \frac{m}{420}\begin{bmatrix} 156 & 0 & 0 & 22l & 54 & 0 & 0 & -13l \\ 0 & 156 & -22l & 0 & 0 & 54 & 13l & 0 \\ 0 & -22l & 4l^2 & 0 & 0 & -13l & -3l^2 & 0 \\ 22l & 0 & 0 & 4l^2 & 13l & 0 & 0 & -3l^2 \\ 54 & 0 & 0 & 13l & 156 & 0 & 0 & -22l \\ 0 & 54 & -13l & 0 & 0 & 156 & 22l & 0 \\ 0 & 13l & -3l^2 & 0 & 0 & 22l & 4l^2 & 0 \\ -13l & 0 & 0 & -3l^2 & -22l & 0 & 0 & 4l^2 \end{bmatrix}, \quad (4\text{-}1)$$

and

$$\mathbf{K}^e = \frac{1}{l^3}\begin{bmatrix} 12EI_y & 0 & 0 & 6EI_y l & -12EI_y & 0 & 0 & 6EI_y l \\ 0 & 12EI_x & -6EI_x l & 0 & 0 & -12EI_x & -6EI_x l & 0 \\ 0 & -6EI_x l & 4EI_x l^2 & 0 & 0 & 6EI_x l & 2EI_x l^2 & 0 \\ 6EI_y l & 0 & 0 & 4EI_y l^2 & -6EI_y l & 0 & 0 & 2EI_y l^2 \\ -12EI_y & 0 & 0 & -6EI_y l & 12EI_y & 0 & 0 & -6EI_y l \\ 0 & -12EI_x & 6EI_x l & 0 & 0 & 12EI_x & 6EI_x l & 0 \\ 0 & -6EI_x l & 2EI_x l^2 & 0 & 0 & 6EI_x l & 4EI_x l^2 & 0 \\ 6EI_y l & 0 & 0 & 2EI_y l^2 & -6EI_y l & 0 & 0 & 4EI_y l^2 \end{bmatrix}, \quad (4\text{-}2)$$

where l is the length of element, A is the section area, E is the Young's modulus, I_x is the second moment of area to x axis, while I_y is the second moment of area to y axis [132]. The external force vector $\mathbf{F}^e$ of one beam element corresponding to the two end nodes 1 and 2 is expressed by

$$\mathbf{F}^e = \begin{bmatrix} F_x^1 & F_y^2 & M_x^1 & M_y^1 & F_x^2 & F_y^2 & M_x^2 & M_y^2 \end{bmatrix}^T. \quad (4\text{-}3)$$

where F_x^1 is the external force in the x direction applied to the node 1, M_x^1 is the moment about the x axis applied to the node 1, *etc.* The displacement $\mathbf{u}^e$ for this element is

$$\mathbf{u}^e = [x_1 \quad y_1 \quad \theta_{x1} \quad \theta_{y1} \quad x_2 \quad y_2 \quad \theta_{x2} \quad \theta_{y2}]^T. \quad (4\text{-}4)$$

where x_1 is the displacement of the node 1 in the x direction, θ_{x1} is the rotation of node 1 about the x axis, *etc.*

The lumped mass representing the RNA was added to the relevant terms in the mass matrix for the top node of the tower. The moments of inertia of the RNA were set to

zero to allow verification of the model against FAST, as will be discussed in Subsection 4.5.1. The mass and stiffness matrices can be easily formed for each element given the material and geometric properties of the tower. Structural damping could be added as Rayleigh damping to this model, but zero structural damping was assumed throughout this chapter so that the aerodynamic damping is the only damping source. The tower is assumed clamped at its bottom. The time integration algorithm used to solve the equation of motions in Equation (3-1) in the time domain was HHT-α method as in Chapter 3.

4.4 Derivation of the aerodynamic damping matrix

4.4.1 Formation of basic equations for aerodynamic loads

Key features of the dynamic response of a wind turbine tower can be captured by modelling it as a cantilevered beam with a lumped mass connected to the free end [6]. The lumped mass at the top represents the RNA mass and the beam accounts for the wind turbine tower as shown in Figure 4-2(b). During normal operation, the rotor is subjected to the loads from the inflow wind, and the whole wind turbine is excited and vibrates. Excluding non-aerodynamic sources of dissipation, the vibration of the tower is damped by the wind-structure interaction – mainly the wind-rotor interaction, although the wind-tower interaction also has a small contribution. As the tower is axisymmetric, motion in the two directions is not coupled through a stiffness mechanism and the results confirm this. In the model presented in Section 4.3, the aerodynamic loads are separated into two parts: the aerodynamic load on a rigid tower/rotor and the aerodynamic damping force captured through a viscous damping matrix. To simplify the tower-rotor interaction and limit the number of variables necessary to describe the system, some modelling assumptions were made:

1. The connections between the tower top (or yaw bearing in FAST), the nacelle, and the rotor are rigid. This means that the displacement, velocity and acceleration of the rotor centre can be described as a combination of the translational and rotation of the tower top. It is assumed that the permanent shaft tilt is zero.

2. The rotor blades are rigid, so blade flapwise and edgewise vibrations are not considered. This means that the relative wind speed experienced by each blade

element is only influenced by the inflow wind speed, the RNA linear/angular velocity and the rotation speed of the rotor.

3. The RNA velocity is much smaller than the inflow wind speed and the speed of the blade elements due to rotor rotation. This allows the aerodynamic forces to be linearised using a first order Taylor expansion. For the FAST 5MW NREL onshore wind turbine, when the mean wind speed is near the cut-in speed of 3 m/s with 10% turbulence intensity, the magnitude of the tower top velocity is around 0.05 m/s and the rotation speed of the blade root can reach 1.8 m/s with the cut-in 6.9 rpm. For higher mean wind speeds, the RNA velocity becomes relatively smaller, so the condition is generally satisfied when the wind turbine is in operation.

In BEM theory, the calculated aerodynamic loads are related to the relative wind speeds experienced by each blade element. Therefore, it is necessary to determine the velocity of each blade element caused by the combined translation and rotation of the rotor. It is assumed that the rotor is facing an inflow wind of steady velocity V_0 pointing in the positive direction of the x axis, as indicated in Figure 4-3. The rotor rotates positively clockwise around the x axis at a speed ω so that a blade element at distance r along the blade length moves at a speed $V_r = \omega r$ perpendicular to the blade and tangential to the circle described by the blade element at r as it rotates. The azimuthal angle $\gamma_i(t)$ indicates the azimuthal position of the ith blade. The FA motion of the tower produces a linear velocity $\dot{x}$ and an angular velocity $\dot{\theta}_y$. The SS motion of the tower leads to a linear velocity $\dot{y}$ and an angular velocity $\dot{\theta}_x$. These velocities cause small variations in the relative wind speeds experienced by blade elements. For an arbitrary blade element at distance r from the hub centre with azimuthal position $\gamma_i(t)$, the relative wind speed experienced in the normal direction, V_{xRel}, can be written as

$$V_{xRel} = V_0 - \dot{x} - \dot{\theta}_y r cos\gamma_i(t), \tag{4-5}$$

and the relative wind speed in tangential direction, V_{rRel}, is

$$V_{rRel} = V_r - \dot{y} cos\gamma_i(t) + \dot{\theta}_x r. \tag{4-6}$$

V_{rRel} is tangential to the trajectory of the blade element as it rotates around the hub axis, perpendicular to the radial direction of a blade in the rotor plane. A positive V_{xRel} is a velocity toward the positive direction of the x axis, while a positive V_{rRel} is a velocity

having the opposite sign to the rotor rotation speed. In Equations (4-5) and (4-6), $\dot{x}$, $\dot{y}cos\gamma_i(t)$, $\dot{\theta}_y rcos\gamma_i(t)$ and $\dot{\theta}_x r$ are caused by the motion of the tower top.

Following from the assumptions listed, the angular velocity $\dot{\theta}_y$ causes the whole rotor to simply rotate around the hub, therefore the resultant linear velocities of the blade elements above the hub have inverse signs compared to those below the hub. As a result, the relative velocity caused by $\dot{\theta}_y$ can be calculated as $\dot{\theta}_y rcos\gamma_i(t)$.

The next step is to find the force and moment expressions of a single blade element for the relative wind velocities in Equations (4-5) and (4-6). The coordinate system used for the resultant forces and moments is consistent with the motion coordinates shown in Figure 4-2. Assuming that the tower is rigid, the steady-state forces in normal and tangential directions applied to one blade element are denoted $dT(V_0, V_r)$ and $dS(V_0, V_r)$ respectively. When the tower is flexible, assuming the changes in relative wind speed experienced by every blade element are sufficiently small, the aerodynamic loads considering the tower top motion can be obtained using a first order Taylor expansion of the forces around the steady-state normal and tangential wind velocities. Effectively, this linearises the aerodynamic forces in terms of velocity.

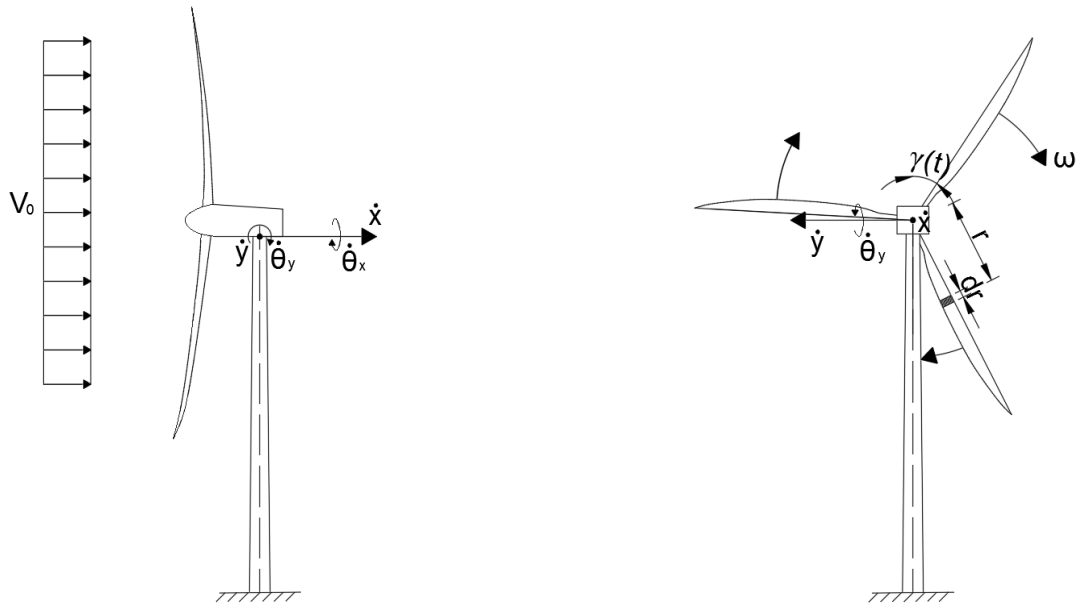

(a) (b)

Figure 4-3. Fore-aft (a) and side-side (b) motions.

The force in the normal direction is given by:

$$dT(V_{xRel}, V_{rRel}) = dT(V_{xRel}, V_{rRel})$$

$$= dT(V_0, V_r) + \frac{\partial(dT)}{\partial V_0}(-\dot{x}) + \frac{\partial(dT)}{\partial V_0}\left(-\dot{\theta}_y r cos\gamma_i(t)\right) \tag{4-7}$$

$$+ \frac{\partial(dT)}{\partial V_r}(-\dot{y} cos\gamma_i(t)) + \frac{\partial(dT)}{\partial V_r}\left(\dot{\theta}_x r\right);$$

and the force in the tangential direction is given by:

$$dS(V_{xRel}, V_{rRel}) = dS(V_{xRel}, V_{rRel})$$

$$= dS(V_0, V_r) + \frac{\partial(dS)}{\partial V_0}(-\dot{x}) + \frac{\partial(dS)}{\partial V_0}\left(-\dot{\theta}_y r cos\gamma_i(t)\right) \tag{4-8}$$

$$+ \frac{\partial(dS)}{\partial V_r}(-\dot{y} cos\gamma_i(t)) + \frac{\partial(dS)}{\partial V_r}\left(\dot{\theta}_x r\right).$$

The moment about the x direction is given by:

$$dM_x(V_{xRel}, V_{rRel}) = dS(V_{xRel}, V_{rRel}) r$$

$$= dS(V_0, V_r) r + \frac{\partial(dS)}{\partial V_0}(-\dot{x}) r + \frac{\partial(dS)}{\partial V_0}\left(-\dot{\theta}_y r^2 cos\gamma_i(t)\right) \tag{4-9}$$

$$+ \frac{\partial(dS)}{\partial V_r}(-\dot{y} r cos\gamma_i(t)) + \frac{\partial(dS)}{\partial V_r}\left(\dot{\theta}_x r^2\right).$$

and the moment about the y direction is given by:

$$dM_y(V_{xRel}, V_{rRel}) = dT(V_{xRel}, V_{rRel}) r cos\gamma_i(t)$$

$$= dT(V_0, V_r) r cos\gamma_i(t) + \frac{\partial(dT)}{\partial V_0}(-\dot{x}) r cos\gamma_i(t)$$

$$+ \frac{\partial(dT)}{\partial V_0}\left(-\dot{\theta}_y r^2 \cos^2\gamma_i(t)\right) + \frac{\partial(dT)}{\partial V_r}(-\dot{y} r \cos^2\gamma_i(t)) \tag{4-10}$$

$$+ \frac{\partial(dT)}{\partial V_r}\left(\dot{\theta}_x r^2 cos\gamma_i(t)\right);$$

The total forces and moments applied to the rotor are obtained by summing the elemental forces and moments along the three blades. As $\sum_{i=1}^{N_b} cos\gamma_i(t) = 0$ for any t, the total force in the x (FA) direction is:

$$F_x = \sum_{i=1}^{N_b} \int_0^R dT(V_{xRel}, V_{rRel}) \\ = N_b \int_0^R dT(V_0, V_r) - \dot{x} N_b \int_0^R \frac{\partial(dT)}{\partial V_0} + \dot{\theta}_x N_b \int_0^R r \frac{\partial(dT)}{\partial V_r}, \tag{4-11}$$

where N_b is the number of blades, and R is the radius of the blade.

The total force in the y (SS) direction is:

$$F_y = -cos\gamma(t) \sum_{i=1}^{N_b} \int_0^R dS(V_{xRel}, V_{rRel}) \\ = \dot{\theta}_y \frac{N_b}{2} \int_0^R r \frac{\partial(dS)}{\partial V_0} + \dot{y} \frac{N_b}{2} \int_0^R \frac{\partial(dS)}{\partial V_r}. \tag{4-12}$$

The negative sign on the left-hand side of the summation operator is due to the fact that for a rotor rotating in the positive direction, the blade at a position above the hub is subjected to a tangential force towards the negative y-direction. This is a consequence of the chosen coordinate system. In addition, it can be easily checked that for a three-blade wind turbine, $\sum_{i=1}^{N_b} cos^2 \gamma_i(t) = N_b/2$.

Eventually, the total moment about the x axis is:

$$M_x = \sum_{i=1}^{N_b} \int_0^R dM_x(V_{xRel}, V_{rRel}) \\ = N_b \int_0^R dS(V_0, V_r) r - \dot{x} N_b \int_0^R r \frac{\partial(dS)}{\partial V_0} + \dot{\theta}_x N_b \int_0^R r^2 \frac{\partial(dS)}{\partial V_r}, \tag{4-13}$$

whereas the total moment about the y axis is:

$$M_y = \sum_{i=1}^{N_b} \int_0^R dM_y(V_{xRel}, V_{rRel}) \tag{4-14}$$

$$= -\dot{\theta}_y \frac{N_b}{2} \int_0^R r^2 \frac{\partial(dT)}{\partial V_0} - \dot{y} \frac{N_b}{2} \int_0^R r \frac{\partial(dT)}{\partial V_r}.$$

The analytical expressions necessary to calculate the partial derivatives in Equations (4-11) to (4-14) are given below, defining the aerodynamic damping matrix in terms of known aerodynamic quantities such as inflow wind speed, blade profile, fluid properties and operational conditions. All notations used here are from the classic steady BEM theory [25]. These partial derivatives are $\frac{\partial(dT)}{\partial V_0}$, $\frac{\partial(dT)}{\partial V_r}$, $\frac{\partial(dS)}{\partial V_0}$ and $\frac{\partial(dS)}{\partial V_r}$. According to BEM theory, the thrust on an element at radius r can be written as

$$dT = \frac{1}{2}\rho[V_0^2(1-a)^2 + V_r^2(1+a')^2]C_n c dr, \tag{4-15}$$

where ρ is the air density, a and a' are the axial and tangential induction factors respectively, c is the chord length, C_n is the normal force coefficient and dr is the increment length for this element. The tangential force can be expressed by

$$dS = \frac{1}{2}\rho[V_0^2(1-a)^2 + V_r^2(1+a')^2]C_t c dr, \tag{4-16}$$

where C_t is the tangential force coefficient. Assuming dT and dS are functions of V_0 and V_r, other intermediate variables such as a, a', C_n, C_t and ϕ can also be treated as functions with regard to V_0 and V_r. ϕ is the sum of the attack angle, pitch and twist angles. According to classic BEM theory, the relationships between these variables are:

$$a = \frac{1}{\frac{4\sin^2\phi}{\sigma C_n} + 1}, \tag{4-17}$$

$$a' = \frac{1}{\frac{4\sin\phi\cos\phi}{\sigma C_t} - 1}, \tag{4-18}$$

$$C_n = C_l\cos\phi + C_d\sin\phi, \tag{4-19}$$

$$C_t = C_l\sin\phi - C_d\cos\phi, \tag{4-20}$$

$$\tan\phi = \frac{V_0(1-a)}{V_r(1+a')} \text{ or } \cot\phi = \frac{V_r(1+a')}{V_0(1-a)}, \tag{4-21}$$

where σ indicates the solidity, C_l and C_d is the lift and drag coefficients respectively;

Firstly, from Equation (4-15), $\frac{\partial(dT)}{\partial V_0}$ can be written as

$$\frac{\partial(dT)}{\partial V_0} = \frac{1}{2}\rho c\left[\frac{\partial(V_{Rel}^2)}{\partial V_0}C_n + V_{Rel}^2\frac{\partial C_n}{\partial V_0}\right]dr, \tag{4-22}$$

where $V_{Rel}^2 = V_0^2(1-a)^2 + V_r^2(1+a')^2$;

$\frac{\partial(dT)}{\partial V_r}$ can be written as

$$\frac{\partial(dT)}{\partial V_r} = \frac{1}{2}\rho c\left[\frac{\partial(V_{Rel}^2)}{\partial V_r}C_n + V_{Rel}^2\frac{\partial C_n}{\partial V_r}\right]dr. \tag{4-23}$$

Similarly, from Equation (4-16),

$$\frac{\partial(dS)}{\partial V_0} = \frac{1}{2}\rho c\left[\frac{\partial(V_{Rel}^2)}{\partial V_0}C_t + V_{Rel}^2\frac{\partial C_t}{\partial V_0}\right]dr; \tag{4-24}$$

and

$$\frac{\partial(dS)}{\partial V_r} = \frac{1}{2}\rho c\left[\frac{\partial(V_{Rel}^2)}{\partial V_r}C_t + V_{Rel}^2\frac{\partial C_t}{\partial V_r}\right]dr. \tag{4-25}$$

The expression for the terms in Equations (4-22) to (4-25) can be expressed as follows:

$$\frac{\partial(V_{Rel}^2)}{\partial V_0} = 2V_0(1-a)^2 - 2V_0^2(1-a)\frac{\partial a}{\partial V_0} + 2V_r^2(1+a')\frac{\partial a'}{\partial V_0}, \tag{4-26}$$

where $\frac{\partial a}{\partial V_0} = \frac{da}{d\phi}\cdot\frac{\partial\phi}{\partial V_0}$ and $\frac{\partial a'}{\partial V_0} = \frac{da'}{d\phi}\cdot\frac{\partial\phi}{\partial V_0}$;

Then

$$\frac{\partial(V_{Rel}^2)}{\partial V_r} = -2V_0^2(1-a)\frac{\partial a}{\partial V_r} + 2V_r(1+a')^2 + 2V_r^2(1+a')\frac{\partial a'}{\partial V_r}, \tag{4-27}$$

where $\frac{\partial a}{\partial V_r} = \frac{da}{d\phi}\cdot\frac{\partial\phi}{\partial V_r}$ and $\frac{\partial a'}{\partial V_r} = \frac{da'}{d\phi}\cdot\frac{\partial\phi}{\partial V_r}$. $\frac{da}{d\phi}$ and $\frac{da\prime}{d\phi}$ can be determined from Equations (4-17) and (4-18):

$$\frac{da}{d\phi} = \frac{-4\left(sin2\phi C_n - \frac{dC_n}{d\phi}sin^2\phi\right)}{\sigma C_n^2\left(\frac{4sin^2\phi}{\sigma C_n} + 1\right)^2}, \tag{4-28}$$

and

$$\frac{da'}{d\phi} = \frac{-4\left(cos2\phi C_t - \frac{dC_t}{d\phi} sin\phi cos\phi\right)}{\sigma C_t^2 \left(\frac{4sin\phi cos\phi}{\sigma C_t} - 1\right)^2}. \tag{4-29}$$

The expressions for $\frac{\partial\phi}{\partial V_0}$ and $\frac{\partial\phi}{\partial V_r}$ can be found from Equation (4-21) using the following two equations:

$$\frac{\partial\phi}{\partial V_0}\left[\frac{d\left(\frac{1+a'}{1-a}\right)}{d\phi} tan\phi + \frac{1}{cos^2\phi}\frac{1+a'}{1-a}\right] = \frac{1}{V_r}, \tag{4-30}$$

and

$$\frac{\partial\phi}{\partial V_r}\left[\frac{d\left(\frac{1-a}{1+a'}\right)}{d\phi} cot\phi - \frac{1}{sin^2\phi}\frac{1-a}{1+a'}\right] = \frac{1}{V_0}. \tag{4-31}$$

where $\frac{d\left(\frac{1+a'}{1-a}\right)}{d\phi} = \frac{\frac{da'}{d\phi}(1-a)+\frac{da}{d\phi}(1+a')}{(1-a)^2}$ and $\frac{d\left(\frac{1-a}{1+a'}\right)}{d\phi} = \frac{-\frac{da}{d\phi}(1+a')-\frac{da'}{d\phi}(1-a)}{(1+a')^2}$. For $\frac{\partial C_n}{\partial V_0}$, $\frac{\partial C_n}{\partial V_r}$, $\frac{\partial C_t}{\partial V_0}$ and $\frac{\partial C_t}{\partial V_r}$, the following four equations can be used:

$$\frac{\partial C_n}{\partial V_0} = \frac{dC_n}{d\phi}\frac{\partial\phi}{\partial V_0}, \tag{4-32}$$

$$\frac{\partial C_n}{\partial V_r} = \frac{dC_n}{d\phi}\frac{\partial\phi}{\partial V_r}, \tag{4-33}$$

$$\frac{\partial C_t}{\partial V_0} = \frac{dC_t}{d\phi}\frac{\partial\phi}{\partial V_0}, \tag{4-34}$$

$$\frac{\partial C_t}{\partial V_r} = \frac{dC_t}{d\phi}\frac{\partial\phi}{\partial V_r}. \tag{4-35}$$

$\frac{dC_n}{d\phi}$ and $\frac{dC_t}{d\phi}$ can be simply derived from Equations (4-19) and (4-20):

$$\frac{dC_n}{d\phi} = \frac{\partial C_l}{\partial\phi} cos\phi + \frac{\partial C_d}{\partial\phi} sin\phi + C_d cos\phi - C_l sin\phi, \tag{4-36}$$

and

$$\frac{dC_t}{d\phi} = \frac{\partial C_l}{\partial\phi} sin\phi - \frac{\partial C_d}{\partial\phi} cos\phi + C_l cos\phi + C_d sin\phi. \tag{4-37}$$

This provides all the terms required to determine damping derivatives.

4.4.2 Aerodynamic load resultants at the tower top

Within the set of assumptions made, the rotor aerodynamic load resultants at the hub are completely described by Equations (4-11) to (4-14), and these loads can be separated into two parts: static (constant) components and "damping" components proportional to the velocities. Only F_x and M_x have a static part equal to $N_b \int_0^R dT(V_0, V_r)$ and $N_b \int_0^R dS(V_0, V_r) r$ respectively. These can easily be calculated using the BEM model in MATLAB or FAST by keeping the tower rigid. They can then be applied as external loads at the tower top in a decoupled model. The other terms in F_x, F_y, M_x and M_y appear as damping components since they depend linearly on the tower top translational or angular velocities. These damping components can be added to the relevant terms for the top node in the damping matrix of the overall system. The matrix format of the forces resultants at the tower top is

$$\mathbf{F}^{Top} = \begin{bmatrix} F_x \\ 0 \\ M_x \\ 0 \end{bmatrix} - \boldsymbol{C}_{Aero} \begin{bmatrix} \dot{x} \\ \dot{y} \\ \dot{\theta}_x \\ \dot{\theta}_y \end{bmatrix}, \tag{4-38}$$

where the aerodynamic damping matrix $\mathbf{C}_{Aero}$ that collects the terms multiplied by the velocity vector $\dot{\mathbf{u}}^{Top} = \left[\dot{x}\ \dot{y}\ \dot{\theta}_x\ \dot{\theta}_y\right]^T$ for the top node can be defined as:

$\mathbf{C}_{Aero}\dot{\mathbf{u}}^{Top} =$

$$\begin{bmatrix} N_b \int_0^R \frac{\partial(dT)}{\partial V_0} & 0 & -N_b \int_0^R r \frac{\partial(dT)}{\partial V_r} & 0 \\ 0 & -\frac{N_b}{2} \int_0^R \frac{\partial(dS)}{\partial V_r} & 0 & -\frac{N_b}{2} \int_0^R r \frac{\partial(dS)}{\partial V_0} \\ N_b \int_0^R r \frac{\partial(dS)}{\partial V_0} & 0 & -N_b \int_0^R r^2 \frac{\partial(dS)}{\partial V_r} & 0 \\ 0 & \frac{N_b}{2} \int_0^R r \frac{\partial(dT)}{\partial V_r} & 0 & \frac{N_b}{2} \int_0^R r^2 \frac{\partial(dT)}{\partial V_0} \end{bmatrix} \begin{bmatrix} \dot{x} \\ \dot{y} \\ \dot{\theta}_x \\ \dot{\theta}_y \end{bmatrix}. \tag{4-39}$$

$\mathbf{C}_{Aero}$ can be written more concisely:

$$\mathbf{C}_{Aero} = \begin{bmatrix} c_{xx} & 0 & c_{x\theta_x} & 0 \\ 0 & c_{yy} & 0 & c_{y\theta_y} \\ c_{\theta_x x} & 0 & c_{\theta_x \theta_x} & 0 \\ 0 & c_{\theta_y y} & 0 & c_{\theta_y \theta_y} \end{bmatrix}. \tag{4-40}$$

$\mathbf{C}_{Aero}$ has a number of relevant structural features:

1) For given inflow wind speed, rotation speed, and pitch angle, the coefficients in the damping matrix are constant and can therefore be calculated using a BEM model before time integration. Therefore, the proposed strategy allows the vibration and aerodynamics to be decoupled in the sense that the aerodynamic calculation can be done once, for a given range of steady-state operating conditions regimes. Changes of the damping matrix due to unsteady wind inflow are not considered in this chapter and assessing how this unsteadiness affects the proposed methodology will be further investigated in Chapter 5.

2) From the structure of this damping matrix, it can be seen that the translational DOFs in the FA and SS are not coupled. Coupling between FA and SS directions only occurs through the off-diagonal terms linking rotational to translational DOFs. For example, $c_{x\theta_x}$ links the FA translational velocity $\dot{x}$ to the rotation around the x-axis $\dot{\theta}_x$.

3) When the tower is assumed to be rigid in the SS direction, two diagonal terms c_{xx} and $c_{\theta_y\theta_y}$, contribute to the damping in the FA direction, which means that both linear and angular motions contribute to the aerodynamic damping in that direction. A similar observation can be made in the SS direction. Coupling would not occur if the tower top rotation was not considered.

4) An important feature of this aerodynamic damping matrix is that although it has clear structural patterns, it is not symmetric. This is not uncommon when considering damping in rotating machineries [133]. It should be remembered that this matrix was derived from the linearisation of the aerodynamic forces rather than from conventional dashpots located within a standard multiple DOF system.

5) Only the symmetric part of this matrix represents genuine energy dissipation. The anti-symmetric part couples the DOFs without contributing to the overall damping of the system. Any matrix M can be decomposed into a symmetric part S and an antisymmetric part A such that $M = S + A$.

The expressions defining this aerodynamic damping matrix allow a better understanding of the nature of the coupling between FA and SS motions and the aerodynamic forces. The complete derivation described in this section provides a model

from which the dynamic response for an operational wind turbine can be rapidly calculated, *e.g.*, for fatigue or reliability analyses. This is particularly useful when calculating the responses of a wind turbine using a more detailed foundation model, which cannot be easily coupled with an aerodynamic rotor model. In this case, the aerodynamic damping is typically defined separately as damping ratios in the FA and SS directions. The aerodynamic damping matrix defined here provides another option which more accurately captures the interaction between the FA and SS motions. In addition, the damping matrix could be used to underpin an experimental methodology to identify the dynamic properties of the system from experimental data. In contrast to conventional operational modal analysis which gives modal damping factors for a structural system (*e.g.* [134][104][105]), damping identification in operational wind turbines could aim to quantify the terms of the aerodynamic damping matrix (*e.g.* using a time-frequency analysis as suggested by Chen *et al.* [114]).

4.5 Results and discussion

4.5.1 Model verification and overall behaviour

FAST model settings for verification

The onshore FAST model described in Section 4.2 was used to verify the results from the proposed model. For consistency with the derivations presented in Section 4.4, the settings "classic BEM theory with the Prandtl and Glauert's corrections" were chosen in FAST's AeroDyn module [135]. To consider the influence of the control system and obtain plausible wind turbine responses for varying normal operating conditions, the standard relationships between wind speed, rotor speed, and pitch angle were used as shown in Figure 3-4 [119]. The rotor speed, pitch angle, and inflow wind speed were kept constant during each simulation.

In contrast to the default settings in FAST, the centre of mass of the RNA was moved to the tower top and the moments of inertia of the RNA relative to the tower top were set to zero. These modification ware necessary to make the FAST model consistent with the FE model used in this chapter. In principle this should not be necessary, but it is not clear how to define specific RNA moments of inertia in the x and y directions at the same time in FAST, so they were set to zero. FAST also requires the tower mode shapes as an input and they were obtained from an eigenfrequency analysis of the FE model.

These modifications do not affect the general dynamic behaviour of the wind turbine highlighted here.

Verification and general description of the response

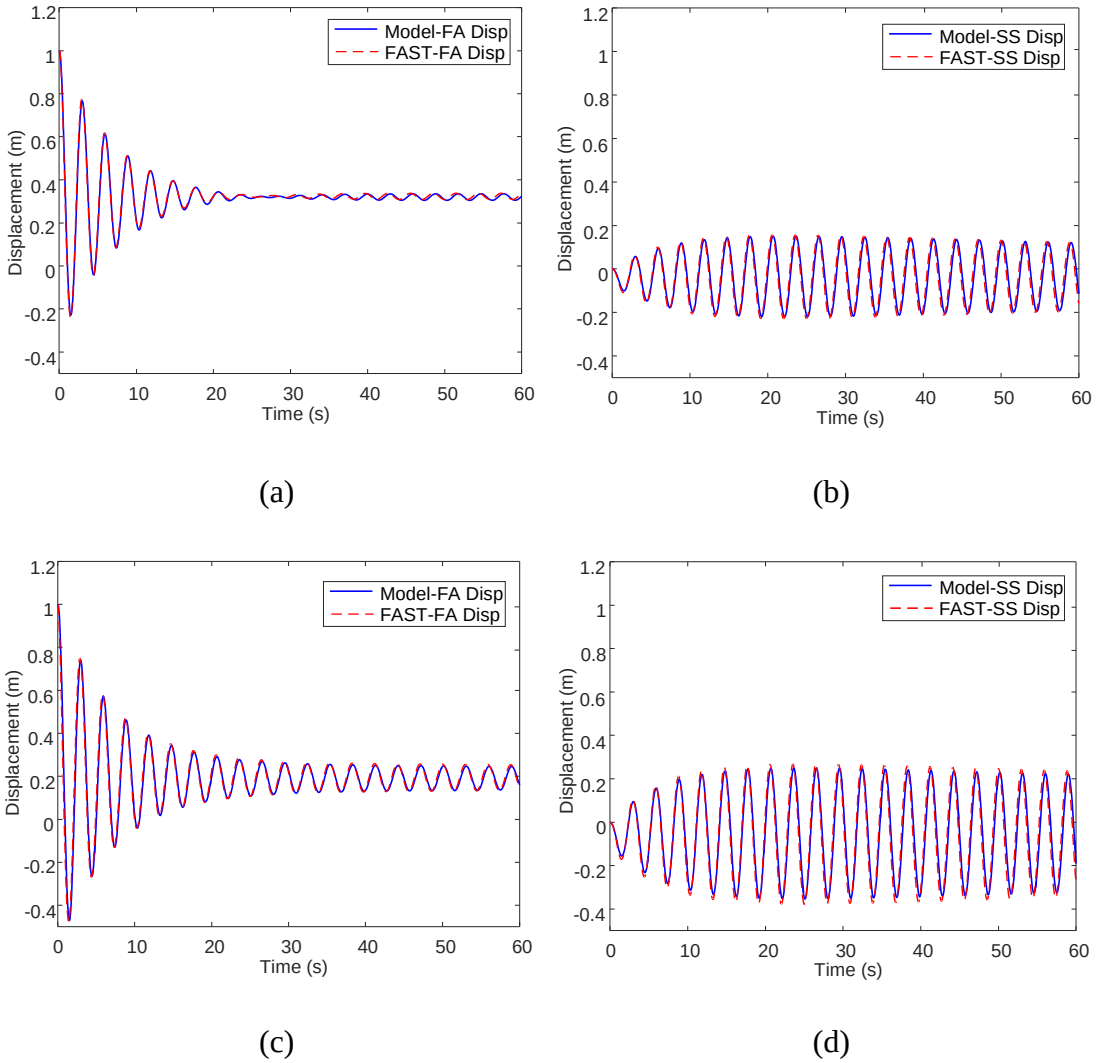

Figure 4-4. FA (a, c) and SS (b, d) displacement response caused by a 1 m initial displacement in the FA direction; Comparison between proposed model and FAST for steady wind speeds of (a-b) 10 m/s, (c-d) 20 m/s.

In the proposed model, the static components of the loads were calculated and applied as external forces and moments. An initial displacement of 1 m in the FA direction was then given to the tower top node to excite dynamic responses comparable to the FAST results. Figure 4-4 shows the time domain responses generated by the proposed model and the corresponding FAST simulation results for two wind velocities – one below the

rated speed: 10 m/s (Figure 4-4(a) and Figure 4-4(b)) and one above the rated speed: 20 m/s (Figure 4-4(c) and Figure 4-4(d)). The agreement is very good and similar agreement was obtained at all other wind speeds.

Comparing the damped responses from the proposed model to that from FAST, small percentage differences in frequency and dynamic amplitude, of up to 1% and 5% respectively, can be observed. These small differences can be explained by the simplifying assumptions underpinning the proposed model (linearisation of forces; no vertical displacement or rotation; resultant forces calculated for undeformed geometry, decoupled time integration). The consistently good agreement obtained confirms that the model adequately captures the underlying physics to the same level of accuracy as FAST. This also confirms that the coupling between the two directions is indeed caused by the off-diagonal terms of the damping matrix and not by stiffness coupling (as there is none in the model). The calculations of aerodynamic forces in the model and FAST are both based on BEM theory. The model implements an approximate approach to extract the derivatives of the aerodynamic forces, while FAST uses BEM theory to calculate the aerodynamic forces on every blade element at every time step. It should be noted that the comparison of the responses from the model and FAST simulation is under same settings, e.g. rigid rotor/blades, so this does not validate the model under more complex settings.

4.5.2 Useful limit cases

The decoupled FE model described in Section 4.3 has identical mass and stiffness distributions in the FA and SS directions; therefore, the bending modes in both directions have identical natural frequencies and mode shapes (at 90^{o} of each other). The first three natural frequencies of the tower and RNA mass system are 0.34 Hz, 3.08 Hz and 9.16 Hz. For a standard wind load spectral density spectrum peaking around 0.1 Hz, only the first bending modes will be significantly excited. The core behaviour of the system is therefore governed by two bending modes with identical natural frequencies (ignoring the asymmetry introduced by the RNA), perpendicular mode shapes, no stiffness coupling (due to symmetry), and higher damping in the FA direction than in the SS direction. A number of limit cases are considered to understand the coupled behaviour of the system, considering only different parts of the full damping matrix derived in Section 4.4 for the time integration of the present model. To

this end, it is useful to decompose the aerodynamic damping matrix, $\mathbf{C}_{Aero}$ as the sum of its symmetric part denoted by $\mathbf{C}_{Aero}^{S}$ and its anti-symmetric denoted by $\mathbf{C}_{Aero}^{A}$. They are defined as:

$$\mathbf{C}_{Aero} = \mathbf{C}_{Aero}^{S} + \mathbf{C}_{Aero}^{A} = \begin{bmatrix} c_{xx} & 0 & c_{x\theta_x}^{S} & 0 \\ 0 & c_{yy} & 0 & c_{y\theta_y}^{S} \\ c_{\theta_x x}^{S} & 0 & c_{\theta_x\theta_x} & 0 \\ 0 & c_{\theta_y y}^{S} & 0 & c_{\theta_y\theta_y} \end{bmatrix} + \begin{bmatrix} 0 & 0 & c_{x\theta_x}^{A} & 0 \\ 0 & 0 & 0 & c_{y\theta_y}^{A} \\ c_{\theta_x x}^{A} & 0 & 0 & 0 \\ 0 & c_{\theta_y y}^{A} & 0 & 0 \end{bmatrix}, \quad (4\text{-}41)$$

where $c_{x\theta_x}^{S} = c_{\theta_x x}^{S} = (c_{x\theta_x} + c_{\theta_x x})/2$, $c_{x\theta_x}^{A} = -c_{\theta_x x}^{A} = (c_{x\theta_x} - c_{\theta_x x})/2$, $c_{y\theta_y}^{S} = c_{\theta_y y}^{S} = (c_{y\theta_y} + c_{\theta_y y})/2$, $c_{y\theta_y}^{A} = -c_{\theta_y y}^{A} = (c_{y\theta_y} - c_{\theta_y y})/2$. From Equation (4-39), the asymmetry of the aerodynamic damping matrix comes from the fact that the cross terms of the elemental force derivatives (like $\frac{\partial(dT)}{\partial V_r}$ and $\frac{\partial(dS)}{\partial V_0}$) are not identical if the minus sign in $-N_b \int_0^R r \frac{\partial(dT)}{\partial V_r}$ due to the selection of the coordinate system is ignored. The nature of the asymmetry can be understood as the mechanical properties of the rotating rotor interacted with the air are different in the in-rotor plane and out-of-rotor plane directions. On the other hand, it is natural to decompose the asymmetric aerodynamic damping matrix into the symmetric and anti-symmetric parts. From the view of energy dissipation, a system with anti-symmetric damping matrix does not lose energy, so the decomposition shows which parts of the aerodynamic damping matrix cause the energy dissipation.

Case 1

If the damping matrix (Equations (4-39)(4-40)) had no off-diagonal terms, the motions in FA and SS directions would be completely decoupled, and the system would behave like two independent single DOFs with identical natural frequencies and different damping levels. The response are shown in Figure 4-5, in which the SS displacement is excited by the constant moment while FA displacement is caused by the initial 1 m displacement and the constant thrust. The wind speed was set to 10 m/s as an example. The initial FA displacement leads to a relatively quickly decaying FA exponential response. However, the decay rate of the SS displacement is much slower. This is because the SS damping is much smaller than the FA damping, as will be observed later (as shown later in Figure 4-9).

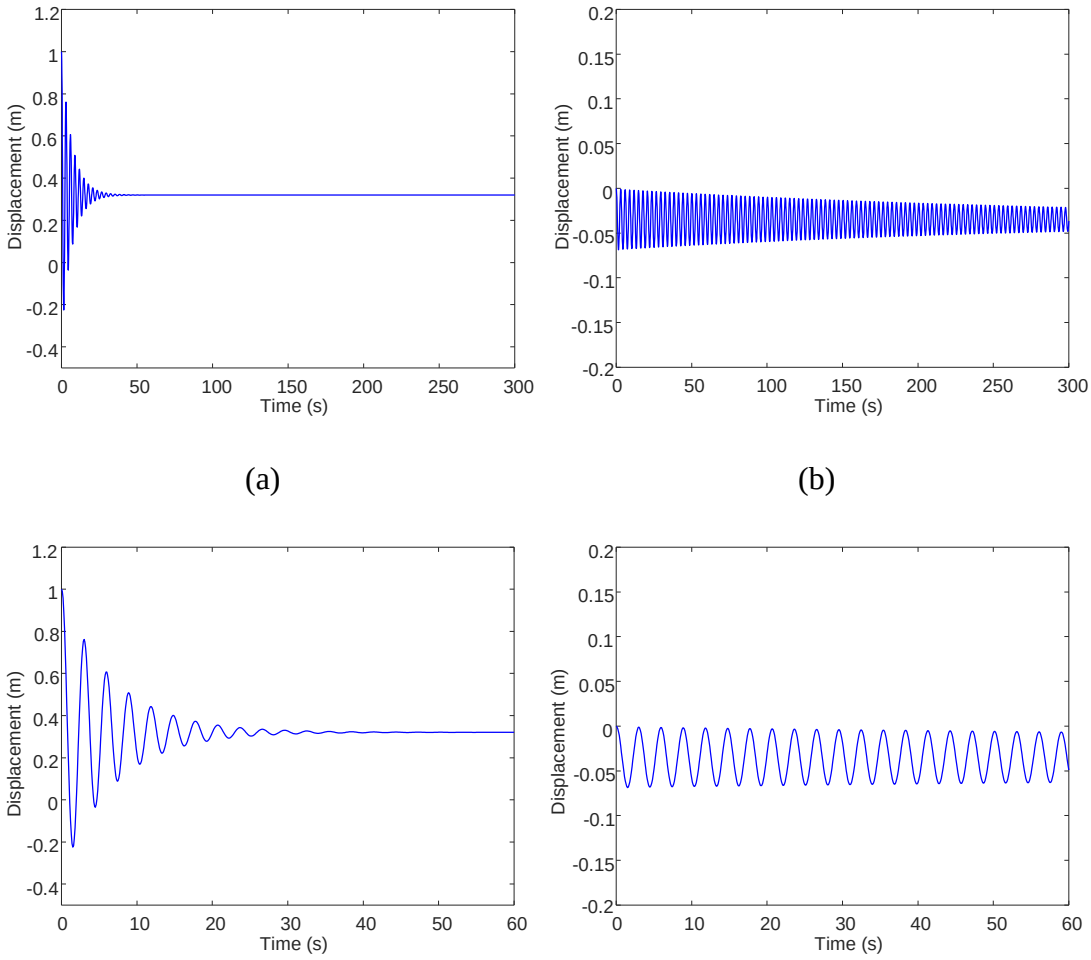

Figure 4-5. FA (a, c) and SS (b, d) displacement response of the model without off-diagonal terms; a 1m initial displacement is applied in the FA direction and wind speed is 10 m/s; (c) and (d) are zooms of (a) and (b).

Case 2

The anti-symmetric components of the full damping matrix are set to zero. Then the two directions are coupled through conventional off-diagonal damping terms. As shown in Figure 4-6, the initial FA displacement leads to a fast decay in the FA direction, but some energy is also transferred to the SS direction so that the SS response initially grows before slowly decaying. This is the overall behaviour observed in Subsection 4.5.1. However, there is no such a point at which the decay envelope of the FA response decreases to almost zero before increasing again in this case.

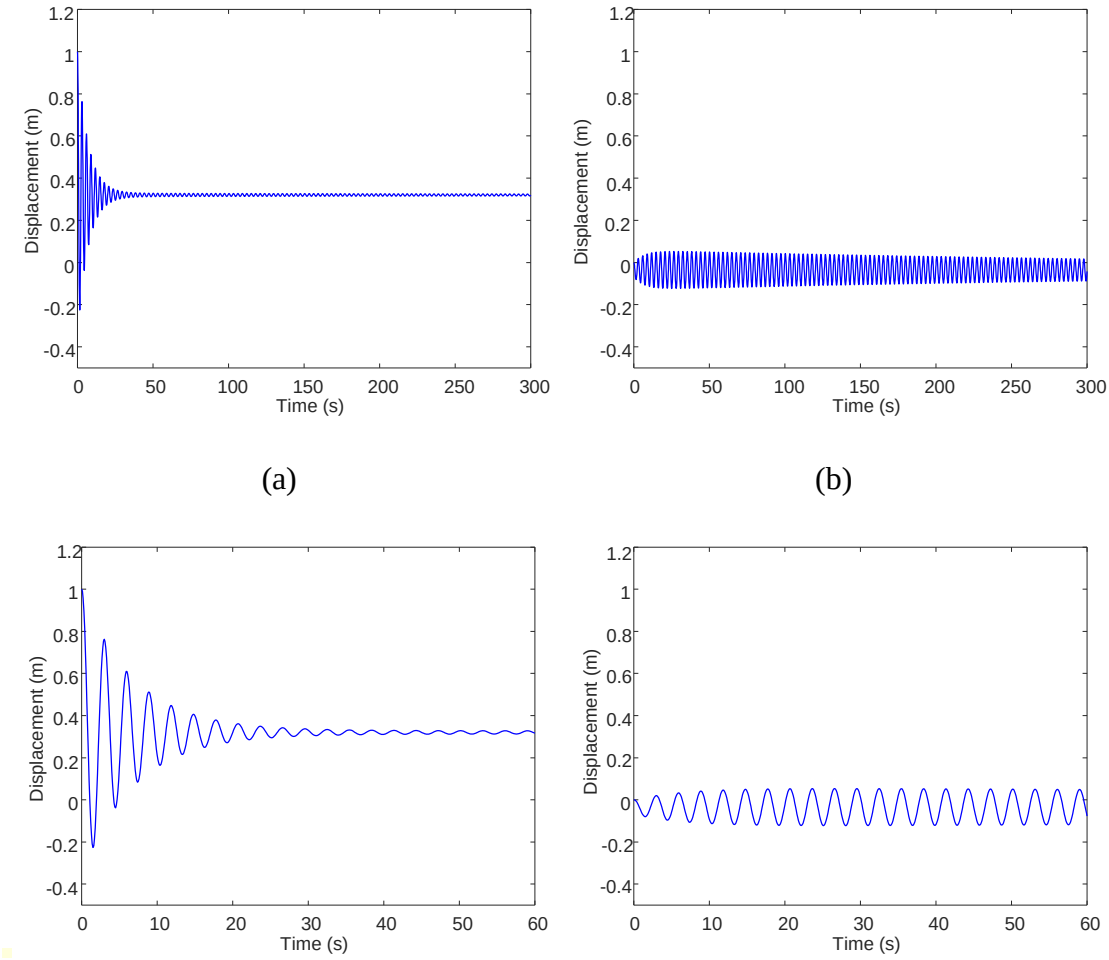

Figure 4-6. FA (a, c) and SS (b, d) displacement response of the model with conventional off-diagonal damping terms; a 1m initial displacement is applied in the FA direction and wind speed is 10 m/s; (c) and (d) are zooms of (a) and (b).

Case 3

Only the off-diagonal, antisymmetric part of the full damping matrix is considered. The two modes are again coupled by the off-diagonal terms and exhibit a beating behaviour: each direction oscillates at its decoupled natural frequency, modulated in amplitude. This behaviour is shown in Figure 4-7. The modulation is out-of-phase between the two directions, so that the energy is constantly transferred back and forth between the FA and the SS directions, but with no overall dissipation.

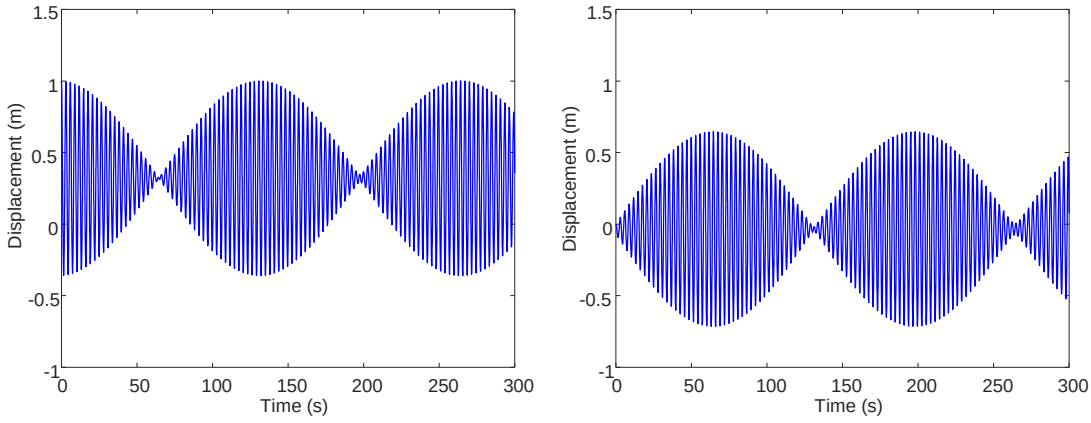

(a) (b)

Figure 4-7. FA (a) and SS (b) displacement response of the model with antisymmetric off-diagonal terms; a 1m initial displacement is applied in the FA direction and wind speed is 10 m/s.

As previously observed, the FA oscillation in Figure 4-4(c) decays monotonically whereas monotonically whereas in Figure 4-4(a) the decay envelope of this oscillation decreases to almost zero at around 25 s before increasing again. This behaviour can be interpreted as the first node of an underlying beating behaviour caused by the anti-symmetric components of the damping matrix. For higher wind speeds, this behaviour disappears. To understand why, it is useful to look at how the coefficients of the damping matrix vary with the wind speed.

Variation of the aerodynamic damping matrix with wind speed

The expressions defining the aerodynamic damping matrix allow a detailed investigation of how the matrix coefficients change with the wind speed. Several effects occur simultaneously and can be observed more clearly by considering the symmetric and anti-symmetric parts of the damping matrix separately. The upper and diagonal plots in Figure 4-8 show the symmetric part of the full damping matrix with each subplot representing the variation of the corresponding coefficient in the matrix with wind speed. It should be noted that the terms in the aerodynamic damping matrix are dependent on the wind turbine operational status. The relationships between the wind speeds and the damping terms shown in Figure 4-8 are representative and correspond to the operational condition represented by Figure 3-4. The lower left half represents

the two non-zero anti-symmetric components. Missing subplots are zero coefficients. c_{xx} and $c_{\theta_y\theta_y}$ are the diagonal terms directly contributing to the FA damping. They both follow a similar trend as can be expected from their mathematical expression in Equation (4-39) increasing up to 11 m/s wind speed and then plateauing at higher speeds. c_{yy} and $c_{\theta_x\theta_x}$, the diagonal terms contributing to SS damping, also follow an increasing trend (but different from the FA damping coefficients): both are almost constant up to 11 m/s wind speed, then increase steadily. The sharp change in behaviour at 11 m/s is caused by the feathering of the blades which starts at that wind speed. This has been confirmed by additional simulation results without feathering (not shown). From these graphs it can be observed that blade feathering limits the FA aerodynamic damping but causes the SS damping to increase as the wind speed increases. This makes sense intuitively, as feathering turns the blades away from the inflow wind but increases their exposure in the tangential direction.

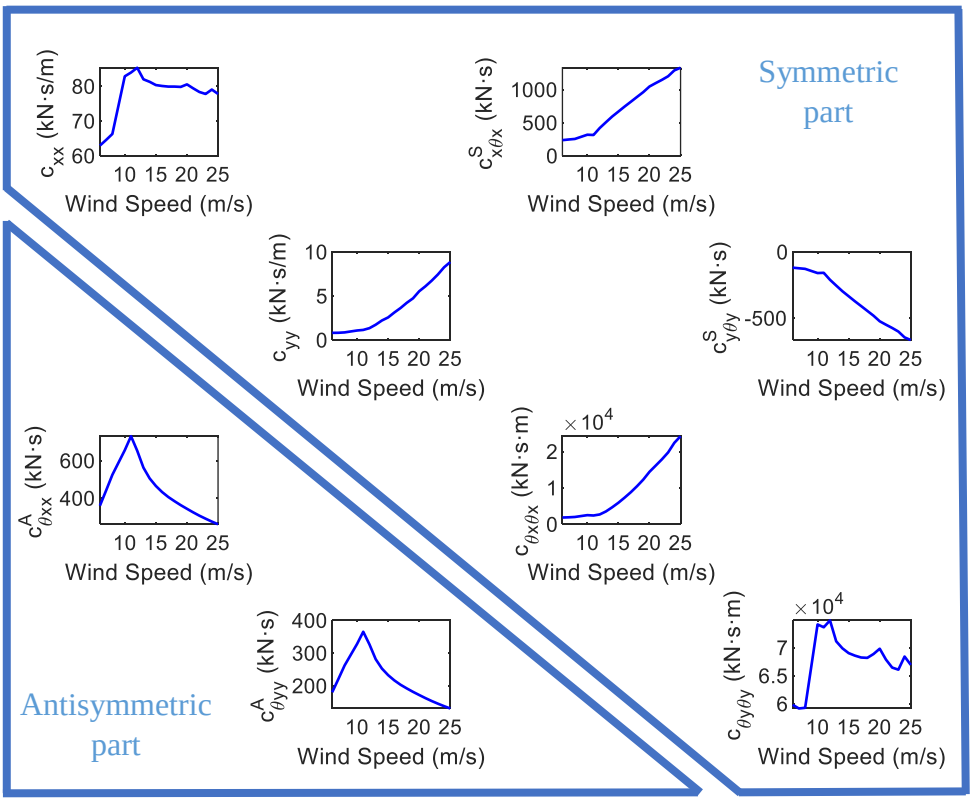

Figure 4-8. Coefficients of symmetric (upper) and antisymmetric (lower) parts of the damping matrix in terms of wind speed.

The symmetric off-diagonal term $c^S_{y\theta_y}$ is always negative, reasonably constant around -120 kNs up to 11 m/s then decreases with wind speed (increases in magnitude) down to -500 kNs at 20 m/s. This means that the coupling between rotation $\dot{\theta}_y$ and the SS translation y is dissipative and increases in intensity with the wind speed and feathering. By contrast the symmetric coefficient $c^S_{x\theta_x}$ is always positive, relatively constant around 250 kNs up to 11 m/s, then increases almost linearly to reach around 1000 kNs at 20 m/s. Positive values in off-diagonal terms indicate a negative damping or positive feedback from the rotation speed $\dot{\theta}_x$ to the FA translation x. This is unusual in conventional vibratory systems, but a wind turbine is not a closed system as the wind inflow constantly feeds energy in. A negative damping term indicates that the vibration coupling between the two relevant degrees of freedom transfers energy from the inflow wind into vibrational energy. From the values in Figure 4-8, this positive feedback is stronger than the dissipative $c^S_{y\theta_y}$ term. This explains why the system appears less damped at 20 m/s than at 10 m/s: in Figure 4-4(c) the FA amplitude is larger in than in Figure 4-4(a). As the FA amplitude is larger, the energy transferred to the SS direction is also larger. This positive feedback is presumably also the reason why in Figure 4-1(a), the FA amplitude is larger when both FA and SS directions are free (solid line) than when SS is rigid. In the latter case $\theta_x = 0$ so this positive feedback is not available.

Finally, both antisymmetric components decrease by about 50% from a maximum at 11 m/s to 20 m/s, therefore reducing the influence of the beating effect. This is indeed what is observed, as the point at which the decay envelope of the FA response decreases to almost zero before increasing again disappears at wind speeds above 11m/s.

4.5.3 Comparison with conventional aerodynamic damping description for wind turbines

The previous observations highlighted that not taking the coupling between the two directions into account could lead to erroneous damping identification. This is explored further in this section. Figure 4-9(a) shows FA damping ratios measured for a range of wind speeds from the response of a model where the SS direction is kept rigid (dashed line) and from a model where both directions are free (solid). Similarly, Figure 4-9(b) shows how the SS damping ratios vary with wind speed depending on whether the coupling with the FA direction is available (solid) or not (dashed). These damping ratios are those of the first bending modes.

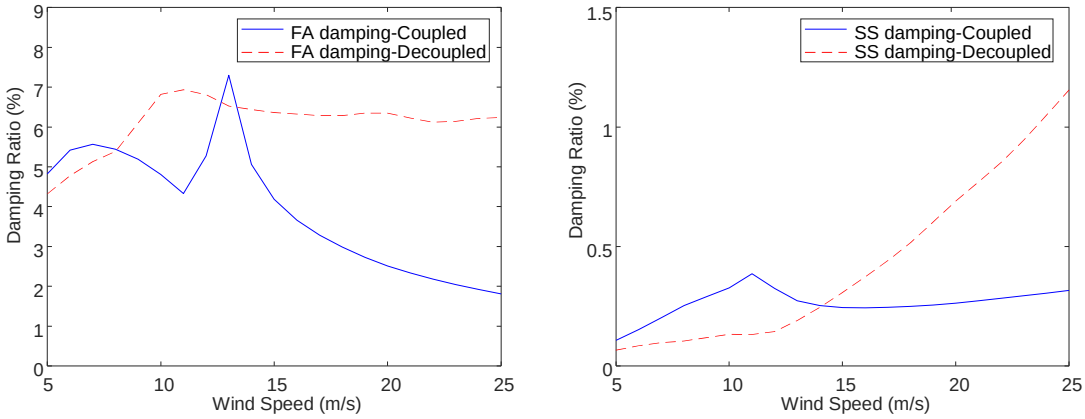

(a) (b)

Figure 4-9. FA damping (a) and SS damping (b) comparisons between the model only having one DOF on (solid) and the model having two DOFs on (dashed).

These damping ratios were obtained using the following procedure. A 1 m initial displacement was applied to the tower top in either FA or SS direction and zero initial displacement was applied in the other direction (where available). Then a 60 s time response was computed for each wind speed. Damping ratios were identified using a sonogram FFT technique [122] on the output responses. As the apparent damping value is dependent on the selection of time window, different damping values can be obtained for one output response depending on the time window chosen for the extraction. Fundamentally the actual damping behaviour is being fitted to the wrong mathematical model so there is no ideal solution to this issue. For the purpose of consistency, the following procedure was followed to extract damping values: the beginning of the time window was kept at 5 s, while the end of the window was gradually increased from 25 s to 55 s in 5 s increments. Then the damping values obtained for each window were averaged to obtain the representative damping values plotted here. This procedure effectively puts more weight on the earlier part of the time series. This is justified by the fact that this is where the decrease in amplitude is more pronounced, therefore where damping identification works best.

First, it is noteworthy that the dashed curve in Figure 4-9(a) is remarkably similar to the coefficients c_{xx} and $c_{\theta_y\theta_y}$ in Figure 4-8 and similarly the dashed curve in Figure 4-9(b) follows closely the evolution of coefficients c_{xx} and $c_{\theta_y\theta_y}$ with the wind speed

in Figure 4-8. This is understandable as the diagonal terms of the matrix represent the damping without any coupling, so they are closely linked to a system where coupling is disabled.

It can be seen from Figure 4-9 that the coupling between FA and SS directions has a significant impact on the damping in both FA and SS directions. Keeping one direction rigid increases the apparent damping in the other direction (30% for the FA damping and or 50% for the SS damping) when the wind speed is below the rated speed while decoupling decreases the damping ratios by more than 50% at 20 m/s. This is consistent with the time series shown in Figure 4-1(a), where the decoupled response showed a much faster decay rate than the coupled vibrations.

4.5.4 Comparison with the FAST model with more complex AeroDyn setting

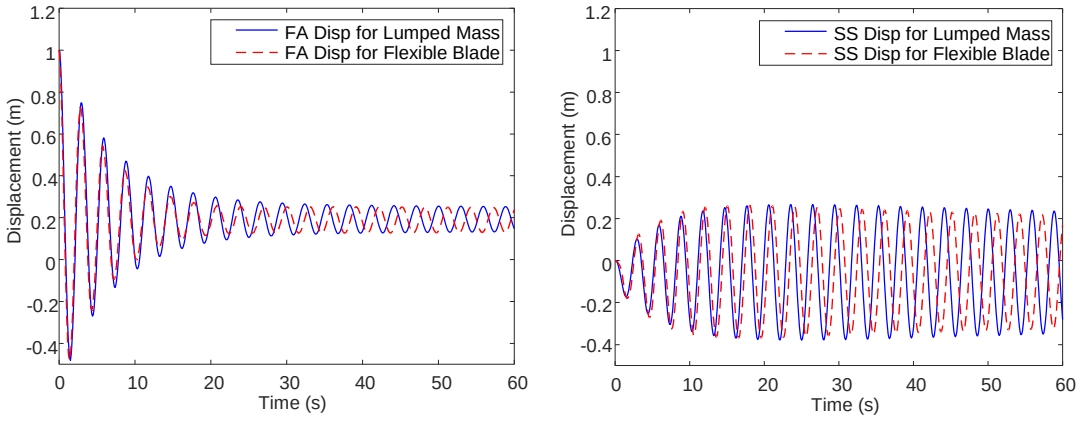

(a) (b)

Figure 4-10. FA (a) and SS (b) displacement response caused by a 1m initial displacement in the FA direction; Comparison between FAST models with a lumped mass, flexible blades for steady wind speed of 20 m/s.

To derive the damping matrix presented in Section 4.4, the blades were assumed to be rigid. To investigate the validity of this assumption, the influence of the flexibility of the blades was studied using FAST simulations. Results from earlier FAST simulations were obtained by lumping the mass of the blades and the nacelle at the tower top to allow a like-for-like comparison with the damping model, which has been presented in Subsection 4.5.1. These results are now compared with FAST outputs obtained from a model with distributed rotor inertia and flapwise and edgewise blade bending modes

enabled. This comparison is shown in Figure 4-10 for a mean wind speed of 20 m/s and a 1 m initial displacement in the FA direction at tower top.

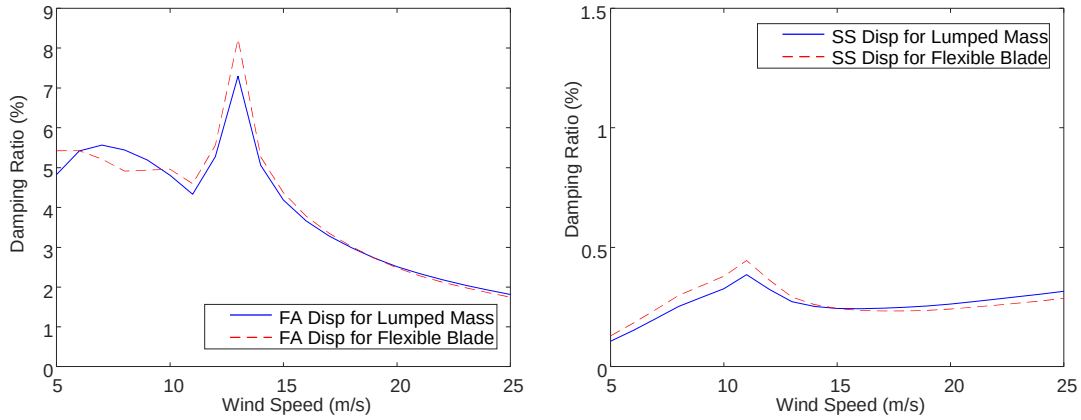

(a) (b)

Figure 4-11. FA damping (a) and SS damping (b) comparisons between the FAST models with a lumped mass and flexible blades.

From this comparison, the natural frequency of the first tower bending modes appear to have been shifted by 3% between the two models (0.34 Hz for the lumped RNA, 0.33 Hz for the flexible blades). This is due to the distribution of the blade masses and the inclusion of blade motions. The decay rates of the responses from the two models are similar, only slightly slower in the flexible blade model. To quantify the decay rates for these two models with different steady wind speeds, the damping ratios were calculated using the same procedure as described in Subsection 4.5.3. From the comparison of damping ratios in Figure 4-11, the decay rates of the two FAST models are very close for all wind speeds. As the proposed model was verified against the FAST model with lumped RNA mass, it can be concluded that ignoring the flexibility of blades in the proposed model do not lead significant differences in terms of aerodynamic damping.

Apart from the flexibility of blades, the effect of a non-zero static shaft tilt and blade precone were also tested. In additional FAST simulations, the shaft tilt and the precone were set to -5 ° and 2.5 ° respectively according to the default turbine configuration in FAST. Response comparison shown in Figure 4-12 confirmed that these two parameters have negligible influence on the aerodynamic damping. Other simulations including wind shear of the incoming wind field and tower shadow were also conducted

to test the influence of 1P and 3P excitation. Results shown in Figure 4-13 confirmed that these effects have no significant effect on the aerodynamic damping. The more observable influence is the difference in static displacement, which is caused by the introduction of wind shear leading to different total thrust and moment.

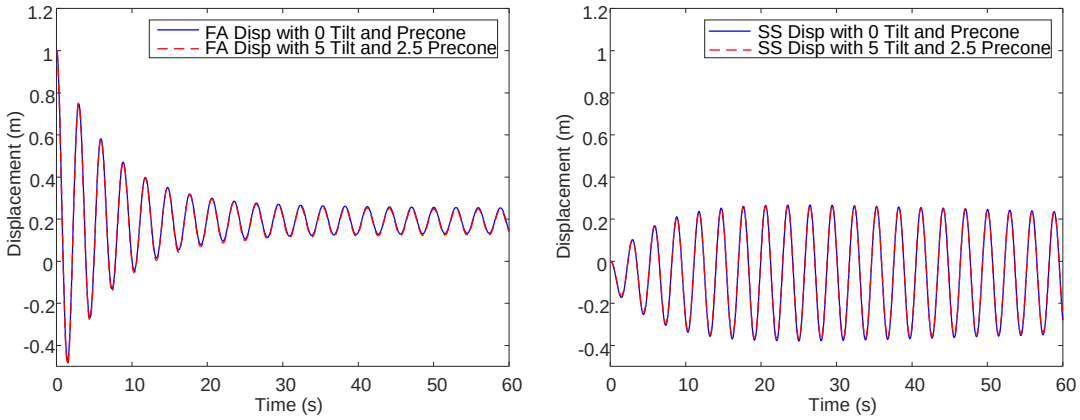

(a) (b)

Figure 4-12. FA (a) and SS (b) displacement response caused by a 1m initial displacement in the FA direction; Comparison between FAST model with zero shaft tilt and precone for all blades and FAST model with -5 °shaft tilt and 2.5 °precone for all blades for steady wind speed of 20 m/s.

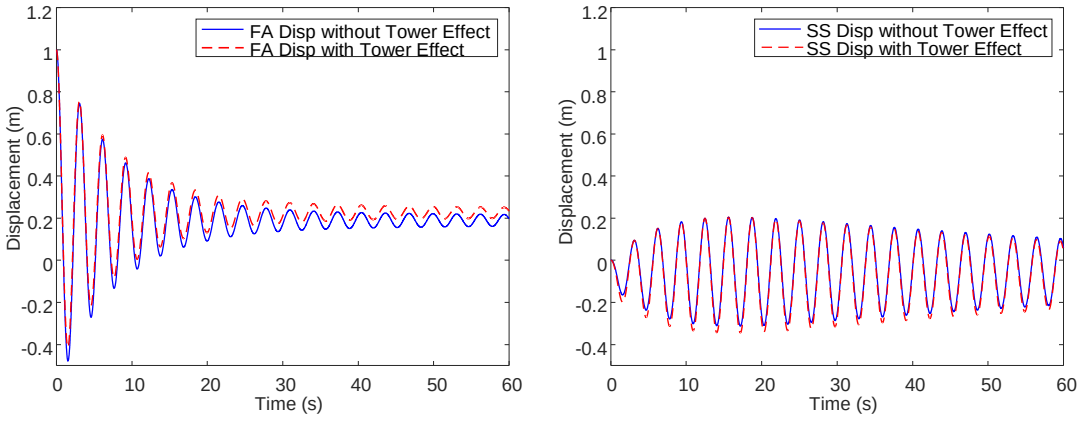

(a) (b)

Figure 4-13. FA (a) and SS (b) displacement response caused by a 1m initial displacement in the FA direction; Comparison between FAST model with no tower effect and wind shear and FAST model considering tower effect and wind shear for steady wind speed of 20 m/s.

4.6 Conclusion

This chapter proposes a novel two-stage methodology that uses BEM theory to derive analytical expressions for the aerodynamic force resultant on the rotor for steady-state operating wind turbines. In the first stage the aerodynamic damping matrix was calculated, and in the second stage the aerodynamic damping matrix can be assigned to a FE model whose responses can be obtained by time integration. From these results an efficient model was developed to predict the dynamic response of the tower/RNA system. The proposed decoupled modelling strategy based on analytical derivations would be particularly well suited for fatigue and reliability analyses.

The aerodynamic forces experienced by the moving rotor are linearised and reduced to a set of resultants comprised of static terms and damping terms expressed through an aerodynamic damping matrix for constant wind speed. Both stages were implemented in MATLAB and the dynamic response was predicted using a FE model of the tower and RNA system. This model was systematically verified against an equivalent FAST model, and a good agreement was obtained, confirming that the proposed model can successfully and efficiently capture the coupling effects between the FA and SS motions.

The closed-form expressions for the damping matrix coefficients give some insight into the links between aerodynamics and the vibration response of the tower. It was shown that the key features of this response are explained by a number of characteristics of the problem:

- Due to the rotational symmetry of the tower, the two fundamental bending modes have similar natural frequencies, which facilitates energy transfer between the two directions,
- Some off-diagonal coefficients of the damping matrix represent positive feedback, amplifying the vibration amplitude at certain wind speeds,
- The non-symmetry of the damping matrix causes a non-dissipative coupling, apparent as a beating behaviour for certain conditions.

It was found that the apparent aerodynamic damping can be significantly influenced by the coupling between FA and SS motions in a wind turbine. As a result, previous widely-used single damping ratio techniques might not be sufficiently accurate to describe the aerodynamic damping characteristics of wind turbines and the derived

aerodynamic damping matrix could form the basis for novel damping identification techniques better suited for wind turbine systems.

Chapter 5 - Aerodynamic Damping Model Considering Turbulent Wind Field

5.1 Introduction

The aerodynamic damping matrix introduced in Chapter 4 was derived with the initial assumption that the inflow wind field is uniformly distributed in the rotor plane and constant in time. However, in a real offshore environment the wind speed in the rotor plane varies in time and space due to turbulence and wind shear. Aerodynamic damping is a function of wind speed, rotor rotation speed and blade pitch angles. When these three parameters are constant, the aerodynamic damping is also constant according to the derivation in Section 4.4. It can be expected that the aerodynamic damping becomes time-varying when the wind field is turbulent and non-uniform. In this chapter, the influence of wind turbulence is studied. In Section 5.2, an extension to the aerodynamic damping matrix derived in Section 4.4 is presented considering a non-uniformly distributed turbulent wind field. Section 5.3 presents a method to simplify the wind turbine FE model with the 4×4 aerodynamic damping matrix to a two degrees of freedom (2-DOF) model using modal decomposition. The introduction of the 2-DOF model is motivated by its simplicity compared to the model with the original 4×4 aerodynamic damping matrix. By only selecting a limited number of modes, the 2-DOF model is more computationally efficient than the original model which requires a full FE model of the tower. Moreover, the 2-DOF model can be used as the basis of aerodynamic damping identification, which will be shown in the next chapter. To distinguish from the 2-DOF model, the full FE model with the 4×4 aerodynamic damping matrix is denoted as “original model”. In Section 5.4, simulation results are given to verify the time-varying aerodynamic damping model and the simplified 2-DOF model. Section 5.5 concludes this chapter.

5.2 Derivation of aerodynamic damping matrix for a non-uniform wind field

To consider a non-uniform inflow wind field, some modifications are needed to the derivation process in Section 4.4. Keeping the initial assumptions that the rotor is rigid and the RNA speed is small, the aerodynamic forces applied to one blade element can still be expressed by Equations (4-7) to (4-10). However, when summing the elemental

blade forces for one blade, the three blades must be considered individually as the total aerodynamic forces subjected by different blades are different due to wind turbulence and different azimuthal positions. In this way, the aerodynamic force resultants can still be linearised as forces applied to a rigid tower plus terms related to the tower top velocities. Having the notations introduced in Chapter 4, the total force at the tower top in the x (FA) direction can be expressed as the sum of thrusts applied to all blades:

$$\begin{aligned} F_x^{Flex}(t) &= \sum_{i=1}^{N_b} \int_0^R dT(V_{xRel}, V_{rRel}) \\ &= \sum_{i=1}^{N_b} \int_0^R dT(V_0, V_r) - \dot{x} \sum_{i=1}^{N_b} \int_0^R \frac{\partial(dT)}{\partial V_0} - \dot{\theta}_y \sum_{i=1}^{N_b} cos\gamma_i(t) \int_0^R r \frac{\partial(dT)}{\partial V_0} \\ &- \dot{y} \sum_{i=1}^{N_b} cos\gamma_i(t) \int_0^R \frac{\partial(dT)}{\partial V_r} + \dot{\theta}_x \sum_{i=1}^{N_b} \int_0^R r \frac{\partial(dT)}{\partial V_r}. \end{aligned} \tag{5-1}$$

Here the force marked with "$Flex$" is the force applied to a flexible wind turbine tower. The total force in the y (SS) direction is:

$$\begin{aligned} F_y^{Flex}(t) &= -\sum_{i=1}^{N_b} cos\gamma_i(t) \int_0^R dS(V_{xRel}, V_{rRel}) \\ &= -\sum_{i=1}^{N_b} cos\gamma_i(t) \int_0^R dS(V_0, V_r) + \dot{x} \sum_{i=1}^{N_b} \cos\gamma_i(t) \int_0^R \frac{\partial(dS)}{\partial V_0} \\ &+ \dot{\theta}_y \sum_{i=1}^{N_b} \cos^2\gamma_i(t) \int_0^R r \frac{\partial(dS)}{\partial V_0} + \dot{y} \sum_{i=1}^{N_b} \cos^2\gamma_i(t) \int_0^R \frac{\partial(dS)}{\partial V_r} \\ &- \dot{\theta}_x \sum_{i=1}^{N_b} cos\gamma_i(t) \int_0^R r \frac{\partial(dS)}{\partial V_r}. \end{aligned} \tag{5-2}$$

The total moment about the x axis is:

$$\begin{aligned} M_x^{Flex}(t) &= \sum_{i=1}^{N_b} \int_0^R dM_x(V_{xRel}, V_{rRel}) \\ &= \sum_{i=1}^{N_b} \int_0^R r dS(V_0, V_r) - \dot{x} \sum_{i=1}^{N_b} \int_0^R r \frac{\partial(dS)}{\partial V_0} - \dot{\theta}_y \sum_{i=1}^{N_b} cos\gamma_i(t) \int_0^R r^2 \frac{\partial(dS)}{\partial V_0} \end{aligned} \tag{5-3}$$

$$-\dot{y}\sum_{i=1}^{N_b} cos\gamma_i(t)\int_0^R r\frac{\partial(dS)}{\partial V_r}+\dot{\theta}_x\sum_{i=1}^{N_b}\int_0^R r^2\frac{\partial(dS)}{\partial V_r},$$

whereas the total moment about the y axis is:

$$\begin{aligned}
&M_y^{Flex}(t)=\sum_{i=1}^{N_b}\int_0^R dM_y(V_{xRel},V_{rRel})\\
&=\sum_{i=1}^{N_b} cos\gamma_i(t)\int_0^R rdT(V_0,V_r)-\dot{x}\sum_{i=1}^{N_b} cos\gamma_i(t)\int_0^R r\frac{\partial(dT)}{\partial V_0}\\
&-\dot{\theta}_y\sum_{i=1}^{N_b}\cos^2\gamma_i(t)\int_0^R r^2\frac{\partial(dT)}{\partial V_0}-\dot{y}\sum_{i=1}^{N_b}\cos^2\gamma_i(t)\int_0^R r\frac{\partial(dT)}{\partial V_r}\\
&+\dot{\theta}_x\sum_{i=1}^{N_b} cos\gamma_i(t)\int_0^R r^2\frac{\partial(dT)}{\partial V_r}.
\end{aligned} \tag{5-4}$$

The derivatives in Equations (5-1) to (5-4) can be found using expressions of partial derivatives in Section 4.4. According to Equations (5-1) to (5-4), the resultant aerodynamic forces from the rotor to the top of a flexible wind turbine tower, $\mathbf{F}_{Flex}^{Top}(t)=\left[F_x^{Flex}(t)\ F_y^{Flex}(t)\ M_x^{Flex}(t)\ M_y^{Flex}(t)\right]^T$, can be rewritten in the following simplified form

$$\mathbf{F}_{Flex}^{Top}(t)=\begin{bmatrix}\sum_{i=1}^{N_b}\int_0^R dT(V_0,V_r)\\ -\sum_{i=1}^{N_b} cos\gamma_i(t)\int_0^R dS(V_0,V_r)\\ \sum_{i=1}^{N_b}\int_0^R rdS(V_0,V_r)\\ \sum_{i=1}^{N_b} cos\gamma_i(t)\int_0^R rdT(V_0,V_r)\end{bmatrix}-\mathbf{C}_{Aero}\begin{bmatrix}\dot{x}\\ \dot{y}\\ \dot{\theta}_x\\ \dot{\theta}_y\end{bmatrix}=\mathbf{F}_{Rigid}^{Top}(t)-\mathbf{C}_{Aero}\dot{\mathbf{u}}^{Top}(t). \tag{5-5}$$

where $\mathbf{F}_{Rigid}^{Top}(t)=\left[F_x^{Rigid}(t)\ F_y^{Rigid}(t)\ M_x^{Rigid}(t)\ M_y^{Rigid}(t)\right]^T$ represents the aerodynamic force vector applied to a rigid wind turbine tower, $\dot{\mathbf{u}}^{Top}=\left[\dot{x}\ \dot{y}\ \dot{\theta}_x\ \dot{\theta}_y\right]^T$ is the velocity vector for the tower top and

$\mathbf{C}_{Aero}=$

$$\begin{bmatrix} \sum_{i=1}^{N_b}\int_0^R \frac{\partial(dT)}{\partial V_0} & \sum_{i=1}^{N_b} cos\gamma_i(t)\int_0^R \frac{\partial(dT)}{\partial V_r} & -\sum_{i=1}^{N_b}\int_0^R r\frac{\partial(dT)}{\partial V_r} & \sum_{i=1}^{N_b} cos\gamma_i(t)\int_0^R r\frac{\partial(dT)}{\partial V_0} \\ -\sum_{i=1}^{N_b}\cos\gamma_i(t)\int_0^R \frac{\partial(dS)}{\partial V_0} & -\sum_{i=1}^{N_b}\cos^2\gamma_i(t)\int_0^R \frac{\partial(dS)}{\partial V_r} & \sum_{i=1}^{N_b} cos\gamma_i(t)\int_0^R r\frac{\partial(dS)}{\partial V_r} & -\sum_{i=1}^{N_b}\cos^2\gamma_i(t)\int_0^R r\frac{\partial(dS)}{\partial V_0} \\ \sum_{i=1}^{N_b}\int_0^R r\frac{\partial(dS)}{\partial V_0} & \sum_{i=1}^{N_b} cos\gamma_i(t)\int_0^R r\frac{\partial(dS)}{\partial V_r} & -\sum_{i=1}^{N_b}\int_0^R r^2\frac{\partial(dS)}{\partial V_r} & \sum_{i=1}^{N_b} cos\gamma_i(t)\int_0^R r^2\frac{\partial(dS)}{\partial V_0} \\ \sum_{i=1}^{N_b} cos\gamma_i(t)\int_0^R r\frac{\partial(dT)}{\partial V_0} & \sum_{i=1}^{N_b}\cos^2\gamma_i(t)\int_0^R r\frac{\partial(dT)}{\partial V_r} & -\sum_{i=1}^{N_b} cos\gamma_i(t)\int_0^R r^2\frac{\partial(dT)}{\partial V_r} & \sum_{i=1}^{N_b}\cos^2\gamma_i(t)\int_0^R r^2\frac{\partial(dT)}{\partial V_0} \end{bmatrix}. \quad (5\text{-}6)$$

$\mathbf{C}_{Aero}$ can be written more concisely:

$$\mathbf{C}_{Aero} = \begin{bmatrix} c_{xx} & c_{xy} & c_{x\theta_x} & c_{x\theta_y} \\ c_{yx} & c_{yy} & c_{y\theta_x} & c_{y\theta_y} \\ c_{\theta_x x} & c_{\theta_x y} & c_{\theta_x\theta_x} & c_{\theta_x\theta_y} \\ c_{\theta_y x} & c_{\theta_y y} & c_{\theta_y\theta_x} & c_{\theta_y\theta_y} \end{bmatrix}. \quad (5\text{-}7)$$

Compared to the aerodynamic damping matrix in Equation (4-40), all the terms in Equation (5-7) can be non-zero. When the inflow wind field is constant in space and time, the aerodynamic damping matrix is constant during the simulation and in the form described by Equation (4-40). When the turbulent wind field is uniformly distributed over the rotor plane but changes over time, the aerodynamic damping matrix is still in the form of Equation (4-40) but becomes time-varying as the initial uniform wind field assumption is fulfilled in every time step. Making the assumption of uniform wind field ignores the fact that different wind speeds seen by the three blades may result in imbalanced aerodynamic forces at the tower top. For a turbulent non-uniform wind field, the aerodynamic damping matrix is time-varying and needs to be calculated by Equation (5-7), as the values of partial derivatives for different blade elements are different. The variations in azimuth angles over time for different blades also contribute to the time-varying damping.

The time-varying damping in this study is modelled by varying the damping matrix in the equation of motions at every time step, which is similar to the methodology of calculating aerodynamic forces using a quasi-steady BEM model which assumes the flow is steady and the momentum is balanced given the particular inflow wind speed at every time step. The difference is that the aerodynamic forces are linearised using aerodynamic damping terms while in a quasi-steady BEM model the aerodynamic forces are calculated using standard BEM iterations given the inflow wind speed.

5.3 Simplification to 2-DOF system using modal decomposition

If the aerodynamic resultants at the tower top are treated as external forces applied to the wind turbine system, the aerodynamic damping is included in the external forces. In this way, the equation of motion of the system can be written as:

$$\mathbf{M}\ddot{\mathbf{u}}(t) + \mathbf{C}_{Struc}\dot{\mathbf{u}}(t) + \mathbf{K}\mathbf{u}(t) = \mathbf{F}^{Flex}(t), \tag{5-8}$$

where $\mathbf{M}$, $\mathbf{C}_{Struc}$ and $\mathbf{K}$ are the mass, structural damping and stiffness matrices respectively. $\mathbf{F}^{Flex}(t)$ is the external aerodynamic force vector applied to a flexible tower and $\mathbf{u}(t)$ is the generalised displacement vector. The wind loads on the tower itself are ignored so $\mathbf{F}^{Flex}(t)$ represents the resultant aerodynamic forces from the rotor at the tower top. As described in Section 5.2, $\mathbf{F}_{Flex}^{Top}(t)$ can be linearised with respect to the tower top velocities. Using the relationship $\mathbf{F}_{Flex}^{Top}(t) = \mathbf{F}_{Rigid}^{Top}(t) - \mathbf{C}_{Aero}\dot{\mathbf{u}}^{Top}(t)$ in Equation (5-5), the linearised equation of motion considering aerodynamic coupling is

$$\mathbf{M}\ddot{\mathbf{u}}(t) + \mathbf{C}\dot{\mathbf{u}}(t) + \mathbf{K}\mathbf{u}(t) = \mathbf{F}^{Rigid}(t), \tag{5-9}$$

where $\mathbf{C}$ is $\mathbf{C}_{Struc}$ plus the terms of $\mathbf{C}_{Aero}$ added at the relevant locations and $\mathbf{F}^{Rigid}(t)$ is the tower top force vector $\mathbf{F}_{Rigid}^{Top}(t)$ padded with zeros for all other degree of freedoms. The response of the system expressed in Equation (5-8) can be calculated using a partial modal decomposition, when $\mathbf{C}_{Struc}$ is assumed as a proportional damping matrix and $\mathbf{F}^{Flex}(t)$ is initially regarded as an external force independent of the dynamic properties of the system. In wind turbines, the FA and SS responses are dominated by the FA and SS first bending modes so only these two modal coordinates will be considered for the derivation below. After modal decomposition, the equations of motion for the first bending modes can be written as:

$$\begin{aligned}
\bar{m}_x\ddot{\alpha}_x(t) + 2\bar{\zeta}_x\sqrt{\bar{m}_x\bar{k}_x}\dot{\alpha}_x(t) + \bar{k}_x\alpha_x(t) &= \boldsymbol{\phi}_x^T\mathbf{F}_x^{Flex}(t), \\
\bar{m}_y\ddot{\alpha}_y(t) + 2\bar{\zeta}_y\sqrt{\bar{m}_y\bar{k}_y}\dot{\alpha}_y(t) + \bar{k}_y\alpha_y(t) &= \boldsymbol{\phi}_y^T\mathbf{F}_y^{Flex}(t),
\end{aligned} \tag{5-10}$$

where $\bar{m}_x$, $\bar{m}_y$, $\bar{k}_x$ and $\bar{k}_y$ are the modal mass and stiffness for the first FA/SS mode respectively, $\bar{\zeta}_x$ and $\bar{\zeta}_y$ are the structural modal damping ratios, and $\alpha_x(t)$ and $\alpha_y(t)$ are the modal coordinates for the first FA and SS modes respectively. The forces applied in the FA and SS directions after modal decomposition are $\mathbf{F}_x^{Flex}(t) = \left[\mathrm{F}_x^{Flex}(t)\ \mathrm{M}_y^{Flex}(t)\right]^T$ and $\mathbf{F}_y^{Flex}(t) = \left[\mathrm{F}_y^{Flex}(t)\ \mathrm{M}_x^{Flex}(t)\right]^T$ multiplied by the truncated

mode shapes. The truncated mode shapes for the first FA and SS bending modes of the system in Equation (5-10) are $\boldsymbol{\phi}_x = [\phi_{x1}\ \phi_{x2}]^T$ and $\boldsymbol{\phi}_y = \left[\phi_{y1}\ \phi_{y2}\right]^T$, where ϕ_{x1} and ϕ_{y1} correspond to the displacement motion while ϕ_{x2} and ϕ_{y2} correspond to the angular motion for the first FA and SS bending modes respectively. The linear and angular velocities at the tower top can be expressed by multiplying the modal shapes by the modal coordinates, *i.e.*, $\dot{x} \approx \phi_{x1}\dot{\alpha}_x(t)$, $\dot{y} \approx \phi_{y1}\dot{\alpha}_y(t)$, $\dot{\theta}_x \approx \phi_{y2}\dot{\alpha}_x(t)$ and $\dot{\theta}_y \approx \phi_{x2}\dot{\alpha}_x(t)$. Since $\mathbf{F}_{Flex}^{Top}(t) = \mathbf{F}_{Rigid}^{Top}(t) - \mathbf{C}_{Aero}\dot{\mathbf{u}}^{Top}(t)$, the modal force in the FA direction, $\boldsymbol{\phi}_x^T\mathbf{F}_x^{Flex}(t)$, can be written as

$$\boldsymbol{\phi}_x^T\mathbf{F}_x^{Flex}(t) =$$

$$[\phi_{x1} \quad \phi_{x2}]\left\{\begin{bmatrix} F_x^{Rigid}(t) \\ \mathrm{M}_y^{Rigid}(t) \end{bmatrix} - \begin{bmatrix} c_{xx} & c_{xy} & c_{x\theta_x} & c_{x\theta_y} \\ c_{\theta_y x} & c_{\theta_y y} & c_{\theta_y\theta_x} & c_{\theta_y\theta_y} \end{bmatrix}\begin{bmatrix} \phi_{x1}\dot{\alpha}_x(t) \\ \phi_{y1}\dot{\alpha}_y(t) \\ \phi_{y2}\dot{\alpha}_y(t) \\ \phi_{x2}\dot{\alpha}_x(t) \end{bmatrix}\right\}.$$

The above equation can be simplified to

$$\begin{aligned} &\boldsymbol{\phi}_x^T\mathbf{F}_x(t) = \phi_{x1}F_x^{Rigid}(t) + \phi_{x2}M_y^{Rigid}(t) \\ &-\left(\phi_{x1}^2 c_{xx} + \phi_{x1}\phi_{x2}c_{x\theta_y} + \phi_{x2}\phi_{x1}c_{\theta_y x} + \phi_{x2}^2 c_{\theta_y\theta_y}\right)\dot{\alpha}_x(t) \\ &-\left(\phi_{x1}\phi_{y1}c_{xy} + \phi_{x1}\phi_{y2}c_{x\theta_x} + \phi_{x2}\phi_{y1}c_{\theta_y y} + \phi_{x2}\phi_{y2}c_{\theta_y\theta_x}\right)\dot{\alpha}_y(t). \end{aligned} \tag{5-11}$$

Similarly, the corresponding SS modal force is

$$\boldsymbol{\phi}_y^T\mathbf{F}_y^{Flex}(t) =$$

$$[\phi_{y1} \quad \phi_{y2}]\left\{\begin{bmatrix} F_y^{Rigid}(t) \\ \mathrm{M}_x^{Rigid}(t) \end{bmatrix} - \begin{bmatrix} c_{yx} & c_{yy} & c_{y\theta_x} & c_{y\theta_y} \\ c_{\theta_x x} & c_{\theta_x y} & c_{\theta_x\theta_x} & c_{\theta_x\theta_y} \end{bmatrix}\begin{bmatrix} \phi_{x1}\dot{\alpha}_x(t) \\ \phi_{y1}\dot{\alpha}_y(t) \\ \phi_{y2}\dot{\alpha}_y(t) \\ \phi_{x2}\dot{\alpha}_x(t) \end{bmatrix}\right\}.$$

The above equation can be simplified to

$$\begin{aligned} &\boldsymbol{\phi}_y^T\mathbf{F}_y(t) = \phi_{y1}F_y^{Rigid}(t) + \phi_{y2}M_x^{Rigid}(t) \\ &-\left(\phi_{y1}\phi_{x1}c_{yx} + \phi_{y1}\phi_{x2}c_{y\theta_y} + \phi_{y2}\phi_{x1}c_{\theta_x x} + \phi_{y2}\phi_{x2}c_{\theta_x\theta_y}\right)\dot{\alpha}_x(t) \\ &-\left(\phi_{y1}^2 c_{yy} + \phi_{y1}\phi_{y2}c_{y\theta_x} + \phi_{y2}\phi_{y1}c_{\theta_x y} + \phi_{y2}^2 c_{\theta_x\theta_x}\right)\dot{\alpha}_y(t). \end{aligned} \tag{5-12}$$

Therefore, the equations of motion for the first bending modes in FA and SS directions can be written in this form:

$$\begin{bmatrix} \bar{m}_x & 0 \\ 0 & \bar{m}_y \end{bmatrix} \begin{bmatrix} \ddot{\alpha}_x(t) \\ \ddot{\alpha}_y(t) \end{bmatrix} + \begin{bmatrix} \bar{c}_{xx} + \bar{s}_x & \bar{c}_{xy} \\ \bar{c}_{yx} & \bar{c}_{yy} + \bar{s}_y \end{bmatrix} \begin{bmatrix} \dot{\alpha}_x(t) \\ \dot{\alpha}_y(t) \end{bmatrix} + \begin{bmatrix} \bar{k}_x & 0 \\ 0 & \bar{k}_y \end{bmatrix} \begin{bmatrix} \alpha_x(t) \\ \alpha_y(t) \end{bmatrix} = \begin{bmatrix} \phi_{x1} F_x^{Rigid}(t) + \phi_{x2} M_y^{Rigid}(t) \\ \phi_{y1} F_y^{Rigid}(t) + \phi_{y2} M_x^{Rigid}(t) \end{bmatrix}, \tag{5-13}$$

where

$$\bar{c}_{xx} = \phi_{x1}^2 c_{xx} + \phi_{x1}\phi_{x2} c_{x\theta_y} + \phi_{x2}\phi_{x1} c_{\theta_y x} + \phi_{x2}^2 c_{\theta_y\theta_y},$$

$$\bar{c}_{xy} = \phi_{x1}\phi_{y1} c_{xy} + \phi_{x1}\phi_{y2} c_{x\theta_x} + \phi_{x2}\phi_{y1} c_{\theta_y y} + \phi_{x2}\phi_{y2} c_{\theta_y\theta_x},$$

$$\bar{c}_{yx} = \phi_{y1}\phi_{x1} c_{yx} + \phi_{y1}\phi_{x2} c_{y\theta_y} + \phi_{y2}\phi_{x1} c_{\theta_x x} + \phi_{y2}\phi_{x2} c_{\theta_x\theta_y},$$

$$\bar{c}_{yy} = \phi_{y1}^2 c_{yy} + \phi_{y1}\phi_{y2} c_{y\theta_x} + \phi_{y2}\phi_{y1} c_{\theta_x y} + \phi_{y2}^2 c_{\theta_x\theta_x},$$

$$\bar{s}_x = 2\bar{\zeta}_x \sqrt{\bar{m}_x \bar{k}_x},$$

$$\bar{s}_y = 2\bar{\zeta}_y \sqrt{\bar{m}_y \bar{k}_y}.$$

Here the "modal" damping matrix $\bar{\mathbf{C}}$ is defined as

$$\bar{\mathbf{C}} = \begin{bmatrix} \bar{c}_{xx} + \bar{s}_x & \bar{c}_{xy} \\ \bar{c}_{yx} & \bar{c}_{yy} + \bar{s}_y \end{bmatrix}. \tag{5-14}$$

The cross terms in $\bar{\mathbf{C}}$ reveal that the FA and SS vibrations are coupled through aerodynamic damping. Unlike traditional damping matrices, $\bar{c}_{xy}$ and $\bar{c}_{yx}$ are non-zero and not identical, making the modal damping matrix asymmetric as the 4×4 aerodynamic damping matrix was. The 2-DOF model described by Equation (5-13) is an approximation of the original model described by Equation (5-9) with only the first bending modes considered. Higher modes could be included in the model using the relevant mode shapes in a similar way. The response of the turbine can be calculated by summing up the contributions from modes considered. This process is useful to lower the order of the system in a physical manner.

5.4 Results and discussion

5.4.1 FAST setting and verification procedure

FAST was used to verify the time-varying damping models developed in Sections 5.2 and 5.3. The onshore wind turbine model in FAST detailed in Chapter 4 is used

throughout this chapter. A customised turbulent wind field generator was written in MATLAB as an alternative to Turbsim for the purpose of generating wind field input in FAST, as Turbsim does not allow a uniform wind field to be generated. The turbulent wind field generator was verified against TurbSim. As an example, the mean wind speed of 20 m/s is selected to show the verification results. A Kaimal spectrum was used as the input both for TurbSim and the turbulent wind field generator. The properties of the Kaimal spectrum were defined according to the turbulence model described in the Appendix B.2 in IEC 61400 edition 3 [136]. Figure 5-1 (a) shows the generated wind speed time series when the turbulence intensity is 10%. It is expected that the power spectrum densities (PSDs) of the generated time series by these two models should be close if the two models are similar. Comparison shown in Figure 5-1(b) confirms the similarity of the PSDs of the wind velocity time series from these two models. For other mean wind speeds, these two spectra are also close. Consequently, the inflow wind fields used for the FAST model and the calculation of aerodynamic damping matrices in this chapter were all obtained using the MATLAB wind field generator. For the purpose of comparison, the tower influence of the wind based on potential flow is not considered in the FAST AeroDyn setting [135] as the tower influence is not included in the derivation of the aerodynamic damping matrix.

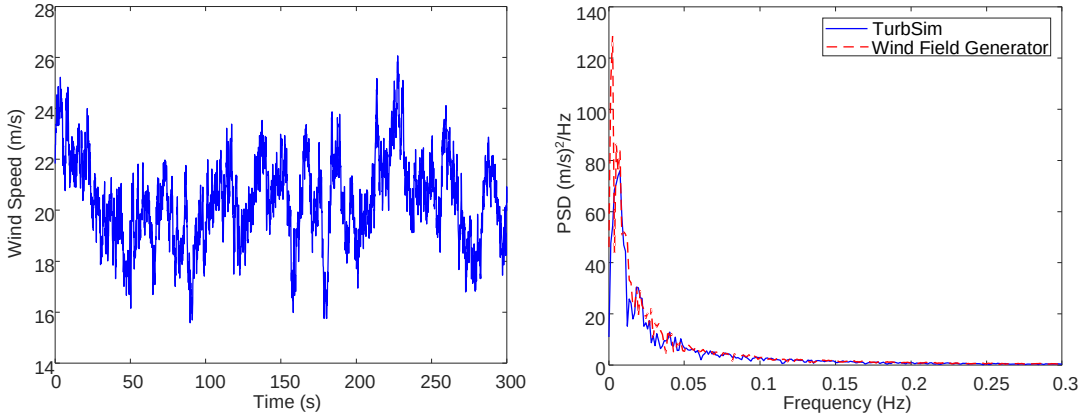

(a) (b)

Figure 5-1. (a) Wind speed time series with 20 m/s mean wind speed and 10% turbulence intensity (b) Comparison of the power spectrum densities of the wind speed time series generated by TurbSim and the customised turbulent wind field generator.

For the FAST simulation and the calculation of the time-varying aerodynamic damping matrices, the operating configuration of wind turbines need to be determined. When the mean wind speed is 20 m/s (comparisons shown latter are based on this mean wind speed), the rotor rotation speed is set to 12.1 rpm and blade pitch angle as 17 °, giving the rated power output. For comparisons with different wind speeds not shown here, the relationship between mean wind speed, pitch angle and rotation speed can be found in Figure 3-4. The intensity of turbulence is 10% if not specified. The length of simulation was selected as 300 s.

For the original model and the 2-DOF model, the stiffness and mass matrices were formed from the material and geometric properties provided in the FAST model to make the models comparable. The aerodynamic damping matrices were calculated using Equation (5-7) and Equation (5-14). The mean wind speed is used to obtain the damping terms when the turbulent wind field is uniform. The case with non-uniform wind field will be introduced in Subsection 5.4.3. The aerodynamic forces applied to the rigid tower can be calculated by the customised BEM model implemented in MATLAB or directly obtained from the FAST model where the tower motions were disabled. With the damping matrices and the external forces, the FA and SS responses at the tower top can be obtained. The structural damping was set to zero in all models as this chapter mainly studies the aerodynamic damping.

A comparison between the original model and the 2-DOF model was carried out when the turbulent field is uniform. Time series comparison in Figure 5-2 shows that the responses calculated from the model with the original aerodynamic damping matrix and the 2-DOF model are very close. To quantify the difference between two responses, a similarity indicator denoted as S_{xy} is introduced. First, two responses $u_x(t)$ and $u_y(t)$ are converted to zero-mean signals $u'_x(t)$ and $u'_y(t)$. Then the squared root of the sum of the squared difference in values between the two signals at each time step is calculated. This value is then divided by the squared root of the sum of squared $u'_x(t)$. The similarity indicator S_{xy} can be expressed by

$$S_{xy} = \sqrt{\frac{\sum_0^T \left(u'_x(t) - u'_y(t)\right)^2}{\sum_0^T {u'_x}^2(t)}}, \tag{5-15}$$

where T is the length of the signal. All time series compared in Section 5.4 have the same duration and time step. The response from FAST or the original model is selected as $u_x(t)$. The value of S_{xy} closer to zero indicates the two signals are more similar. The values of the similarity indicator are 0.01 and 0.11 for the FA and SS responses respectively when comparing the original model and the 2-DOF model. These differences are relatively small compared to those from the comparison between the 2-DOF model and the FAST model which will be shown later. This confirms that the modal decomposition is an accurate way of simplifying the original model and demonstrates that the responses are dominated by the first bending modes and the contribution of higher modes is very small. As similar responses are obtained by the original model and the 2-DOF model, the focus will be the comparison between the responses generated by the 2-DOF model and the FAST model for identical conditions.

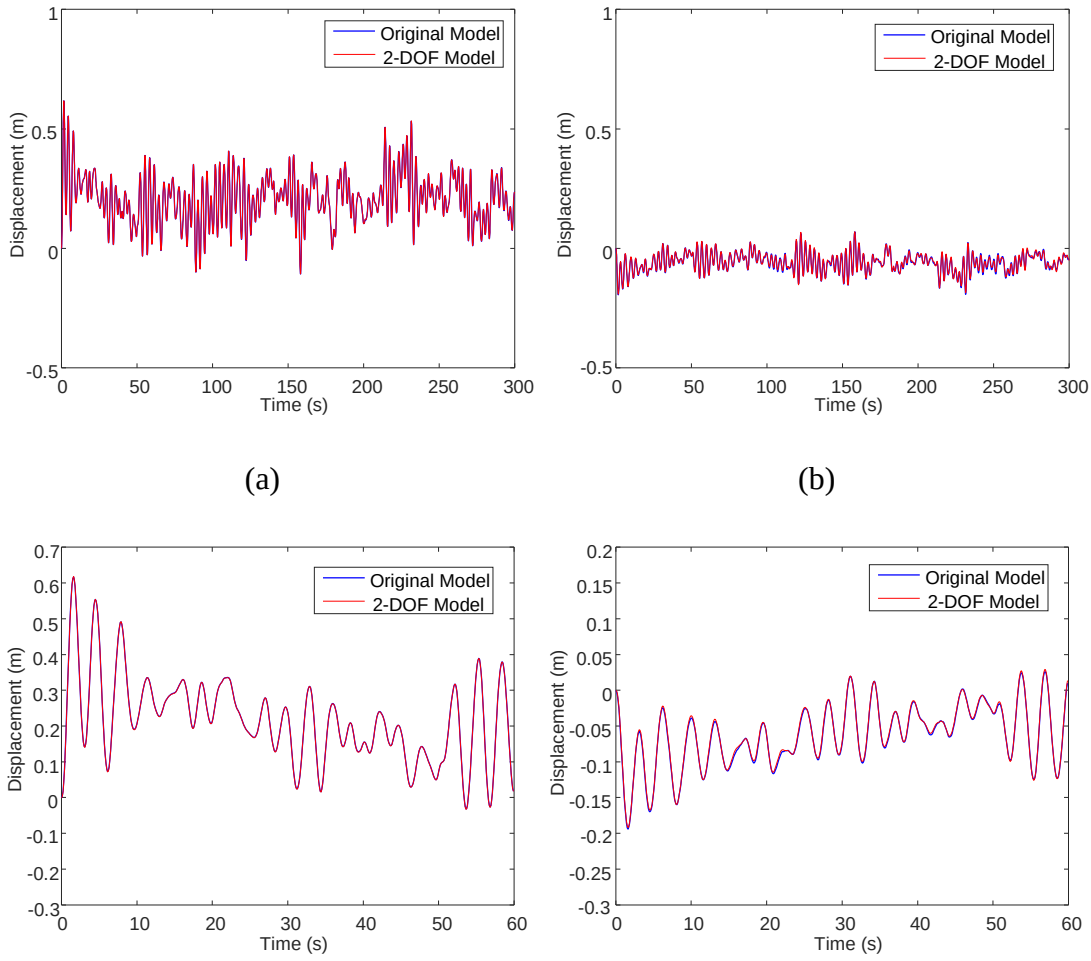

Figure 5-2. Comparison of the FA (a, c) and SS (b, d) responses from the original model and the 2-DOF model; (c) and (d) are zooms of (a) and (b).

5.4.2 Comparison between the 2-DOF model and the FAST model with uniform wind field

First, the case with uniform wind field is considered. Figure 5-3 shows the comparison between results from the 2-DOF model with the constant aerodynamic damping matrix and the FAST model with a mean wind speed of 20 m/s. As can be seen, the FA response from the FAST model and the 2-DOF model agree well, while for the SS response slight differences can be observed. For the responses given in Figure 5-3, the values of the similarity indicator are 0.07 and 0.29 for the FA and SS responses respectively.

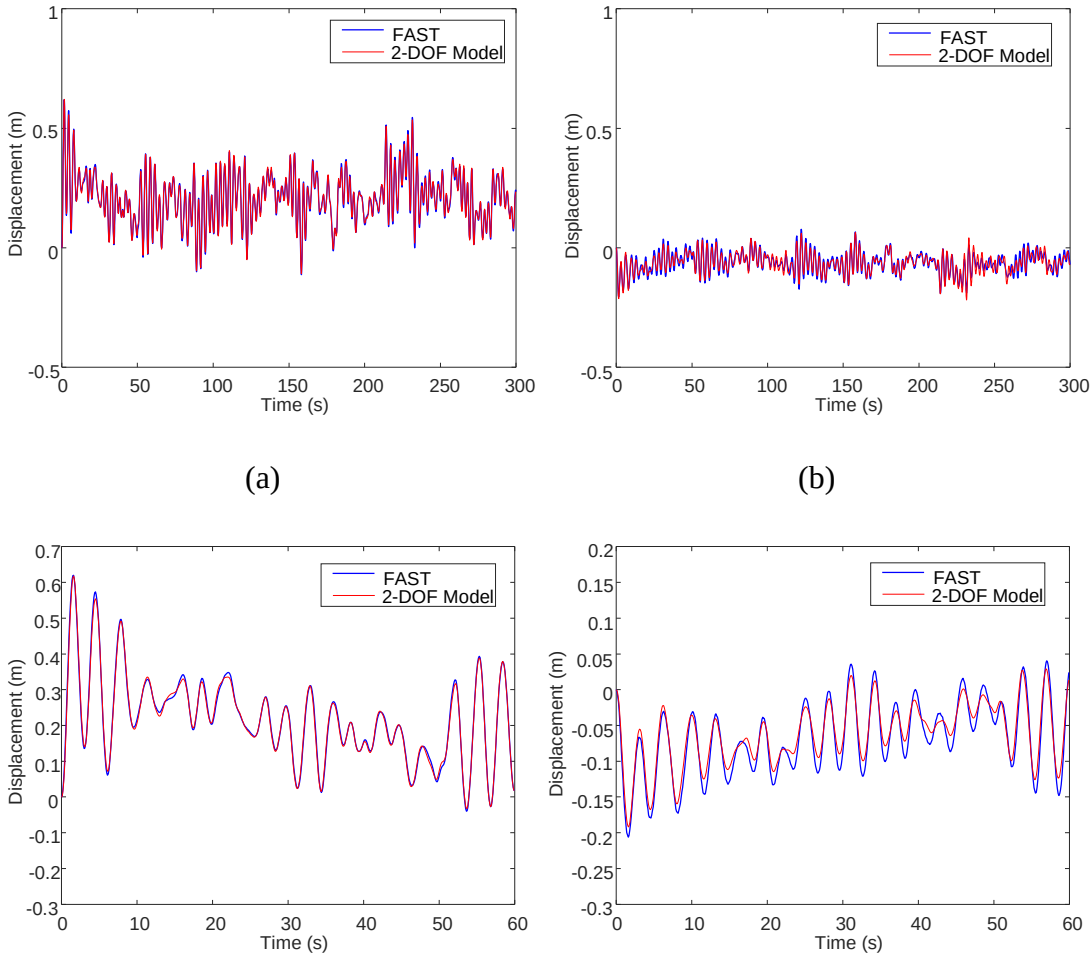

Figure 5-3. Comparison of the FA (a, c) and SS (b, d) responses from the 2-DOF model with the constant aerodynamic damping matrix and the FAST model; (c) and (d) are zooms of (a) and (b).

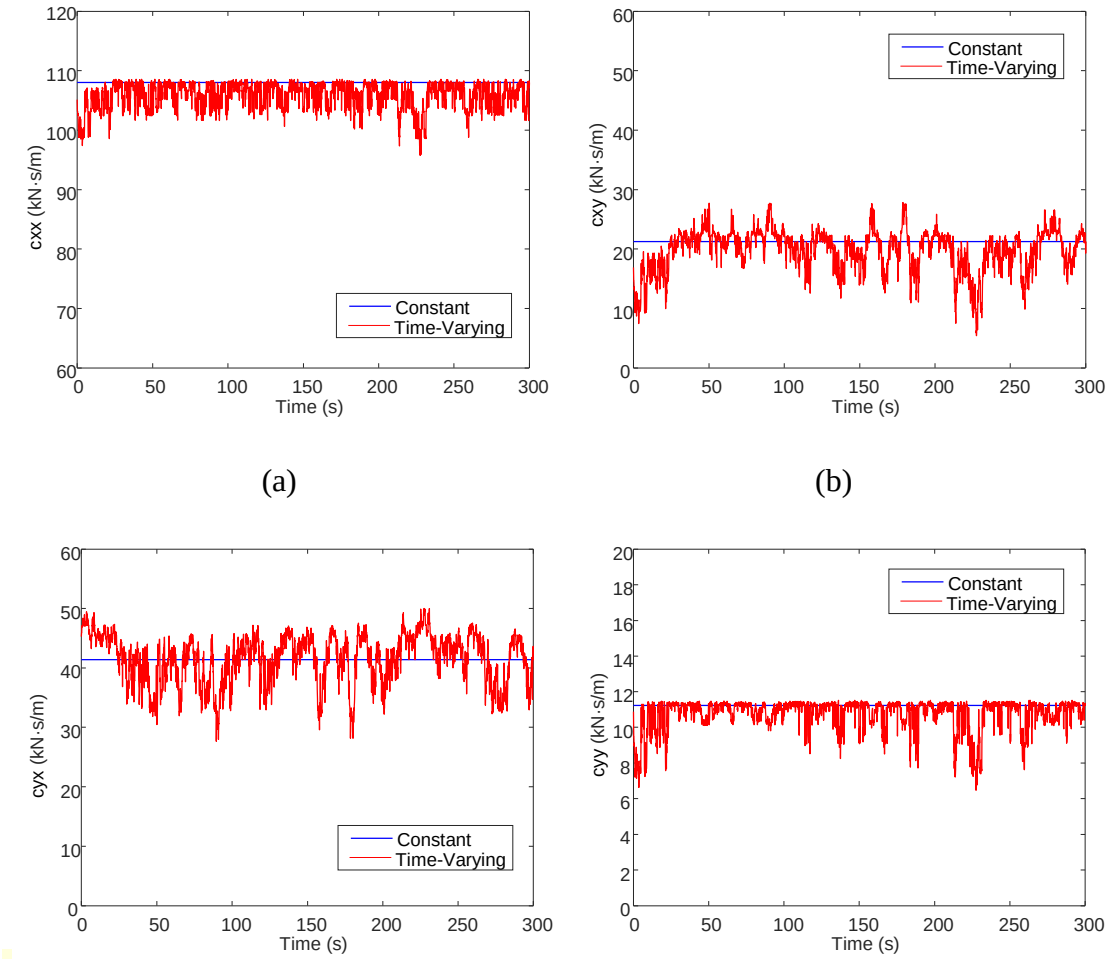

Figure 5-4. Comparison of $\bar{c}_{xx}$ (a), $\bar{c}_{xy}$ (b), $\bar{c}_{yx}$ (c) and $\bar{c}_{yy}$ (d) in the constant aerodynamic damping matrix and the time-varying aerodynamic damping matrix.

Considering the aerodynamic damping matrix as time-varying by calculating the damping coefficients at every time step for the turbulent wind velocity, the time-varying damping coefficients are plotted in Figure 5-4. The mean values of the time-varying coefficients $\bar{c}_{xx}$, $\bar{c}_{xy}$, $\bar{c}_{yx}$ and $\bar{c}_{yy}$ are 105.7, 19.8, 41.5 and 10.7 kN·s/m with standard deviations of 2.3, 3.6, 4.2 and 0.9 kN·s/m. For $\bar{c}_{xx}$ and $\bar{c}_{yy}$, their mean values are lower than the calculated constant values. For $\bar{c}_{xy}$ and $\bar{c}_{yx}$, their mean values are close to the constant values but they are more variable compared to $\bar{c}_{xx}$ and $\bar{c}_{yy}$. Then the responses of the 2-DOF model with the time-varying damping matrix are compared with the FAST responses in Figure 5-5. Compared to the results from the 2-DOF model with the constant damping matrix in Figure 5-3, the SS response generated by the 2-DOF model

with the time-varying matrix is closer to the FAST response. The values of the similarity indicator for FA and SS responses are 0.06 and 0.24 which are lower than the values with the constant damping matrix, indicating that the 2-DOF model with the time-varying damping matrix can better represent the FAST model.

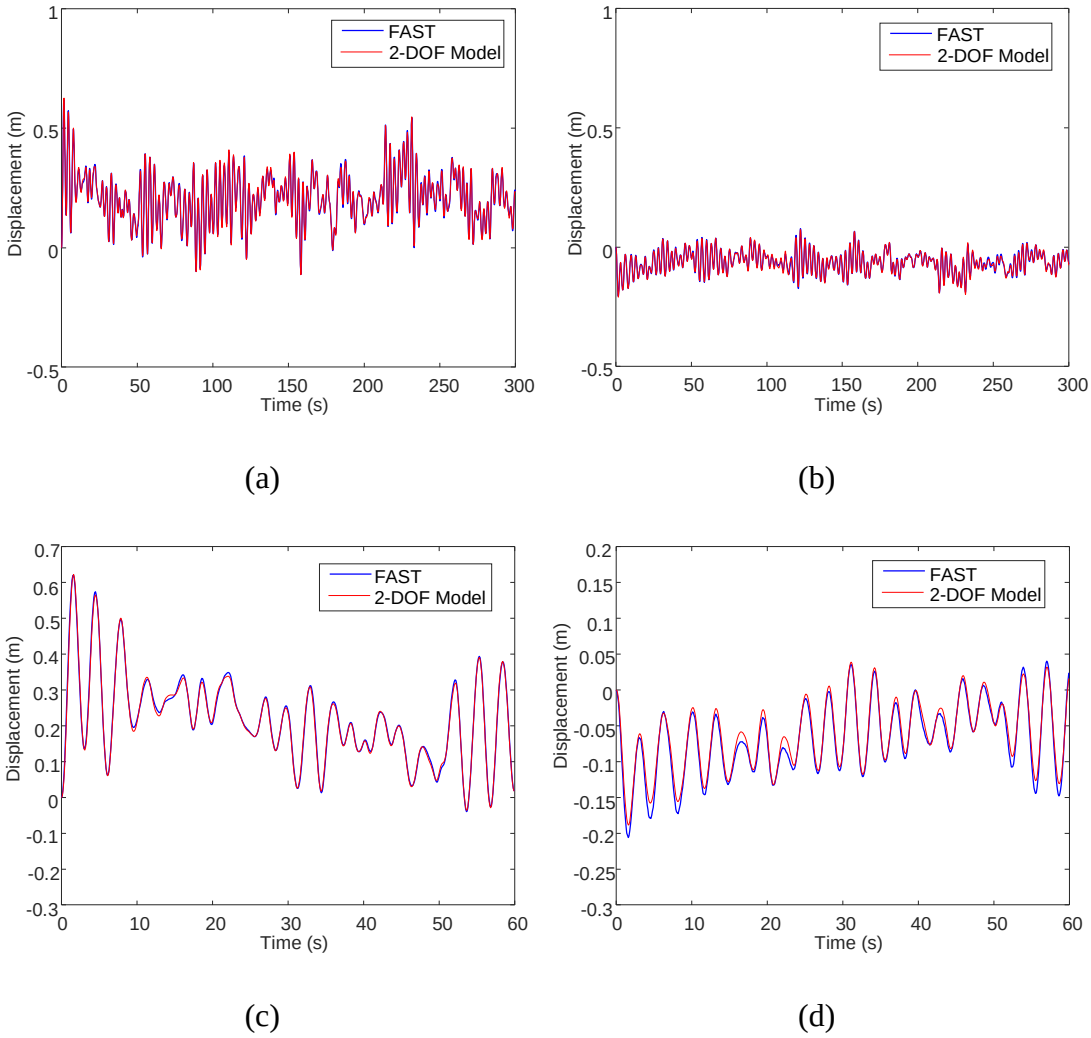

Figure 5-5. Comparison of the FA (a, c) and SS (b, d) responses from the 2-DOF model with the time-varying aerodynamic damping matrix and the FAST model; (c) and (d) are zooms of (a) and (b).

The influence of turbulence intensity was investigated. The same comparison procedure between the 2-DOF model with the constant aerodynamic damping matrix and the FAST model was carried out for wind fields of mean wind speed 20 m/s and turbulence intensity increased from 4% to 10% in 2% steps. As shown in Figure 5-6, the value of the similarity indicator is generally large when the turbulence intensity is large. When

the turbulence intensity is small, the aerodynamic damping in FAST is less varying as the variation in wind speed is smaller. Thus, this demonstrates that a constant aerodynamic damping matrix can better capture the dynamic response of wind turbines in a less turbulent wind field, resulting in smaller value of the similarity indicator when turbulence intensity is low.

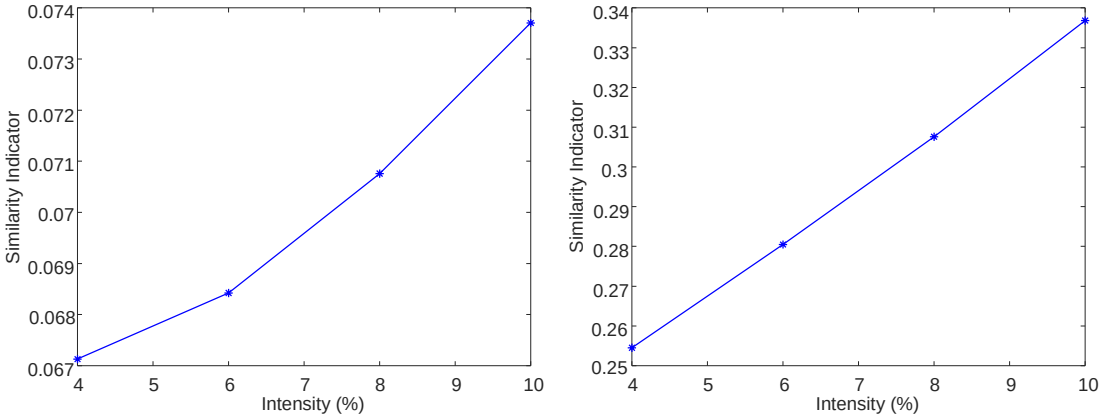

(a) (b)

Figure 5-6. Relationship between the turbulence intensity and similarity indicator value for FA (a) and SS (b) responses; similarity indicator value is calculated by comparing responses from the 2-DOF model with the constant aerodynamic damping matrix and the FAST model.

Then the relationship between the turbulence intensity and the time-varying damping matrix was studied by changing the intensity of the inflow uniform wind field from 2% to 20% in 2% steps, as shown in Figure 5-7. For every intensity, the mean values (red solid rectangulars) and the standard deviations (blue vertical lines with marks) of the four damping coefficients were calculated and are compared to the constant values. Figure 5-7 shows that the standard deviations of the damping coefficients increase when the turbulence intensity increases. The relative standard deviations of $\bar{c}_{xx}$ and $\bar{c}_{yy}$ (from 0.6% to 20.8%) are smaller compared to those of $\bar{c}_{xy}$ and $\bar{c}_{yx}$ (from 2.7% to 34.1%), meaning that the diagonal terms are less variable than the off-diagonal terms. The mean values of $\bar{c}_{xx}$ and $\bar{c}_{xy}$ are alwayes smaller or larger than the constant values, while the mean values of $\bar{c}_{yx}$ and $\bar{c}_{yy}$ fluctuate around the constant values.

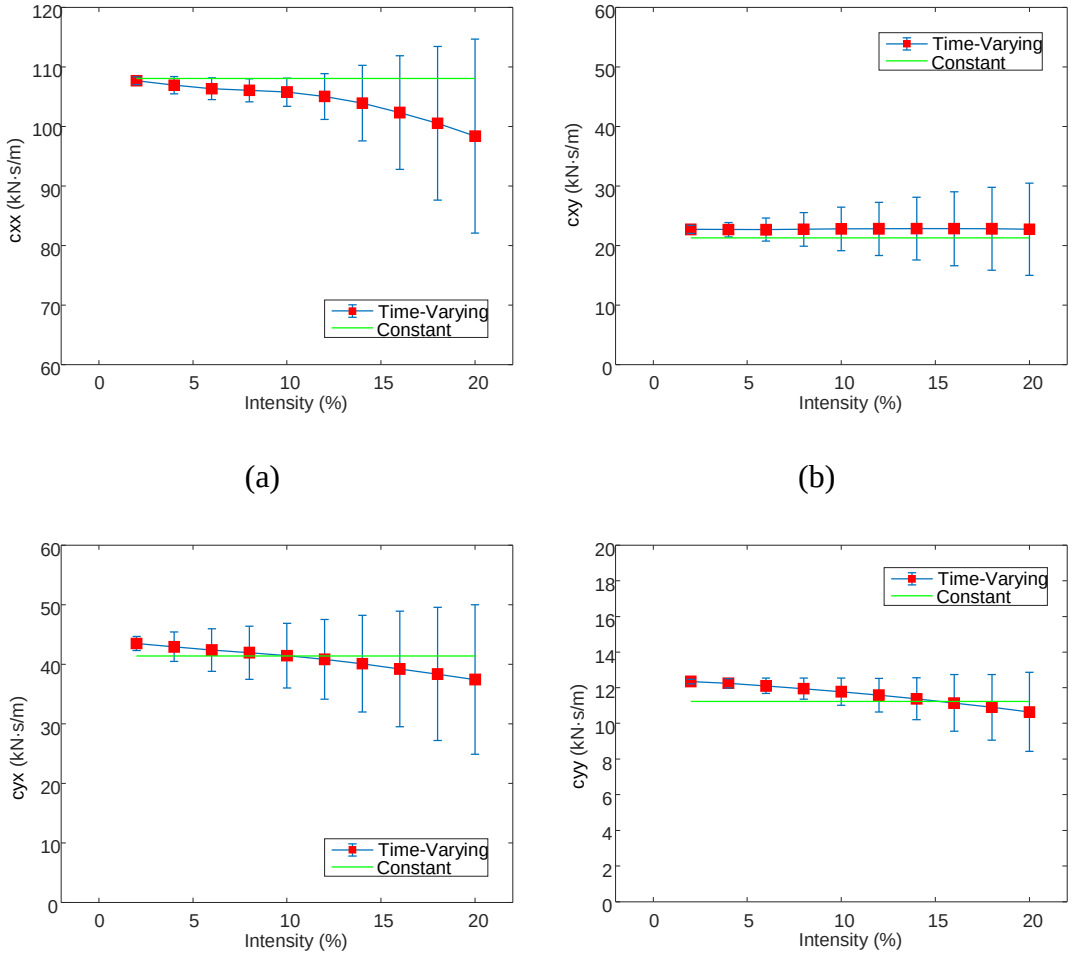

Figure 5-7. Relationship between the turbulence intensity and the mean values and standard deviations of $\bar{c}_{xx}$ (a), $\bar{c}_{xy}$ (b), $\bar{c}_{yx}$ (c) and $\bar{c}_{yy}$ (d); the mean values and standard deviations are calculated from the 2-DOF model with time-varying damping matrix with a uniform wind field.

5.4.3 Comparison between the 2-DOF model and the FAST model with non-uniform wind field

In this subsection, a comparison is then made between the FAST model and the 2-DOF model with the constant aerodynamic damping matrix for a non-uniform wind field. In the FAST model, the non-uniform inflow wind field with mean wind speed of 20 m/s was used as the input and the tower was allowed to vibrate in the FA and SS directions.

The wind field is divided into a 11×11 rectangular grid and the distance between adjacent two grid points is 20 m. The centre of the grid is at 90m height, which is close to the tower top at 87.6 m. This wind field was also generated by the customized turbulent wind field generator. For the 2-DOF model, the external modal forces used here were derived from the aerodynamic forces applied to the rigid tower considering the same inflow field as the FAST model. The response comparison shown in Figure 5-8 indicates that the FA and SS responses from these two models are close, with similarity indicators of 0.04 for the FA response and 0.14 for the SS response. For non-uniform wind fields, a constant aerodynamic damping matrix can sufficiently represent the damping characteristics of the wind turbine.

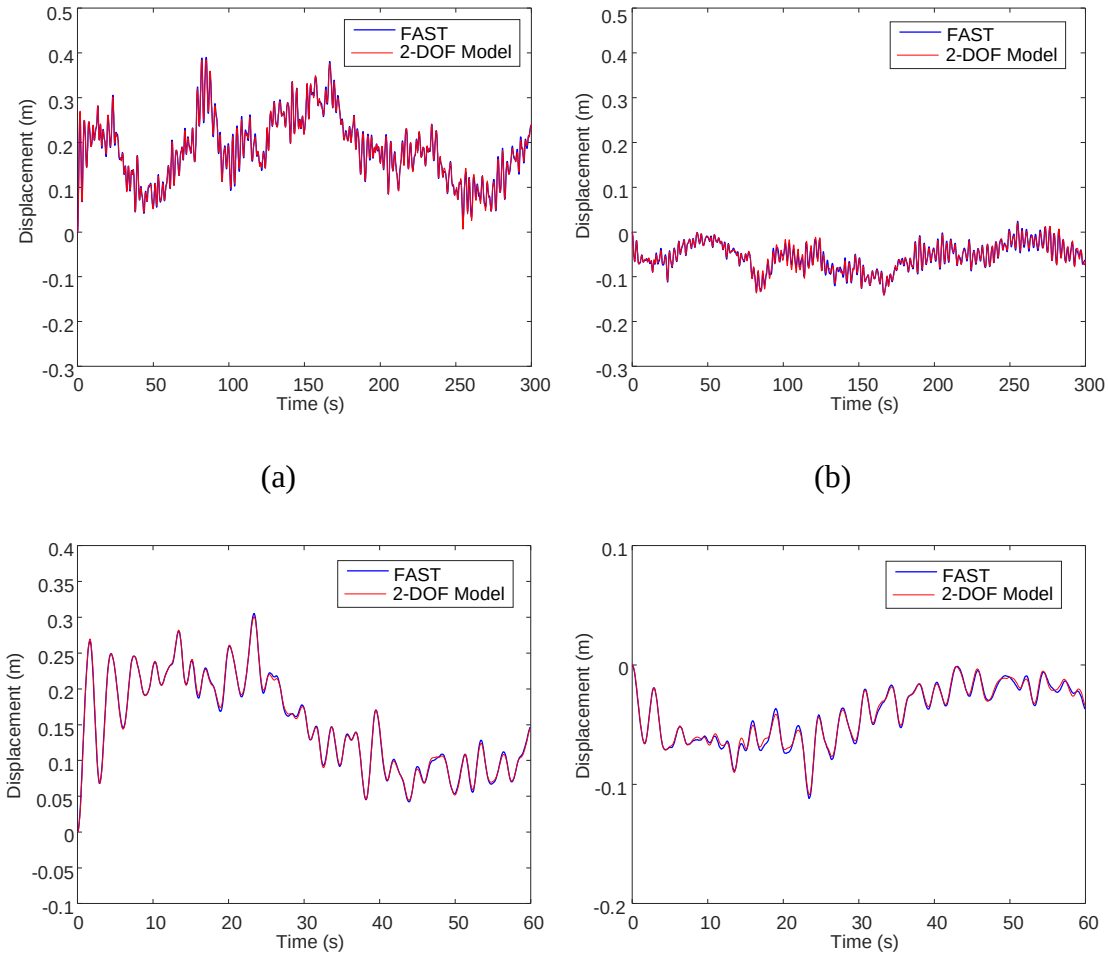

Figure 5-8. Comparison of the FA (a, c) and SS (b, d) responses from the 2-DOF model with the constant aerodynamic damping matrix and the FAST model when the inflow wind field is non-uniform; (c) and (d) are zooms of (a) and (b).

Then a comparison was made between the 2-DOF model with the time-varying aerodynamic damping matrix and the FAST model. The modal aerodynamic forces applied to the rigid tower and the time-varying modal aerodynamic damping were calculated using Equations (5-13) and (5-14) given the wind speeds at all grid points at every time step. Figure 5-9 shows that the time-varying damping terms fluctuate around the constant damping terms calculated from the mean wind speed. The variation of the diagonal terms $\bar{c}_{xx}$ and $\bar{c}_{yy}$ is less than that of the off-diagonal terms $\bar{c}_{xy}$ and $\bar{c}_{yx}$.

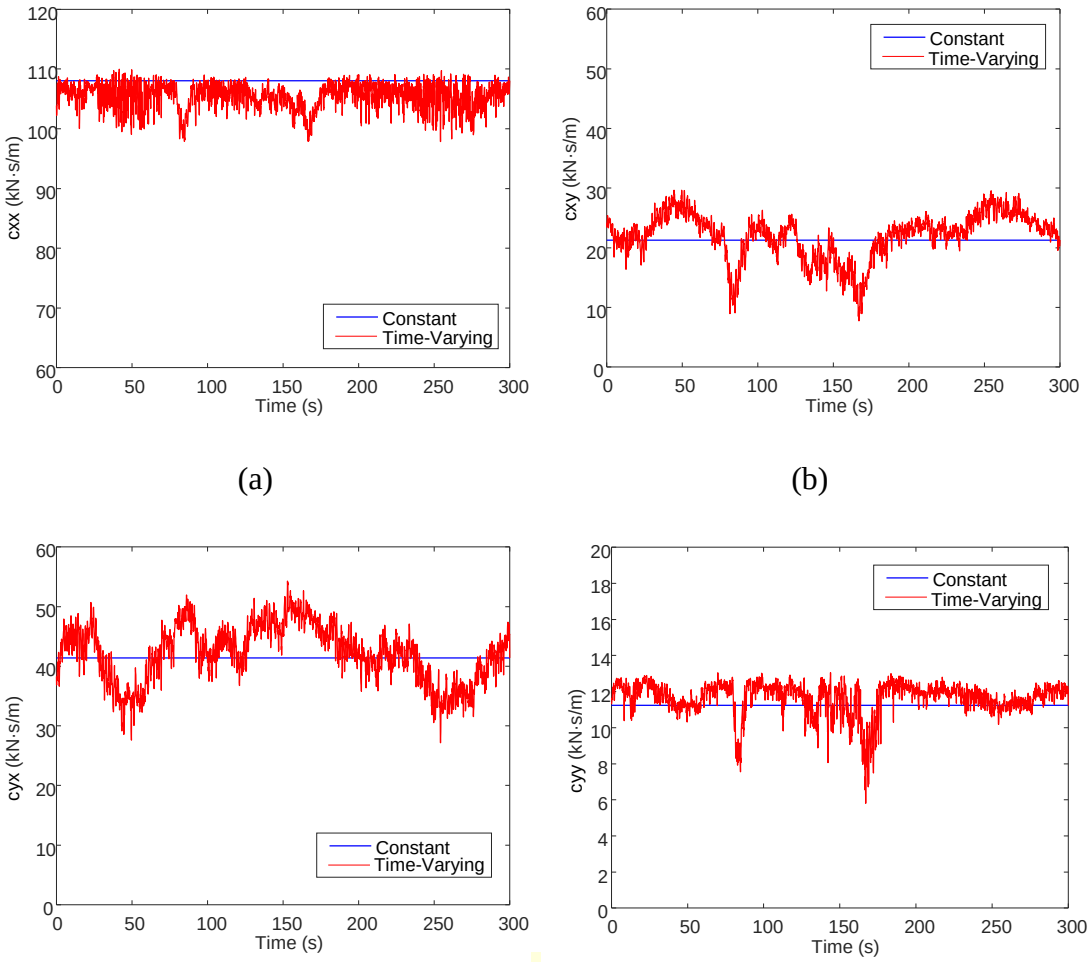

Figure 5-9. Comparison of $\bar{c}_{xx}$ (a), $\bar{c}_{xy}$ (b), $\bar{c}_{yx}$ (c) and $\bar{c}_{yy}$ (d) in the constant aerodynamic damping matrix and the time-varying aerodynamic damping matrix.

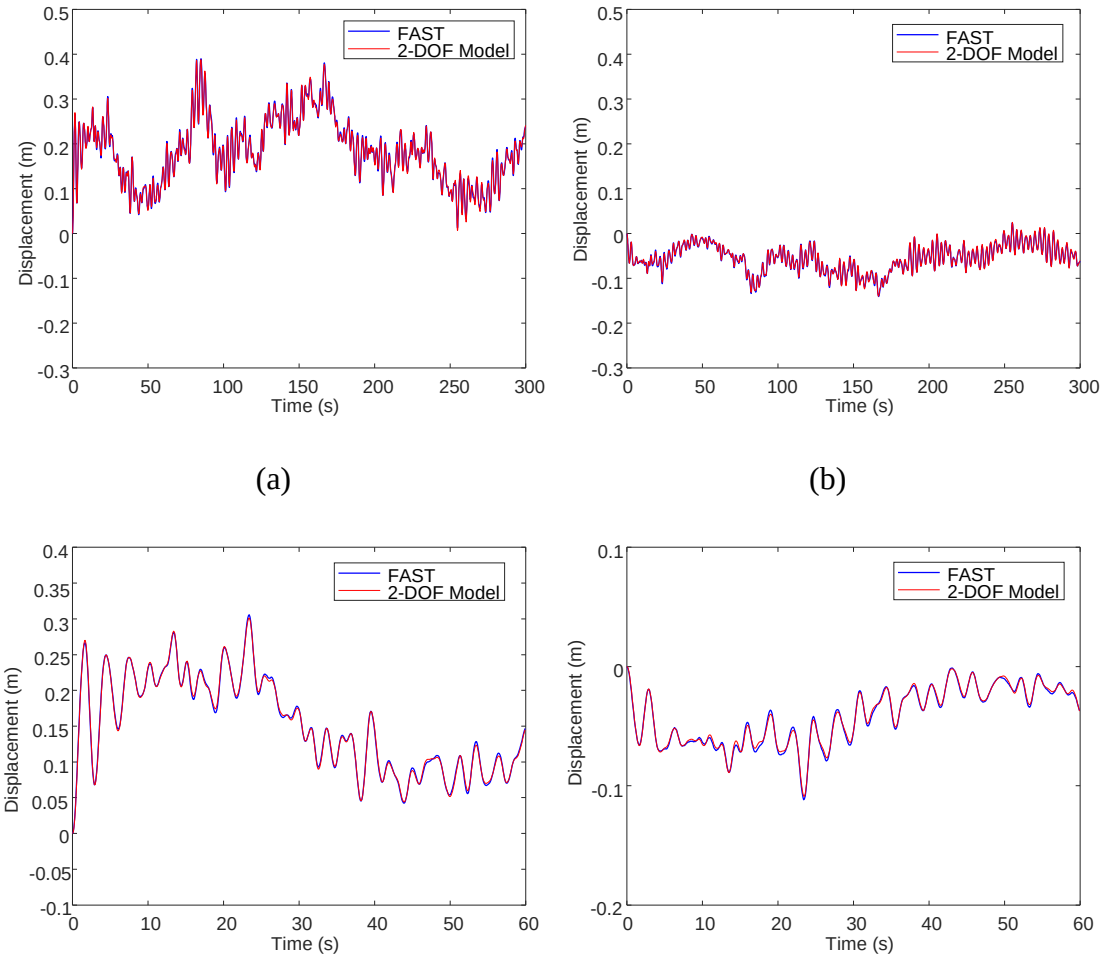

Figure 5-10. Comparison of the FA (a, c) and SS (b, d) responses from the 2-DOF model with the time-varying aerodynamic damping matrix and the FAST model when the inflow wind field in non-uniform; (c) and (d) are zooms of (a) and (b).

The damping coefficients in Figure 5-9 can be described statistically. The mean values of $\bar{c}_{xx}$ is 105.4 kN·s/m which is slightly lower than the constant value of 108.1 kN·s/m when the mean speed is 20 m/s. For the other three coefficients, their mean values are very close to the constant values. However, the off-diagonal coefficients are more variable compared to the diagonal coefficients, with standard deviations of 3.8 and 4.8 kN·s/m for $\bar{c}_{xy}$ and $\bar{c}_{yx}$ respectively compared to 2.1 and 0.9 kN·s/m for $\bar{c}_{xx}$ and $\bar{c}_{yy}$ respectively. The responses from the 2-DOF model and the FAST model are very close as shown in Figure 5-10. For these results, the similarity indicator are 0.04 and 0.06 for FA and SS motions respectively, which are smaller than the values related to the

previous results when comparing the 2-DOF model with the constant damping matrix and the FAST model in Figure 5-8. The smaller differences for the 2-DOF model with the time-varying damping matrix are expected as a time-varying damping matrix can better capture the aerodynamic forces at the tower top.

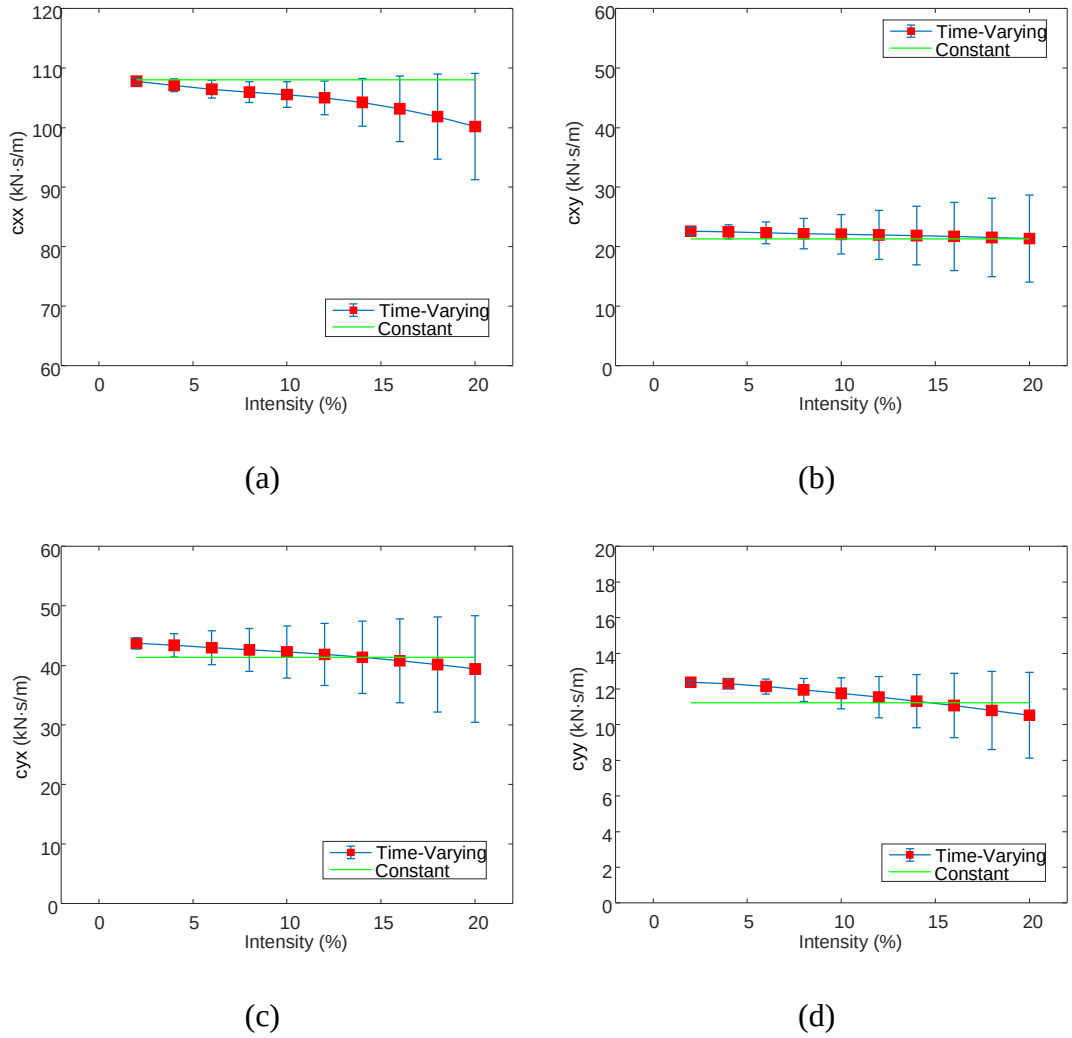

Figure 5-11. Relationship between the turbulence intensity and the mean values and standard deviations of $\bar{c}_{xx}$ (a), $\bar{c}_{xy}$ (b), $\bar{c}_{yx}$ (c) and $\bar{c}_{yy}$ (d); the mean values and standard deviations are calculated from the 2-DOF model with time-varying damping matrix with a non-uniform wind field.

The statistical properties of the time-varying damping matrix were also studied with different turbulence intensities of the non-uniform wind field from 2% to 20% in 2% steps, as shown in Figure 5-11. Overall, compared to the 2-DOF model with a uniform wind field, the damping coefficients in the 2-DOF model with a non-form wind field

are less variable. For example, the relative standard deviations of $\bar{c}_{xx}$ are from to 0.5% to 8.9%, a smaller range compared to the case with a uniform wind field. This is easy to interpret since a non-uniform wind field contains many grid points at which the instant wind speeds are averaged at every time step, resulting in less fluctuating damping coefficients. $\bar{c}_{xx}$ is the least variable parameter as the relative standard deviations of the other three damping coefficients are from 0.9% to 34%. However, the relationship between the mean values of the damping coefficients and the turbulence intensities is quite similar to that when the wind field is uniform. The mean values of $\bar{c}_{xx}$ are always smaller than the constant values while those of $\bar{c}_{xy}$ always larger; the mean values of $\bar{c}_{yx}$ and $\bar{c}_{yy}$ can be larger or smaller than the constant values.

5.4.4 Comparison between the 2-DOF model and the model with damping ratios

In the 2-DOF model, the modal aerodynamic damping matrix provides a novel description of the aerodynamic damping for operating wind turbines, different from the traditional description using damping ratios. Many researchers have given analytical expressions for the FA damping [73], while analytical expressions for both the FA and SS damping were only provided Valamanesh and Myers [70] and Equations (3-23) and (3-41) in this thesis. Comparison was made between the responses generated by the 2-DOF model with the constant aerodynamic damping matrix and the models with estimated damping ratios using the methods provided by these two papers. The derivation of damping ratios in [70] does not consider the difference in induction factors for different blade elements, but here this difference was considered by individually calculating relevant terms for each blade element and summing their values for one blade to obtain the damping ratio for the entire rotor. For a mean wind speed of 20 m/s, the response comparison is shown in Figure 5-12. Damping ratios estimated by the method by Valamanesh and Myers [70] and the method in Section 3.3 are identical, so the responses generated by these two models with damping ratios are identical. The FA responses generated from the models with damping ratios are very close to the 2-DOF model, with a similarity indicator of 0.13. However, the SS responses from the models with damping ratios indicate much lower SS aerodynamic damping when compared to the SS response from the 2-DOF model with a similarity indicator of 0.86. From Figure 5-3, we know the 2-DOF model is able to generate similar responses in both FA and SS directions compared to that from FAST, showing that the models with damping ratios perform worse with regard to the SS damping.

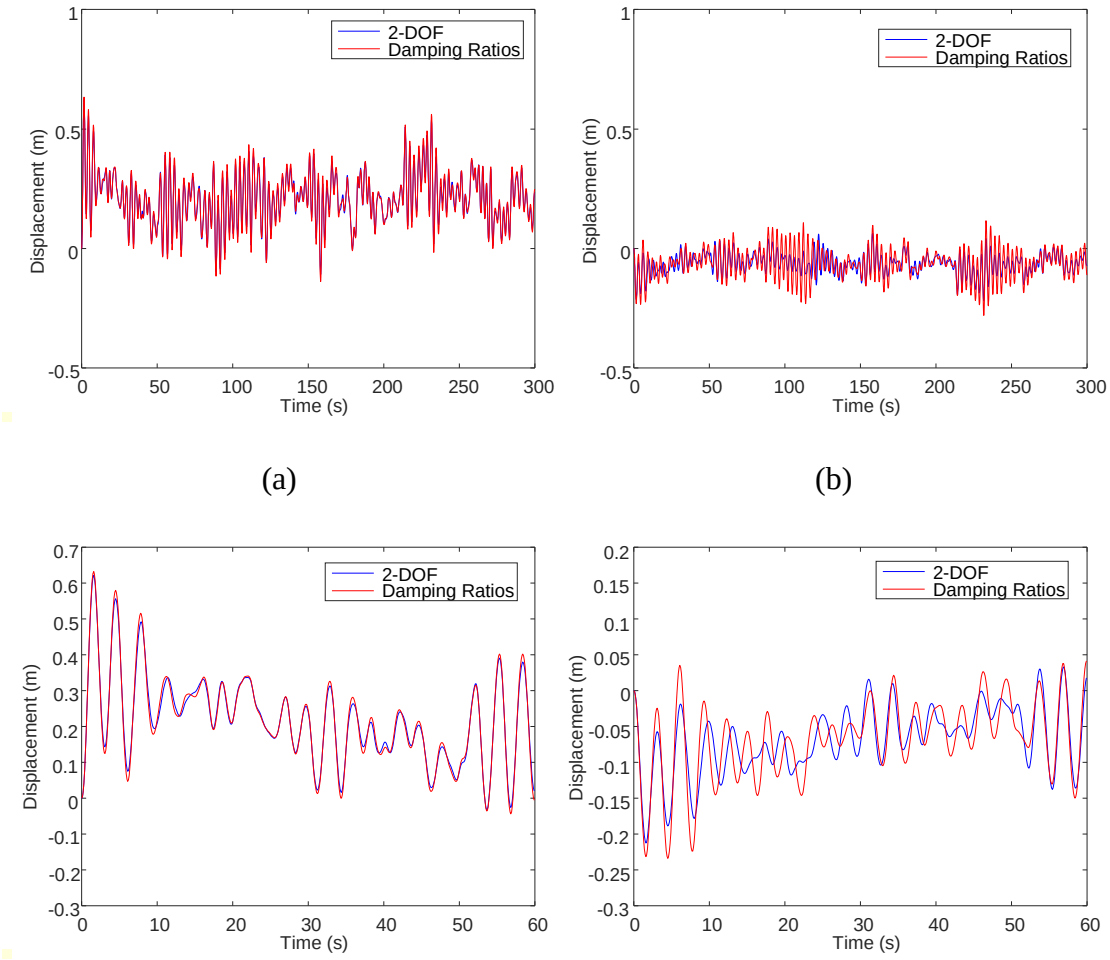

Figure 5-12. Comparison of the FA (a, c) and SS (b, d) responses from the 2-DOF model with the constant aerodynamic damping matrix and the model with estimated damping ratios; (c) and (d) are zooms of (a) and (b).

Overall, the verification results shown in this section demonstrate that the original model and the 2-DOF model are able to generate similar responses for the same input as the FAST model, confirming that the modal damping matrix in the 2-DOF model describes the aerodynamic damping in the wind turbine system sufficiently. On the other hand, the models with traditional aerodynamic damping ratios cannot describe the SS damping well. Thus, aerodynamic damping identification based on the aerodynamic damping matrix could be worthwhile.

5.5 Conclusion

This chapter presented an extension of the aerodynamic damping matrix considering wind turbulence. For a wind field uniformly distributed in the rotor plane, the form of the aerodynamic damping matrix follows what has been derived in Section 4.4. However, it requires some modifications to the derivation in Section 4.4 when considering a non-uniformly distributed wind field. The newly derived aerodynamic damping matrix in Section 5.2 is time-varying and more complex. It is found that the model with the original 4×4 aerodynamic damping matrix can be reduced to a 2-DOF model using partial modal decomposition.

The developed model with the original aerodynamic damping matrix and the 2-DOF model were verified with simulation results from FAST. It was found that when the wind field is uniformly distributed in the rotor plane but changes over time, assuming a constant aerodynamic damping matrix from the mean wind speed results in FA responses close to the responses from the FAST model. However, there are some difference in the SS direction. Using a time-varying damping matrix can reduce the difference for the SS motion. For a non-uniform wind field, comparison results show that the model with the constant aerodynamic matrix can generate responses sufficiently close to that from FAST, and a better approximation can be obtained using a time-varying aerodynamic damping matrix as expected. Additional comparison shows that a model with conventional damping ratios is able to generate similar responses in the FA direction but performs much worse in the SS direction. The model with aerodynamic damping matrix performs much better than the model with damping ratios by generating similar responses in both the FA and SS directions compared to those from FAST.

Chapter 6 - Novel Method for Aerodynamic Damping Identification

6.1 Introduction

According to the literature reviewed in Section 2.5, the identification of the aerodynamic damping of operating wind turbines in previous studies aimed at obtaining the damping ratios in the FA and SS directions separately. These studies implicitly assumed that the wind turbine system can be decoupled in terms of FA and SS motions as the damping identification techniques were applied on measured data only for the FA or SS direction. However, Chapters 4 and 5 showed that the rotating blades introduce significant damping coupling between the FA and SS directions for operating wind turbines. This finding leads to a different way of looking at the aerodynamic damping by introducing an aerodynamic damping matrix and casts some doubts on previous research as the wind turbine system behaves dynamically in a quite different way from that traditionally assumed by decoupled FA and SS motions. It was found that even for the simplest case where a free vibration decay superimposed on a steady-state operating regime (constant wind field), simply assigning two damping ratios in the FA and SS directions does not provide an adequate description of the dynamic behaviour of a wind turbine tower. These advances in the modelling of aerodynamic damping motivate the development of an identification method that directly extracts the aerodynamic damping matrix.

This chapter explores the possibilities for the identification of the aerodynamic damping matrix. Section 6.2 introduces the damping identification procedure and Section 6.3 provides the identification results using simulated data. Section 6.4 concludes this chapter.

6.2 Damping identification procedure

6.2.1 FRF-based damping identification method

Following the derivation in Sections 5.2 and 5.3, the aerodynamic damping can be expressed by either the original 4×4 aerodynamic damping matrix or the 2×2 modal aerodynamic damping matrix in the 2-DOF model. It is clear that it is easier to identify the 2×2 modal aerodynamic damping matrix as the 2-DOF model has only two DOFs.

However, the number of DOF of the FE model with the original 4×4 aerodynamic damping matrix is dependent on the number of beam element, which would complicate the identification of the 4×4 aerodynamic damping matrix. Further, identifying a modal damping matrix is of more interest as most conventional dynamic system identification methods aim at obtaining modal properties other than the physical stiffness, mass and damping matrices. As a result, the objective in this chapter is to identify the modal damping matrix $\bar{\mathbf{C}}$ in Equation (5-14) from measured responses in the FA and SS directions.

The strategy for doing this is different from traditional identification methods which usually aim at obtaining modal damping ratios and implicitly assume that the structure is classically damped (proportional damping). As the damping matrix to be identified is not symmetric, a more general damping identification matrix method proposed by Chen *et al*. [137] was used. This method estimates the damping matrix from the frequency response functions (FRFs) of the structure and assumes that the mass and stiffness matrices for the "undamped system" are already known. Chen *et al.*'s method is briefly described here as subsequent developments are based on it.

Given a dynamic system with mass, stiffness, and damping matrices $\mathbf{M}$, $\mathbf{K}$ and $\mathbf{C}$ excited by an external force $\mathbf{f}$, the equation of motion is

$$\mathbf{M}\ddot{\mathbf{u}} + \mathbf{C}\dot{\mathbf{u}} + \mathbf{K}\mathbf{u} = \mathbf{f}, \tag{6-1}$$

where $\mathbf{u}$ is the displacement vector. Rewriting this equation of motion in frequency domain,

$$(-\omega^2\mathbf{M} + i\omega\mathbf{C} + \mathbf{K})\mathbf{U}(\omega) = \mathbf{F}(\omega). \tag{6-2}$$

And the FRF matrix $\mathbf{H}(\omega)$ at frequency ω is defined as:

$$\mathbf{H}(\omega) = (-\omega^2\mathbf{M} + i\omega\mathbf{C} + \mathbf{K})^{-1}. \tag{6-3}$$

The "normal" FRF $\mathbf{H}^{\mathbf{N}}(\omega)$ is defined with the undamped system:

$$\mathbf{H}^{\mathrm{N}}(\omega) = [\mathbf{K} - \omega^2\mathbf{M}]^{-1}. \tag{6-4}$$

With the "normal" FRF, the frequency domain equation of motion can be written as

$$[\mathbf{H}^{\mathrm{N}}(\omega)]^{-1}\mathbf{U}(\omega) + i\omega\mathbf{C}\mathbf{U}(\omega) = \mathbf{F}(\omega), \tag{6-5}$$

or

$$\mathbf{U}(\omega) + i\mathbf{G}(\omega)\mathbf{U}(\omega) = \mathbf{H}^{N}(\omega)\mathbf{F}(\omega), \tag{6-6}$$

where

$$\mathbf{G}(\omega) = \omega \mathbf{H}^{N}(\omega)\mathbf{C}. \tag{6-7}$$

Therefore, the relationship between the measured FRF $\mathbf{H}(\omega)$ and the "normal" FRF $\mathbf{H}^{\mathrm{N}}(\omega)$ is

$$\mathbf{H}^{N}(\omega) = [\mathbf{I} + i\mathbf{G}(\omega)]\mathbf{H}(\omega), \tag{6-8}$$

where $\mathbf{I}$ is an identity matrix. Since $\mathbf{H}^{N}(\omega)$ and $\mathbf{G}(\omega)$ are real matrices, the imaginary part of the RHS in the above equation is zero, giving

$$\mathbf{G}(\omega) = -\mathrm{im}\big(\mathbf{H}(\omega)\big)\big[\mathrm{Re}\big(\mathbf{H}(\omega)\big)\big]^{-1}. \tag{6-9}$$

Finally, the damping matrix at any given frequency can be expressed by

$$\mathbf{C} = \frac{1}{\omega}[\mathbf{H}^{\mathbf{N}}(\omega)]^{-1}\mathbf{G}(\omega). \tag{6-10}$$

This damping identification method needs prior knowledge of the stiffness and mass matrices and the measurement of a full FRF matrix.

Now rewrite Equation (5-13) in a simplified form by denoting the modal external forces in the FA and SS directions as $\bar{f}_x^{Rigid}(t) = \phi_{x1}F_x^{Rigid}(t) + \phi_{x2}M_y^{Rigid}(t)$ and $\bar{f}_y^{Rigid}(t) = \phi_{y1}F_y^{Rigid}(t) + \phi_{y2}M_x^{Rigid}(t)$ respectively, and assuming the modal shape factors $\phi_{x1} = \phi_{y1} = 1$. Then the equations of motion of the 2-DOF system can be written as follow:

$$\begin{bmatrix} \bar{m}_x & 0 \\ 0 & \bar{m}_y \end{bmatrix}\begin{bmatrix} \ddot{x}(t) \\ \ddot{y}(t) \end{bmatrix} + \begin{bmatrix} \bar{c}_{xx} + \bar{s}_x & \bar{c}_{xy} \\ \bar{c}_{yx} & \bar{c}_{yy} + \bar{s}_y \end{bmatrix}\begin{bmatrix} \dot{x}(t) \\ \dot{y}(t) \end{bmatrix} + \begin{bmatrix} \bar{k}_x & 0 \\ 0 & \bar{k}_y \end{bmatrix}\begin{bmatrix} x(t) \\ y(t) \end{bmatrix} = \begin{bmatrix} \bar{f}_x^{Rigid}(t) \\ \bar{f}_y^{Rigid}(t) \end{bmatrix}, \tag{6-11}$$

where $x(t) = \phi_{x1}\alpha_x(t)$ and $y(t) = \phi_{y1}\alpha_y(t)$ are the FA and SS displacements respectively. In this 2-DOF model, the 2×2 FRF matrix $\mathbf{H}(\omega)$ can be expressed as

$$\mathbf{H}(\omega) = \begin{bmatrix} H_{xx}(\omega) & H_{xy}(\omega) \\ H_{yx}(\omega) & H_{yy}(\omega) \end{bmatrix}, \tag{6-12}$$

where the term H_{xy} represents the harmonic response in the x (FA) direction caused by a single harmonic force applied in the y (SS) direction and other terms following this convention. Once $\mathbf{H}(\omega)$ is obtained, $\mathbf{G}(\omega)$ can be calculated using Equation (6-9). The modal stiffnesses and masses, and the mode shapes in Equation (6-11) can be obtained

by traditional OMA methods on a parked turbine, from which $\mathbf{H}^{\mathrm{N}}(\omega)$ can be determined. Then the damping matrix can be obtained by averaging the calculated frequency-dependent damping terms using Equation (6-10).

Two methods to obtain the FRFs were investigated. The first method uses responses only caused by the wind loading, while in the second method the FRF matrix is obtained using responses caused by the combination of wind loading and a series of harmonic forces. The former method only requires the installation of sensors to measure the vibration response, which is easier to implement as no additional equipment is needed to generate controlled excitations. In contrast, the second method is closer to conventional experimental modal analysis (EMA). The details of these two methods are given in the following two subsections. The introduction of the second method is because the first method is unable to accurately estimate the aerodynamic damping matrix when using data from FAST, which will be shown in Subsection 6.3.2.

6.2.2 FRF measurement using responses caused by wind loading only

The FRF matrix can be estimated given the input and output time series for a typical stationary random process. Denoting the input force vector as $\mathbf{F}(t)$ and the output displacement vector as $\mathbf{U}(t)$, the relationship between the input and output can be written in the frequency domain as $\mathbf{U}(\omega) = \mathbf{H}(\omega)\mathbf{F}(\omega)$, where $\mathbf{U}(\omega)$ and $\mathbf{F}(\omega)$ are the Fourier transforms of $\mathbf{F}(t)$ and $\mathbf{U}(t)$ respectively and $\mathbf{H}(\omega)$ is the FRF matrix. According to Bendat and Piersol [138], for a multiple-input multiple-output (MIMO) system, $\mathbf{H}(\omega)$ can be calculated by

$$\mathbf{H}(\omega) = \mathbf{G}_{fu}^{T}\left(\mathbf{G}_{ff}^{-1}\right)^{T}, \tag{6-13}$$

where $\mathbf{G}_{fu}$ is the cross spectral density (CSD) matrix of $\mathbf{F}(t)$ and $\mathbf{U}(t)$ and $\mathbf{G}_{ff}$ is the CSD matrix of $\mathbf{F}(t)$. For instance, the CSD matrix of the external forces in Equation (6-11) is a 2 ×2 matrix, which is constructed storing the cross spectral densities between the FA force $\bar{f}_x^{Rigid}(t)$ and the SS force $\bar{f}_y^{Rigid}(t)$ as the off-diagonal terms, and the auto spectral densities of these two forces as the diagonal terms.

For the 2-DOF system, the FRF matrix can be obtained using the following steps:

1. Measure the inflow wind speed $\mathbf{W}(t)$ and the displacements of the tower top $\mathbf{U}(t)$ in the FA and SS directions.

2. Subtract the tower motions from the inflow wind speed to obtain the inflow wind speed acting on a rigid tower/rotor $\mathbf{W}^{Rigid}(t)$. Calculate the aerodynamic forces $F_x^{Rigid}(t)$, $F_y^{Rigid}(t)$, $M_x^{Rigid}(t)$and $M_y^{Rigid}(t)$ using the BEM code with $\mathbf{W}^{Rigid}(t)$.
3. With the two inputs and two outputs for the 2-DOF system obtained, *i.e.* the input external forces $\bar{f}_x^{Rigid}(t)$and $\bar{f}_y^{Rigid}(t)$, and the output displacement time-series in FA and SS directions $x(t)$ and y(t), the transfer functions $\mathbf{H}(\omega)$ can be estimated using Equation (6-13).

In practice, displacement responses can readily be obtained from simulations or acceleration measurements. However, input aerodynamic forces cannot easily be measured so some method must be devised to estimate them in an experimental context.

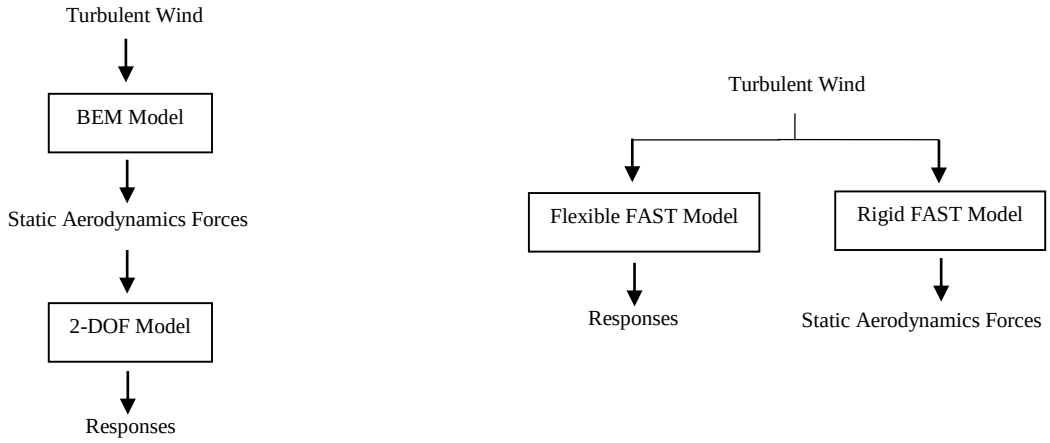

(a) (b)

Figure 6-1. Schematic for the data generation processes using data generated by the 2-DOF model (a) and FAST model (b).

Two computational schemes were devised to obtain the required input forces and output responses in order to identify the damping based on the FRF measurement method. The first process is based on the data generated by the 2-DOF model with the modal aerodynamic damping matrix (constant or time-varying) introduced in Section 5.3, while the second process is based on the data generated by the FAST model. These are shown diagrammatically in Figure 6-1. In the first process (Figure 6-1(a)), the inflow wind time series are generated from a Kaimal spectrum and the forces time series (thrust

and moment) are calculated using a customised BEM MATLAB code that converts the wind speed into forces. The generated aerodynamic forces are regarded as forces applied on a rigid tower of the original model. For the 2-DOF model, the thrust and moment need to be multiplied by the mode shapes to obtain the modal forces and then applied to the 2-DOF model. The outputs are the two responses in FA and SS directions.

In the second simulation process (Figure 6-1(b)), both the aerodynamic loading and the responses are directly obtained from FAST simulations. This approach should arguably produce more realistic data. In order to make the FAST model closer to the MATLAB models, specific settings for the simulations were used in FAST. First, the inflow wind field assumes wind velocities only in the FA direction. Second, the pitch angle and the rotor speed were kept constant during the whole simulation. These can be influenced by the control system in reality. In the FAST process, the turbulent wind field was produced from a Kaimal spectrum using the wind field generator described in Subsection 5.4.1. This turbulent field was then applied to two FAST models. FA and SS tower motions were allowed in the first model named "flexible FAST model" but disabled in the second model named "rigid FAST model". The second setting is to obtain the "static aerodynamic forces" applied to a rigid tower. In reality, the static aerodynamic forces can only be estimated from the absolute wind speed seen by the rotor. In the calculation of the CSD matrices, the inputs are the responses from the flexible model and the static aerodynamic forces from the rigid model.

6.2.3 FRF measurement using responses caused by harmonic excitations

Traditional EMA uses harmonic forces as external excitations was considered [139]. For external excitations with controlled frequencies applied to the wind turbine, the FRF matrix can be obtained from the steady state responses. For frequency ω, Equation (6-14) below can be used to calculate the corresponding frequency point in the FRF matrix:

$$H_{ij}(\omega) = \frac{U_i(\omega)}{F_j(\omega)}, \tag{6-14}$$

where $H_{ij}(\omega)$ refers to the frequency response at location i due to the force applied at location j. For example, the component $H_{xy}(\omega)$ in Equation (6-12) is calculated by the FFT of the response in the FA direction, $U_x(\omega)$ divided by the FFT of the external harmonic force, $F_y(\omega)$ at frequency ω. In the FAST model which can be represented

as a 2-DOF system (as similar responses can be produced from the 2-DOF model compared to FAST responses), it is required to apply the excitation in FA and SS directions separately and measure the responses in FA and SS directions. With the applied excitations and measured responses, all four FRFs can be obtained. The response of an operating wind turbine is caused by the combination of the aerodynamic loading and the harmonic excitation at a particular frequency. The harmonic excitation must be large enough so that it produces a discernible component at that frequency in the response spectrum. This FRF "measurement" was conducted using data from the open-source package OpenFAST by NREL [140]. Additional code was written into the source code of OpenFAST to allow harmonic forces to be applied at the tower top with different frequencies and amplitudes. These forces can be separately applied in the FA/SS directions. The modified OpenFAST code was then compiled using Microsoft Visual Studio 2015 to generate a new FAST executable file, from which the dynamic responses of wind turbines can be obtained and used to calculate the FRF matrix.

6.3 Identification results

In this section, the NREL 5 MW reference onshore wind turbine introduced in Chapters 4 and 5 was used to test the identification process developed in the previous section. Using modal decomposition in Section 5.3, the corresponding 2-DOF model can be obtained. The modal mass matrix is

$$\begin{bmatrix} 1834 & 0 \\ 0 & 1834 \end{bmatrix} (kN/m).$$

The modal stiffness matrix is

$$\begin{bmatrix} 3990 & 0 \\ 0 & 3900 \end{bmatrix} (kN \cdot s^2/m).$$

The modal stiffness and mass matrices for the 2-DOF model were assumed known before the estimation of damping matrix. Zero structural damping is assumed throughout this chapter as the focus is on the identification of aerodynamic damping. It was proved in Section 5.4 that a constant modal aerodynamic damping matrix is sufficient to characterise the aerodynamic damping in wind turbines for both uniform and non-uniform turbulent wind fields. Therefore, for simplicity the constant modal aerodynamic damping matrix is the target to identify other than a time-varying damping matrix.

6.3.1 Results by FRF measurements using responses caused by wind loading only

Data generated by the 2-DOF model

The case with a mean wind speed of 20 m/s and a turbulence intensity of 10% is still used as an example to demonstrate the identification results. Using the processes described in Section 5.3, the modal aerodynamic modal damping matrix of the 2-DOF model were obtained. The calculated aerodynamic damping matrix is

$$\begin{bmatrix} 108.1 & 21.3 \\ 41.4 & 11.2 \end{bmatrix} (kN \cdot s/m),$$

which is the target to identify. This modal aerodynamic damping matrix was set constant in the 2-DOF model in MATLAB to generate the displacement time series.

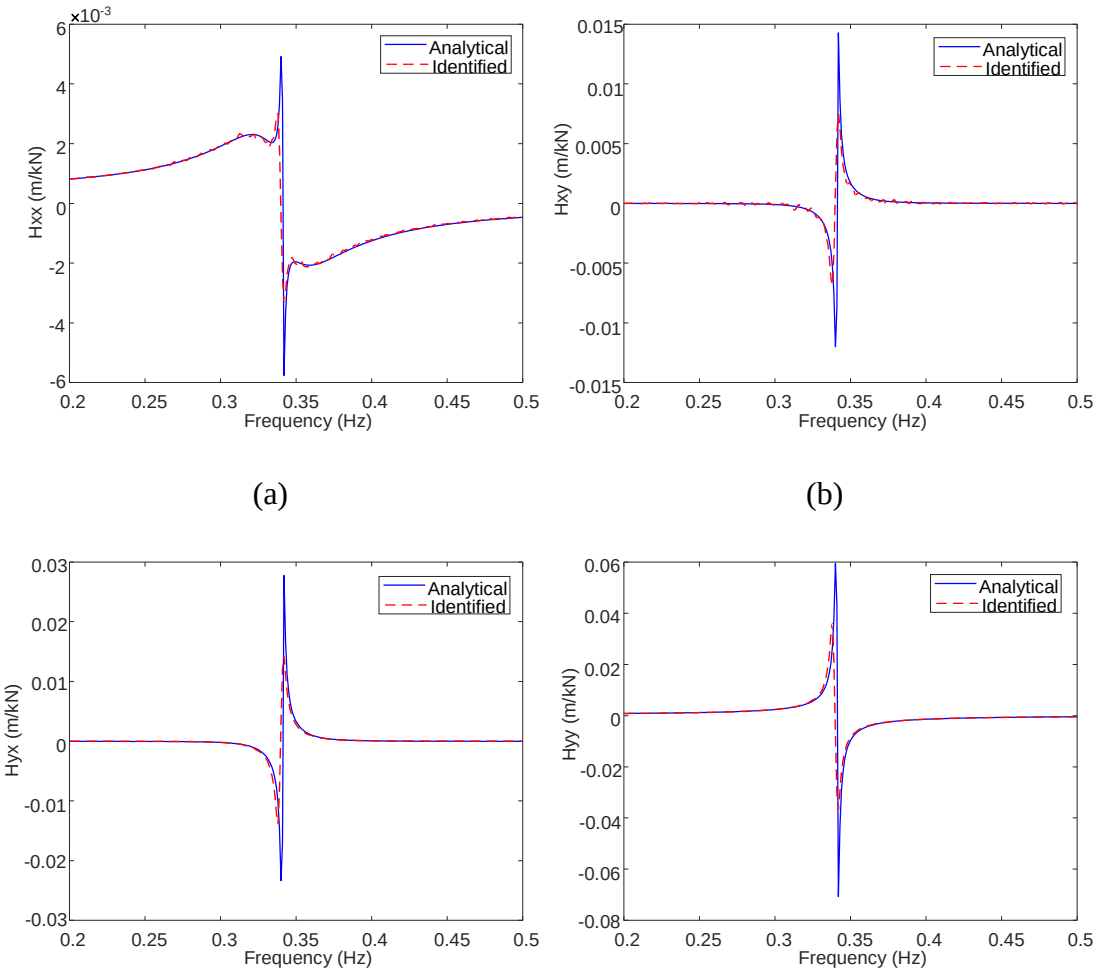

Figure 6-2. Comparison the real part of analytical and identified H_{xx} (a), H_{xy} (b), H_{yx} (c) and H_{yy} (d) with data from the 2-DOF model.

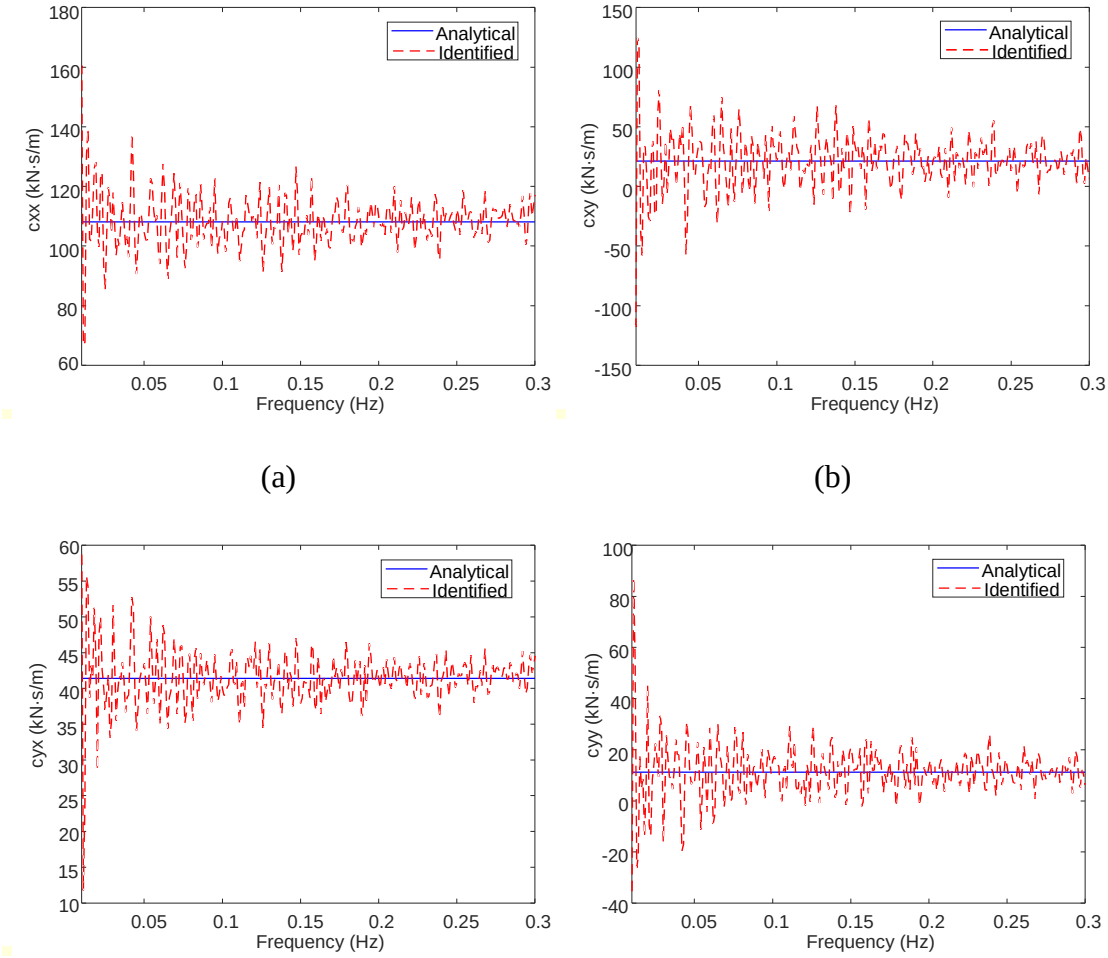

Figure 6-3. Comparison of the analytical and identified frequency-dependent $\bar{c}_{xx}$ (a), $\bar{c}_{xy}$ (b); $\bar{c}_{yx}$ (c) and $\bar{c}_{yy}$ (d) with data from the 2-DOF model.

The CSD matrices were calculated from the displacement and force time series as described in Subsection 6.2.2. In the next step, the FRFs from the CSD matrices were calculated following Equation (6-13). During the calculation of the FRFs, some issues needed to be addressed. First, significant correlation between the two inputs to the 2-DOF model (thrust and torque both generated by the same turbulent wind field) causes errors in the FRF estimation [138]. Second, a leakage error (caused by systematic error in PSD calculation as a result of the finite length of time series [141]) was observed when the length of measured time series is not long enough (*e.g.* less than 30 min). These errors can be reduced using a window function for the PSD calculation and a longer time series. Hamming windows whose length are 1/8 of the length of the input

time series were used here. In practice a longer time series is a limitation, but as the damping identification is an operational identification method, long-time monitored data can be available (but might vary due to change of mean wind speed). The estimation results of the real part of the FRFs are shown in Figure 6-2, compared with the analytical results. Overall the estimation results agree well with the analytical results. The estimation of the FRFs was obtained by averaging 10 simulations of 1-hour duration. For larger simulation numbers and durations, the estimation of damping parameters becomes more accurate.

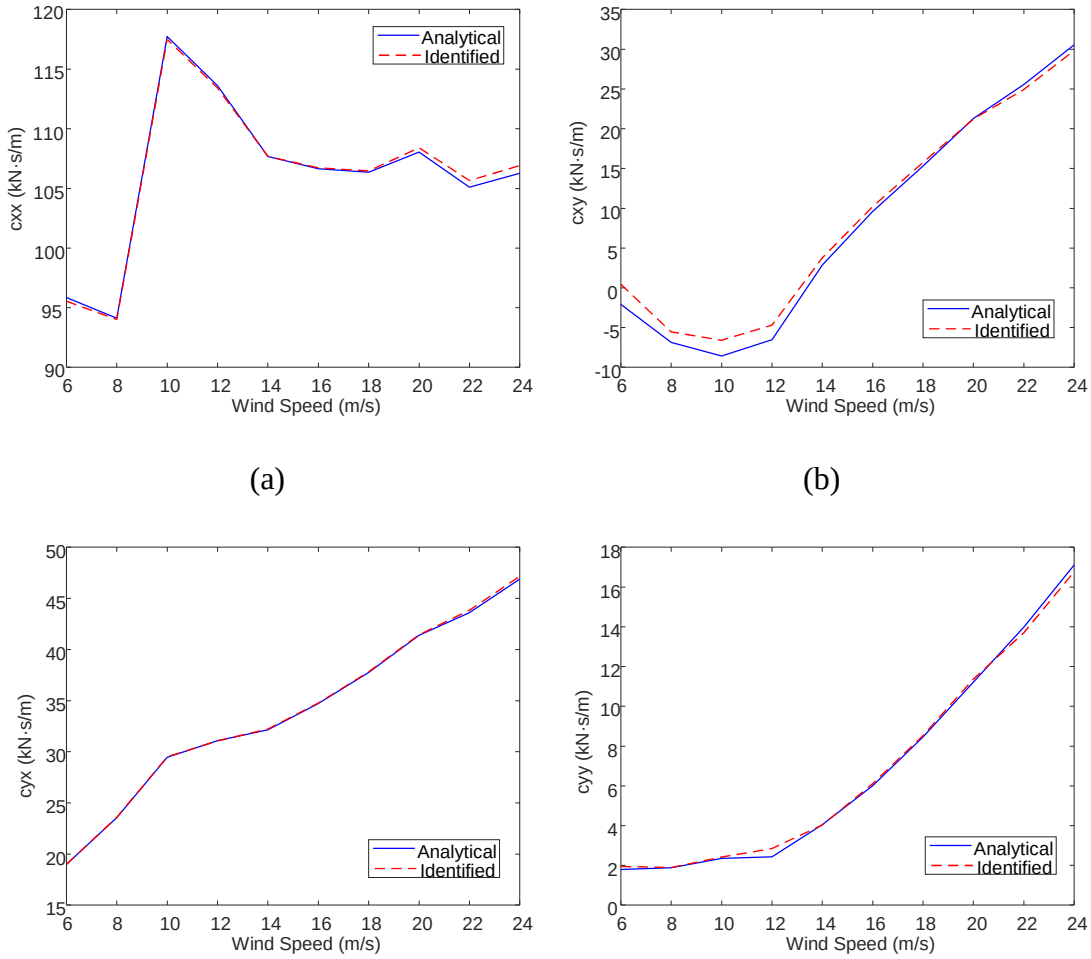

Figure 6-4. Comparison of the analytical and identified $\bar{c}_{xx}$ (a), $\bar{c}_{xy}$ (b); $\bar{c}_{yx}$ (c) and $\bar{c}_{yy}$ (d) with wind loading only and uniform wind field for the mean wind speeds from 6 m/s to 24 m/s in 2 m/s steps; response data is from the 2-DOF model.

Obtaining the FRFs for the 2-DOF model, the damping matrix was estimated following

the method by Chen *et al.*'s Method introduced in Subsection 6.2.1. The estimated frequency-dependent damping matrix is shown in Figure 6-3, fluctuating around the analytical solution. There are some peaks near the resonance in the identified frequency-dependent damping terms, especially for $\bar{c}_{xx}$ in Figure 6-3(a) and $\bar{c}_{yx}$ in Figure 6-3(c). These peaks can be related to the estimated FRFs which have some difference near the resonance frequency compared to the analytical values as shown in Figure 6-2. Averaging the frequency-dependent matrix from 0.01 Hz to 0.3 Hz, an estimation of the aerodynamic damping matrix can be obtained as

$$\begin{bmatrix} 108.4 & 21.2 \\ 41.5 & 11.4 \end{bmatrix} (kN \cdot s/m).$$

The frequency range for averaging from 0.01 Hz to 0.3 Hz has been tested for a wide range of parameters to obtain reliable averaged damping coefficients. This frequency range includes most the power in the spectrum of turbulent wind as shown in Figure 5-1, except the initial small range from 0 Hz to 0.01 Hz in which the estimated damping values undergo very large variation. The estimated aerodynamic matrix is close to the analytical values with percentage differences for the four damping coefficients:

$$\begin{bmatrix} 0.3 & -0.3 \\ -0.2 & 1.2 \end{bmatrix} (\%).$$

For mean wind speeds in the range of 6 m/s to 24 m/s in 2 m/s steps, more identification tests were carried out. As shown in Figure 6-4, good agreements between the analytical and identified values can also be found.

Data generated by the FAST model

Following the FAST data generation process described in Subsection 6.2.2, an example with mean wind speed of 20 m/s is presented. Again, 10 simulations of 1-hour duration were averaged to obtain the FRF estimation. The real part of the FRFs is shown in Figure 6-5, and the corresponding damping matrix estimation is shown in Figure 6-6. It can be seen that the estimation of the FRF is not very accurate. The damping calculation gave the averaged modal aerodynamic damping coefficients as

$$\begin{bmatrix} 92.3 & 154.6 \\ -19.3 & 215.9 \end{bmatrix} (kN \cdot s/m).$$

The percentage difference to the analytically derived matrix is

$$\begin{bmatrix} -14.5 & 627 \\ -146 & 1822 \end{bmatrix} (\%),$$

showing that the identified values do not agree well with the expected values.

For the data generated by FAST with turbulent wind excitation, the calculated FRF matrix is very noisy and does not show a good agreement with the calculated FRF matrix of the 2-DOF model using theoretical derivations. Similar FRF estimation errors were obtained from responses generated by the 2-DOF model with time-varying damping matrix, demonstrating that the variation of the aerodynamic damping in operating wind turbines causes this difference.

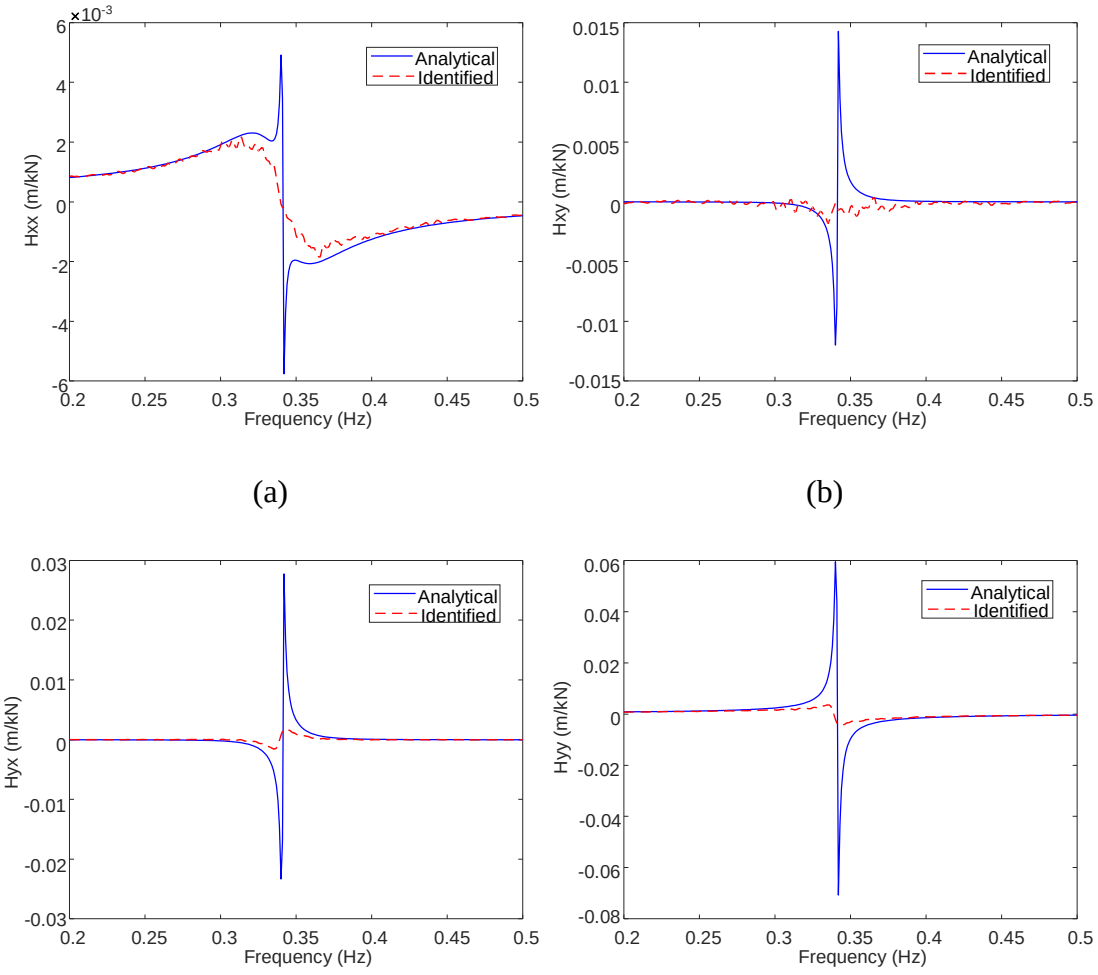

Figure 6-5. Comparison the real part of analytical and identified H_{xx} (a), H_{xy} (b), H_{yx} (c) and H_{yy} (d) with data from the FAST model.

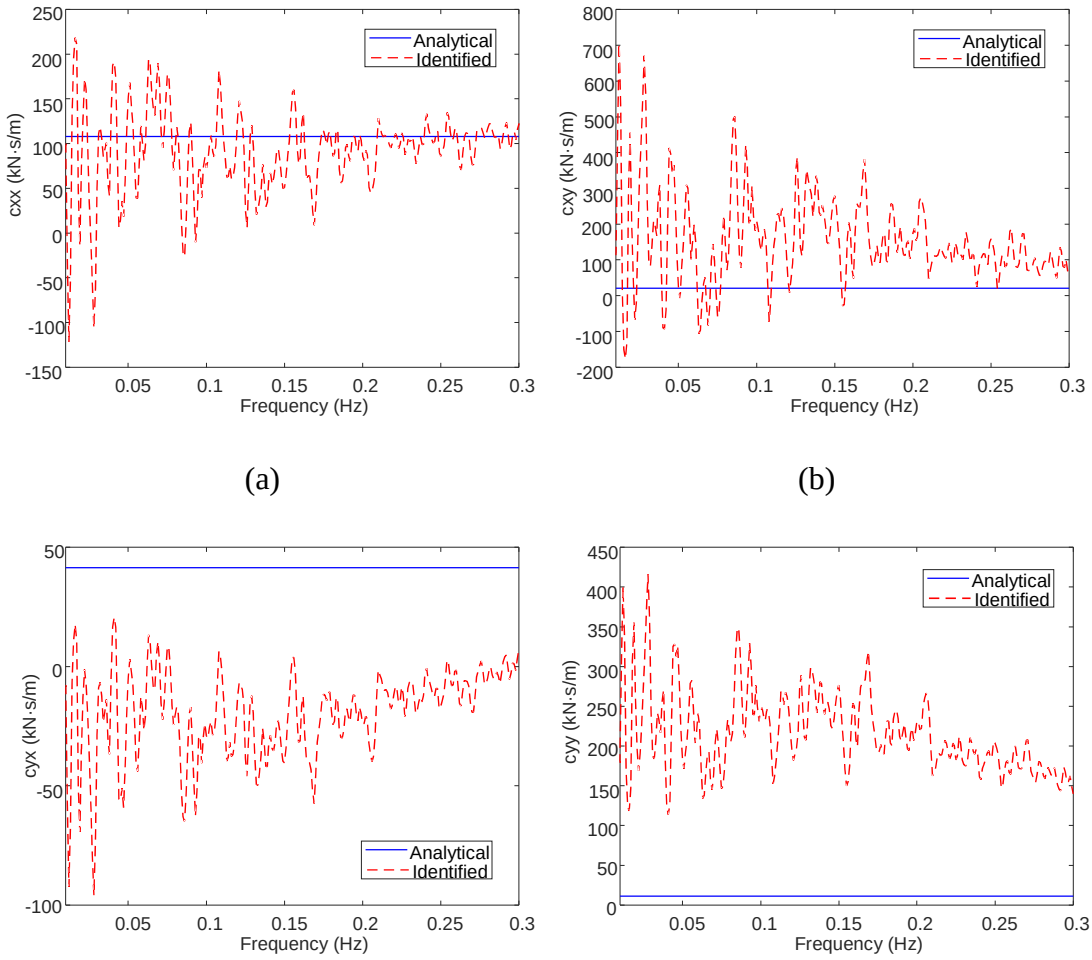

Figure 6-6. Comparison of the analytical and identified frequency-dependent $\bar{c}_{xx}$ (a), $\bar{c}_{xy}$ (b); $\bar{c}_{yx}$ (c) and $\bar{c}_{yy}$ (d) with data from the FAST model.

Damping identification tests with additional parameters

As discussed in the previous content in this section, the aerodynamic damping identification based on FRF measurements described by Subsection 6.2.2 works well when using data generated by the 2-DOF model with the constant damping matrix in MATLAB but does not work well when using data from FAST or data from the 2-DOF model with time-varying damping matrix. It is valuable to test the identification method with more parameters such as the turbulence intensity and the simulation length. For instance, keeping the mean wind speed as 20 m/s, the turbulence intensity of the inflow wind was changed from 2% to 20% with 2% increment. In this way, the variation of the input force to the 2-DOF model increases when the turbulence intensity increases.

Using the responses generated by the 2-DOF model with different turbulence intensities, the aerodynamic damping coefficients were calculated and compared to the analytical values.

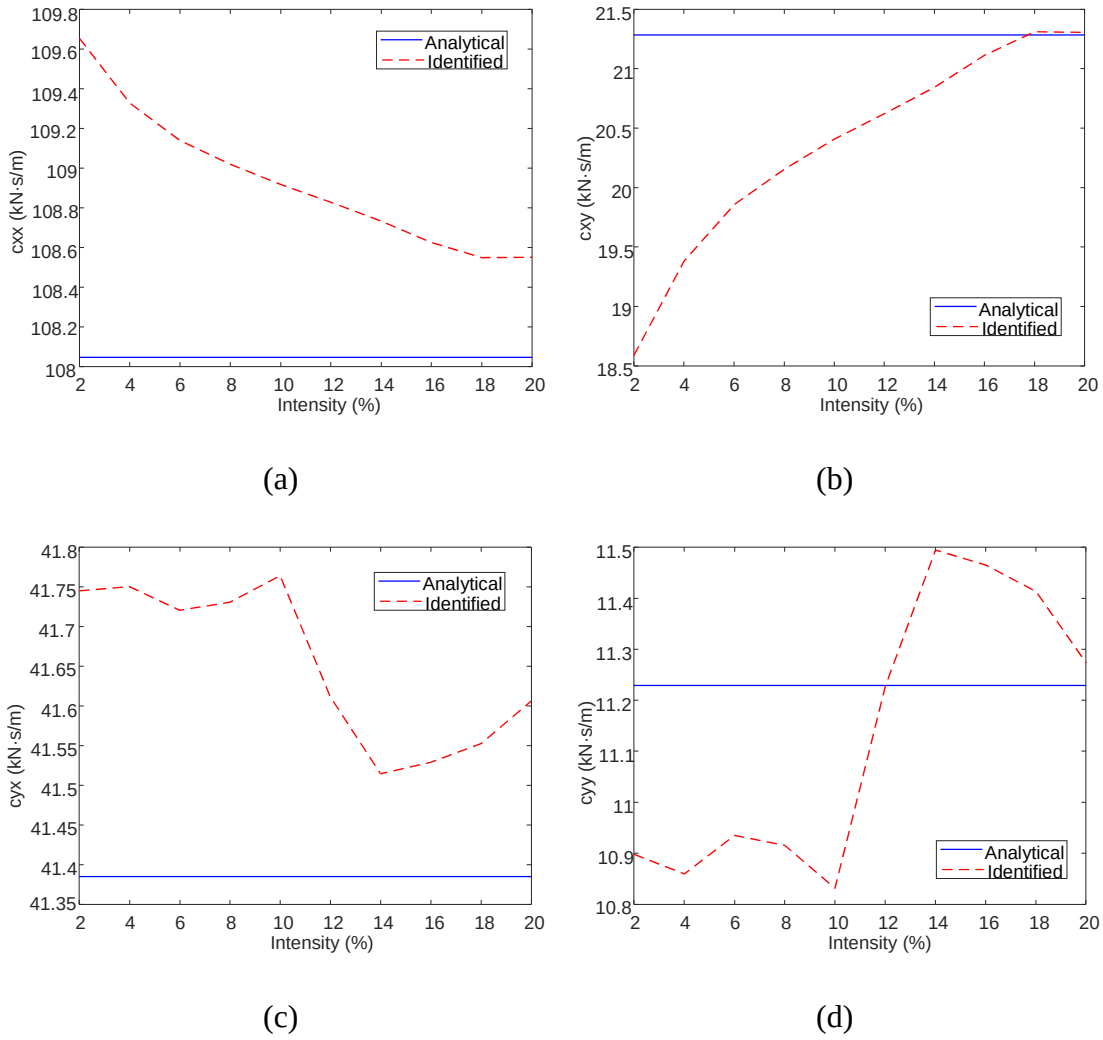

Figure 6-7. Comparison of the analytical and identified $\bar{c}_{xx}$ (a), $\bar{c}_{xy}$ (b); $\bar{c}_{yx}$ (c) and $\bar{c}_{yy}$ (d) with wind loading only and uniform wind field for the turbulence intensity from 2% to 20% in 2% steps; response data is from the 2-DOF model with the constant damping matrix.

First, the modal aerodynamic damping matrix in the 2-DOF was set constant. The damping coefficients comparison shown in Figure 6-7 demonstrates that overall the difference between the identified values and the analytical values is quite small. However, there is a trend that larger turbulence intensity reduces the difference. This is because larger intensity corresponds to larger forces applied to the rigid tower which

are the input forces to the 2-DOF system, resulting in stronger vibration responses and thus better PSD estimations. Particularly, the simulation time for the result in Figure 6-7 is 3 hours, but the result is from only one long simulation without any averaging. It was found that shorter simulation time leads to larger errors (for example, 2000 s simulation leads to coefficient differences of around 30%).

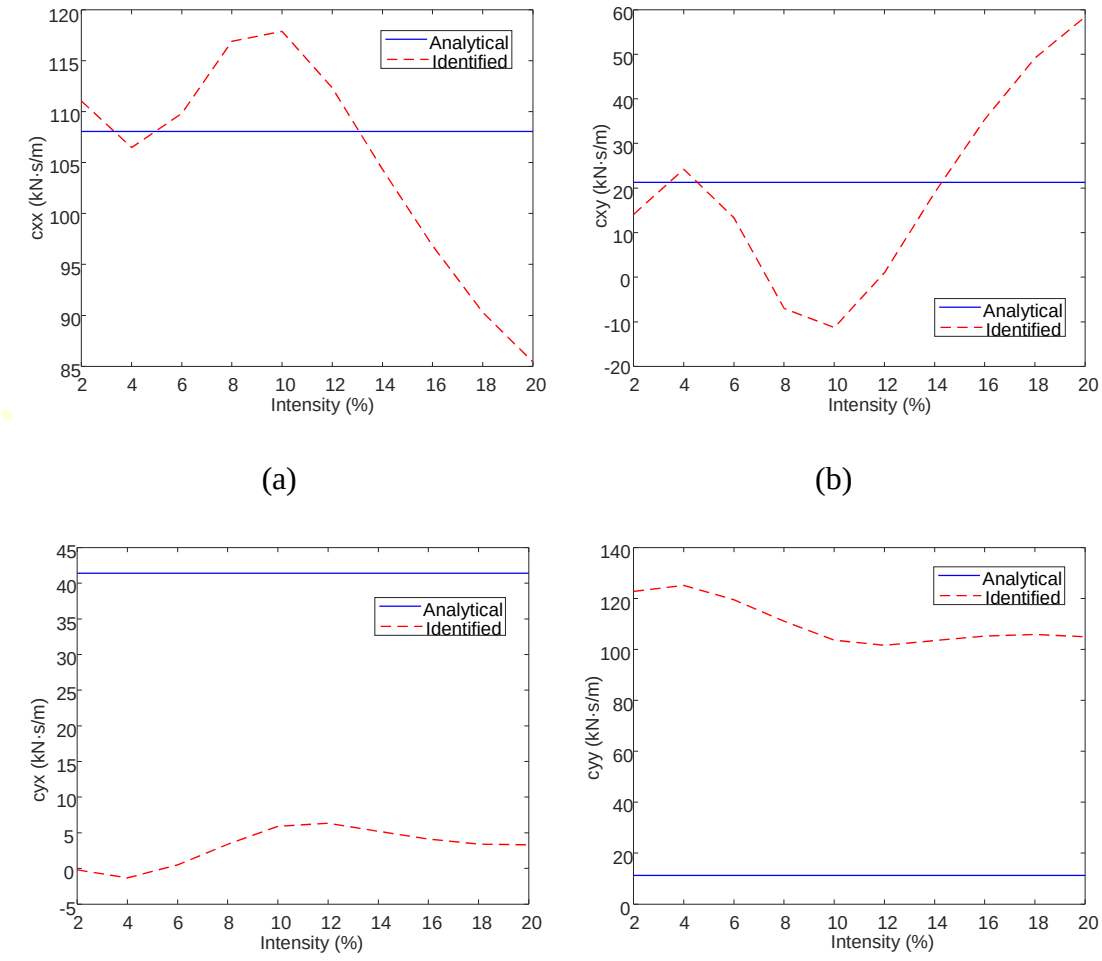

Figure 6-8. Comparison of the analytical and identified $\bar{c}_{xx}$ (a), $\bar{c}_{xy}$ (b); $\bar{c}_{yx}$ (c) and $\bar{c}_{yy}$ (d) with wind loading only and uniform wind field for the turbulence intensity from 2% to 20% in 2% steps; response data is from the 2-DOF model with the time-varying damping matrix.

Then the modal aerodynamic damping matrix was set as time-varying and the damping coefficients were identified with corresponding responses using the same settings. The comparison between the identified values and the analytical values is shown in Figure

6-8, which demonstrates no common trend for the identified damping coefficients with the turbulence intensity. The differences in the damping coefficients are large except $\bar{c}_{xx}$, especially for $\bar{c}_{yy}$ whose lowest difference is 806%.

The responses generated by FAST are quite similar to the responses from the 2-DOF model with the time-varying damping, so the identification results given FAST data is similar to the results shown in Figure 6-8. Therefore, the invalidity of the identification method using data from FAST in this section cannot be overcome by choosing different turbulence intensities. The turbulence intensity influences not only the forces applied to the rigid tower, but also influences the variation of the time-varying damping coefficients. Although smaller turbulence intensity corresponds to a steadier aerodynamic damping matrix, the variation of the forces applied to the rigid tower also becomes smaller. Thus, the contributions from the forces applied to the rigid tower and the time-varying damping matrix to the responses cannot be distinguished. The damping identification based on the CSD matrix is dependent on the quality of the PSDs of the responses and the input forces and. As a result, the identification cannot work well for a time-varying system.

Comparison not shown here demonstrates that the accuracy of the identification based on wind loading becomes worse when considering a non-uniform wind field. This can be understood as the FRF estimation using Equation (6-13) originates from a stochastic stationary process requiring the input to be a broad-band white noise. However, when the inflow wind field is non-uniform, the wind loading contains harmonics. The identification method based on ambient wind loading only works for conditions where the wind field can be controlled so that the wind field is uniform in space. Therefore, it is important to find another way of obtaining the FRF matrix accurately for a real wind turbine excited by the ambient wind field. This is the motivation for studying the identification method based on harmonic excitations described in Subsection 6.2.3.

6.3.2 Results by FRF measurements using harmonic excitations

For a mean wind speed of 20 m/s the force amplitude was chosen to be 10 kN and the harmonic excitation frequency from 0.2 Hz to 0.5 Hz, as this range contains the resonance frequency and allowed to obtain stable averaged damping coefficients. The computation time is quite long to obtain all the 2000 s response time series with the excitations of all frequencies, so the frequency resolution has to be properly chosen.

The frequency increment for the harmonic forces was 0.01 Hz, except for the range from 0.3 Hz to 0.38 Hz where a smaller frequency increment of 0.004 Hz was chosen to obtain higher resolutions around the resonance frequency (0.34 Hz). The forces were separately applied in the FA and SS directions and corresponding responses recorded. Other FAST settings were kept the same as stated at the beginning of Section 6.3. The FRFs were obtained by dividing the FFT of steady state responses with the FFT of the applied harmonic forces. Initially, the wind field was constant. The FRF comparison shown in Figure 6-9 indicates that the estimated FRFs are clear and accurate at most frequencies except near the resonance. Thus, as expected, estimations of the aerodynamic damping coefficients shown in Figure 6-10 are very accurate with percentage difference less than 10% compared to the analytical values.

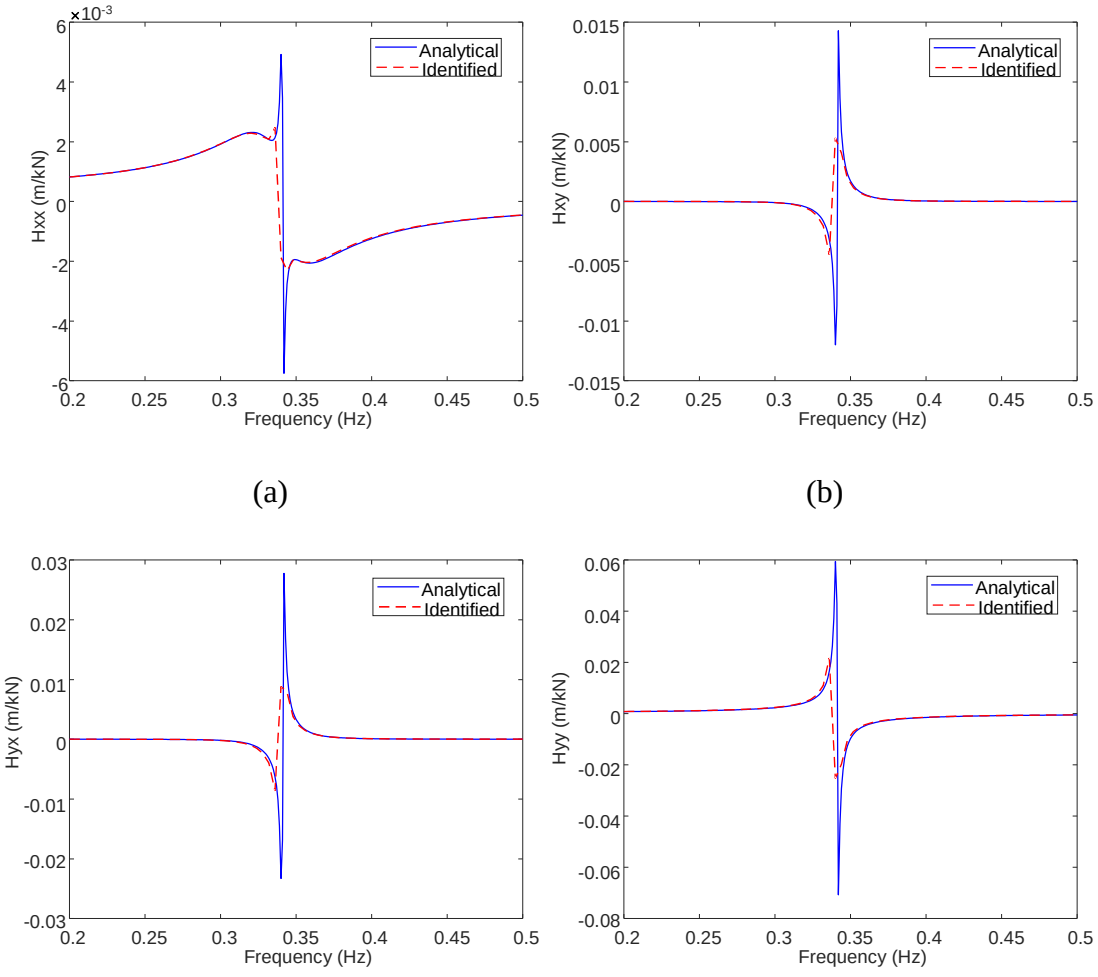

Figure 6-9. Comparison the real part of analytical and identified H_{xx} (a), H_{xy} (b), H_{yx} (c) and H_{yy} (d) with harmonic excitations and constant wind field.

The large difference between the analytical and identified values near the resonance frequency in Figure 6-10 can be explained by the FRF calculation procedure. When the harmonic excitations of frequencies near the natural frequency were applied at the tower top, the sources of the frequency contents near the resonance frequency in the responses cannot easily be distinguished as the harmonic excitations and the vibration dominated by the first bending modes are both near the resonance frequency. This complicates the FRF estimation near resonance.

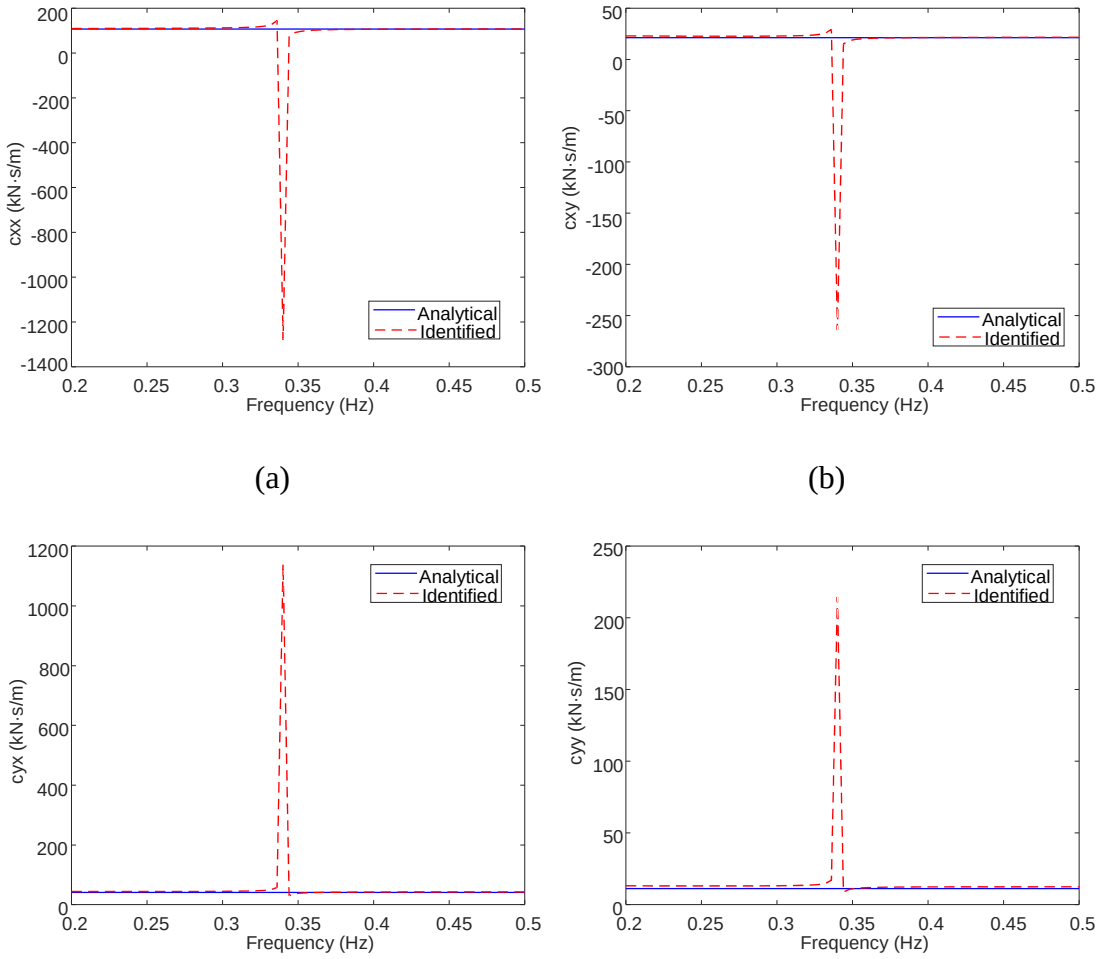

Figure 6-10. Comparison of the analytical and identified frequency-dependent $\bar{c}_{xx}$ (a), $\bar{c}_{xy}$ (b); $\bar{c}_{yx}$ (c) and $\bar{c}_{yy}$ (d) with harmonic excitations and constant wind field.

Another test was conducted with non-uniform turbulent wind fields whose mean wind speed is 20 m/s. For harmonic excitations, the responses in the FA and SS directions were used to obtain the real part of FRF curves shown in Figure 6-11. A small offset

was found around the resonance frequency, but for frequencies away from the resonance a good agreement between the analytical FRF curves and the identified curves was obtained. The calculation of the four aerodynamic damping coefficients was carried out and the frequency-dependent estimations of these coefficients are shown in Figure 6-12. The averaged damping matrix in the frequency range from 0.2 Hz to 0.5 Hz is

$$\begin{bmatrix} 108.5 & 20.3 \\ 44.4 & 11.5 \end{bmatrix} (kN \cdot s/m),$$

which is close to the analytical values with small percentage differences:

$$\begin{bmatrix} 0.4 & -4.6 \\ 7.3 & 2.2 \end{bmatrix} (\%).$$

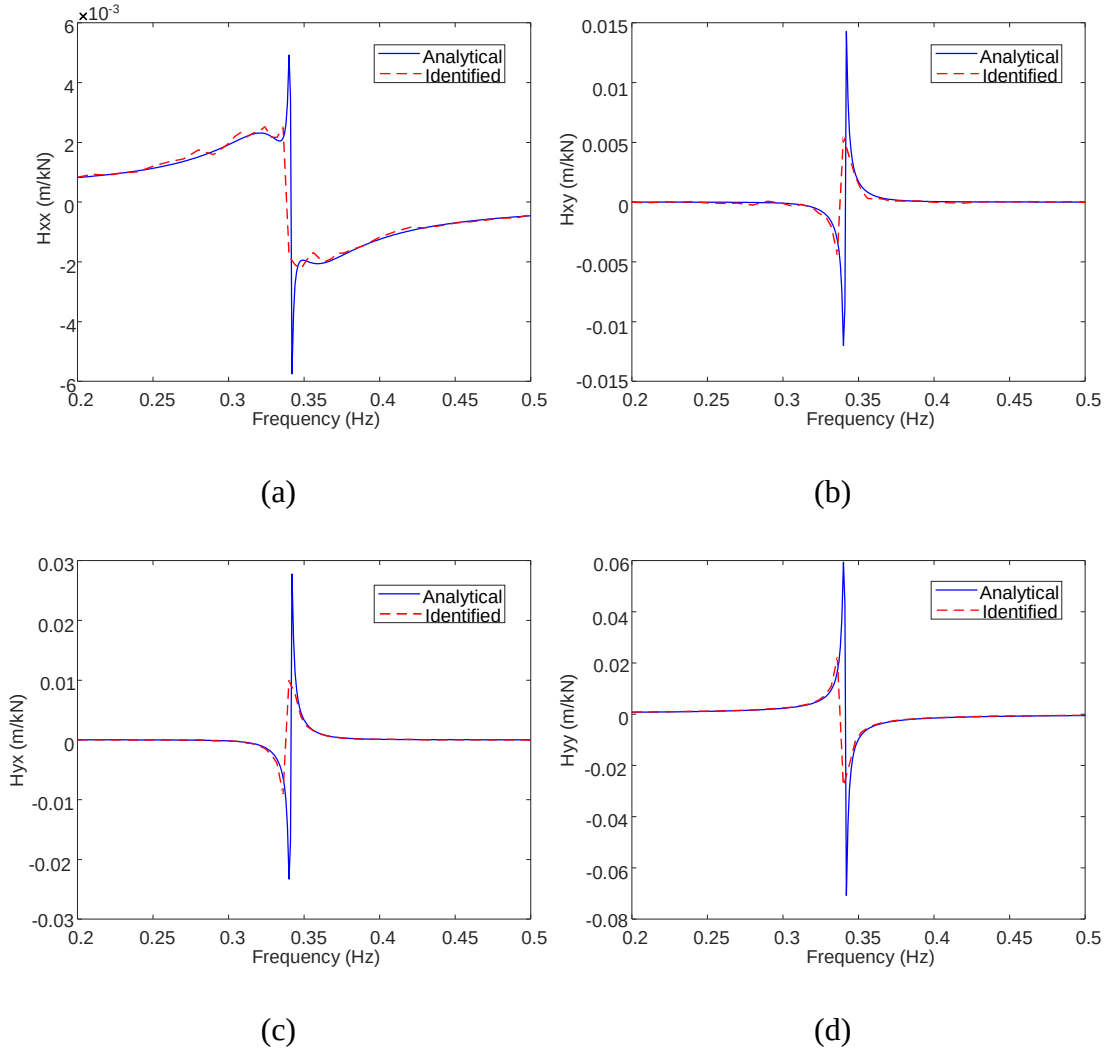

Figure 6-11. Comparison the real part of analytical and identified H_{xx} (a), H_{xy} (b), H_{yx} (c) and H_{yy} (d) with with harmoinc excitations and non-uniform wind field.

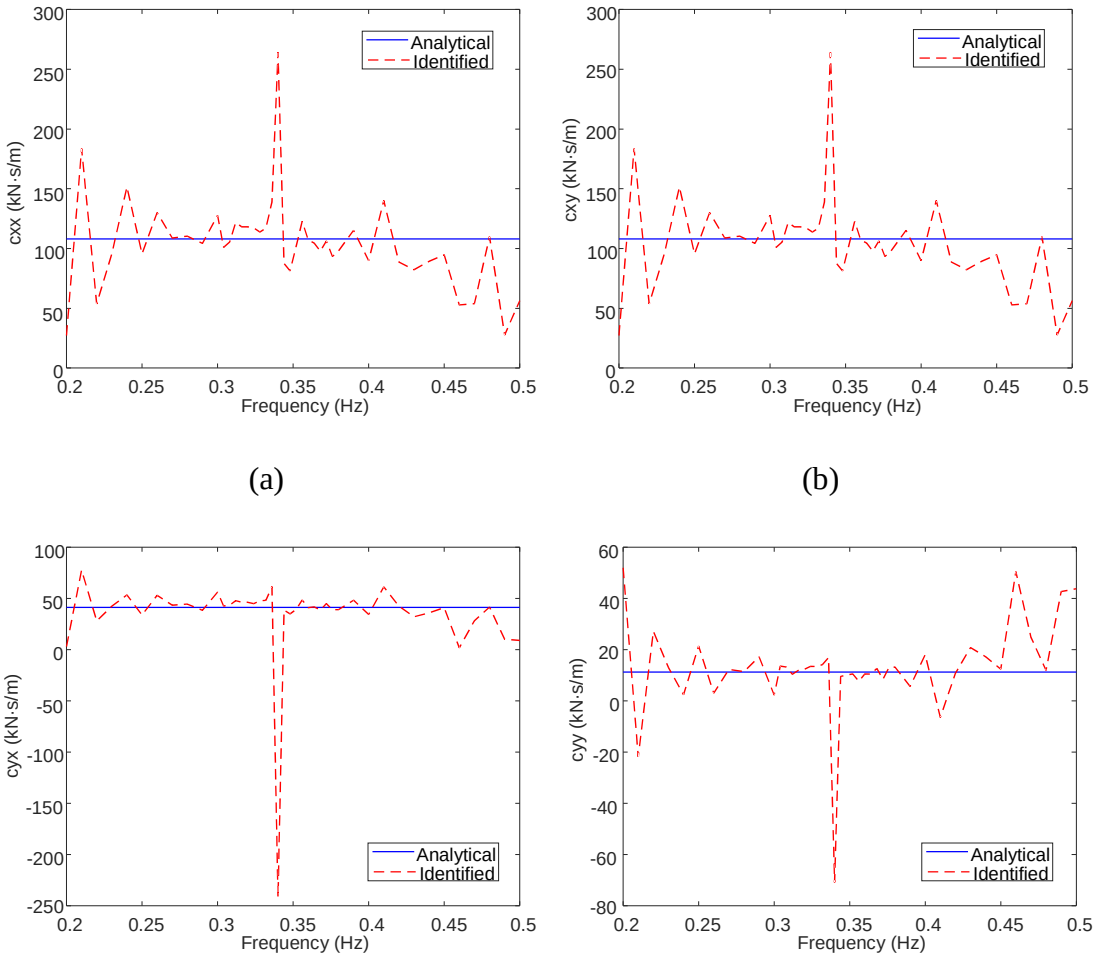

Figure 6-12. Comparison of the analytical and identified frequency-dependent $\bar{c}_{xx}$ (a), $\bar{c}_{xy}$ (b); $\bar{c}_{yx}$ (c) and $\bar{c}_{yy}$ (d) with with harmonic excitations and non-uniform wind field.

The identification with harmonic excitations was undertaken for non-uniform wind fields with mean wind speeds from 6 m/s to 20 m/s in 2 m/s steps. The identified results compared with analytical values are shown in Figure 6-13, confirming the generally good performance of the identification procedure using harmonic excitations. The percentage differences for the estimations of $\bar{c}_{xx}$ and $\bar{c}_{yx}$ are less than 10%, while for $\bar{c}_{yy}$ the percentage differences are less than 30%. For $\bar{c}_{xy}$, most percentage differences are around 20%. The accuracy of this method depends on the amplitude of the harmonic excitation, with larger harmonic forces giving more accurate results since in the frequency domain the corresponding response due to the harmonic excitation is distinct

and easier to identify.

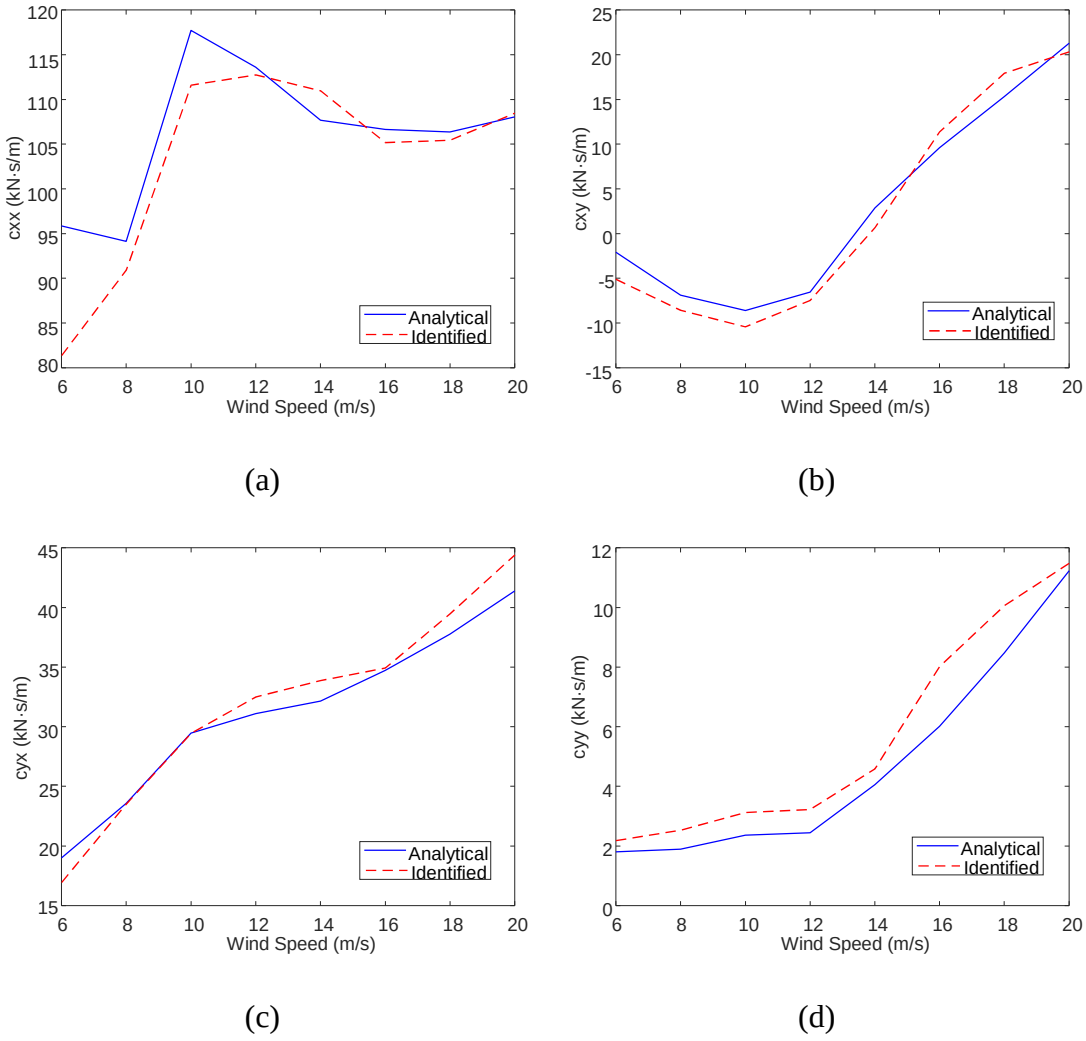

Figure 6-13. Comparison of the analytical and identified $\bar{c}_{xx}$ (a), $\bar{c}_{xy}$ (b); $\bar{c}_{yx}$ (c) and $\bar{c}_{yy}$ (d) with with harmonic excitations and non-uniform wind field for the mean wind speeds from 6 m/s to 20 m/s in 2 m/s steps.

When the amplitude of the harmonic excitation is too low, it is hard to obtain FRFs accurate enough to achieve good estimation of the damping matrix. For the 5 MW reference onshore turbine used in this study, when the amplitudes of the harmonic excitation are lower than 5 kN the damping matrix estimation is poor. Tests were also carried out with harmonic excitations with amplitudes of 100 kN, from which the estimation of the FRFs and the damping matrix is more accurate. However, in practice it is difficult to apply large excitations of amplitude 100 kN. The selection of the force amplitude depends on the size, inertia and stiffness of the wind turbine, with smaller

wind turbines requiring smaller forces for the identification based on harmonic excitations. In practice, besides shakers to excite wind turbines, active tuned mass dampers could be used to harmonically excite the wind turbine (if installed), and this method was recommended by Oh and Ishihara [142].

6.3.3 Comparison of results from the model with identified damping ratios and the 2-DOF model with identified aerodynamic damping matrix

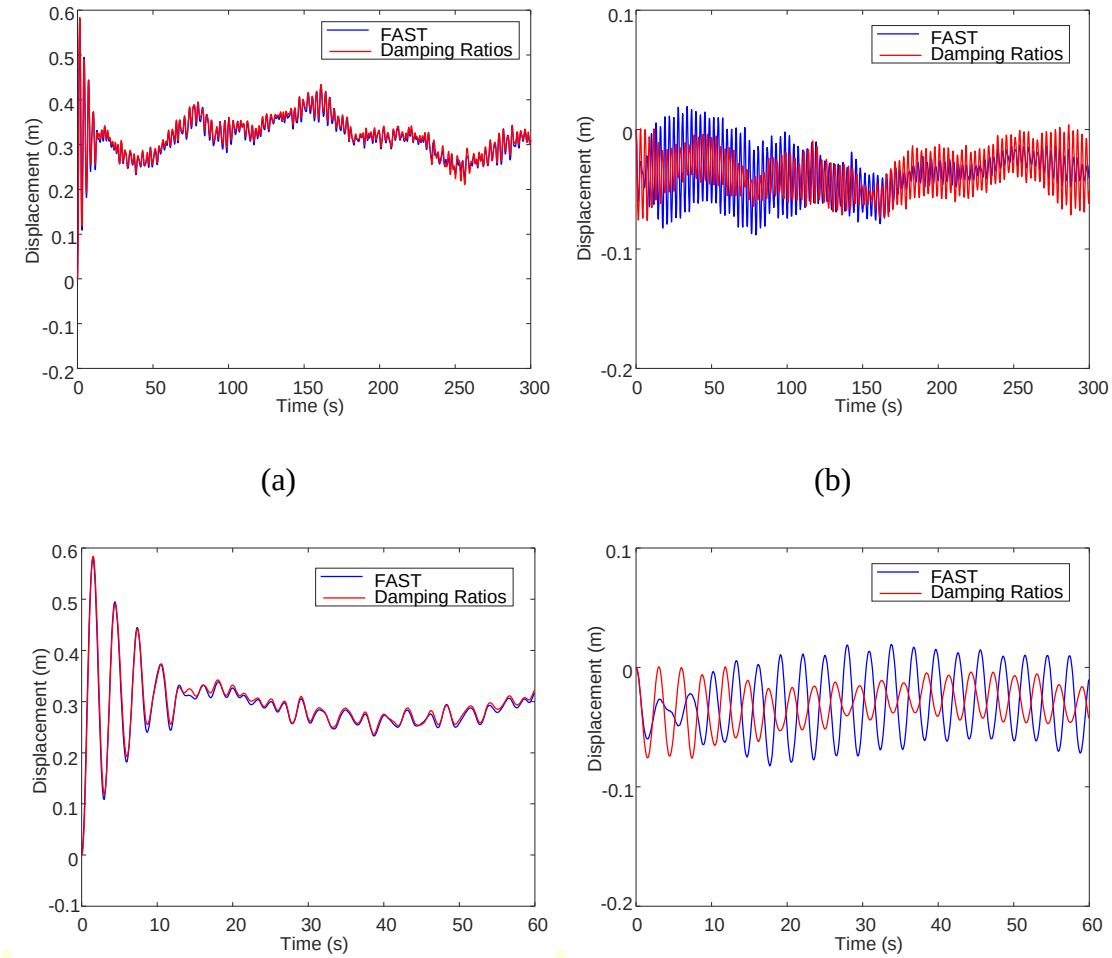

Figure 6-14. Comparison of the FA (a, c) and SS (b, d) responses from the model with damping ratios and the FAST model when the mean wind speed is 10 m/s; (c) and (d) are zooms of (a) and (b).

It is valuable to compare the influence of aerodynamic damping descriptions using the aerodynamic damping matrix and the damping ratios. Since in FAST the aerodynamic damping is implicitly defined, aerodynamic damping must be determined from the

responses. It is more practical to obtain the aerodynamic damping using OMA without any controlled excitation. However, classical OMA techniques without any modification, which assume the external excitations are white noise and do not contain harmonics, do not work well for wind turbines [71]. From Equation (6-11), the external forces that excite the vibration in the FA/SS direction can be regarded as the combination of two parts: the wind loads applied to a rigid tower and the harmonic excitation related to the motion in the SS/FA direction. As a result, to avoid the limitations of classical OMA techniques, the determination of the aerodynamic damping used the same methodology as mentioned in Subsection 6.3.3, *i.e.,* through the FRFs measured from responses from the FAST model under harmonic excitations. Moreover, the damping identification through methodology based on EMA is normally deemed more accurate than that through OMA.

First, an example with a non-uniform turbulent wind field and a mean wind speed of 10 m/s is selected. After obtaining the FRFs, the damping ratios were calculated from measured H_{xx} and H_{yy} separately using a traditional Q-factor based method [143], resulting in damping ratios 7.18% and 0.29% in the FA and SS directions respectively. The Q-factor method estimates the damping ratio using the half-power bandwidth of the response spectrum or the FRF of a vibration system at the resonance. These two damping ratios can be converted into damping coefficients for the single-DOF systems representing the first bending modes in the FA and SS directions. On the other hand, the aerodynamic damping matrix can also be calculated from the full measured FRF matrix. The calculated two damping ratios and aerodynamic matrix were assigned to the 2-DOF model to reproduce the responses with the same external forces which are related to the wind loads applied to the rigid tower. Figure 6-14 shows the comparison between the responses from the model with damping ratios and the FAST model, while Figure 6-15 compares the responses from the model with the aerodynamic matrix and the FAST model. The similarity indicator gives 0.11 for the FA motion and 1.25 for the SS motion when comparing the responses in Figure 6-14, and 0.10 for the FA motion and 0.15 for the SS motion when comparing the responses in Figure 6-15.

For the FA motion, the models with aerodynamic damping matrix and damping ratios can both reproduce responses close to those from the FAST model in this case. However, for the SS motion, the aerodynamic matrix performs much better than the damping

ratios. This clearly shows that the aerodynamic damping can be much better captured by the aerodynamic damping matrix compared to the damping ratios.

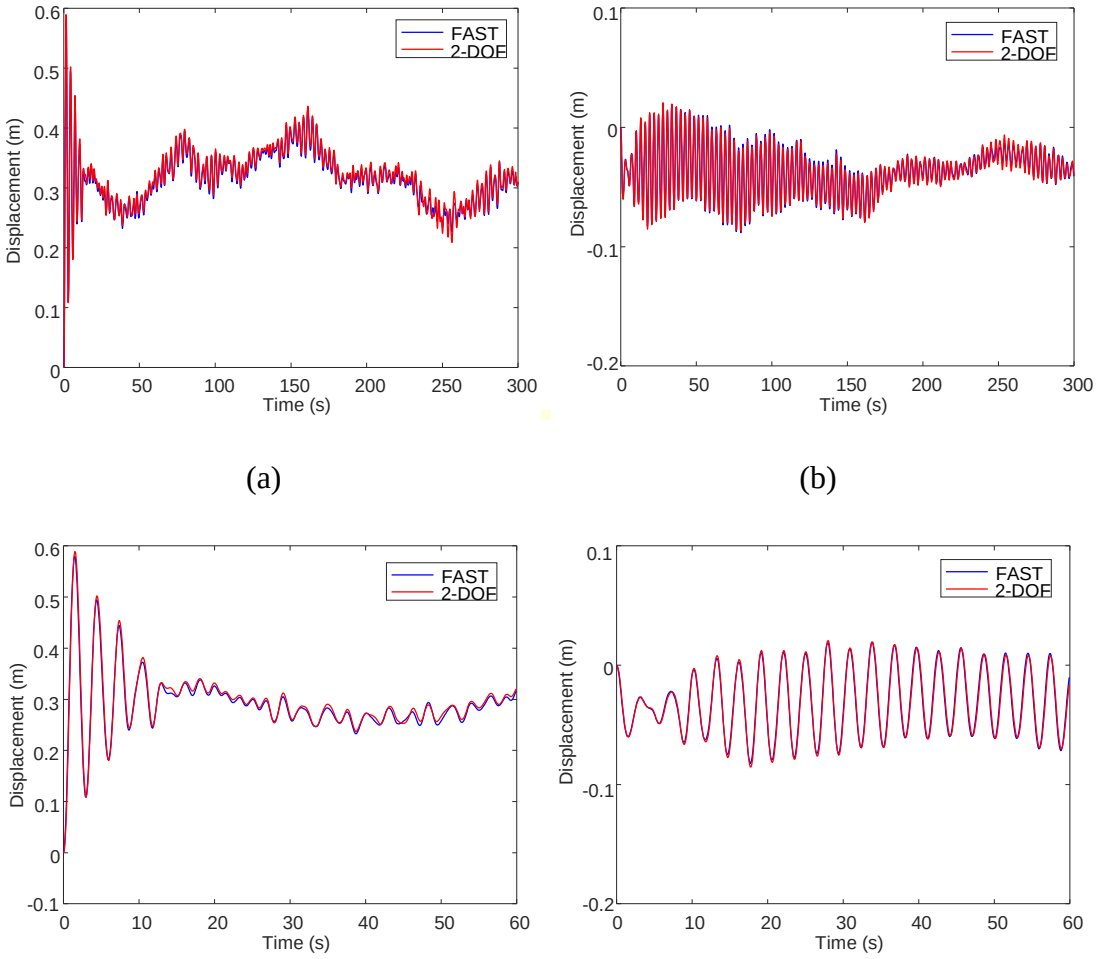

Figure 6-15. Comparison of the FA (a, c) and SS (b, d) responses from the 2-DOF model and the FAST model when the mean wind speed is 10 m/s; (c) and (d) are zooms of (a) and (b).

Another test was conducted with a non-uniform turbulent wind field whose mean wind speed is 20 m/s. Following the same procedure as the previous example with 10 m/s mean wind speed, the comparison between the 2-DOF model and the model with damping ratios was conducted. The magnitude of the measured H_{xx} and H_{yy}, which are corresponding to the FA and SS motions respectively, are shown in Figure 6-16. The estimated FA and SS damping ratios are both 0.29% when applying the Q-factor method to these two FRFs, which is in contradiction with the fact that the FA damping

is much larger than the SS damping. This can be explained by the similar magnitude shapes of H_{xx} and H_{yy} near resonance. However, it is clear the magnitude of H_{xx} is much lower than that of H_{yy}, meaning that the FA damping is larger than the SS damping. Thus, the estimations by the Q-factor method are not reliable in this case.

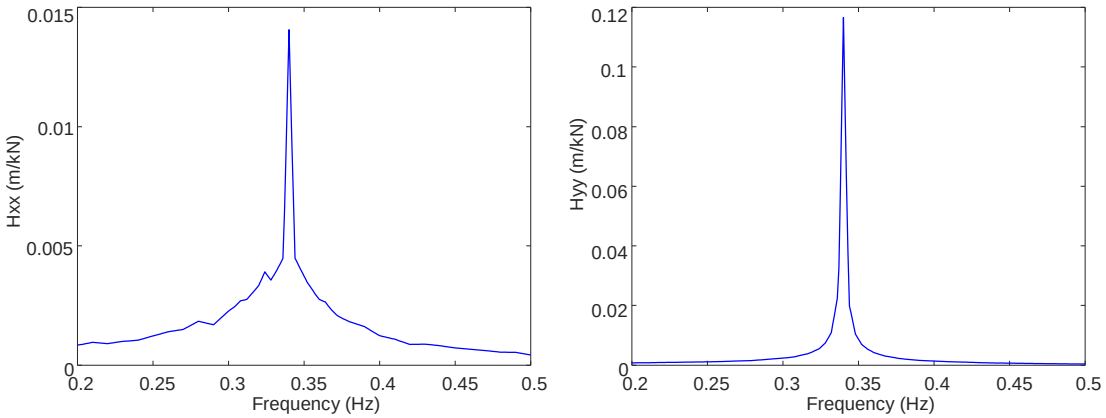

(a) (b)

Figure 6-16. The magnitude of identified H_{xx} (a) and H_{yy} (b) with with harmoinc excitations and non-uniform wind field.

Then the identified damping ratios were assigned and responses were compared. In Figure 6-17, a very large difference in the responses from the model with damping ratios and the FAST model can be observed, where the similar indicator gives 0.63 in the FA direction and 0.67 in the SS direction.

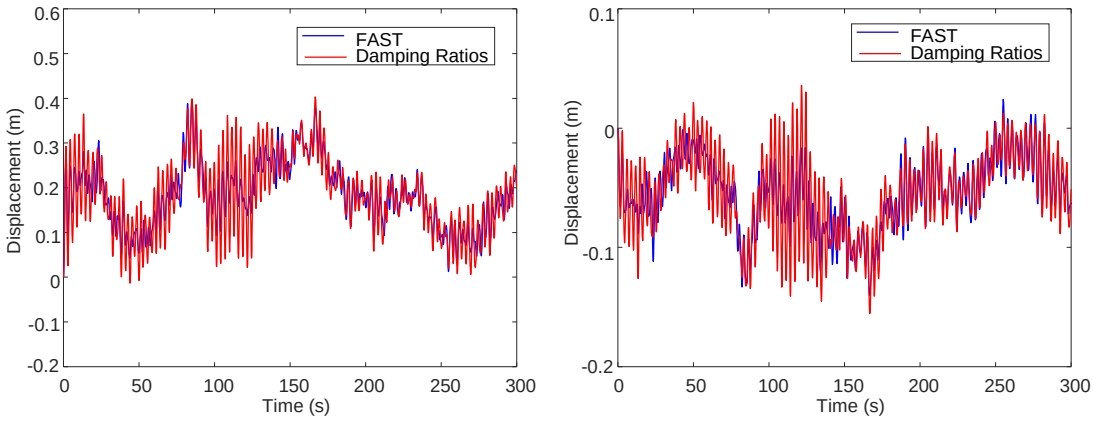

(a) (b)

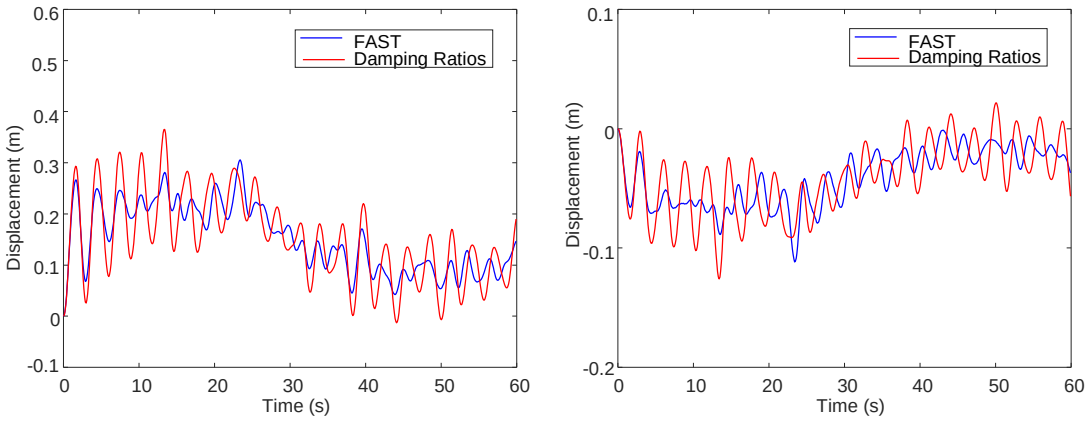

(c) (d)

Figure 6-17. Comparison of the FA (a, c) and SS (b, d) responses from the model with damping ratios and the FAST model when the mean wind speed is 20 m/s; (c) and (d) are zooms of (a) and (b).

On the other hand, the comparison between the 2-DOF model and the FAST model in Figure 6-18 shows that the 2-DOF model is still able to generate very similar responses compared to the FAST model, and the values of the similarity indicator are 0.04 and 0.13 in the FA and SS directions respectively.

Some points can explain the difference caused by the different damping descriptions using aerodynamic damping matrix and damping ratios. First, the measured FRFs in the FA/SS direction are different from the one from real single DOF model because of aerodynamic coupling in the FA and SS directions. Second, the Q-factor method estimates the damping for a single DOF system, which cannot be theoretically suitable to estimate the damping of a coupled 2-DOF system. Thus, the estimation of damping ratios from the measured FRFs from operating wind turbines is difficult and lacks theoretical foundation.

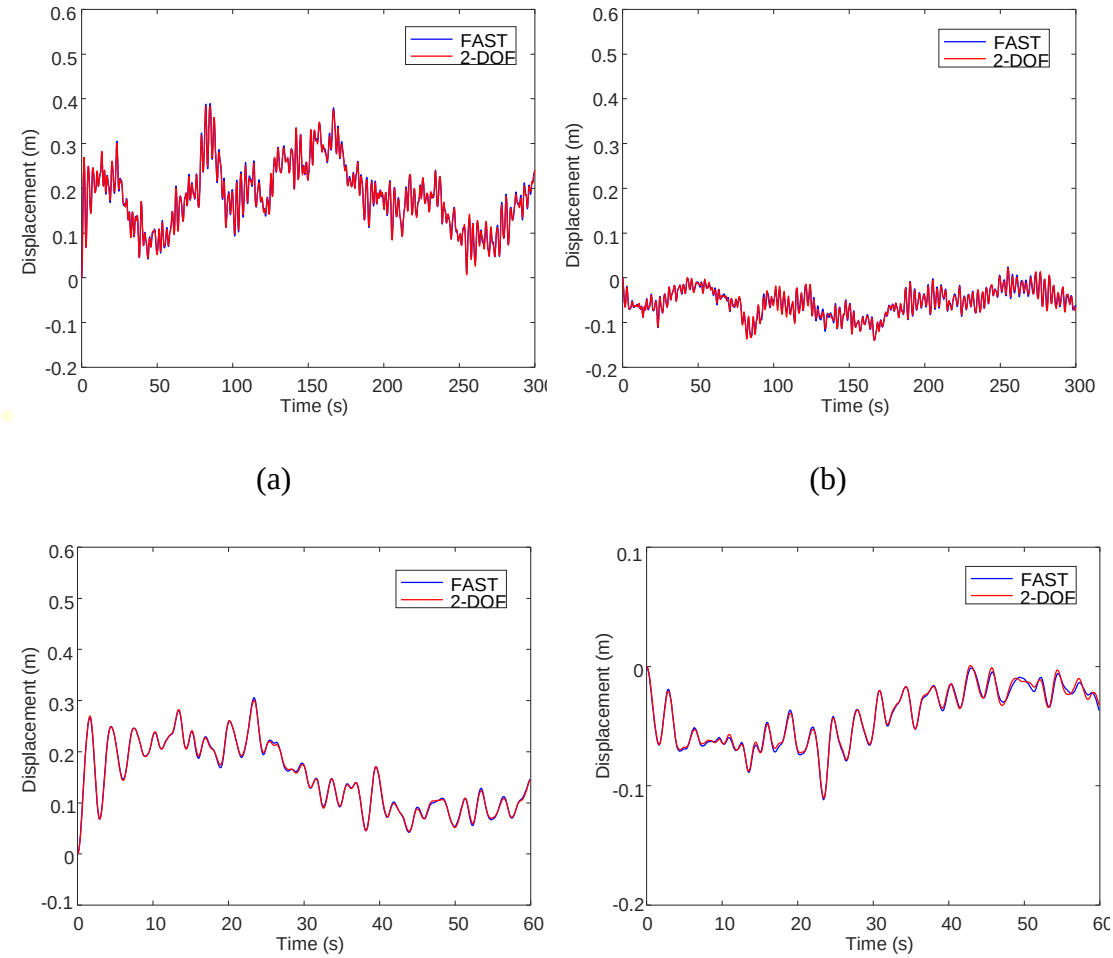

Figure 6-18. Comparison of the FA (a, c) and SS (b, d) responses from the 2-DOF model and the FAST model when the mean wind speed is 20 m/s; (c) and (d) are zooms of (a) and (b).

6.4 Conclusion

In this chapter, an FRF-based aerodynamic damping identification procedure was developed. Once the FRFs of the operating wind turbine system are measured, a frequency-dependent aerodynamic damping matrix can be first calculated through a matrix-based identification method. Then the final predication of the aerodynamic damping matrix is obtained by averaging the frequency-dependent damping terms in an appropriate frequency range. The quality of the damping identification is highly dependent on the quality of the measured FRFs.

Two methods to obtain the FRFs were devised. In this first method, it is assumed that the wind turbine is only subjected to wind loads and the aerodynamic forces applied to a rigid wind turbine tower can be estimated in advance. Thus, the FRFs can be obtained from measured responses and the estimated aerodynamic forces. This method works well for the data obtained from the 2-DOF model with the constant modal aerodynamic damping matrix in MATLAB. However, it cannot accurately predict the aerodynamic damping matrix using the data obtained from FAST. This is because in FAST the aerodynamic damping is indeed time-varying when the inflow field changes over time.

The second method is similar to traditional EMA, which requires successively applying harmonic external excitations with a range of frequencies to the wind turbine tower. The FRF matrix for a particular frequency point can be obtained from the FFT of the responses divided by the FFT of the applied external excitations at that frequency. Results show that the aerodynamic damping matrix can be extracted with good accuracy using this method. However, in practice the size of devices that generate the harmonic forces needs careful consideration. The external forces applied to the large-size wind turbines should be large enough so that the corresponding responses to the harmonic forces are observable and able to produce good FRF estimation.

Finally, results from models with identified damping ratios and modal aerodynamic damping matrix were compared. It showed that for same measured FRFs, the model with aerodynamic damping matrix is much better than the model with damping ratios in terms of simulating the dynamic responses of operating wind turbines with same aerodynamic forces applied to a rigid tower, especially for the SS vibration.

Chapter 7 - Conclusions and Future Work

7.1 Variation of damping values and first-principle damping models

Vibration damping in offshore wind turbines is a critical parameter to predict the dynamic response. Although much research has been done to characterise energy dissipation in OWTs, published values vary widely and uncertainties remain as to what values should be used at the design stage, when actual measurements are not available. Following a detailed literature survey, it was found that the reported damping values for aerodynamic, structural and soil damping are in a relatively wide range, while the hydrodynamic damping is much smaller and contributes little to the total damping. The aerodynamic damping is significantly dependent on the operating conditions of the wind turbines. For instance, aerodynamic damping can be very different for parked wind turbines and wind turbines operating under different mean wind speeds. Compared to aerodynamic damping which can contribute more than 5% damping ratios in the total damping of operating wind turbines, contributions from structural and soil damping are both in the range of 0.2% to 1.5%. However, for parked wind turbines, structural and soil damping become more significant as the aerodynamic damping drops to less than 0.3%. Furthermore, the damping in the FA direction is much larger than that in the SS direction for operating wind turbines.

First-principle models were developed to calculate the damping contributions from aerodynamic, hydrodynamic, and soil damping. The damping values calculated by these models were compared to reported damping values and results from FAST simulations. The dependence on operating conditions for aerodynamic damping was confirmed by the BEM-based aerodynamic damping model, and the difference in the FA and SS aerodynamic damping can be estimated by this model. Hydrodynamic damping in OWTs was found to be much lower than the values in previous studies and in current code recommendations, which is due to the significant size effect of the monopile diameter. Soil damping calculated by the nonlinear p-y curve based model is generally in the range of reported values. It was found that soil damping is strongly dependent on the stiffness of the wind turbine system.

7.2 Modelling of aerodynamic damping in wind turbines

Free vibration tests carried out in FAST demonstrated the existence of coupling between the FA and SS motions. However, conventional damping ratios separately assigned in the FA and SS directions cannot correctly capture this coupling. A new aerodynamic damping model was developed to consider the FA and SS motions simultaneously, resulting in the so-called "aerodynamic damping matrix" which is a new aerodynamic damping description for wind turbine tower vibrations. The derivation of the aerodynamic damping matrix is based on BEM theory and the linearisation of aerodynamic forces from the rotor at the wind turbine tower top. Unlike conventional proportional damping matrices, the aerodynamic damping matrix is asymmetric and the off-diagonal terms in the matrix account for the coupling of the FA and SS motions. The aerodynamic damping matrix was initially derived by assuming the blades as rigid and the inflow wind field as constant. Then the aerodynamic damping model was extended to consider a turbulent inflow wind field, in which the aerodynamic damping matrix becomes time-varying. Moreover, it was shown that the wind turbine model with the original 4×4 aerodynamic damping matrix can be simplified to a 2-DOF model using a partial modal decomposition.

The aerodynamic damping model was first tested with the constant inflow wind field, showing that the model with the constant aerodynamic damping matrix is able to generate accurately displacement time series from FAST with equivalent assumptions such as rigid blades and zero permanent shaft tilt. These assumptions were then tested with FAST simulations considering blade flexibility, initial shaft tilt, and blade precone. Results showed that the aerodynamic damping model is sufficient to capture the main damping characteristics of the wind turbine system. Then the damping model was verified with a turbulent uniform wind field and a turbulent non-uniform wind field. Results showed that the model with the constant aerodynamic damping matrix is still able to generate responses in good agreement with those from FAST. However, a time-varying damping matrix better models the time-varying damping feature for wind turbines operating in turbulent wind fields. Overall, the results confirmed the potential of the aerodynamic damping model to accurately capture the tower-rotor interaction and the coupling between the FA and SS motions.

7.3 Identification of aerodynamic damping matrix

A FRF-based aerodynamic damping identification procedure was developed to obtain the modal aerodynamic damping matrix in the 2-DOF system. Two methods to measure the FRFs were devised: the first one does not require controlled excitations but requires an estimation of aerodynamic forces applied to a rigid wind turbine tower; for the second method, harmonic excitations with a range of frequencies were applied at the tower top. Numerical simulations were carried out to test the feasibility of the damping identification procedure, in which two types of data were used: the responses generated by the 2-DOF wind turbine model in MATLAB and the responses from FAST/OpenFAST.

The first FRF generation method is able to obtain a good estimation of FRFs using the responses from the 2-DOF model with the constant aerodynamic damping matrix. Therefore, an accurate damping matrix estimation was obtained from these FRFs. However, the first method failed to calculate accurate FRFs compared to analytical FRFs for the data from FAST, resulting in very large errors in the calculation of damping terms. This is due to the time-varying features of aerodynamic damping when the wind field is turbulent.

The second method was successfully tested with turbulent wind fields with a range of mean wind speeds using a data model written for OpenFAST. Applying a controlled frequency excitation, the corresponding frequency content in the responses can be easily identified. The damping identification procedures based on conventional damping ratios and the aerodynamic damping matrix were compared. Results showed that the model with the identified aerodynamic damping matrix is able to generate closer responses to that from FAST than the model with damping ratios, especially for the SS motion.

7.4 Future work

From the literature review, one issue emerges as particularly deserving of further investigation: there is still no data available for the structural damping in large OWTs, even though this contribution is probably not insignificant. The estimated hydrodynamic damping by the simplified model was found to be much lower than recommended in current codes of practice, which can be explained by the size effect of the monopile. Although the contribution from hydrodynamic damping is small, it is

valuable to study how much hydrodynamic damping exists in large-size OWTs numerically and experimentally.

The decoupled model with the aerodynamic damping matrix developed in this study can be used to quickly predict fatigue damage in OWTs. Further studies can be carried out to test the performance of this model. It was shown that the FA and SS motions are linked by the aerodynamic damping, so it is of interest to calculate the fatigue life of wind turbines considering the FA and SS vibrations simultaneously and compare the results to calculations which only focuses on the FA vibration.

The aerodynamic damping model in this study assumes that the blades are rigid. Although the influence of the blade flexibility on aerodynamic damping is not significant according to the comparison with simulated responses, it is worthwhile to improve the aerodynamic damping model by including the blade flexibility. Another issue is that the aerodynamic damping model is based on the widely used BEM theory. However, more complex models of aerodynamics for wind turbines such as CFD model are more accurate than BEM theory. It will be valuable to compare the responses generated by the model with the aerodynamic damping matrix and the responses from more complex models.

Given the importance of the aerodynamic damping component, there is comparatively little reliable experimental data available to test numerical predictions. The aerodynamic damping matrix is proven to be a better description of aerodynamic damping compared to damping ratios and an identification procedure has been devised to obtain it. After the successful implementation with simulated data, this identification procedure should be tested with experimental data obtained from real wind turbines.

References

[1] European Wind Energy Association. *Wind energy scenarios for 2030*, https://www.ewea.org/fileadmin/files/library/publications/reports/EWEA-Wind-energy-scenarios-2030.pdf (2015).

[2] Wind Europe. *Wind energy in Europe in 2018: trends and statistics*, https://windeurope.org/wp-content/uploads/files/about-wind/statistics/WindEurope-Annual-Statistics-2018.pdf (2019).

[3] International Renewable Energy Agency. *Floating foundations: a game changer for offshore wind power*, http://www.irena.org/-/media/Files/IRENA/Agency/Publication/2016/IRENA_Offshore_Wind_Floating_Foundations_2016.pdf (2016).

[4] Wind Europe. *The European offshore wind industry - key trends and statistics 2016*, https://windeurope.org/wp-content/uploads/files/about-wind/statistics/WindEurope-Annual-Offshore-Statistics-2016.pdf (2017).

[5] Prendergast LJ, Gavin K, Doherty P. An investigation into the effect of scour on the natural frequency of an offshore wind turbine. *Ocean Eng* 2015; 101: 1–11.

[6] Tempel J Van Der. *Design of support structures for offshore wind turbines*. PhD Thesis. Delft University of Technology, 2006.

[7] Bilgili M, Yasar A, Simsek E. Offshore wind power development in Europe and its comparison with onshore counterpart. *Renew Sustain Energy Rev* 2011; 15: 905–915.

[8] Weijtjens W, Verbelen T, De Sitter G, et al. Foundation structural health monitoring of an offshore wind turbine—a full-scale case study. *Struct Heal Monit An Int J* 2016; 15: 389–402.

[9] Shirzadeh R, Devriendt C, Bidakhvidi MA, et al. Experimental and computational damping estimation of an offshore wind turbine on a monopile foundation. *J Wind Eng Ind Aerodyn* 2013; 120: 96–106.

[10] Ziegler L, Gonzalez E, Rubert T, et al. Lifetime extension of onshore wind turbines: A review covering Germany, Spain, Denmark, and the UK. *Renew Sustain Energy Rev* 2018; 82: 1261–1271.

[11] Zaaijer MB. Comparison of monopile , tripod , suction bucket and gravity base design

for a 6 MW turbine. In: *Mediterranean and Other European Seas (OWEMES Conference)*. Naples, Italy, 2003.

[12] Burton T, Jenkins N, Sharpe D, et al. *Wind Energy Handbook*. Second Edi. John Wiley & Sons, 2011.

[13] Carswell W, Johansson J, Løvholt F, et al. Foundation damping and the dynamics of offshore wind turbine monopiles. *Renew Energy* 2015; 80: 724–736.

[14] Adhikari S, Bhattacharya S. Dynamic analysis of wind turbine towers on flexible foundations. *Shock Vib* 2012; 19: 37–56.

[15] Damgaard M, Zania V, Andersen LV, et al. Effects of soil–structure interaction on real time dynamic response of offshore wind turbines on monopiles. *Eng Struct* 2014; 75: 388–401.

[16] Zaaijer MB. *Sensitivity analysis for foundations of offshore wind turbines*. Technical Report OWTES Task 4.1. Delft University of Technology, 2002.

[17] Petersen B, Pollack M, Connell B, et al. *Evaluate the effect of turbine period of vibration requirements on structural design parameters: technical report of findings*. Technical Report M10PC00066-8. Applied Physical Sciences Corp., 2010.

[18] Tempel J Van Der, Molenaar J, David P. Wind turbine structural dynamics - a review of the principles for modern power generation, onshore and offshore. *Wind Eng* 2002; 26: 211–222.

[19] Vorpahl F, Schwarze H, Fischer T, et al. Offshore wind turbine environment, loads, simulation, and design. *Wiley Interdiscip Rev Energy Environ* 2013; 2: 548–570.

[20] Cheng PW. *A reliability based design methodology for extreme responses of offshore wind turbines*. PhD Thesis. Delft University of Technology, 2002.

[21] Germanischer Lloyd (GL). *Guideline for the certification of offshore wind turbines*. Hamburg, 2005.

[22] Det Norske Veritas (DNV). *DNV-OS-J101 Design of Offshore Wind Turbine Structures*. 2014.

[23] Leite OB. *Review of design procedures for monopile offshore wind structures*. Master Thesis. University of Porto, 2015.

[24] Glauert H. Aerodynamic theory. *J R Aeronaut Soc* 1930; 34: 409–414.

[25] Hansen M. *Aerodynamics of wind turbines*. Second Edi. Routledge, 2008.

[26] Hansen MOL, Sørensen JN, Voutsinas S, et al. State of the art in wind turbine aerodynamics and aeroelasticity. *Prog Aerosp Sci* 2006; 42: 285–330.

[27] Glauert H. *A general theory of the autogyro*. HM Stationery Office, 1926.

[28] Pitt DM, Peters DA. Theoretical prediction of dynamic-inflow derivatives. *Vertica* 1981; 5: 21–34.

[29] Micallef D, Sant T. A review of wind turbine yaw aerodynamics. In: *Wind Turbines - Design, Control and Applications*. InTech, 2016.

[30] Jeon M, Lee S, Lee S. Unsteady aerodynamics of offshore floating wind turbines in platform pitching motion using vortex lattice method. *Renew Energy* 2014; 65: 207–212.

[31] Thé J, Yu H. A critical review on the simulations of wind turbine aerodynamics focusing on hybrid RANS-LES methods. *Energy* 2017; 138: 257–289.

[32] Niebsch J, Ramlau R, Nguyen TT. Mass and aerodynamic imbalance estimates of wind turbines. *Energies* 2010; 3: 696–710.

[33] Rezaei R, Fromme P, Duffour P. Fatigue life sensitivity of monopile-supported offshore wind turbines to damping. *Renew Energy* 2018; 123: 450–459.

[34] Muskulus M, Schafhirt S. Reliability-based design of wind turbine support structures. In: *Proceedings of the Symposium on Reliability of Engineering System*. Hangzhou, China, 2015.

[35] Bisoi S, Haldar S. Dynamic analysis of offshore wind turbine in clay considering soil–monopile–tower interaction. *Soil Dyn Earthq Eng* 2014; 63: 19–35.

[36] Muskulus M. Simplified rotor load models and fatigue damage estimates for offshore wind turbines. *Philos Trans R Soc London A Math Phys Eng Sci* 2015; 373: 20140347.

[37] Schafhirt S, Muskulus M. Decoupled simulations of offshore wind turbines with reduced rotor loads and aerodynamic damping. *Wind Energy Sci* 2018; 3: 25.

[38] Sarpkaya T. *Wave forces on offshore structures*. Cambridge University Press, 2010.

[39] Veldkamp HF, Tempel J Van Der. Influence of wave modelling on the prediction of fatigue for offshore wind turbines. *Wind Energy* 2005; 8: 49–65.

[40] Negro V, López-Gutiérrez J-S, Esteban MD, et al. Uncertainties in the design of support structures and foundations for offshore wind turbines. *Renew Energy* 2014; 63: 125–132.

[41] Henderson AR, Zaaijer MB, Hassan G, et al. Hydrodynamic loading on offshore wind turbine support structures. *Eng Integr* 2008; 25: 24–31.

[42] Faltinsen O. *Sea loads on ships and offshore structures*. Cambridge University Press, 1993.

[43] Lombardi D, Bhattacharya S, Muir Wood D. Dynamic soil–structure interaction of monopile supported wind turbines in cohesive soil. *Soil Dyn Earthq Eng* 2013; 49: 165–180.

[44] Malhotra S. Selection, design and construction of offshore wind turbine foundations. In: *Wind turbines*. InTech, 2011.

[45] Zaaijer MB. Foundation modelling to assess dynamic behaviour of offshore wind turbines. *Appl Ocean Res* 2006; 28: 45–57.

[46] Adhikari S, Bhattacharya S. Vibrations of wind-turbines considering soil-structure interaction. *Wind Struct An Int J* 2011; 14: 85–112.

[47] Arany L, Bhattacharya S, Adhikari S, et al. An analytical model to predict the natural frequency of offshore wind turbines on three-spring flexible foundations using two different beam models. *Soil Dyn Earthq Eng* 2015; 74: 40–45.

[48] Arany L, Bhattacharya S, Hogan SJ, et al. Dynamic soil-structure interaction issues of offshore wind turbines. In: *Proceedings of the 9th International Conference on Structural Dynamics, EURODYN 2014*. Porto, Portugal, 2014.

[49] Zania V. Natural vibration frequency and damping of slender structures founded on monopiles. *Soil Dyn Earthq Eng* 2014; 59: 8–20.

[50] Damgaard M, Andersen LV, Ibsen LB, et al. A probabilistic analysis of the dynamic response of monopile foundations: Soil variability and its consequences. *Probabilistic Eng Mech* 2015; 41: 46–59.

[51] Harte M, Basu B, Nielsen SRK. Dynamic analysis of wind turbines including soil-structure interaction. *Eng Struct* 2012; 45: 509–518.

[52] International Electrotechnical Commission (IEC). *IEC 61400-3 Wind turbines - Part 3: Design requirements for offshore wind turbines*. 2009.

[53] American Petroleum Institute (API). *Recommended practice for planning, designing and constructing fixed offshore platforms — working stress design*. 2007.

[54] Reese L, Van Impe W, Holtz R. *Single piles and pile groups under lateral loading*. CRC

Press, 2010.

[55] Naggar MH El, Bentley KJ. Dynamic analysis for laterally loaded piles and dynamic p-y curves. *Can Geotech J* 2000; 37: 1166–1183.

[56] Van Buren E, Muskulus M. Improving pile foundation models for use in bottom-fixed offshore wind turbine applications. *Energy Procedia* 2012; 24: 363–370.

[57] Abdel-Rahman K, Achmus M. Finite element modelling of horizontally loaded monopile foundations for offshore wind energy converters in Germany. In: *Proceedings of the International Symposium on Frontiers in Offshore Geotechnics*. Perth, WA, Australia, 2005.

[58] Achmus M, Abdel-Rahman K, Kuo Y-S. Numerical modelling of large diameter steel piles under monotonic and cyclic horizontal loading. In: *Proceedings of the 10th International Symposium on Numerical Models in Geomechanics*. Rhodes, Greece, 2007.

[59] Achmus M, Abdel-Rahman K, Kuo YS. Behavior of large diameter monopiles under cyclic horizontal loading. In: *Proceedings of the 12th International Colloquium On Structural And Geotechnical Engineering*. Cairo, Egypt, 2007.

[60] Achmus M, Kuo YS, Abdel-Rahman K. Behavior of monopile foundations under cyclic lateral load. *Comput Geotech* 2009; 36: 725–735.

[61] Byrne BW, Mcadam R. New design methods for large diameter piles under lateral loading for offshore wind applications. In: *Proceedings of the 3rd International Symposium on Frontiers in Offshore Geotechnics*. Oslo, Norway, 2015.

[62] Zdravkovi L, Taborda DMG, Potts DM, et al. Numerical modelling of large diameter piles under lateral loading for offshore wind applications. In: *Proceedings of the 3rd International Symposium on Frontiers in Offshore Geotechnics*. Oslo, Norway, 2015.

[63] Jonkman JM, Buhl MLJ. *FAST user's guide*. Technical Report NREL/EL-500-38230. National Renewable Energy Laboratory: Golden, CO, USA, October 2005.

[64] Torben J, Melchior A, Version D. *How 2 HAWC2, the user's manual*. Technical Report Risø-R-1597(ver. 3-1)(EN). Risø National Laboratory, Denmark, 2007.

[65] Jonkman J. The new modularization framework for the FAST wind turbine CAE tool. In: *51st AIAA Aerospace Sciences Meeting, Grapvine Texas*. Dallas, Texas, 2013.

[66] Jonkman BJ, Kilcher L. *TurbSim user's guide : version 1. 06.00*. Technical Report. National Renewable Energy Laboratory: Golden, CO, USA, 2012.

[67] Jonkman BJ, Jonkman JM. *FAST v8.16.00a-bjj user's guide*. National Renewable Energy Laboratory, https://wind.nrel.gov/nwtc/docs/README_FAST8.pdf (2016).

[68] Fontana C, Carswell W, Arwade SR, et al. Sensitivity of the dynamic response of monopile-supported offshore wind turbines to structural and foundation damping. *Wind Eng* 2015; 39: 609–628.

[69] Devriendt C, Jordaens PJ, De Sitter G, et al. Damping estimation of an offshore wind turbine on a monopile foundation. In: *EWEA 2012*. Copenhagen, Denmark, 2012.

[70] Valamanesh V, Myers AT. Aerodynamic damping and seismic response of horizontal axis wind turbine towers. *J Struct Eng* 2014; 140: 1–9.

[71] Ozbek M, Meng F, Rixen DJ. Challenges in testing and monitoring the in-operation vibration characteristics of wind turbines. *Mech Syst Signal Process* 2013; 41: 649–666.

[72] Tarp-Johansen NJ, Andersen L, Christensen ED, et al. Comparing sources of damping of cross-wind motion. In: *Proceeding of the Copenhagen Offshore Conference*. Stockholm, Sweden, 2009.

[73] Salzmann DJC, Tempel J Van Der. Aerodynamic damping in the design of support structures for offshore wind turbines. In: *The European Offshore Wind Conference & Exhibition*. Copenhagen, Denmark, 2005.

[74] Freris LL. *Wind energy conversion systems*. New York: Prentice Hall, 1990.

[75] Kühn M. *Dynamics and design optimization of offshore wind energy conversion systems*. PhD Thesis. Delft University of Technology, 2001.

[76] Liu X, Lu C, Li G, et al. Effects of aerodynamic damping on the tower load of offshore horizontal axis wind turbines. *Appl Energy* 2017; 204: 1101–1114.

[77] Cook MF, Vandiver JK. Measured and predicted dynamic response of a single pile platform to random wave excitation. In: *Offshore Technology Conference*. Houston, Texas, 1982.

[78] Johanning L, P. W. Bearman, Graham JMR. Hydrodynamic damping of a large scale piercing circular in planar oscillatory motion. *J Fluids Struct* 2001; 16: 891–908.

[79] J. R. Chaplin, C. H. Retzler. Hydrodynamic damping of the vertical motion of a horizontal cylinder beneath waves at large scale. *J Fluids Struct* 2001; 16: 929–940.

[80] Germanischer Lloyd (GL). Overall damping for piled offshore support structures. In: *Guideline for the Certification of Offshore Wind Turbines*. 2005.

[81] Damgaard M, Ibsen LB, Andersen LV, et al. Cross-wind modal properties of offshore wind turbines identified by full scale testing. *J Wind Eng Ind Aerodyn* 2013; 116: 94–108.

[82] Novak M. Dynamic stiffness and damping of piles. *Canadian Geotechnical Journal* 1974; 11: 574–598.

[83] Gazetas G, Dobry R. Horizontal response of piles in layered soils. *J Geotech Eng* 1984; 110: 20–40.

[84] Seed HB, Idriss IM. *Soil moduli and damping factors for dynamic response analyses*. Technical Report NO. EERC 70-10. Earthquake Engineering Research Centre, University of California, Berkeley, 1970.

[85] Darendeli MB. *Development of a new family of normalized modulus reduction and material damping curves*. PhD Thesis. The University of Texas at Austin, 2001.

[86] European Standard. *EN 1991-1-4 Eurocode 1: Actions on structures -Part 1-4: General actions -Wind actions.* The European Union: Bruxelles, Belgium, 2005.

[87] Barltrop NDP, Adams AJ. *Dynamics of fixed marine structures*. Butterworth-Heinemann, 1991.

[88] Lackner M, Rotea MA. Passive structural control of offshore wind turbines. *Wind Energy* 2010; 14: 373–388.

[89] Rahman M, Ong ZC, Chong WT, et al. Performance enhancement of wind turbine systems with vibration control: A review. *Renew Sustain Energy Rev* 2015; 51: 43–54.

[90] Brodersen ML, Høgsberg J. Damping of offshore wind turbine tower vibrations by a stroke amplifying brace. *Energy Procedia* 2014; 53: 258–267.

[91] Colwell S, Basu B. Tuned liquid column dampers in offshore wind turbines for structural control. *Eng Struct* 2009; 31: 358–368.

[92] Brodersen ML, Høgsberg J. Hybrid damper with stroke amplification for damping of offshore wind turbines. *Wind Energy* 2016; 19: 2223–2238.

[93] Fitzgerald B, Basu B. Active tuned mass damper control of wind turbine nacelle/tower vibrations with damaged foundations. *Key Eng Mater* 2013; 569–570: 660–667.

[94] Stewart GM, Lackner M. Effect of actuator dynamics on active Structural control of offshore wind turbines. *Eng Struct* 2011; 33: 1807–1816.

[95] Li J, Zhang Z, Chen J. Experimental Study on Vibration Control of Offshore Wind

Turbines Using a Ball Vibration Absorber. *Energy Power Eng* 2012; 04: 153–157.

[96] Chen J, Liu Y, Bai X. Shaking table test and numerical analysis of offshore wind turbine tower systems controlled by TLCD. *Earthq Eng Eng Vib* 2015; 14: 55–75.

[97] Schaumann P, Wilke F, Lochte-Holtgreven S. Nonlinear structural dynamics of offshore wind energy converters with grouted transition piece. In: *Proceedings of the European Wind Energy Conference*. Brussels, Belgium, 2008.

[98] Versteijlen WG, Metrikine A V., Hoving JS, et al. Estimation of the vibration decrement of an offshore wind turbine support structure caused by its interaction with soil. In: *Proceedings of the EWEA Offshore 2011 Conference*. Amsterdam, Netherlands, 2011.

[99] Damgaard M, Andersen JKF. Natural frequency and damping estimation of an offshore wind turbine structure. In: *Proceedings of the Twenty-second 2012 International Offshore and Polar Engineering Conference*. Rhodes, Greece, 2012.

[100] Damgaard M, Andersen JKF, Ibsen LB, et al. Time-varying dynamic properties of offshore wind turbines evaluated by modal testing. In: *Proceedings of the 18th International Conference on Soil Mechanics and Geotechnical Engineering*. Paris, France, 2013.

[101] El-Kafafy M, Devriendt C, Sitter G De, et al. Damping estimation of offshore wind turbines using state-of-the-art operational modal analysis techniques. In: *International Conference on Noise and Vbration Engineering*. Leuven, Belgium, 2012.

[102] Shirzadeh R, Weijtjens W, Guillaume P, et al. The dynamics of an offshore wind turbine in parked conditions: A comparison between simulations and measurements. *Wind Energy* 2014; 18: 1685–1702.

[103] Devriendt C, Jordaens PJ, Van Ingelgem Y, et al. Monitoring of resonant frequencies and damping values of an offshore wind turbine. *IET Renew Power Gener* 2014; 8: 433–441.

[104] Koukoura C, Natarajan A, Vesth A. Identification of support structure damping of a full scale offshore wind turbine in normal operation. *Renew Energy* 2015; 81: 882–895.

[105] Bajrić A, Høgsberg J, Rüdinger F. Evaluation of damping estimates by automated Operational Modal Analysis for offshore wind turbine tower vibrations. *Renew Energy* 2018; 116: 153–163.

[106] Schaumann P, Seidel M. Eigenschwingverhalten von windenergieanlagen–berechnungen und messungen. In: *Tagungsband DEWEK (2000)*. Wilhelmshaven,

Germany, 2000.

[107] Ozbek M, J. Rixen D. Operational modal analysis of a 2.5 MW wind turbine using optical measurement techniques and strain gauges. *Wind Energy* 2013; 17: 367–381.

[108] Hansen MH, Thomsen K, Fuglsang P, et al. Two methods for estimating aeroelastic damping of operational wind turbine modes from experiments. *Wind Energy* 2006; 9: 179–191.

[109] Zendehbad M, Chokani N, Abhari RS. Experimental study of aero-mechanical damping of full-scale wind turbines. In: *Proceedings of IGTI2014*. Dusseldorf, Germany, 2014.

[110] Weijtjens W, Rasoul Shirzadeh, Gert De Sitter, et al. Classifying resonant frequencies and damping values of an offshore wind turbine on a monopile foundation for different operational conditions. In: *Proceedings of the European Wind Energy Association*. Barcelona, Spain, 2014.

[111] Dong X, Lian J, Yang M, et al. Operational modal identification of offshore wind turbine structure based on modified stochastic subspace identification method considering harmonic interference. *J Renew Sustain Energy* 2014; 6: 033128.

[112] Dong X, Lian J, Wang H, et al. Structural vibration monitoring and operational modal analysis of offshore wind turbine structure. *Ocean Eng* 2018; 150: 280–297.

[113] Hu W-H, Thöns S, Rohrmann RG, et al. Vibration-based structural health monitoring of a wind turbine system. Part I: Resonance phenomenon. *Eng Struct* 2015; 89: 260–272.

[114] Chen B, Zhang Z, Hua X, et al. Identification of aerodynamic damping in wind turbines using time-frequency analysis. *Mech Syst Signal Process* 2017; 91: 198–214.

[115] James III GH, Carne TG, Lauffer, et al. The natural excitation technique (NExT) for modal parameter extraction from operating wind turbines. *Int J Anal Exp Modal Anal* 1993; 10: 260–277.

[116] Tcherniak D, Chauhan S, Hansen MH. Applicability limits of operational modal analysis to operational wind turbines. In: *Proceedings of the 28th International Modal Analysis Conference*. Jacksonville, Florida, 2010.

[117] Chen C, Duffour P. Modelling damping sources in monopile-supported offshore wind turbines. *Wind Energy* 2018; 21: 1121–1140.

[118] Bisoi S, Haldar S. Design of monopile supported offshore wind turbine in clay considering dynamic soil–structure-interaction. *Soil Dyn Earthq Eng* 2015; 63: 19–35.

[119] Jonkman JM, Butterfield S, Musial W, et al. *Definition of a 5-MW reference wind turbine for offshore system development*. Technical Report NREL/TP-500-38060. National Renewable Energy Laboratory: Golden, CO, USA, 2009.

[120] Reddy JN. *Solutions manual for an introduction to the finite element method*. New York: McGraw-Hill, 2005.

[121] Gavin HP. *Numerical integration in structural dynamics*. Duke University, http://people.duke.edu/~hpgavin/cee541/NumericalIntegration.pdf (2016).

[122] Hodges CH, Power J, Woodhouse J. The use of the sonogram in structural acoustics and an application to the vibrations of cylindrical shells. *J Sound Vib* 1985; 101: 203–218.

[123] Salmon R. *Introduction to Ocean Dynamics*. University of California, San Diego, http://linkinghub.elsevier.com/retrieve/pii/S0074614200800066 (2000).

[124] Kuiper GL, Metrikine A V., Battjes JA. A new time-domain drag description and its influence on the dynamic behaviour of a cantilever pipe conveying fluid. *J Fluids Struct* 2007; 23: 429–445.

[125] Chaplin JR. Hydrodynamic damping of a cylinder at $\beta \approx 106$. *J Fluids Struct* 2000; 0: 1101–1117.

[126] Cook MF. *Damping estimation, response prediction and fatigue calculation of an operational single pile platform*. Master Thesis. Massachusetts Institute of Technology, 1978.

[127] Petrauskas C. *Hydrodynamic damping and "added mass" for flexible offshore platforms*. Technical Paper No. 76-18. Hydraulic Engineering Lab, University of California, Berkeley, 1976.

[128] Jamieson P. *Innovation in wind turbine design*. John Wiley & Sons, 2011.

[129] Subramanian N. *Steel structures - design and practice*. Oxford University Press, 2011.

[130] Petersen JT, Madsen H a, Bjorck A, et al. *Prediction of dynamic loads and induced vibrations in stall*. Technical Report NO. 1045(EN). Forskningscenter Risoe, Denmark, 1998.

[131] Wright JR, Cooper JE. *Introduction to aircraft aeroelasticity and loads*. Second Edi. John Wiley & Sons Ltd, 2014.

[132] Panzer H, Hubele J. *Generating a parametric finite element model of a 3D cantilever Timoshenko beam using MATLAB*. Technical Report Vol. TRAC-4. Institute of

Automatic Control, Technical University of Munich, 2009.

[133] Gutiérrez-Wing ES. *Modal analysis of rotating machinery structures*. PhD Thesis. Imperial College London, 2003.

[134] Devriendt C, Magalhaes F, Weijtjens W, et al. Structural health monitoring of offshore wind turbines using automated operational modal analysis. *Struct Heal Monit* 2014; 13: 644–659.

[135] Jonkman JM, Hayman GJ, Jonkman BJ, et al. *AeroDyn v15 user's guide and theory manual*. Technical Report. National Renewable Energy Laboratory: Golden, CO, USA, 2015.

[136] International Electrotechnical Commission (IEC). IEC 61400-1 Wind turbine generator systems - Part 1: Design requirements. 2005; 2005: 1–92.

[137] Chen SY, M. S. Ju, Y. G. Tsuei. Estimation of mass, stiffness and damping matrices from frequency response functions. *J Vib Acoust* 1996; 118: 78–82.

[138] Bendat JS, Allan G. Piersol. *Random data analysis and measurement procedures*. Second Edi. John Wiley & Sons, 2010.

[139] Ewins DJ. *Modal testing: theory, practice and application*. Second Edi. Research Studies Press LTD., 2000.

[140] National Renewable Energy Laboratory (NREL). FAST v8 and the transition to OpenFAST, https://wind.nrel.gov/nwtc/docs/README_OpenFAST.pdf (2017).

[141] Pintelon R, Schoukens J. *System identification: a frequency domain approach*. Second Edi. John Wiley & Sons, 2012.

[142] Oh S, Ishihara T. Structural parameter identification of a 2.4 MW bottom fixed wind turbine by excitation test using active mass damper. *Wind Energy* 2018; 21: 1232–1238.

[143] Adhikari S, Woodhouse J. Identification of damping: Part 1, viscous damping. *J Sound Vib* 2001; 243: 43–61.